SAPIENZA
UNIVERSITÀ DI ROMA

Chemistry of Calcium batteries

Facoltà di Ingegneria Civile e Industriale

Dipartimento di Ingegneria Chimica Materiali Ambiente
Corso di laurea in Processi Chimici per l'Industria e per l'Ambiente

Andrea Ceppetelli

Matricola 1708977

Relatore (Sapienza)

Sergio Brutti

Relatore (U.Montpellier)

Lorenzo Stievano

A.A. 2024-2025

Finanziato dall'Unione europea NextGenerationEU

Ministero dell'Università e della Ricerca

Italiadomani
PIANO NAZIONALE DI RIPRESA E RESILIENZA

THÈSE POUR OBTENIR LE GRADE DE DOCTEUR DE L'UNIVERSITÉ DE MONTPELLIER

En Chimie des Materiaux

École doctorale Siences Chimiques Balard

Unité de recherche ICGM

En partenariat international avec Università di Roma La Sapienza, ITALIE

Chimie des batteries au calcium

Présentée par Andrea Ceppetelli
Le 16/12/2025

Sous la direction de Lorenzo Stievano et Sergio Brutti

Devant le jury composé de

Lorenzo STIEVANO, Pr., IGCM, Université de Montpellier	Directeur de thèse
Sergio BRUTTI, Assoc. Pr., Università di Roma La Sapienza	Directeur de thèse
Giovanni Battista Appetecchi, ENEA	Rapporteur
Fannie ALLOIN, Dr., CNRS, LEPMI Saint Martin d'Hères	Rapporteuse
Alexandre PONROUCH, Researcher, Institut de Ciència de Materialss de Barcelona	Examinateur
Laure MONCONDUIT Dr., ICGM, Université de Montpellier	Examinatrice
Giuseppe A. Elia, ELIA, Assoc. Pr., Politecnico di Torino	Examinateur
Arcangelo CELESTE, RTDA Researcher, Università di Roma La Sapienza	Examinateur
Laura SILVESTRI, Researcher, ENEA Casaccia	Invitée

UNIVERSITÉ DE MONTPELLIER

Abstract

This PhD thesis addresses the fundamental components of calcium-based batteries, i.e., electrolytes, cathodes, and anodes, through a systematic and integrated investigation aimed at advancing both the understanding and the feasibility of this emerging energy storage technology.

The electrolyte studies focused on the development and evaluation of two novel calcium salts, Ca-FPB and $CaB_{12}H_{12}$, as well as on the adoption of $Ca(TFSI)_2$ in glyme- and phosphate-based solvents. Ca-FPB demonstrated high electrochemical stability and reversible Ca plating/stripping, though its complex, moisture-sensitive synthesis limits scalability. $CaB_{12}H_{12}$ exhibited promising reversibility in specific solvent/additive combinations but with restricted stability windows. These studies highlighted the critical role of electrolyte formulation in enabling stable interphases and reproducible electrochemistry.

To support accurate electrode testing, a pseudo-capacitive three-electrode setup was also developed, providing a stable environment without the complications of metallic calcium.

On the cathode side, intercalation materials such as the Prussian Blue Analogue MF21 were investigated. MF21 demonstrated reversible Ca^{2+} intercalation with structural retention, though capacity fading in full-cell configurations underscored persistent interfacial issues. Tests in the pseudo-capacitive setup confirmed improved stability, at the expense of capacity, pointing to complex electrolyte–electrode interactions that remain to be fully understood.

Anode investigations comprised both intercalation- and alloy-type materials. TiO_2-nanotubes in the anatase phase showed modest but reversible Ca^{2+} intercalation while maintaining structural integrity, suggesting potential for divalent ion storage. Alloy-type anodes were studied in detail, with Ca–Zn and Ca–Sn systems prepared via different synthetic approaches. A systematic screening demonstrated that arc melting is the most effective route for producing homogeneous alloys, outperforming annealing and ball milling. Comparative studies revealed superior cycling stability for Zn-rich Ca–Zn alloys, leading to the identification of $CaZn_2$ as the most promising formulation, further characterized structurally and electrochemically. In parallel, Ca–Sn alloys were preliminarily evaluated, showing initial activity but also rapid deactivation linked to volume expansion and unstable SEI growth.

Overall, this work provides a comprehensive assessment of the limitations and prospects of calcium-based batteries. It establishes methodological guidelines for electrolyte formulation, electrode testing, and alloy synthesis, while identifying $CaZn_2$ as a benchmark alloy composition for further studies.

Although commercialization of Ca-based batteries remains distant, the results presented here contribute to understanding the fundamental processes governing their performance and to laying the groundwork for the rational design of next-generation multivalent energy storage technologies.

Résumé

Cette thèse de doctorat traite des composants fondamentaux des batteries au calcium, c'est-à-dire les électrolytes, les cathodes et les anodes, à travers une investigation systématique et intégrée visant à faire progresser à la fois la compréhension et la faisabilité de cette technologie émergente de stockage de l'énergie.

Les études sur les électrolytes se sont concentrées sur le développement et l'évaluation de deux nouveaux sels de calcium, Ca-FPB et $CaB_{12}H_{12}$, ainsi que sur l'utilisation de $Ca(TFSI)_2$ dans des solvants de type glymes et phosphates. Le Ca-FPB a démontré une grande stabilité électrochimique et la possibilité de dépôt/dissolution réversible du calcium métallique à température ambiante, bien que sa synthèse complexe et sensible à l'humidité limite son extensibilité. Le $CaB_{12}H_{12}$ a montré une réversibilité prometteuse dans certaines combinaisons solvant/additif, mais avec des fenêtres de stabilité restreintes. Ces résultats ont mis en évidence le rôle critique de la formulation des électrolytes pour permettre la formation d'interphases stables et une électrochimie reproductible.

Afin de soutenir une évaluation précise des électrodes, un dispositif pseudo-capacitif à trois électrodes a également été développé, fournissant un environnement stable sans les complications liées au calcium métallique.

Du côté des cathodes, des matériaux d'intercalation tels que l'analogue bleu de Prusse MF21 ont été étudiés. Le MF21 a démontré une intercalation réversible de Ca^{2+} avec maintien de la structure, bien que la perte rapide de capacité en configuration pile entière ait souligné des problèmes interfaciales persistants. Les tests dans la configuration pseudo-capacitive ont confirmé une meilleure stabilité, au détriment de la capacité, indiquant des interactions complexes électrolyte–électrode qui restent à élucider.

Les investigations sur les anodes ont porté à la fois sur des matériaux d'intercalation et d'alliage. Les nanotubes de TiO_2 en phase anatase ont montré une intercalation modeste mais réversible de Ca^{2+} tout en conservant leur intégrité structurelle, suggérant un potentiel pour le stockage d'ions divalents. Les anodes d'alliage ont été étudiées en détail, en particulier les systèmes Ca–Zn et Ca–Sn préparés par différentes approches de synthèse. Un criblage systématique a démontré que la fusion par arc est la méthode la plus efficace pour produire des alliages homogènes, surpassant le recuit et le broyage mécanique. Les études comparatives ont révélé une stabilité de cyclage supérieure pour les alliages Ca–Zn riches en zinc, menant à l'identification de $CaZn_2$ comme la formulation la plus prometteuse, caractérisée plus en détail sur les plans structural et électrochimique. En parallèle, les alliages Ca–Sn ont été évalués de manière préliminaire, montrant une activité initiale mais également une désactivation rapide liée à la croissance instable de la SEI.

Dans l'ensemble, ce travail fournit une évaluation complète des limites et des perspectives des batteries au calcium. Il établit des lignes directrices méthodologiques pour la formulation des électrolytes, l'évaluation des électrodes et la synthèse des alliages, tout en identifiant $CaZn_2$ comme composition de référence pour de futures études. Bien que la commercialisation des batteries au calcium demeure lointaine, les résultats présentés ici contribuent à une meilleure compréhension des processus fondamentaux qui régissent leurs performances et posent les bases de la conception rationnelle des technologies de stockage multivalent de nouvelle génération.

Table of Content

Abstract……5

Résmé……7

1 Chapter I: Introduction ……16

1.1 Context and Motivation ……16

1.2 From Lithium-Ion Batteries (LIBs) to Multivalent Metals ……18

1.3 History of Progress in Calcium Batteries ……20

1.4 Ongoing Challenges ……24

1.4.1 Ca metal negative electrode (or counter-electrode): ……24

1.4.2 Electrolytes: ……25

1.4.3 Ca cathodes: ……25

1.5 Goal and Structure of the Thesis ……26

1.6 Bibliography ……28

2 Chapter II: Calcium aprotic electrolytes ……36

2.1 2.1 Introduction ……36

2.1.1 Electrolytes characteristics ……36

2.1.2 Early Developments of Calcium Electrolytes for Rechargeable Batteries ……37

2.1.3 Revisiting of the Traditional Calcium Salts ……38

2.1.4 Advanced Calcium Electrolytes with weakly-Coordinating Anion (WCA) ……40

2.2 Preliminary examination of Ca-FPB: a promising Salt for Aprotic Electrolytes in Calcium-based Secondary Batteries ……40

2.2.1 Introduction ……40

2.2.2 Experimental section ……41

2.2.3 Results and discussion ……42

2.2.4 Electrochemical characterization ……43

2.2.5 Conclusion ……45

2.3 Extending the boron-based salt variety: the case of $CaB_{12}H_{12}$ ……45

2.3.1 Introduction ……45

2.3.2 Experimental section ……46

2.3.2.1 Synthesis of calcium dodecahydro-closo-dodecaborate ……46

2.3.2.2 Physico-chemical characterization ……47

2.3.3 Results and discussion ……48

2.3.4 Conclusion ……59

2.4 General conclusion ……60

2.5 Bibliography....62
3 Chapter III:....70
3.1 Introduction....70
3.2 Manufacture of AC electrode....71
3.3 Pseudo-capacitive approach....71
3.4 Conclusions....74
3.5 Bibliography....75
4 Chapter IV....83
4.1 Introduction to Cathode Materials for CIBs: Focus on Prussian Blue Analogues....83
4.2 PBA as cathode for CIBs....85
4.2.1 Introduction....85
4.2.2 Experimental Section....85
4.2.3 Result and discussion....87
4.2.4 Conclusion....92
4.3 Bibliography....94
5 Chapter V....99
5.1 Introduction....99
5.2 Nanostructured titanium oxide nanotubes as negative electrode for CIBs....101
5.2.1 Experimental methods....101
5.2.1.1 Synthesis of the anatase nanotubes....101
5.3 Results....105
5.3.1 Preliminary anatase nanotubes characterization....105
5.3.2 Electrochemical Performance....107
5.3.3 Post mortem analysis by ex situ XANES....109
5.3.4 EXAFS data analysis....113
5.3.5 Conclusions....116
5.4 Ca-based alloy....118
5.4.1 Introduction....118
5.4.2 Ca-Zn alloy....118
5.4.2.6 Physico-chemical characterization....123
5.4.3 Results and discussion....124
5.4.4 Conclusion....135
5.5 Preliminary examination of Ca-Sn alloy....136
5.5.1 Experimental section....136
5.5.2 Result and discussion....138
5.5.3 Conclusion....142

5.6 Bibliography.....143
6 Chapter VI.....150
6.1 General Conclusions.....150
6.2 Perspectives.....153

List of Figures and Tables

Figure 1.1 International Energy agency (IEA, 2025), Change in electricity demand by region, 2021-2027.[4] 16
Figure 1.2 Change in global surface temperature compared to the long-term average from 1951 to 1980. on the right shows the change in global surface temperatures. Dark blue shows areas cooler than average. Dark red shows areas warmer than average.[6] 17
Figure 1.3 Scopus analysis of Ca battery publications [37] 19
Figure 1.4 a) Timeline of Ca use in battery technology,[35] b) Evolution and advances of lithium battery technologies.[38] 20
Figure 2.1. (a) Schematic representation of the Ca-FPB synthesis; (b) Infrared spectrum with vibrational modes of the different bonds indicated; (c) ^{11}B- and (d) ^{19}F NMR spectra; (e) ^{11}B- and (f) ^{19}F NMR spectra in the presence of water over 7 h. 43
Figure 2.2 EDX analysis of Ca deposit on carbon coated aluminium respectively. 44
Figure 2.3 Schematic representation of autoclave synthesis of $CaB_{12}H_{12}$ 47
Figure 2.4 a) ^{1}H CP-MAS ^{11}B NMR spectra of the solids obtained after synthesis at 200°, 215° and 230°C (the solids were dissolved in DMSO); b) IR spectra of $Ca(BH_4)_2$, diglyme and the $CaB_{12}H_{12}$ synthesized salts at the three different temperatures 49
Figure 2.5 a) LSV and b) CV of all the electrolytes formulations. 50
Figure 2.6 LSV and CV of $CaB_{12}H_{12}$@215 in line a) and $CaB_{12}H_{12}$@230 in line b) at the three different concentrations. 51
Figure 2.7 a) LSV and b) CV of $CaB_{12}H_{12}$@215 in NMP at 0.1, 0.25 and 0.5M 51
Figure 2.8 conductivity plot of $CaB_{12}H_{12}$@215 at 0.1, 0.25 and 0.5M 52
Figure 2.9 Electrochemical stability window of $CaB_{12}H_{12}$ a) 0.5M and b) 0.25M in NMP 54
Figure 2.10. Ca | $CaB_{12}H_{12}$@215 0.25M in NMP | Ca cell tested by a) OCV and GC at different current with b) EIS after every 10 minutes during OCV and c) after every discharge of the GC 55
Figure 2.11. Ca | $CaB_{12}H_{12}$@215 0.25M in NMP | Ca cell tested by a) OCV and GC at different current with b) EIS after every 10 minutes during OCV and c) after every discharge of the GC. 55
Figure 2.12 CV of a) $CaB_{12}H_{12}$@215 0.5M and b) with BF_3OEt_2 as additive. 57
Figure 2.13 ESW of $CaB_{12}H_{12}$@215 0.5M with BF_3OEt_2 as additive 57
Figure 2.14 Ca | $CaB_{12}H_{12}$@215 0.5M in NMP +0.01M BF_3OEt_2 | Ca cell tested by a) OCV and GC at different current with b) EIS after every 10 minutes during OCV and c) after every discharge of GC. 58
Figure 2.15 a) potential profile of the galvanostatic plating of Ca on Au; b) light optic microscope image of Ca deposit; c) backscattered electrode image of Ca deposit with, on the right, the EDX elemental mapping. 59
Figure 3.1 a) Scheme of the three-electrode Swagelok cell. b) Cyclic voltammogram (CV) of 0.05 M Fc in 0.5 M $Ca(TFSI)_2$ in DME solution at 10 mV s−1 (WE and QRE: Au, CE: AC). c) Position of the Fc+/Fc vs. SHE (upper), vs Au QRE and the Ca^{2+}/Ca (below). 71
Figure 3.2 a) stability CV with same cell configuration and scan rate of Figure 3.1; b) calculated redox potential of the CV in figure 3.1. plotted versus time. 73
Figure 4.1 Galvanostatic cycling of a) pristine MF21 and b) depotassiated (-K)MF21 against Ca metal; c) galvanostatic cycling of MF21 vs K. 87
Figure 4.2 a) Whatman and Ca metal electrode after 3 cycles; b) and c) represent the galvanostatic cycling of the depotassiated (-K)MF21 against Ca metal, respectively before and after the renewing of the passivated Ca electrode and Whatman separator. 88

Figure 4.3 a)XRF table, b) and c) galvanostatic curve of the samples with circled the corresponding state of charge, representing the depotassiation and calciation of MF21 respectively 89
Figure 4.4 a) b) c) are the XRD pattern of the samples on the right i.e. pristine, at EOC and EOD respectively; and d) the corresponding table. 90
Figure 4.5 a), b) and c) are the Mossbauer spectroscopy of the samples of the electrode pristine, at EOC and EOD respectively; d) report the corresponding table results. 90
Figure 4.6 galvanostatic curves of charge and discharge on the left and on the right the corresponding in situ XRD on the right of MF21 vs Ca; the patterns of the PBA show obvious peaks at about 19.5; 28.8; 35.4; 40.7 and 43.8 that gradually shift to smaller angles by monophasic mechanism. 91
Figure 4.7 Galvanostatic cycling of MF21 against AC counter electrode and Au as QRE with $Ca(TFSI)_2$ 0.5M in DME as electrolyte. 92
Figure 5.1 Morphological evolution of the hydrated NTs at various stages of the Na^+/H^+ ion-exchange process. The $Na_2Ti_3O_7$ phase obtained by hydrothermal reaction has been titrated with 0.01m aqueous HCl and the intermediate samples have been collected by filtration at different pH values and were dried at 80 °C overnight in air. The Na/Ti atomic ratio has been derived from EDX data. 105
Figure 5.2 TEM micrograph of the a-NTs after annealing at 380 °C 106
Figure 5.3(a) Raman spectra and (b) XRD patterns of the $H_2Ti_3O_7$ precursor and the TiO2 NTs after annealing. The vibrational modes and the Bragg lines are indexed by the TiO_2 anatase lattice (space group I41/amd). *These peaks are due to the sample holder. 107
Figure 5.4 Performance of the a- NTs electrodes by using the (C1) or (C2) cell configurations. Current rate 5 mAg^{-1}; shown cycles are 2-5 of the whole galvanostatic test and are obtained after 1 activation cycle. 108
Figure 5.5 Performance of the a-NT pelletized electrodes in Li, Na, and Ca metal half-cell..... 110
Figure 5.6 Normalized experimental XANES spectra (a) at the Ti K-edge, collected on pristine a-NTs and after full electrochemical intercalation of the Li^+, Na^+, and Ca^{2+} ions; (b) at the Ca K-edge, collected on the $CaCO_3$ standard, on a 0.1 M $CaCl_2$ aqueous solution,[20] and on a-NTs after full electrochemical Ca^{2+} intercalation. In the inset of Figure 6a the pre-edge peak region showing the A1, A2, A3, and B transitions is magnified. The upper inset of Figure 6b shows the energy region with the [1s3p] and [1s3s] double-electron excitation channels, while the lower inset shows the pre-edge peak region corresponding to the 1s→3d transition..... 112
Figure 5.7. Analysis of the Ca K-edge EXAFS spectrum collected on a-NTs after full electrochemical Ca^{2+} intercalation. Upper panel: Ca-O theoretical signal (blue line) compared with the experimental data (red dots) and resulting residuals (green dots). Lower panel: non-phase shift corrected FTs of the best-fit EXAFS theoretical signal (blue line) and of the experimental data (red dots)..... 114
Figure 5.8 Analysis of the Ca K-edge EXAFS spectrum collected on a-NTs after full electrochemical Ca^{2+} intercalation carried out with the inclusion of the Ca-Ti contribution. Upper panel: Ca-O and Ca-Ti theoretical signals, total theoretical contribution (blue lines) compared with the experimental data (red dots) and resulting residuals (green dots). Lower panel: non-phase shift corrected Fourier transform (FT) of the best-fit EXAFS theoretical signal (blue line) and the experimental data (red dots)..... 115
Figure 5.9 a) voltage profile of galvanostatic charge of aNT; b) XRD of pristine electrode of aNTS and b) after calciation of figure a). the two * peaks are attributed to the copper current collector; c) magnification of the shifted peak of figure b)..... 116
Figure 5.10 Schematic representation of arc melting synthesis procedure of Ca-Zn alloy 121

Figure 5.11. XRD patterns of Ca–Zn alloys with nominal Ca_5Zn_3 composition synthesized by annealing (a) and arc melting (b), compared with reference patterns of Ca_5Zn_3 (ICSD 55584) and Ca_3Zn (ICSD 58948).....125
Figure 5.12. SEM micrographs of Ca–Zn alloys with nominal Ca_5Zn_3 composition synthesized by annealing (a, b) and arc melting (c, d), with corresponding EDX quantitative analyses reported in the tables below each image. Annealed samples show surface oxides (a) and Ca-rich/Zn-deficient regions (b), indicating compositional inhomogeneities, while arc-melted alloys display a more homogeneous microstructure with no pronounced deviations in Ca/Zn ratios.....126
Figure 5.13 Galvanostatic cycling (GC) profiles of Ca–Zn alloys in symmetric cells with $Ca(TFSI)_2$ 0.4 M in G1, G2, and TEP as electrolyte: (a) comparison between Ca_5Zn_3 samples synthesized by annealing and arc melting; (b) comparison between arc-melted Ca-rich (Ca_5Zn_3) and Zn-rich ($CaZn_2$) alloys. 127
Figure 5.14 Diffraction pattern acquired for the 4 batch of $CaZn_2$.....128
Figure 5.15 a) Rietveld Refinement, $CaZn_2$ phase was identified using the Inorganic Crystal Structure Database (ICSD, code: 418971), while $CaZn_3$ phase was modelled based on crystallographic data extracted from the literature[79] and implemented into a custom FullProf .pcr file for Rietveld refinement; b) SEM images and c) EDX maps and spectrum of $CaZn_2$ 129
Figure 5.16 $CaZn_2$ | Ca(TFSI)2 0.4M in G1, G2, TEP | $CaZn_2$ – Symmetric cell configuration: a) cyclic voltammetry; b) galvanostatic cycling with c) EIS performed at the end of each cycle; d) Nyquist plot and the equivalent circuit of the EIS 131
Figure 5.17 a) cyclic voltammetry in symmetric cell configuration of Ca metal and $CaZn_2$ based electrode; b) electrochemical stability window of the WCA-type electrolyte; c) comparison of the anodic stability of the two $Ca(TFSI)_2$-based electrolyte. 132
Figure 5.18 a) Voltage-capacity profile and b) cycling performance of the galvanostatic cycling of NTCDA | Ca(TFSI)2 0.4M in G1,G2, TEP | $CaZn_2$. In this configuration, lithium metal was employed as a quasi-reference electrode (QRE) due to its well-defined and relatively close electrochemical potential to that of calcium (with a difference of approximately 0.17 V),[81,82] as well as the ease of handling and cell assembly it offers due to his softness and ductility of lithium make it easier to process and integrate into the cell configurations, facilitating reproducible and robust cell assembly. This choice enabled simplified cell architecture and reliable potential control during the cathode cycling experiments. 132
Figure 5.19. Galvanostatic profile of single discharge to further characterize the NCTDA-based cathode by EDX shown below.....133
Figure 5.20 (a–c) Cross-sectional SEM images of the discharged NTCDA cathode, showing the locations of point EDX analyses performed progressively from the current collector side (a) to the separator interface (c). For each position, the corresponding elemental composition in atomic percentage is reported in the table below the image. 134
Figure 5.21 Galvanostatic profile of partially discharged NCTDA-based cathode to further characterize by EDX shown below. 134
Figure 5.22 (a–c) Cross-sectional SEM images of the partially discharged NTCDA cathode, showing the locations of point EDX analyses performed progressively from the current collector side (a) to the separator interface (c). For each position, the corresponding elemental composition in atomic percentage is reported in the table below the image. 135
Figure 5.23 (a) and (d) SEM image and corresponding EDX elemental distribution on the right; (b) and (c) show point EDX analyses on different morphologies, with the corresponding elemental composition tables on the right. 138
Figure 5.24. XRD patterns of Ca–Sn alloys with varying Ca:Sn atomic ratios synthesized via arc melting, compared with standard reference patterns from the ICSD database for the following

phases: CaO (ICSD 26959), Ca_2Sn (ICSD 659611), $CaSn_3$ (ICSD 58934), CaSn (ICSD 165193), and $Ca_{0.15}Sn_{0.85}$ (ICSD 58963). 139
Figure 5.25 CV in symmetric cell configuration of the CaSn alloy with the different Sn/Ca ratio. 140
Figure 5.26 GC in symmetric cell configuration of the Ca-Sn alloy with the different Sn/Ca ratio 141

Chapter I: Introduction

1.1 Context and Motivation

Batteries constitute one of the most vital technologies driving modern society, serving crucial roles across various sectors, including electric mobility, consumer electronics, and energy storage systems for renewable sources. The escalating demand for portable and efficient energy solutions drives the battery sector into a realm of continuous research and innovation aimed at enhancing performance, lowering production costs, and mitigating environmental impact.[1] A striking projection, shown in figure 1.1, indicates that global electricity consumption is expected to grow at its most rapid rate between 2025 and 2027, driven by factors such as increased industrial production and a surge in air conditioning usage, alongside significant expansion of global data centers.[2] Notably, a 4.3% rise in global and it is expected to stabilize at nearly 4% annually leading up to 2027. Over this period, an unprecedented increase of approximately 3,500 TWh in electricity consumption is anticipated, roughly equivalent to the annual electricity needs of Japan,[2] alongside a marked escalation from a mere 2.5% increase in 2023 linked to fluctuations in regions like China, India, and Southeast Asia.[3]

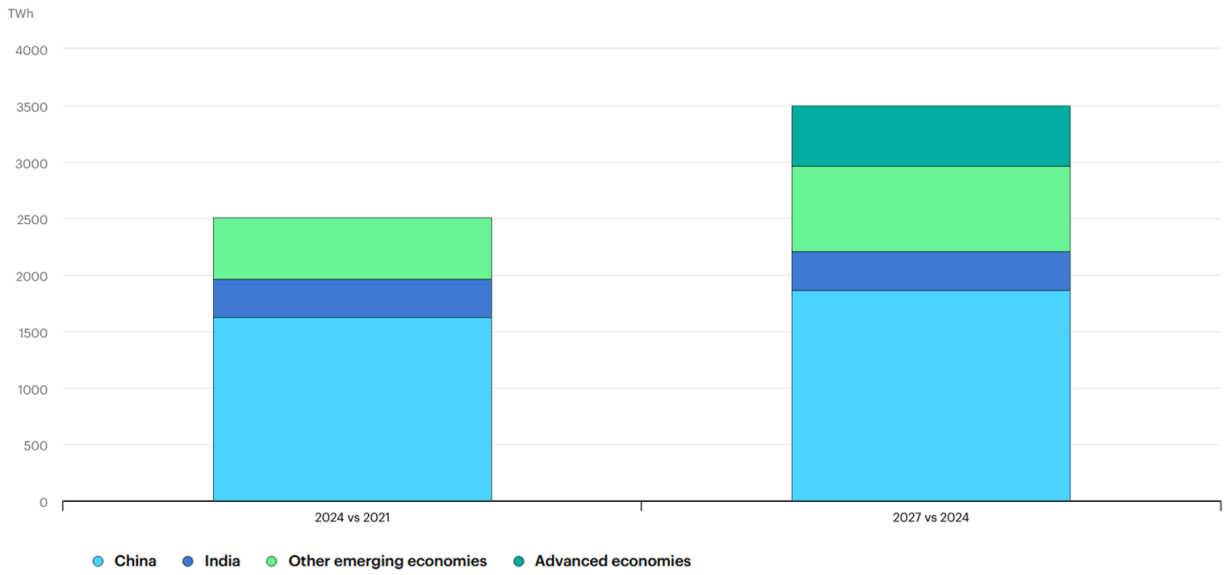

Figure 1.1.1 International Energy agency (IEA, 2025), Change in electricity demand by region, 2021-2027[4]

In addition, climate change is increasingly recognized as the most urgent global challenge, a feeling shared by a large consensus of scientists worldwide. The Intergovernmental Panel on Climate Change (IPCC) consistently provides comprehensive assessments illustrating the current state of climate change and its severe implications.[4] Data demonstrates that the ten warmest years on record have transpired since 2005, with five of the hottest years clustered between 2015 and 2020, evidencing a significant global temperature rise of approximately 1.2°C since pre-industrial times (see figure 1.2).[5]

Projections signal that unless drastic reductions in greenhouse gas emissions occur, the pivotal threshold of 1.5°C may be breached within the next 15 to 20 years. The commitments established by the 2015 Paris Agreement have been overshadowed by a surge in fossil fuel usage and deforestation, intensifying temperature escalations and threatening dire consequences, which include extreme weather phenomena, rising sea levels, and profound ecological disruptions.[6,7]

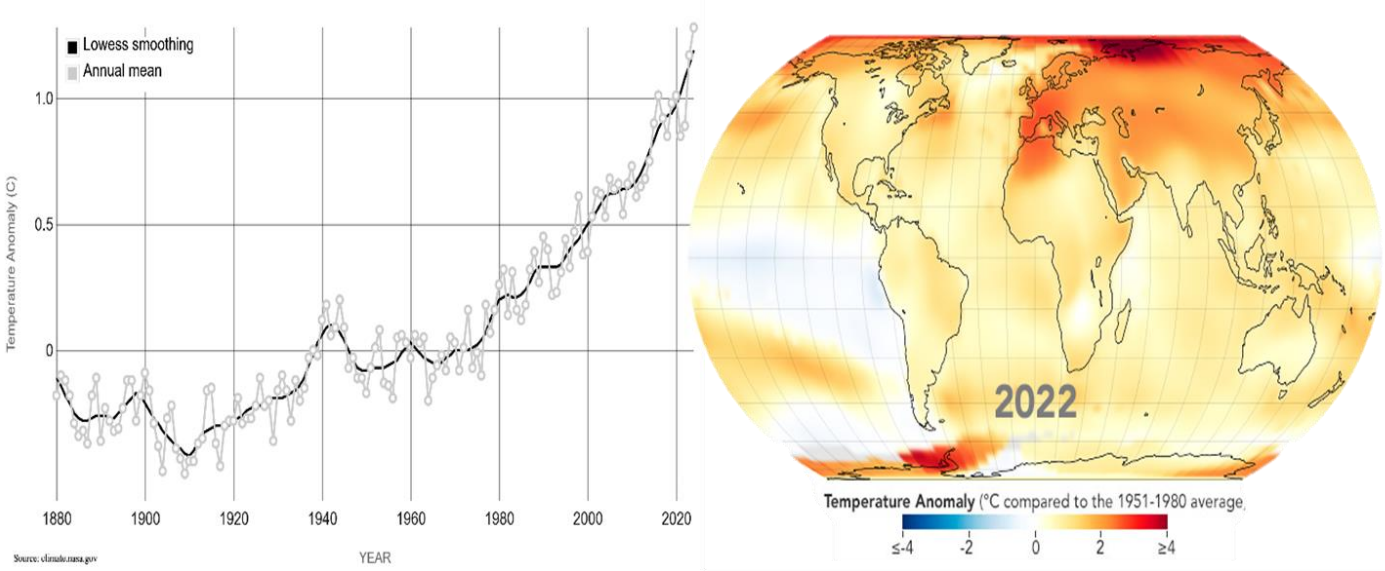

Figure 1.2Change in global surface temperature compared to the long-term average from 1951 to 1980. on the right shows the change in global surface temperatures. Dark blue shows areas cooler than average. Dark red shows areas warmer than average.[6]

In this context of urgent carbon emission reductions, energy storage has emerged as a cornerstone for establishing a more flexible and sustainable energy infrastructure. Vital to achieving decarbonization across electricity, heating, and transportation sectors is the enhancement of energy storage capacities. [8–11] An array of energy storage technologies continues to be explored and refined, categorized based on materials employed, mechanisms for energy storage, responsiveness, and duration. This broad spectrum encompasses mechanical, electrochemical, electrical, thermochemical, chemical, and thermal energy storage systems.[8,12]

The development of efficient and cost-effective batteries is increasingly recognized as a key factor in achieving environmental sustainability. This assertion is supported by a growing body of literature that emphasizes the vital role of advanced battery technologies.[13] Renewable energy sources such as wind and solar are essential replacements for fossil fuels, but their inherent intermittency drives the demand for robust storage solutions that ensure energy availability throughout differing demand periods. Wind energy generation, for example, is contingent on weather conditions, while solar energy production is confined to daylight hours; consequently, scalable and economical battery technologies are fundamental for reliable energy access.[11,14] Moreover, economic drivers, along with environmental and strategic motivations, propel the gradual transition from conventional combustion-based energy mechanisms towards renewable sources,[15–17] thereby amplifying the imperative for

advanced battery solutions that can readily meet rising demand associated with transportation electrification.

1.2 From Lithium-Ion Batteries (LIBs) to Multivalent Metals

Lithium-ion batteries (LIBs) represent a leading technology due to their high energy efficiency, making them appear as ideal candidates to facilitate this energy transition. The achievements of the LIB technology catalysed the widespread adoption of portable electronic devices within society, presenting a near-term avenue for sustainable transportation solutions that require reduced environmental impacts alongside providing stationary energy storage capabilities for renewable energy derived from solar and wind sources. While LIBs have seen significant optimization over the past two decades and the costs associated have evidenced a declining trajectory,[18,19] the technology is currently approaching inherent limits regarding energy density which typically range between 200 and 250 Wh/kg depending on the specific chemistry used.[19,20] Historically, the pursuit of higher energy densities has been a significant impetus driving innovations within battery research. Nonetheless, intrinsic constraints imposed by the existing material and structural paradigms of LIBs pose increasingly challenging obstacles to overcome.[21,22]

Taken together, these factors indicate that conventional LIBs technology alone is unlikely to meet the long term demands for higher energy density and large-scale deployment, thereby providing a strong motivation for the development of post lithium-ion chemistries.

Furthermore, LIBs rely on critical materials such as lithium (Li), nickel (Ni) and cobalt (Co), elements notorious for their prohibitive costs and susceptible to geopolitical supply disruptions, as well as with environmental ramifications and market fluctuations. In addition to technical limitations, this strong dependence on critical and unevenly distributed raw materials further increases the strategic risk associated with relying solely on LIB technology for future energy storage needs.[23] These considerations render the exploration and development of alternative battery chemistries not just advantageous but essential for creating more sustainable, less resource-dependent solutions poised for scalable application.[24,25]

Application of multivalent ions such as Mg^{2+}, Ca^{2+}, or Al^{3+} as charge carriers is particularly compelling. Such multivalent ions hold the potential to enable an increased capacity for storage and electron transport per ion, theoretically doubling the charge storage capacity compared to monovalent ions such as Li^{+} or Na^{+}. This capacity can alternatively translate to achieving equivalent charge

storage with approximately half the number of ions, thereby diminishing the demands placed on ionic transport, potentially enhancing overall battery performance.[26,27]

Within this broader family of multivalent systems, calcium has recently attracted particular attention as it combines several of these advantages with favourable abundance, cost and redox properties.

Among the spectrum of candidate multivalent metals, calcium emerges as an exceptional candidate due to its advantageous integration of properties. Being the fifth most abundant element on Earth's crust, it is more readily available than lithium, sodium, potassium, magnesium, and zinc, coupled with its economically favourable profile owing to its low industrial costs.[28] Notably, calcium is non-toxic, presents a high melting point (842 °C) for safe operations and exhibits the most negative redox potential (−2.87 V vs. SHE) among its multivalent counterparts. Furthermore, with a density of 1.54 g/cm³ and a specific charge capacity of 1.34 Ah/g, calcium metal anodes possess a theoretical volumetric energy density of 2.06 Ah/cm³. In comparison, conventional graphite anodes utilized in current LIBs average around 0.97 Ah/cm³, indicating the potential for achieving a twofold enhancement in energy density using calcium-based materials.[29]

These metrics illustrate why calcium-based devices are increasingly regarded as promising candidates for next generation rechargeable batteries that could offer higher energy density with lower reliance on critical raw materials. Moreover, it is anticipated that theoretically Ca^{2+} ions display superior ionic mobility in liquid electrolytes relative to Mg^{2+} or Al^{3+}, attributable to a comparatively lower charge density (or charge-to-radius ratio).[28,30] This results in a diminished polarizing effect, enhancing the transport kinetics. The ionic radius of Ca^{2+} is remarkably similar to that of Na^{+}, i.e., approximately 1.00 Å, while that of Na^{+} is around 1.02 Å. This close correspondence in ionic dimensions facilitates the behaviour of these cations in various chemical contexts, particularly regarding their capacity for intercalation and deintercalation within a range of materials. Na^{+} ions are known for their ease of insertion into and extraction from layered structures, such as transition metal oxides and clays, largely because their size allows effective coordination within a wide range of host structures, which facilitates ion insertion and extraction.[31–33] Although interest in calcium-ion batteries has surged only in recent years (see Figure 1.3), the use of calcium in electrochemical systems has historical roots that precede the development of lithium-based battery technologies.[34] A pictorial timeline of the use of Ca and Li in batteries is shown in the Figure 1.4 a and b respectively.[34,35]

Taken together, these considerations justify the significant research efforts currently devoted to calcium-based systems, which aim to combine the high energy density and cost advantages of calcium metal with more sustainable, large scale and geopolitically robust energy storage technologies.

1.3 History of Progress in Calcium Batteries

The earliest documented application of calcium within the domain of battery technology can be traced back to 1935, wherein the element was utilized not as an electroactive constituent but rather as an alloying agent to reinforce lead grids in lead-acid batteries.[36,37] The identification of calcium as an electrochemically active metal dates back to 1964, emerging from studies on primary thermal batteries designed for use in aerospace and defence sectors. Essential to these designs were high-melting-point electrolytes characterized by mixtures of various metal chlorides that remained inert at ambient conditions to prevent self-discharge during prolonged storage, only activating thermally when required. A notable example of such a cell configuration was the Ca/KCl–LiCl–AgCl–K_2CrO_4/Ag cell, which exhibited discharge capabilities extending up to 450 °C for approximately 11 minutes, despite enduring challenges associated with Li–Ca alloy formation at the anode.[38]

Subsequent explorations concerned the surface modification of calcium anodes, particularly through the formation of $CaCO_3$ via treatment with acetic acid. However, this pathway elucidated complex interfacial chemistries, often resulting in mixed corrosion products, such as Ca_2CrO_4Cl and $KCaCl_3$.[39] Moreover, attempts to replace chloride-based electrolytes with lower-melting nitrates encountered limitations attributed to the formation of a passivation layer primarily composed of CaO, restricting the redox catalysis of calcium to a single-electron transfer per calcium atom, drastically hampering reversibility. Additives, such as halide salts, were explored to disrupt these passivation layers and enhance ionic mobility.[40]

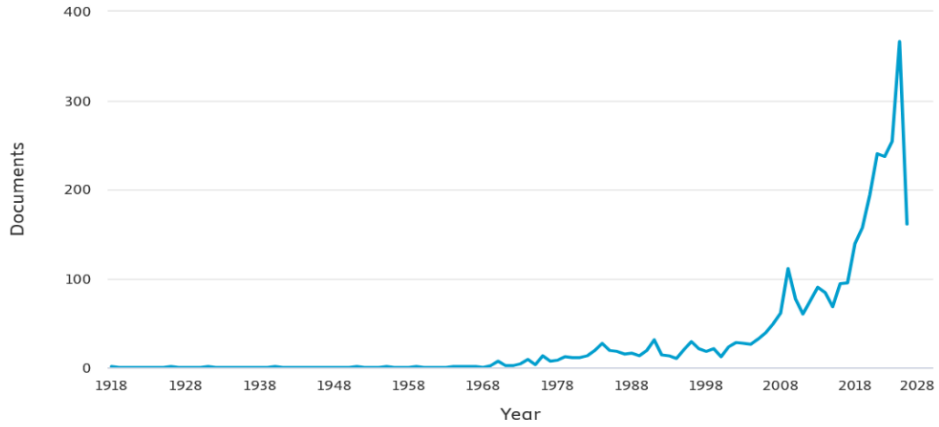

Figure 1.3 Scopus analysis of Ca battery publications [37]

Simultaneously, high-temperature battery concepts were broached, encompassing rechargeable systems employing Ca–Si alloy anodes and β″-alumina solid electrolytes conducting Ca^{2+} ions operating at approximately 580 °C, along with configurations utilizing Ca–Y alloy anodes

complemented by fluoride-conducting solid electrolytes. Investigations even spanned into assembling Ca–O_2 cells engaging zirconia-based electrolytes.[41,42] While limited charge-discharge cycles could be demonstrated, insufficient characterization of the fundamental redox mechanisms precipitated a pronounced decline in further inquiry into these avenues.

Around the same period, Staniewicz et al. proposed Ca–$SOCl_2$ cells as prospective alternatives to Li–$SOCl_2$ systems, accentuating safety advantages conferred by calcium's incapacity to form plating during reversible operations.[43] Subsequent characterizations attributed this behavior to the production of ionic insulator passivation layers predominantly composed of $CaCl_2$, which limited electrochemical performance.[44–46] Future research ventured into related designs achieving slightly elevated cell voltages, yet prominent issues surrounding calcium electrode corrosion produced rapid capacity losses, with an estimated decline of 10% observed within a mere two-week shelf-storage period.[47]

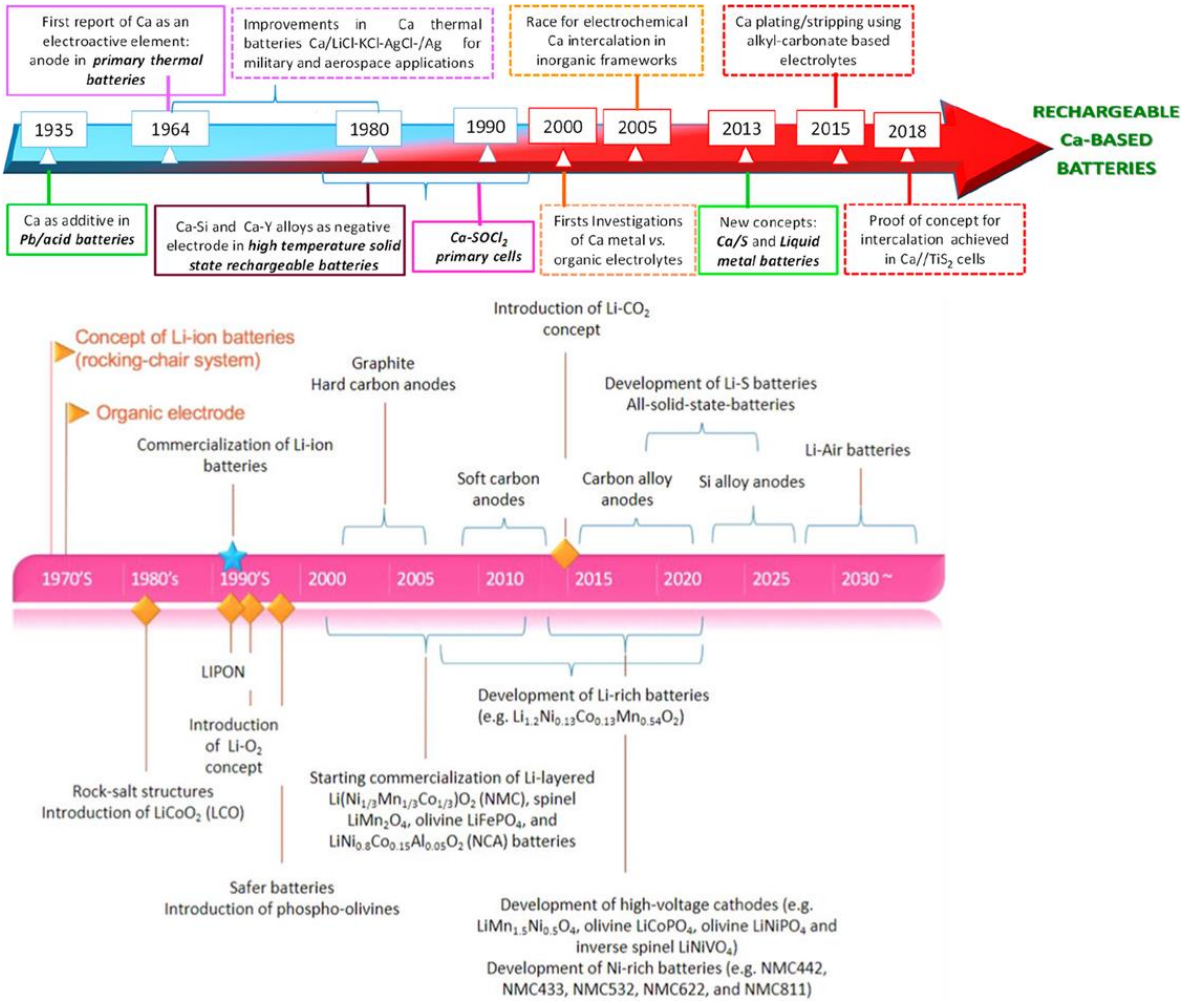

Figure 1.4 Timeline of Ca use in battery technology,[35] b) Evolution and advances of lithium[38]

Advancements included the investigation of additives, such as $Ca(AlCl_4)_2$, $Sr(AlCl_4)_2$, and $Ba(AlCl_4)_2$, aimed at modifying passivation layers and curtailing corrosion.[43,47,48] Notably, the reactivity between calcium metal and the stainless-steel casing materials, echoes challenges reflected in lithium systems,

became evident during investigations. Despite these diverse explorations, calcium-based systems consistently failed to present compelling advantages compared to established lithium technologies, resulting in their retention within niche military applications.[49]

The challenges associated with calcium metal deposition stymied further explorations into secondary calcium batteries. Despite these setbacks, foundational studies conducted by Aurbach et al. evaluated the behavior of calcium metal in organic electrolytes typified by those eulogized during the early evolution of lithium-ion battery technology.[50] These investigations encompassed solvents such as acetonitrile (ACN), tetrahydrofuran (THF), γ-butyrolactone (gBL), and propylene carbonate (PC), utilizing calcium-containing salts such as $Ca(ClO_4)_2$ and $Ca(BF_4)_2$. The findings confirmed that the established passivation layers on calcium metal were largely impermeable to Ca^{2+} ions, mirroring observations from $SOCl_2$-based systems, thus blocking te reversible plating and stripping of calcium.

By the early 2000s, LIBs were firmly established within the market landscape,[51] the renewed interest in metal anodes and multivalent-ion chemistries emerged as a strategic route to enhance energy density, with calcium-based systems viewed as an exotic research avenue. Despite promising findings in magnesium systems utilizing organohaloaluminate-based electrolytes that permitted reversible Mg deposition,[52] parallel breakthroughs for calcium failed to materialize principally due to the unavailability of suitable electrolytes. This limitation shifted early investigations toward studying Ca^{2+} intercalation into host materials, frequently utilizing non-metallic anodes such as activated carbon. [53]

The genesis of early studies into Ca^{2+} intercalation traces back to the 1960s and 1970s, inspired by pioneering research within intercalation chemistry.[54] These formative explorations focused on layered compounds with van der Waals structures (specifically, WS_2, TaS_2, TiS_2, MoO_3, and V_2O_5) facilitating the intercalation of various cations. While lithium and other alkali metals dominated earlier studies, occasional investigations into calcium were conducted, predominantly through chemical intercalation employing aqueous hydroxide solutions or through calcium metal dissolved in liquid ammonia.[55–57]

The emergence and rapid advancement of LIBs technology during the 1970s gradually shifted attention away from multivalent systems, resulting in a long period of limited exploration into calcium-based electrochemistry. However, interest in calcium began to re-emerge in the early 21st century, driven by the aforementioned motivations. This resurgence was marked by electrochemical investigations into Prussian Blue Analogues (mostly hexacyanoferrates) in aqueous electrolytes.[58,59] Additional efforts utilizing organic solvents, such as ACN and PC, employing V_2O_5 as host material, demonstrated Ca^{2+} intercalation validated through electrochemical assessments and powder X-ray diffraction.[60–62]

In the subsequent decade, the growing demand for sustainable energy storage solutions reinvigorated attention towards calcium-based systems, strongly motivated by the previously discussed challenges. New battery concepts like Ca/S batteries displayed initial electrochemical activity despite limited reversibility.[63] Concurrently, the advent of liquid metal batteries unfolded, employing molten salt electrolytes positioned between two immiscible liquid metal electrodes.[64] Although pure calcium proved unsatisfactory due to its significant reactivity and solubility in molten salts, Ca-based alloys with melting points near 600 °C retained advantageous potential when infused with halide electrolytes.[65–68] However, practical implementation is still obstructed by unresolved engineering challenges surrounding corrosion resistance, sealing integrity, and thermal regulation.[37]

Further investigations into hexacyanoferrates within aqueous[69] and organic[70] mediums yielded markedly reversible Ca^{2+} insertion behaviours. The incorporation of water into organic electrolytes proved beneficial, albeit the nuances defining precise redox mechanisms and the influence of water molecules—both intrinsic and introduced—remain elusive.[71,72] Drawing from prevailing literature surrounding LIBs cathodes, efforts to repurpose similar intercalation materials for calcium have intensified, although the disparity between the electrochemical traits of Li^+ and Ca^{2+} accentuates the need for bespoke materials designed specifically for calcium applications.[73,74]

The end of 2016 marked a watershed moment when the feasibility for reversible calcium metal plating and stripping was empirically demonstrated, as elucidated in foundational studies by Ponrouch et al., who employed conventional alkyl carbonate-based organic electrolytes to facilitate this phenomenon.[75] While limitations in interfacial stability and oxidative resistance remained, the results catalyzed further research into electrode materials for calcium battery applications.

Progression was punctuated by findings from Bruce et al., who illustrated reversible Ca plating at ambient temperature using a liquid electrolyte based on calcium borohydride $Ca(BH_4)_2$ in tetrahydrofuran (THF).[76] A solid electrolyte interphase (SEI) rich in calcium hydride (CaH_2) emerged as a critical enabler facilitating this reversibility; however, the electrochemical stability of this electrolyte was confined to approximately 2.5 V vs. Ca^{2+}/Ca, thereby considerably constraining its feasibility for full-cell configurations demanding escalated operational voltages.

A transformative shift transpired alongside unprecedented endeavours from both the Zhao-Karger and Nazar research groups, who concurrently introduced calcium bis-tetrakis(hexafluoroisopropyloxy) borate, $Ca[B(hfip)_4]_2$, as a pioneering electrolyte formulation.[77,78] This advancement allowed reversible calcium metal plating and stripping at room temperature, within an impressively large electrochemical stability window (ESW) ascending to 4.0 V vs. Ca^{2+}/Ca. Nevertheless, ongoing investigations into how $Ca[B(hfip)_4]_2$/DME solutions influence passivation

during aging and cycling have produced enlightening yet surprising results. While the initially formed passivation layers during aging allowed for reversible calcium plating and stripping, prolonged exposure to $CaB(hfip)_{42}$/DME electrolytes induced progressive degradation of the calcium metal surface, leading to the development of a secondary passivation layer. This ongoing corrosion process significantly increased interfacial resistance, ultimately resulting in electrochemical failure of the electrode. [79] Thus, underscoring the dualistic behavior of $CaB(hfip)_{42}$, which not only promote initial SEI formation but concurrently generates extensive instability through continual chemical assault on the interfacial structures.

Parallel explorations into unique electrochemical cell configurations, particularly those integrating activated carbon (AC) as the counter electrode alongside a quasi-reference electrode (QRE), were launched aimed at evaluating Ca-ion positive electrode materials.[80–82] These studies emerged in response to the limited spectrum of electrolytes capable of sustaining effective Ca stripping and deposition, typically characterized by low coulombic efficiency. This scenario rendered calcium metal an unreliable candidate for counter/reference electrode application.[81] The absence of a dependable and standardized configuration for characterizing candidate positive electrode materials within Ca^{2+} injection systems constrained the advancement of the field. However, the AC/QRE setup exhibited commendable stability and reproducibility with 0.5 M $Ca(TFSI)_2$ in DME, proving instrumental in the electrochemical characterization of bilayered V_2O_5 cathodes, thus presenting a viable methodology for the screening of cathode materials within calcium-battery architectures.[81]

The confluence of these breakthroughs has birthed a practical trajectory towards the plausible development of calcium battery technologies operable at ambient temperatures, laying the groundwork for future innovations aimed at high-energy-density and cost-effective energy storage systems.

1.4 Ongoing Challenges

Summarizing the pivotal insights gleaned from the extensive exploration of calcium batteries yields several critical observations:

1.4.1 Ca metal negative electrode (or counter-electrode):

The challenges associated with calcium metal are prominently underscored by the interphase formation dominated by the development of a Ca-ion impermeable interface largely constituted of oxides and other stable species like CaF_2 in the case of fluorinated electrolytes, hindering Ca reactivity.[83,84] An exploration into the stability dynamics of CaO relative to other metals is elucidated by the Ellingham−Richardson diagram,[85] which plots the Gibbs free energy (ΔG) shifts of oxidation reactions against temperature. A more negative ΔG for a reaction signifies a higher thermodynamic

drive supporting its spontaneous occurrence. The downward trajectory of metal lines encased within the diagram indicates increasing metal reactivity and progressively challenging oxide reduction. Consequently, the superior stability of CaO compared to MgO and Al_2O_3 clearly indicates that the formation of CaO-based passivation layers is thermodynamically favoured. This poses significant challenges for calcium electrochemistry, as such layers hinder Ca^{2+} ion transport and prevent effective interaction between Ca^{2+} ions and the metal electrode. The use of metallic calcium as an anode in calcium batteries has only recently become viable, primarily due to the development of tailored electrolyte formulations.

1.4.2 Electrolytes:

The nature of calcium electrolytes plays a pivotal role in the development of calcium batteries, as their degradation behavior influences both calcium ion activity and the reversibility of electrochemical processes. Electrochemical reversibility of calcium at room temperature has long been recognized as a critical challenge. Emerging electrolyte candidates exhibit promising performance at room temperature against calcium metal, suggesting the feasibility of practical calcium-based batteries.

However, these systems face significant limitations, including high costs, complex or moisture-sensitive synthesis protocols, and limited electrochemical stability. Some innovative electrolyte formulations, enable reversible calcium plating; however, the complexity of achieving stable electrochemical processes remains critical in the realization of fully functional cells[86]. Consequently, the research surrounding calcium battery technologies identifies critical challenges that necessitate further investigation, including the need for cost-effective and stable electrolyte systems that are less sensitive to environmental conditions.[87]

1.4.3 Ca cathodes:

Despite the progress made within the domain of calcium cathodes, the notable absence of standardized electrolytes and efficient negative electrodes significantly decelerates advancements in this field.[34,88] It is worth noting that one of the benchmark positive electrode materials for magnesium batteries, the Chevrel phases,[89,90] is unfortunately not suitable for calcium-based systems. Despite the similar divalent nature of Mg^{2+} and Ca^{2+}, the significantly larger ionic radius of Ca^{2+} (~1.00 Å vs. ~0.72 Å for Mg^{2+}) hinders its diffusion within the relatively narrow diffusion channels of the Chevrel structure, leading to poor electrochemical performance. [84,89] Research indicates that the compatibility of calcium with cathode materials remains a significant challenge, requiring extensive characterization of materials. To address these challenges, several investigations have explored

capacitive counter electrodes that balance cathodic charges through the formation of electric double layers on activated carbon surfaces.[91–94] Activated carbon electrodes are noted for their excellent charge storage capabilities due to this formation of electric double layers, enhancing performance in various electrochemical applications. However, notable challenges persist, particularly due to inefficiencies in the standardization of procedures for material evaluation and development.[34,91] Nonetheless, major obstacles remain, particularly reflected in the lack of standardized protocols for the evaluation and development of materials.

1.5 Goal and Structure of the Thesis

Recent advancements in calcium battery research, particularly the demonstration of reversible calcium metal plating and stripping at room temperature, have renewed interest in calcium-based energy storage as a promising post-lithium alternative. Although calcium exhibits several intrinsic advantages, numerous fundamental challenges remain and must be addressed before this chemistry can be translated into practical and functional devices.

In this context, this doctoral research aims to investigate the three fundamental components of calcium batteries: the anode, the cathode, and the electrolyte. These components are deeply interconnected, and their mutual interactions give rise to specific scientific and technological challenges that must be overcome to enable the advancement of this technology.

Electrolyte — As a crucial bridging component linking the anode and cathode, the electrolyte plays a pivotal role in battery function. Its development requires careful consideration of both chemical and electrochemical stability across wide voltage ranges. This work investigates the electrochemical behavior of two innovative calcium-based salt formulations, aiming to achieve optimal performance and compatibility with calcium metal.

Positive electrode — The divalent nature of Ca^{2+} presents substantial limitations in terms of diffusion kinetics and intercalation into conventional host structures, which were primarily designed for monovalent ions like Li^{+}. Therefore, this thesis focuses on Prussian Blue Analogues, which open framework structure offer promising pathways for accommodating calcium ions.

Negative electrode — While calcium metal is theoretically ideal as an anode due to its high capacity and low redox potential, achieving stable and reversible calcium deposition remains a major obstacle. After considerable attention to the synthesis and optimization of novel electrolytes capable of supporting calcium metal. In parallel, different type of calcium-based negative electrodes have been investigated, including an intercalation-type TiO_2 nanotube anode and two alloy-based systems: Ca–

Zn and Ca–Sn with the common goal of achieving compatibility with more conventional electrolyte formulations.

By addressing these three interdependent elements through a multidisciplinary lens, this research aspires to contribute significantly towards advancing both the fundamental grasp and the practical advancement of calcium battery technology.

1.6 Bibliography

(1) Schmidt, T. S.; Beuse, M.; Zhang, X.; Steffen, B.; Schneider, S. F.; Pena-Bello, A.; Bauer, C.; Parra, D. Additional Emissions and Cost from Storing Electricity in Stationary Battery Systems. *Environ Sci Technol* **2019**, *53* (7), 3379–3390. https://doi.org/10.1021/ACS.EST.8B05313/ASSET/IMAGES/LARGE/ES-2018-05313C_0007.JPEG.

(2) *Executive summary – Electricity 2025 – Analysis - IEA*. https://www.iea.org/reports/electricity-2025/executive-summary (accessed 2025-04-07).

(3) Wang, S.; Yu, J.; Okubo, K. Life Cycle Assessment on the Reuse and Recycling of the Nickel-Metal Hydride Battery: Fleet-Based Study on Hybrid Vehicle Batteries from Japan. *J Ind Ecol* **2021**, *25* (5), 1236–1249. https://doi.org/10.1111/JIEC.13126.

(4) Forster, P. M.; Smith, C. J.; Walsh, T.; Lamb, W. F.; Palmer, M. D.; von Schuckmann, K.; Trewin, B.; Allen, M.; Andrew, R.; Birt, A.; Borger, A.; Boyer, T.; Broersma, J. A.; Cheng, L.; Dentener, F.; Friedlingstein, P.; Gillett, N.; Gutiérrez, J. M.; Gütschow, J.; Hauser, M.; Hall, B.; Ishii, M.; Jenkins, S.; Lamboll, R.; Lan, X.; Lee, J.-Y.; Morice, C.; Kadow, C.; Kennedy, J.; Killick, R.; Minx, J.; Naik, V.; Peters, G.; Pirani, A.; Pongratz, J.; Ribes, A.; Rogelj, J.; Rosen, D.; Schleussner, C.-F.; Seneviratne, S.; Szopa, S.; Thorne, P.; Rohde, R.; Rojas Corradi, M.; Schumacher, D.; Vose, R.; Zickfeld, K.; Zhang, X.; Masson-Delmotte, V.; Zhai, P. Indicators of Global Climate Change 2022: Annual Update of Large-Scale Indicators of the State of the Climate System and the Human Influence . **2023**. https://doi.org/10.5194/ESSD-2023-166.

(5) *Climate Change - NASA Science*. https://science.nasa.gov/climate-change/ (accessed 2025-04-22).

(6) Akinyele, D. O.; Rayudu, R. K. Review of Energy Storage Technologies for Sustainable Power Networks. *Sustainable Energy Technologies and Assessments* **2014**, *8*, 74–91. https://doi.org/10.1016/J.SETA.2014.07.004.

(7) Akinyele, D.; Belikov, J.; Levron, Y. Battery Storage Technologies for Electrical Applications: Impact in Stand-Alone Photovoltaic Systems. *Energies 2017, Vol. 10, Page 1760* **2017**, *10* (11), 1760. https://doi.org/10.3390/EN10111760.

(8) Malik, F. H.; Hussain, G. A.; Alsmadi, Y. M. S.; Haider, Z. M.; Mansoor, W.; Lehtonen, M. Integrating Energy Storage Technologies with Renewable Energy Sources: A Pathway Toward Sustainable Power Grids. *Sustainability 2025, Vol. 17, Page 4097* **2025**, *17* (9), 4097. https://doi.org/10.3390/SU17094097.

(9) Olabi, A. G. Renewable Energy and Energy Storage Systems. *Energy* **2017**, *136*, 1–6. https://doi.org/10.1016/J.ENERGY.2017.07.054.

(10) Ould Amrouche, S.; Rekioua, D.; Rekioua, T.; Bacha, S. Overview of Energy Storage in Renewable Energy Systems. *Int J Hydrogen Energy* **2016**, *41* (45), 20914–20927. https://doi.org/10.1016/J.IJHYDENE.2016.06.243.

(11) Scrosati, B. History of Lithium Batteries. https://doi.org/10.1007/s10008-011-1386-8.

(12) Zhao, B.; Hu, J.; Hui, D.; Qu, Z.; Liu, L.; Gao, C. Broadband Equivalent Modeling and Common-Mode Voltage Conduction Analysis of Electrochemical Energy Storage System. *IEEE Access* **2023**, *11*, 44167–44175. https://doi.org/10.1109/ACCESS.2023.3270327.

(13) *Scopus - Analyze search results | Signed in*. https://www.scopus.com/term/analyzer.uri?sort=plf-f&src=s&sid=1413303347ea7079aa03e5bcd4d60251&sot=a&sdt=a&sl=22&s=TITLE-ABS-

KEY%28battery%29&origin=resultslist&count=10&analyzeResults=Analyze+results (accessed 2025-05-21).

(14) Beaudet, A.; Larouche, F.; Amouzegar, K.; Bouchard, P.; Zaghib, K. Key Challenges and Opportunities for Recycling Electric Vehicle Battery Materials. *Sustainability 2020, Vol. 12, Page 5837* **2020**, *12* (14), 5837. https://doi.org/10.3390/SU12145837.

(15) Prime, J.; Abdulkadir Ahmed, I.; Akande, D.; Elhassan, N.; Escamilla, G.; Jamdade, A.; Melnikov, Y.; Whiteman, A. Renewable Energy Statistics 2024, International Renewable Energy Agency. **2024**, 2–10.

(16) Hassan, Q.; Algburi, S.; Sameen, A. Z.; Al-Musawi, T. J.; Al-Jiboory, A. K.; Salman, H. M.; Ali, B. M.; Jaszczur, M. A Comprehensive Review of International Renewable Energy Growth. *Energy and Built Environment* **2024**. https://doi.org/10.1016/J.ENBENV.2023.12.002.

(17) Hassan, Q.; Algburi, S.; Sameen, A. Z.; Al-Musawi, T. J.; Al-Jiboory, A. K.; Salman, M.; Ali, M.; Jaszczur, M. ARTICLE IN PRESS Energy and Built Environment Xxx (Xxxx) Xxx A Comprehensive Review of International Renewable Energy Growth. **2024**. https://doi.org/10.1016/j.enbenv.2023.12.002.

(18) Nykvist, B.; Nilsson, M. Rapidly Falling Costs of Battery Packs for Electric Vehicles. *Nature Climate Change 2014 5:4* **2015**, *5* (4), 329–332. https://doi.org/10.1038/nclimate2564.

(19) Fotouhi, A.; Auger, D. J.; Propp, K.; Longo, S.; Wild, M. A Review on Electric Vehicle Battery Modelling: From Lithium-Ion toward Lithium–Sulphur. *Renewable and Sustainable Energy Reviews* **2016**, *56*, 1008–1021. https://doi.org/10.1016/J.RSER.2015.12.009.

(20) Kwon, B.; Ha, S.; Kim, D. M.; Koo, D.; Lee, J.; Lee, K. T. Electrochemically Active Red P/BaTiO3-Based Protective Layers Suppressing Li Dendrite Growth for Li Metal Batteries. *Adv Mater Interfaces* **2020**, *7* (20), 2001037. https://doi.org/10.1002/ADMI.202001037.

(21) Accardo, A.; Dotelli, G.; Musa, M. L.; Spessa, E. Life Cycle Assessment of an NMC Battery for Application to Electric Light-Duty Commercial Vehicles and Comparison with a Sodium-Nickel-Chloride Battery. *Applied Sciences 2021, Vol. 11, Page 1160* **2021**, *11* (3), 1160. https://doi.org/10.3390/APP11031160.

(22) Junlong, L.; Leung, &; Wah, A. O. A Critical Review on Electric Vehicle Batteries — Based on Life Cycle Assessment Method. *Studies in Social Science & Humanities* **2023**, *2* (8), 33–50. https://doi.org/10.56397/SSSH.2023.08.05.

(23) Stoppato, A.; Benato, A.; De Vanna, F. Environmental Impact of Energy Systems Integrated with Electrochemical Accumulators and Powered by Renewable Energy Sources in a Life-Cycle Perspective. *Applied Sciences 2021, Vol. 11, Page 2770* **2021**, *11* (6), 2770. https://doi.org/10.3390/APP11062770.

(24) Hiremath, M.; Derendorf, K.; Vogt, T. Comparative Life Cycle Assessment of Battery Storage Systems for Stationary Applications. *Environ Sci Technol* **2015**, *49* (8), 4825–4833. https://doi.org/10.1021/ES504572Q/SUPPL_FILE/ES504572Q_SI_001.PDF.

(25) Kern, A.; Johnson, J. X.; Mathieu, J. L. Environmental Impacts of Using Energy Storage Aggregations to Provide Multiple Services.

(26) Barke, A.; Cistjakov, W.; Steckermeier, D.; Thies, C.; Popien, J. L.; Michalowski, P.; Pinheiro Melo, S.; Cerdas, F.; Herrmann, C.; Krewer, U.; Kwade, A.; Spengler, T. S. Green Batteries for Clean Skies: Sustainability Assessment of Lithium-Sulfur All-Solid-State Batteries for Electric Aircraft. *J Ind Ecol* **2023**, *27* (3), 795–810. https://doi.org/10.1111/JIEC.13345.

(27) He, H.; Tian, S.; Tarroja, B.; Ogunseitan, O. A.; Samuelsen, S.; Schoenung, J. M. Flow Battery Production: Materials Selection and Environmental Impact. *J Clean Prod* **2020**, *269*, 121740. https://doi.org/10.1016/J.JCLEPRO.2020.121740.

(28) Stievano, L.; de Meatza, I.; Bitenc, J.; Cavallo, C.; Brutti, S.; Navarra, M. A. Emerging Calcium Batteries. *J. Power Sources* **2021**, *482* (August 2020), 228875. https://doi.org/10.1016/j.jpowsour.2020.228875.

(29) Liu, Y. ; Zhang, C. ; Hao, Z. ; Cai, X. ; Liu, C. ; Zhang, J. ; Wang, S. ; Chen, Y.; Liu, Y.; Zhang, C.; Hao, Z.; Cai, X.; Liu, C.; Zhang, J.; Wang, S.; Chen, Y. Study on the Life Cycle Assessment of Automotive Power Batteries Considering Multi-Cycle Utilization. *Energies 2023, Vol. 16, Page 6859* **2023**, *16* (19), 6859. https://doi.org/10.3390/EN16196859.

(30) Wang, M.; Jiang, C.; Zhang, S.; Song, X.; Tang, Y.; Cheng, H.-M. Reversible Calcium Alloying Enables a Practical Room-Temperature Rechargeable Calcium-Ion Battery with a High Discharge Voltage. **2018**. https://doi.org/10.1038/s41557-018-0045-4.

(31) Smith, L.; Ibn-Mohammed, T.; Astudillo, D.; Brown, S.; Reaney, I. M.; Koh, S. C. L. The Role of Cycle Life on the Environmental Impact of Li6.4La3Zr1.4Ta0.6O12 Based Solid-State Batteries. *Adv Sustain Syst* **2021**, *5* (2), 2000241. https://doi.org/10.1002/ADSU.202000241.

(32) Rajapakse, M.; Karki, B.; Abu, U. O.; Pishgar, S.; Musa, M. R. K.; Riyadh, S. M. S.; Yu, M.; Sumanasekera, G.; Jasinski, J. B. Intercalation as a Versatile Tool for Fabrication, Property Tuning, and Phase Transitions in 2D Materials. *npj 2D Materials and Applications 2021 5:1* **2021**, *5* (1), 1–21. https://doi.org/10.1038/s41699-021-00211-6.

(33) Zhou, J.; Lin, Z.; Ren, H.; Duan, X.; Shakir, I.; Huang, Y.; Duan, X. Layered Intercalation Materials. *Advanced Materials* **2021**, *33* (25), 2004557. https://doi.org/10.1002/ADMA.202004557.

(34) Arroyo-De Dompablo, M. E.; Ponrouch, A.; Johansson, P.; Palacín, M. R. Achievements, Challenges, and Prospects of Calcium Batteries. *Chem Rev* **2020**, *120* (14), 6331–6357. https://doi.org/10.1021/ACS.CHEMREV.9B00339/ASSET/IMAGES/LARGE/CR9B00339_0016.JPEG.

(35) Shanmukaraj, D.; Ranque, P.; Ben Youcef, H.; Rojo, T.; Poizot, P.; Grugeon, S.; Laruelle, S.; Guyomard, D. Review—Towards Efficient Energy Storage Materials: Lithium Intercalation/Organic Electrodes to Polymer Electrolytes—A Road Map (Tribute to Michel Armand). *J Electrochem Soc* **2020**, *167* (7), 070530. https://doi.org/10.1149/1945-7111/AB787A.

(36) Li, X.; Zhang, Y.; Liao, Y.; Yu, G. Environmental Impact Assessment of Battery Boxes Based on Lightweight Material Substitution. *Scientific Reports 2024 14:1* **2024**, *14* (1), 1–13. https://doi.org/10.1038/s41598-024-53238-2.

(37) Arroyo-De Dompablo, M. E.; Ponrouch, A.; Johansson, P.; Palacín, M. R. Achievements, Challenges, and Prospects of Calcium Batteries. *Chem Rev* **2020**, *120* (14), 6331–6357. https://doi.org/10.1021/ACS.CHEMREV.9B00339/ASSET/IMAGES/LARGE/CR9B00339_0016.JPEG.

(38) Ding, Y.; Zhang, C.; Zhang, L.; Zhou, Y.; Yu, G. Pathways to Widespread Applications: Development of Redox Flow Batteries Based on New Chemistries. *Chem* **2019**, *5* (8), 1964–1987. https://doi.org/10.1016/J.CHEMPR.2019.05.010/ASSET/531530B8-6843-4B59-BC9A-F12581CD67C8/MAIN.ASSETS/GR8.JPG.

(39) Nissen, D. A. A Study of the Anode-Electrolyte Interface in a Thermal Battery. *J Electrochem Soc* **1979**, *126* (2), 176–180. https://doi.org/10.1149/1.2129001/XML.

(40) Miles, M. H.; Fine, D. A.; Fletcher, A. N. The Calcium Anode in Molten Nitrate Electrolytes. *J Electrochem Soc* **1978**, *125* (8), 1209–1214. https://doi.org/10.1149/1.2131651/XML.

(41) Sammells, A. F.; Schumacher, B. Secondary Calcium Solid Electrolyte High Temperature Battery. *J Electrochem Soc* **1986**, *133* (1), 235–236. https://doi.org/10.1149/1.2108533/XML.

(42) Pujare, N. U.; Semkow, K. W.; Sammells, A. F. A Calcium Oxygen Secondary Battery. *J Electrochem Soc* **1988**, *135* (1), 260–261. https://doi.org/10.1149/1.2095574/XML.

(43) Staniewicz, R. J. A Study of the Calcium-Thionyl Chloride Electrochemical System. *J Electrochem Soc* **1980**, *127* (4), 782–789. https://doi.org/10.1149/1.2129758/XML.

(44) Bradley, J.; Mitchell, P. J.; Hagan, W. P.; Tuck, C. D. S. Reduction of Calcium Corrosion in Thionyl Chloride-Based Electrolytes. *J Power Sources* **1989**, *28* (4), 361–365. https://doi.org/10.1016/0378-7753(89)80065-5.

(45) Peled, E.; Meitav, A.; Brand, M. Calcium Thionyl Chloride High-Rate Reserve Cell. *J Electrochem Soc* **1981**, *128* (9), 1936–1938. https://doi.org/10.1149/1.2127768/XML.

(46) Peled, E.; Tulman, R.; Golan, A.; Meitav, A. Calcium / Ca (AlCl4) 2 — Thionyl Chloride High Rate Cell. *J Electrochem Soc* **1984**, *131* (10), 2314–2316. https://doi.org/10.1149/1.2115248/XML.

(47) Peled, E.; Elster, E.; Tulman, R.; Kimel, J. Calcium/Ca(AlCl4)2-Thionyl Chloride (TC) Cell. Effect of Temperature and Cell Parameters on Performance. *J Power Sources* **1985**, *14* (1–3), 93–98. https://doi.org/10.1016/0378-7753(85)88017-4.

(48) Elster, E.; Cohen, R.; Peled, E. Solid Electrolyte Interphase (SEI) Electrodes Part VII. The Electrochemical Behaviour of Calcium in Ba(AlCl4)2 and Sr(AlCl4)2□thionyl Chloride Solutions (Extended Abstract). *J Power Sources* **1989**, *26* (3–4), 423–425. https://doi.org/10.1016/0378-7753(89)80157-0.

(49) J, B.; P, M. Current Status of Calcium/Thionyl Chloride Batteries. *Chemistry & Industry (Chichester)* **1990**, No. 5, 135–137.

(50) Aurbach, D.; Skaletsky, R.; Gofer, Y. The Electrochemical Behavior of Calcium Electrodes in a Few Organic Electrolytes. *J Electrochem Soc* **1991**, *138* (12), 3536–3545. https://doi.org/10.1149/1.2085455/XML.

(51) Blomgren, G. E. The Development and Future of Lithium Ion Batteries. *J Electrochem Soc* **2017**, *164* (1), A5019–A5025. https://doi.org/10.1149/2.0251701JES/XML.

(52) Aurbach, D.; Lu, Z.; Schechter, A.; Gofer, Y.; Gizbar, H.; Turgeman, R.; Cohen, Y.; Moshkovich, M.; Levi, E. Prototype Systems for Rechargeable Magnesium Batteries. *Nature 2000 407:6805* **2000**, *407* (6805), 724–727. https://doi.org/10.1038/35037553.

(53) Amatucci, G. G.; Badway, F.; Singhal, A.; Beaudoin, B.; Skandan, G.; Bowmer, T.; Plitz, I.; Pereira, N.; Chapman, T.; Jaworski, R. Investigation of Yttrium and Polyvalent Ion Intercalation into Nanocrystalline Vanadium Oxide. *J Electrochem Soc* **2001**, *148* (8), A940. https://doi.org/10.1149/1.1383777/XML.

(54) Whittingham, M. S. Chemistry of Intercalation Compounds: Metal Guests in Chalcogenide Hosts. *Progress in Solid State Chemistry* **1978**, *12* (1), 41–99. https://doi.org/10.1016/0079-6786(78)90003-1.

(55) Guilmeau, E.; Maignan, A.; Wan, C.; Koumoto, K. On the Effects of Substitution, Intercalation, Non-Stoichiometry and Block Layer Concept in TiS2 Based Thermoelectrics. *Physical Chemistry Chemical Physics* **2015**, *17* (38), 24541–24555. https://doi.org/10.1039/C5CP01795E.

(56) Lerf, A.; Schöllhorn, R. Solvation Reactions of Layered Ternary Sulfides AxTiS2, AxNbS2, and AxTaS2. *Inorg Chem* **1977**, *16* (11), 2950–2956. https://doi.org/10.1021/IC50177A057/ASSET/IC50177A057.FP.PNG_V03.

(57) Schöllhorn, R.; Meyer, H. Cathodic Reduction of Layered Transition Metal Chalcogenides. *Mater Res Bull* **1974**, *9* (9), 1237–1245. https://doi.org/10.1016/0025-5408(74)90042-7.

(58) Chen, S. M. Preparation, Characterization, and Electrocatalytic Oxidation Properties of Iron, Cobalt, Nickel, and Indium Hexacyanoferrate. *Journal of Electroanalytical Chemistry* **2002**, *521* (1–2), 29–52. https://doi.org/10.1016/S0022-0728(02)00677-0.

(59) Wang, R. Y.; Wessells, C. D.; Huggins, R. A.; Cui, Y. Highly Reversible Open Framework Nanoscale Electrodes for Divalent Ion Batteries. *Nano Lett* **2013**, *13* (11), 5748–5752. https://doi.org/10.1021/NL403669A/SUPPL_FILE/NL403669A_SI_001.PDF.

(60) Hayashi, M.; Arai, H.; Ohtsuka, H.; Sakurai, Y. Electrochemical Characteristics of Calcium in Organic Electrolyte Solutions and Vanadium Oxides as Calcium Hosts. *J Power Sources* **2003**, *119–121*, 617–620. https://doi.org/10.1016/S0378-7753(03)00307-0.

(61) Hayashi, M.; Arai, H.; Ohtsuka, H.; Sakurai, Y. Electrochemical Insertion/Extraction of Calcium Ions Using Crystalline Vanadium Oxide. *Electrochemical and Solid-State Letters* **2004**, *7* (5), A119. https://doi.org/10.1149/1.1675951/XML.

(62) Bervas, M.; Klein, L. C.; Amatucci, G. G. Vanadium Oxide–Propylene Carbonate Composite as a Host for the Intercalation of Polyvalent Cations. *Solid State Ion* **2005**, *176* (37–38), 2735–2747. https://doi.org/10.1016/J.SSI.2005.09.009.

(63) See, K. A.; Gerbec, J. A.; Jun, Y. S.; Wudl, F.; Stucky, G. D.; Seshadri, R. A High Capacity Calcium Primary Cell Based on the Ca–S System. *Adv Energy Mater* **2013**, *3* (8), 1056–1061. https://doi.org/10.1002/AENM.201300160.

(64) Kim, H.; Boysen, D. A.; Newhouse, J. M.; Spatocco, B. L.; Chung, B.; Burke, P. J.; Bradwell, D. J.; Jiang, K.; Tomaszowska, A. A.; Wang, K.; Wei, W.; Ortiz, L. A.; Barriga, S. A.; Poizeau, S. M.; Sadoway, D. R. Liquid Metal Batteries: Past, Present, and Future. *Chem Rev* **2013**, *113* (3), 2075–2099. https://doi.org/10.1021/CR300205K/ASSET/CR300205K.FP.PNG_V03.

(65) Kim, H.; Boysen, D. A.; Ouchi, T.; Sadoway, D. R. Calcium–Bismuth Electrodes for Large-Scale Energy Storage (Liquid Metal Batteries). *J Power Sources* **2013**, *241*, 239–248. https://doi.org/10.1016/J.JPOWSOUR.2013.04.052.

(66) Ouchi, T.; Kim, H.; Ning, X.; Sadoway, D. R. Calcium-Antimony Alloys as Electrodes for Liquid Metal Batteries. *J Electrochem Soc* **2014**, *161* (12), A1898–A1904. https://doi.org/10.1149/2.0801412JES/XML.

(67) Poizeau, S.; Sadoway, D. R. Application of the Molecular Interaction Volume Model (MIVM) to Calcium-Based Liquid Alloys of Systems Forming High-Melting Intermetallics. *J Am Chem Soc* **2013**, *135* (22), 8260–8265. https://doi.org/10.1021/JA4013886/ASSET/IMAGES/MEDIUM/JA-2013-013886_0009.GIF.

(68) Ouchi, T.; Kim, H.; Spatocco, B. L.; Sadoway, D. R. Calcium-Based Multi-Element Chemistry for Grid-Scale Electrochemical Energy Storage. *Nature Communications 2016 7:1* **2016**, *7* (1), 1–5. https://doi.org/10.1038/ncomms10999.

(69) Wang, R. Y.; Wessells, C. D.; Huggins, R. A.; Cui, Y. Highly Reversible Open Framework Nanoscale Electrodes for Divalent Ion Batteries. *Nano Lett* **2013**, *13* (11), 5748–5752. https://doi.org/10.1021/NL403669A/SUPPL_FILE/NL403669A_SI_001.PDF.

(70) Shiga, T.; Kondo, H.; Kato, Y.; Inoue, M. Insertion of Calcium Ion into Prussian Blue Analogue in Nonaqueous Solutions and Its Application to a Rechargeable Battery with Dual Carriers. *Journal of Physical Chemistry C* **2015**, *119* (50), 27946–27953. https://doi.org/10.1021/ACS.JPCC.5B10245/SUPPL_FILE/JP5B10245_SI_002.PDF.

(71) Tojo, T.; Sugiura, Y.; Inada, R.; Sakurai, Y. Reversible Calcium Ion Batteries Using a Dehydrated Prussian Blue Analogue Cathode. *Electrochim Acta* **2016**, *207*, 22–27. https://doi.org/10.1016/J.ELECTACTA.2016.04.159.

(72) Lipson, A. L.; Han, S. D.; Kim, S.; Pan, B.; Sa, N.; Liao, C.; Fister, T. T.; Burrell, A. K.; Vaughey, J. T.; Ingram, B. J. Nickel Hexacyanoferrate, a Versatile Intercalation Host for Divalent Ions from Nonaqueous Electrolytes. *J Power Sources* **2016**, *325*, 646–652. https://doi.org/10.1016/J.JPOWSOUR.2016.06.019.

(73) Liu, M.; Rong, Z.; Malik, R.; Canepa, P.; Jain, A.; Ceder, G.; Persson, K. A. Spinel Compounds as Multivalent Battery Cathodes: A Systematic Evaluation Based on Ab Initio Calculations. *Energy Environ Sci* **2015**, *8* (3), 964–974. https://doi.org/10.1039/C4EE03389B.

(74) Rong, Z.; Malik, R.; Canepa, P.; Sai Gautam, G.; Liu, M.; Jain, A.; Persson, K.; Ceder, G. Materials Design Rules for Multivalent Ion Mobility in Intercalation Structures. *Chemistry of Materials* **2015**, *27* (17), 6016–6021. https://doi.org/10.1021/ACS.CHEMMATER.5B02342/SUPPL_FILE/CM5B02342_SI_001.PDF.

(75) Ponrouch, A.; Tchitchekova, D.; Frontera, C.; Bardé, F.; Dompablo, M. E. A. De; Palacín, M. R. Assessing Si-Based Anodes for Ca-Ion Batteries: Electrochemical Decalciation of CaSi2. *Electrochem commun* **2016**, *66*, 75–78. https://doi.org/10.1016/J.ELECOM.2016.03.004.

(76) Wang, D.; Gao, X.; Chen, Y.; Jin, L.; Kuss, C.; Bruce, P. G. Plating and Stripping Calcium in an Organic Electrolyte. *Nature Materials 2017 17:1* **2017**, *17* (1), 16–20. https://doi.org/10.1038/nmat5036.

(77) Li, Z.; Fuhr, O.; Fichtner, M.; Zhao-Karger, Z. Towards Stable and Efficient Electrolytes for Room-Temperature Rechargeable Calcium Batteries. *Energy Environ Sci* **2019**, *12* (12), 3496–3501. https://doi.org/10.1039/C9EE01699F.

(78) Shyamsunder, A.; Blanc, L. E.; Assoud, A.; Nazar, L. F. Reversible Calcium Plating and Stripping at Room Temperature Using a Borate Salt. *ACS Energy Lett* **2019**, *4* (9), 2271–2276. https://doi.org/10.1021/ACSENERGYLETT.9B01550/SUPPL_FILE/NZ9B01550_SI_001.PDF.

(79) Lin, H.; Meng, J.; Guo, W.; Li, R.; Yi, Y.; Ma, Y.; Cheung, C. F.; Aurbach, D.; Xu, Z. L. Deciphering the Dynamic Interfacial Chemistry of Calcium Metal Anodes. *Energy Environ Sci* **2024**, *17* (18), 6548–6558. https://doi.org/10.1039/D4EE01257G.

(80) Dugas, R.; Forero-Saboya, J. D.; Ponrouch, A. Methods and Protocols for Reliable Electrochemical Testing in Post-Li Batteries (Na, K, Mg, and Ca). *Chemistry of Materials* **2019**, *31* (21), 8613–8628. https://doi.org/10.1021/ACS.CHEMMATER.9B02776/ASSET/IMAGES/LARGE/CM9B02776_0011.JPEG.

(81) Liu, X.; Elia, G. A.; Passerini, S. Evaluation of Counter and Reference Electrodes for the Investigation of Ca Battery Materials. *Journal of Power Sources Advances* **2020**, *2*, 100008. https://doi.org/10.1016/J.POWERA.2020.100008.

(82) Jao, W. Y.; Tseng, L. C.; Lin, Y.; Chen, Y. C.; Hu, C. C. Stability Promotion of Carbon-Based Quasi-Reference Electrodes in Nonaqueous Calcium Ion Electrolytes. *Journal of Physical Chemistry C* **2024**, *128*, 2025. https://doi.org/10.1021/ACS.JPCC.4C05509/ASSET/IMAGES/LARGE/JP4C05509_0005.JPEG.

(83) Liang, J.; Wang, M.; Zhu, S.; Zhu, D.; Wang, R.; Wang, J.; Cui, L.; Huang, M.; Zhang, W.; An, Q.; Zhang, L.; Zhao, K. Corrosion of Calcium Metal in Ca(TFSI)2/DMAc Electrolyte and Its Solution via Alloy Interface and Competitive Solvation. *Angewandte Chemie International Edition* **2025**, e202502729. https://doi.org/10.1002/ANIE.202502729.

(84) Ponrouch, A.; Frontera, C.; Bardé, F.; Palacín, M. R. Towards a Calcium-Based Rechargeable Battery. *Nature Materials 2015 15:2* **2015**, *15* (2), 169–172. https://doi.org/10.1038/nmat4462.

(85) Transactions and Communications. *Journal of the Society of Chemical Industry* **1944**, *63* (5), 125–160. https://doi.org/10.1002/JCTB.5000630501.

(86) Leon, N. J.; Xie, X.; Yang, M.; Driscoll, D. M.; Connell, J. G.; Kim, S.; Seguin, T.; Vaughey, J. T.; Balasubramanian, M.; Persson, K. A.; Liao, C. Room-Temperature Calcium Plating and Stripping Using a Perfluoroalkoxyaluminate Anion Electrolyte. *Journal of Physical Chemistry C* **2022**, *126* (32), 13579–13584. https://doi.org/10.1021/ACS.JPCC.2C03272/SUPPL_FILE/JP2C03272_SI_001.PDF.

(87) Wang, Y.-S.; Yeh, H.-W.; Tang, Y.-H.; -, al; Asselin, G. M.; Paden, O.; Qiu, W. Steps Towards the Use of TiS2 Electrodes in Ca Batteries. *J Electrochem Soc* **2020**, *167* (7), 070532. https://doi.org/10.1149/1945-7111/AB7A82.

(88) Biria, S.; Pathreeker, S.; Genier, F. S.; Hosein, I. D. A Highly Conductive and Thermally Stable Ionic Liquid Gel Electrolyte for Calcium-Ion Batteries. *ACS Appl Polym Mater* **2020**, *2* (6), 2111–2118. https://doi.org/10.1021/ACSAPM.9B01223/SUPPL_FILE/AP9B01223_SI_001.PDF.

(89) Stievano, L.; de Meatza, I.; Bitenc, J.; Cavallo, C.; Brutti, S.; Navarra, M. A. Emerging Calcium Batteries. *J Power Sources* **2021**, *482*, 228875. https://doi.org/10.1016/J.JPOWSOUR.2020.228875.

(90) Aurbach, D.; Lu, Z.; Schechter, A.; Gofer, Y.; Gizbar, H.; Turgeman, R.; Cohen, Y.; Moshkovich, M.; Levi, E. Prototype Systems for Rechargeable Magnesium Batteries. *Nature 2000 407:6805* **2000**, *407* (6805), 724–727. https://doi.org/10.1038/35037553.

(91) Liu, X.; Elia, G.; Passerini, S. Evaluation of Counter and Reference Electrodes for the Investigation of Ca Battery Materials. *ECS Meeting Abstracts* **2022**, *MA2022-01* (1), 63. https://doi.org/10.1149/MA2022-01163MTGABS.

(92) Xu, Z. L.; Park, J.; Wang, J.; Moon, H.; Yoon, G.; Lim, J.; Ko, Y. J.; Cho, S. P.; Lee, S. Y.; Kang, K. A New High-Voltage Calcium Intercalation Host for Ultra-Stable and High-Power Calcium Rechargeable Batteries. *Nat Commun* **2021**, *12* (1). https://doi.org/10.1038/S41467-021-23703-X.

(93) Chae, M. S.; Heo, J. W.; Hyoung, J.; Hong, S. T. Double-Sheet Vanadium Oxide as a Cathode Material for Calcium-Ion Batteries. *ChemNanoMat* **2020**, *6* (7), 1049–1053. https://doi.org/10.1002/CNMA.202000011.

(94) Chae, M. S.; Kwak, H. H.; Hong, S. T. Calcium Molybdenum Bronze as a Stable High-Capacity Cathode Material for Calcium-Ion Batteries. *ACS Appl Energy Mater* **2020**, *3* (6), 5107–5112. https://doi.org/10.1021/ACSAEM.0C00567/SUPPL_FILE/AE0C00567_SI_001.PDF.

(95) Shyamsunder, A.; Blanc, L. E.; Assoud, A.; Nazar, L. F. Reversible Calcium Plating and Stripping at Room Temperature Using a Borate Salt. *ACS Energy Lett* **2019**, *4* (9), 2271–2276. https://doi.org/10.1021/ACSENERGYLETT.9B01550.

(96) Gummow, R. J.; Vamvounis, G.; Kannan, M. B.; He, Y. Calcium-Ion Batteries: Current State-of-the-Art and Future Perspectives. *Advanced Materials* **2018**, *30* (39), 1801702. https://doi.org/10.1002/ADMA.201801702.

(97) Kisu, K.; Kim, S.; Shinohara, T.; Zhao, K.; Züttel, A.; Orimo, S. ichi. Monocarborane Cluster as a Stable Fluorine-Free Calcium Battery Electrolyte. *Scientific Reports 2021 11:1* **2021**, *11* (1), 1–8. https://doi.org/10.1038/s41598-021-86938-0.

(98) Celeste, A.; Agostini, M.; De Bonis, A.; Brutti, S. Insight the Lithiation Process of Micro and Nanoparticles TiO2-Anatase Based Electrodes. *Electrochim Acta* **2025**, *535*, 146618. https://doi.org/10.1016/J.ELECTACTA.2025.146618.

(99) Liu, Z.; Andreev, Y. G.; Robert Armstrong, A.; Brutti, S.; Ren, Y.; Bruce, P. G. Nanostructured TiO2(B): The Effect of Size and Shape on Anode Properties for Li-Ion Batteries. *Progress in Natural Science: Materials International* **2013**, *23* (3), 235–244. https://doi.org/10.1016/J.PNSC.2013.05.001.

Chapter II: Calcium aprotic electrolytes

2.1 2.1 Introduction

This chapter focuses on calcium-based electrolytes, with particular emphasis on the development of new electrolytes compatible with calcium metal. To provide context and highlight the rationale behind the design of novel systems, we will first report what an electrolyte is, and which are its main characteristics. It will follow a first review on calcium electrolytes studied until now, starting from traditional formulations and progressing to more innovative approaches. The recent advancements have inspired the development and investigation of two new undocumented salts, which represent the core of this chapter.

2.1.1 Electrolytes characteristics

The electrolyte is one of the three fundamental components of electrochemical cells, playing a pivotal role in facilitating ionic conduction between the anode and cathode. It enables the redox reactions that are critical for energy conversion and storage processes.[1,2] The composition and aggregation state of the electrolyte, being liquid, solid, or gel, are essential for the performance of electrochemical systems, as they must include freely dissociated ions to enable efficient ionic transport when subjected to an electric field.[1,2] The fundamental characteristics for electrolytes in electrochemical applications, particularly in batteries, include:

1. Ionic Conductivity: A successful electrolyte must exhibit sufficient ionic mobility to minimize the internal resistance of the cell, ensuring efficient charge transport. The ionic conductivity of electrolytes directly impacts the battery's performance, with higher ionic conductivities correlated with better energy efficiency in energy storage systems.[3–5]

2. Electrochemical Stability: The electrolyte must possess a wide electrochemical stability window to prevent decomposition at the operating potentials of the cell. A stable electrolyte ensures that the performance remains reliable over extended usage.[6–8]

3. Chemical Compatibility: it is essential that the electrolyte exhibits minimal chemical reactivity with electrode materials and other cell components. However, a limited interfacial reactivity is unavoidable, particularly in systems employing highly reducing or oxidizing electrodes, and typically results in the formation of a solid interphase composed of electrolyte decomposition products on the electrode surface, known as the Solid Electrolyte Interphase (SEI). [8–10]

4. Interfacial stability: the electrolyte should promote the spontaneous formation of a stable SEI on the negative electrode surface. This SEI layer should be electronically insulating to prevent

further parasitic reactions, yet ionically conductive to allow continued transport of charge carriers (e.g., Ca^{2+}). Its stability, both chemical and mechanical, over prolonged cycling and varying temperatures is also critical, along with maintaining a thin and homogeneous profile to avoid the increase of the interfacial resistance.[9–11]

The rational design of electrolytes that consider both bulk and interfacial properties is critical for improving the performance, longevity, and safety of electrochemical energy storage and conversion systems. This design complexity reflects the need for a balanced approach to enhance the operational benchmarks expected of modern batteries.[10–13]

Once established the general framework for electrolyte functionality, attention can now be devoted to calcium electrolytes. The next section explores their historical evolution, current challenges, and the motivations driving the search for novel calcium salt chemistries.

2.1.2 Early Developments of Calcium Electrolytes for Rechargeable Batteries

Early investigations into liquid calcium electrolytes were driven by the research of safer alternatives to Li-based primary batteries, specifically Li/Thionyl chloride (Li–$SOCl_2$), dating back to the 1980s.[14,15] Calcium–$SOCl_2$ (Ca–$SOCl_2$) batteries were explored as a promising alternative due to their comparable electrochemical properties: they offered a cell voltage of 3.64 V and an energy density of 1230 mWh g^{-1}, closely matching the 3.65 V and 1474 mWh g^{-1} of Li–$SOCl_2$ cells. Stankiewicz hypothesized that the higher melting point of calcium (839 °C) relative to lithium (180 °C) would mitigate risks related to anode melting during possible short-circuit events.[14]

In one of the foundational studies, a $Ca(AlCl_4)_2$–$SOCl_2$ electrolyte with concentrations up to 2.0 M was synthesized by reacting $CaCl_2$ and $AlCl_3$ in a 1:2 molar ratio within $SOCl_2$ as the solvent.[15,16] The resulting electrolyte was evaluated for its corrosive behavior on calcium metal. It was observed that Ca corrosion followed a battery-like electrochemical reaction pathway, leading to the formation of $CaCl_2$ on the metal surface, as characterized by X-ray diffraction (XRD) and infrared spectroscopy (IR). Gaseous SO_2 and elemental sulphur were proposed as additional byproducts. Notably, $SOCl_2$ alone resulted in a significantly slower corrosion rate, suggesting that Ca^{2+} solvation accelerates solvent reduction at the Ca surface. Due to ongoing corrosion, the capacity of Ca–$SOCl_2$ batteries was observed to decline to 50% after just one month of storage. The study also revealed that the presence of residual water and excess $AlCl_3$ in the electrolyte can significantly enhance calcium corrosion. Two additional electrolytes—$Ca(FeCl_4)_2$–$SOCl_2$ and $Ca(SbCl_6)_2$–$SOCl_2$—were also synthesized, though both exhibited even faster degradation of the calcium anode.[14,16,17]

Staniewicz found limited evidence for Ca plating through the passivating $CaCl_2$ layer, which appeared to function as a SEI. [14] He proposed that Cl^- ions migrate through defects in the $CaCl_2$ layer, enabling the deposition of Ca metal at highly negative potentials (–10 V vs. Ca^{2+}/Ca at 1.24 mA cm^{-2}). Peled and colleagues extended this work, also using $Ca(AlCl_4)_2$–$SOCl_2$ electrolytes, and concluded that $CaCl_2$ formed a passivation layer (<100 Å thick) with poor Ca^{2+} conductivity.[15,16] They observed that this layer could only be electrolyzed under high overpotentials, precluding the possibility of rechargeability as potential safety advantage over Li–$SOCl_2$ systems. Additionally, battery performance was found to be sensitive to both electrolyte composition and temperature.

In 1991, Aurbach and co-workers examined the electrochemical behavior of calcium electrodes in various electrolytes, including $Ca(ClO_4)_2$, $Ca(BF_4)_2$, TBA(ClO_4), and TBA(BF_4) (where TAB stands for tetrabutylammonium), dissolved in acetonitrile, γ-butyrolactone (BL), tetrahydrofuran (THF), and propylene carbonate (PC).[18] Limited details were provided for $Ca(BF_4)_2$, but the results indicated that both the electrolyte salt and the solvent significantly influenced the morphology and passivation of the Ca anode.[18] ClO_4^- was found to undergo reduction more readily than BF_4^-, leading to the formation of $CaCl_2$ and higher stripping currents in $Ca(ClO_4)_2$-BL compared to TBA$(ClO_4)_2$-BL. The reaction between Ca metal and solvents such as BL and PC yielded various products, including esters, carboxylates, and inorganic species such as $CaCO_3$, rather than the $ROCO_2Li$ observed in Li systems.[19] The presence of even trace water (20 ppm) led to $Ca(OH)_2$ formation, and exposure to air caused $CaCO_3$ formation. Overall, no evidence of calcium deposition was found at room temperature in any of the studied systems, primarily due to the formation of insulating passivation films, underscoring the challenge of reversible Ca deposition and stripping.[18,19]

2.1.3 Revisiting of the Traditional Calcium Salts

Early investigations into traditional calcium electrolytes (e.g., $Ca(BF_4)_2$, $Ca(ClO_4)_2$, $Ca(TFSI)_2$) showed limited success due to the formation of passivation layers on Ca metal with poor Ca^{2+} conductivity at room temperature. However, in 2016, Palacín and colleagues revisited these salts in carbonate solvents (EC/PC mixture), highlighting that $Ca(BF_4)_2$ enabled quasi-reversible Ca plating/stripping at 100 °C with relatively low overpotential (0.10 V) and high ionic conductivity.[20] Yet, coulombic efficiency remained low (~40%) due to side reactions. Among the salts tested, only $Ca(BF_4)_2$ showed significant deposition, indicating the importance of the anion.

Later, Hosein et al. demonstrated that 1.0 M $Ca(BF_4)_2$ in EC/PC could achieve Ca with improved coulombic efficiency (up to 95%), although with broader overpotential range (from -1.7 to 2V vs Ca^{2+}/Ca), suggesting sluggish electron transfer. SEM, XRD, and FTIR analysis revealed that the SEI formed at room temperature was mainly organic, lacking the CaF_2 observed at high temperatures.[21]

Ponrouch et al. further studied the SEI composition formed with $Ca(BF_4)_2$ and $Ca(TFSI)_2$ in carbonate-based electrolyte.[22] TEM showed a thinner SEI with $TFSI^-$ (12–20 nm) compared to BF_4^- (70–80 nm). However, despite the thinner SEI with $TFSI^-$ based electrolyte, it mainly consists of degradation products of the electrolyte, such us calcium carbonate and traces of CaF_2 derived from salt decomposition. XPS and FTIR suggested that borate species (BO_x-based polymers) in the SEI formed from BF_4^- anion decomposition that play a key role in facilitating Ca^{2+} transport. In fact, the $TFSI^-$-based SEI, although thinner, does not exhibit significant electrochemical activity unless pre-passivated with BF_3 diethyl ether, which improves performance even in TFSI-based electrolytes.

In 2018, Bruce et al. demonstrated the first calcium electrolyte operating at room temperature, consisting of 1.5 M $Ca(BH_4)_2$ in tetrahydrofuran (THF).[23] Cyclic voltammetry on Au electrodes showed efficient Ca plating/stripping (94.8%) with anodic stability up to 3.0 V and an initial overpotential of ~250 mV, which decreased to ~100 mV upon cycling. Coulombic efficiency increased from 93% to ~96% over 25 cycles. Powder XRD and Fourier-transform infrared spectroscopy (FTIR) identified metallic Ca as the main product, with minor CaH_2. SEM , time-of-flight secondary ion mass spectrometry (TOF-SIMS), and gas chromatography–mass spectrometry (GC-MS) indicated that CaH_2 forms via chemical reaction between deposited Ca and THF, acting as a passivation layer but not as an active SEI.

Gewirth et al. further investigated the $Ca(BH_4)_2$–THF system, revealing via Raman spectroscopy that Ca^{2+} is primarily solvated by THF.[24] Electrochemical studies on Au and Pt (platinum) microelectrodes (2–20 mV s^{-1}) showed scan rate–dependent deposition behavior. The authors proposed a dehydrogenation step of BH_4^- prior to Ca deposition, with BH_3(THF) detected via LIFDI-MS (liquid injection field desorption ionization mass spectrometry) and H^- species facilitating nucleation. CaH_2 forms atop the deposited Ca. Numerical simulations indicated higher catalytic activity of Pt (38.7 s^{-1}) vs. Au (3.0 s^{-1}) for BH_4^- dehydrogenation, influencing Ca morphology: slower kinetics on Au favour uniform deposition, while limited hydride diffusion on Pt leads to irregular growth.

Jiao et al. achieved further improvement using a mixed $Ca(BH_4)_2^-/LiBH_4$ electrolyte. This formulation enabled over 200 cycles at room temperature with coulombic efficiencies up to 99.1% and stable full-cell performance (Ca‖LTO).[25] SEM showed spherical Ca deposition, while XPS and MD simulations revealed that $LiBH_4$ reduces the solvation strength of Ca^{2+}, thus improving deposition efficiency. $LiBH_4$ acts as a solvation structure modulator, enhancing electrolyte performance.

2.1.4 Advanced Calcium Electrolytes with weakly-Coordinating Anion (WCA)

As previously discussed, one of the main limitations in the application of conventional calcium salts in non-aqueous electrolytes is their poor compatibility with calcium metal, primarily due to the formation of passivating interphases that hinder Ca^{2+} transport and suppress reversible electrodeposition. To overcome this issue, recent research has focused on the use of weakly coordinating anions (WCAs), a class of large, chemically inert anions characterized by their low Lewis basicity and poor nucleophilicity.[25–30] WCAs function by minimizing strong interactions with metal cations, thereby promoting higher degrees of ionic dissociation within the electrolyte.[25,28–30] This leads to enhanced cation mobility and reduced formation of contact ion pairs, both of which are essential for achieving efficient charge transport and stable electrochemical interfaces.[28–30]

This approach was first proven effective in magnesium-based battery systems, where WCAs such as $CB_{11}H_{12}^-$,[31] $Al(hfip)_4^-$,[32] and $B(hfip)_4^-$ [33] enabled high electrochemical stability and reversible Mg^{2+} deposition by suppressing side reactions at the metal interface and facilitating the formation of conductive SEIs.[34–37] Building on these advances, the same design principles have been successfully applied to calcium-based electrolytes. Notably, salts such as $Ca(B(hfip)_4)_2$ have demonstrated excellent oxidative stability (up to 4.5 V vs. Ca^{2+}/Ca) and allow for reversible calcium plating and stripping at room temperature.[27] The weak interaction between the $B(hfip)_4^-$ anion and Ca^{2+} favours labile solvation structures and lowers the desolvation energy at the metal surface, improving electrochemical reversibility.[38,39] Similarly, $Ca(CB_{11}H_{12})_2$ exhibits high chemical and electrochemical stability and forms thin, stable SEIs that enable efficient calcium ion transport even under strongly reducing conditions.[26,40]

Overall, the development of electrolytes based on weakly coordinating, non-nucleophilic anions represent a promising strategy to enable practical and reversible calcium electrochemistry.[19] These systems address critical limitations such as high overpotentials, irreversible side reactions, and limited interfacial conductivity, thus paving the way for the design of high-performance calcium batteries. For this reason, in the following sections, two innovative calcium salts will be discussed: one based on a fluorinated borate anion and the other featuring a halogen-free anionic structure.

2.2 Preliminary examination of Ca-FPB: a promising Salt for Aprotic Electrolytes in Calcium-based Secondary Batteries

2.2.1 Introduction

Taking inspiration from Mg perfluorinated pinacolatoborate, $Mg[B(O_2C_2(CF_3)_4)_2]_2$ (abbreviated as Mg-FPB), which is anodically stable, electrochemically active Mg electrolyte featuring the low

coordination anion FPB, [41] herein we report the synthesis and characterization of Ca perfluorinated pinacolatoborate, $Ca[B(O_2C_2(CF_3)_4)_2]_2$ (abbreviated as Ca-FPB) which reveals promising behavior as salt for calcium batteries in terms of electrochemical stability window and the ability to reversibly deposit and dissolve calcium metal.

2.2.2 Experimental section

2.2.2.1 Synthesis of Ca-FPB

$Ca[B(O_2C_2(CF_3)_4)_2]_2$ (Ca-FPB) was synthesized synthetized from Calcium Borohydride and Hexafluoro-2,3-bis(trifluoromethyl)-2,3-butanediol. In an argon-filled glovebox (MBraun, T = 25°C, $H_2O \leq 0.1$ ppm, $O_2 \leq 0.1$ ppm), 0.055 g (0.8 mmol) of $Ca(BH_4)_2$ was dissolved in 60 mL of dry DME with stirring for 1 hour. Separately, 1.123 g (3.36 mmol) of hexafluoro-2,3-bis(trifluoromethyl)-2,3-butanediol (5% excess) was dissolved in 8 mL of anhydrous DME. This solution was then added dropwise over 1 hour to the $Ca(BH_4)_2$ solution using a syringe pump, during which hydrogen gas (H_2) was released. After the addition of the hexafluoro-2,3-bis(trifluoromethyl)-2,3-butanediol solution, the mixture was stirred for an additional 2 hours. After this time, the solution was transferred to a hermetically sealed bottle and removed from the glovebox. The bottle was then placed in an oven at 80°C and stirred for 24 hours.

After heating, the bottle was returned to the glovebox, and the resulting solution was added dropwise to 150 mL of dry cyclohexane under stirring. A white suspension was formed, filtered, and washed with fresh dry cyclohexane three times. The resulting powder was dried overnight under dynamic vacuum inside the glovebox chamber. 1 g of powder was obtained, corresponding to 92% of the theoretical yield. A schematic representation of the synthesis route of this salt is shown in Figure 2.1a.

2.2.2.2 Physico-chemical characterization

The synthesised salt was characterised by IR using a Nexus spectrometer (ThermoFisher, equipped with an attenuated total reflection accessory from 600 to 4000 cm^{-1}). The sample was transferred to the IR apparatus in a vial under Ar atmosphere to minimize the direct contact with ambient air. Complementary nuclear magnetic resonance (NMR) analyses were carried out with a BRUKER Ultrashield Avance 400 (^{11}B and ^{19}F nucleus, 128 MHz)

2.2.2.3 Electrolyte formulation and preparation

The electrolyte formulations were obtained by dissolving an appropriate amount of the synthesized Ca-FPB salt in dry DME in order to obtain a concentration of 0.25 M. The solvent (i.e., DME) used for the electrolyte formulation (anhydrous grade from Sigma Aldrich/Merck) was opened and dried for 5 days with activated molecular sieves (3A, Sigma Aldrich/Merck) in the glovebox before use. After the addition of a weighted amount of Ca-FPB to the solvent in the glovebox, the solution was

stirred overnight in sealed vials also kept inside the same glovebox. A clear solution was obtained after filtration through a 45µm PTFE syringe filter. All materials handling was performed inside an argon-filled glovebox.

2.2.2.4 Electrochemical tests

Calcium metal disk electrodes with a diameter of 12 mm were punched out from a Ca metal foil (ACI alloy Inc.). The surface of the calcium metal disks was scratched with a scalpel immediately before use. Whatman glass fibre separators (GF/A Cytiva, thickness 0.26 mm) were soaked with a known volume (80 µL) of each electrolyte during cell assembly (ECC-STD laboratory cells by El-Cell Gmbh) inside an Ar-filled glovebox. Asymmetric stainless steel (SS)| electrolyte | Ca cell configurations were employed for preliminary electrochemical experiments such us cyclic voltammetry (CV) at scan rates of 25 mV s^{-1} with current limitation of 10 mA. Additionally, as a preliminary investigation asymmetric SS | electrolyte | Ca configuration was employed to evaluate the electrochemical stability window (ESW) of the electrolyte by cathodic linear sweep voltammetry (LSV) up to 5.5 V vs. Ca and anodic CV up to 0.01 V vs Ca with scan rate of 2 mV s^{-1} in two different cell. In order to verify the successful deposition of Ca metal onto an inert substrate, a specific asymmetric cell (Ca | electrolyte | Al carbon coated) was subjected to extended galvanostatic plating, and the nature and morphology of the deposited material was characterized by SEM coupled with energy dispersive X-ray (EDX) analysis (Oxford Instruments X-Max 50 mm2). All electrochemical tests were carried out using Biologic MPG electrochemical testing devices at room temperature.

2.2.3 Results and discussion

2.2.3.1 Physico-chemical characterization

The IR spectrum of Ca-FPB is presented in Figure 2.1b, and the bands were assigned accordingly. The bands cantered at 2900 cm^{-1} and 1470 cm^{-1} correspond to the stretching and rocking vibrational modes of C−H bonds. Some solvent molecules remain coordinated to the structure and cannot be removed, even after drying the sample under a dynamic vacuum. The absence of bands in the ranges of 3000-3400 cm^{-1} (O−H stretching) and 2100-2500 cm^{-1} (B−H stretching) confirms that all $Ca(BH_4)_2$ and hexafluoro-2,3-bis(trifluoromethyl)-2,3-butanediol were consumed.[42] Between 700 and 1300 cm^{-1}, several bands are observed, which are attributed to the stretching modes of the C−F (100-1300 cm^{-1}), B−O (800-1000 cm^{-1}), and C−O (1000-1200 cm^{-1}) bonds in the FPB anion, as well as the bending modes of the C−H in the coordinated solvent. [43–46] All bands are consistent with the expected molecular structure shown in Figure 2.1a.

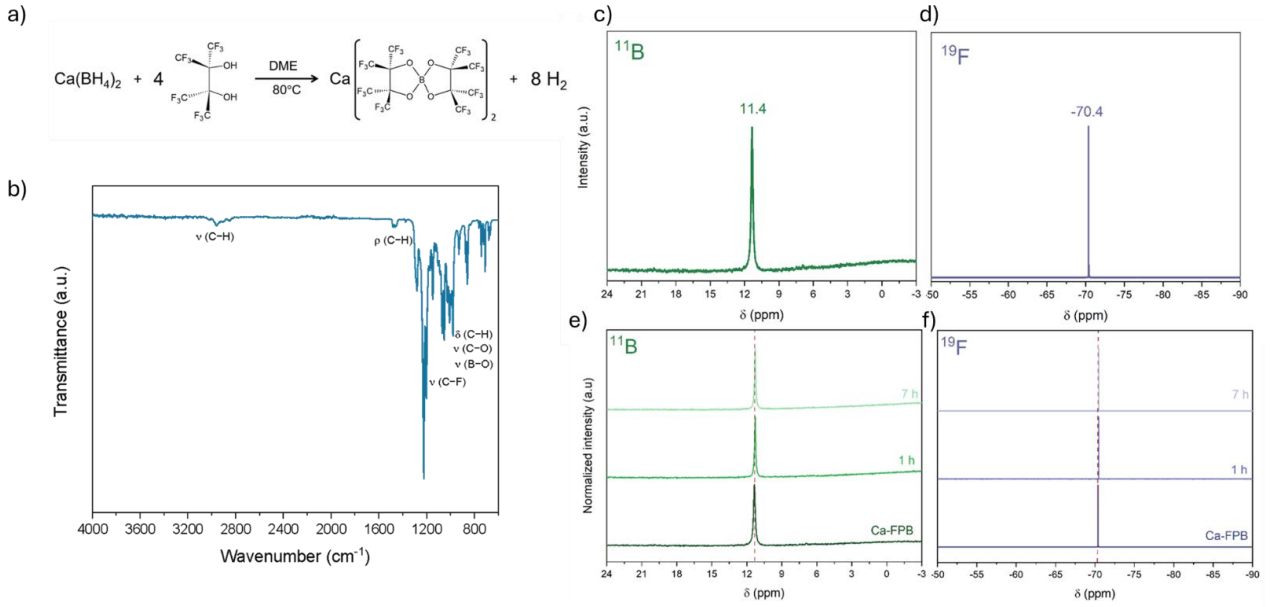

Figure 2.1. (a) Schematic representation of the Ca-FPB synthesis; (b) Infrared spectrum with vibrational modes of the different bonds indicated; (c) ^{11}B- and (d) ^{19}F NMR spectra; (e) ^{11}B- and (f) ^{19}F NMR spectra in the presence of water over 7 h.

In order to confirm a uniform product distribution, Ca-FPB was analysed by liquid-state NMR (Figure 1 c and d). The ^{11}B and ^{19}F spectra both show a single environment, centred at 11.4 ppm and -70.4 ppm, respectively. This is consistent with the tetrahedral geometry of the FPB anion and aligns with similar FPB analogs based on Li, Na, and Mg.[41,47,48]

To assess the chemical stability of the compound in the presence of water, a small amount of Ca-FPB ($2.4\text{x}10^{-4}$ mmol) was contacted with a slightly higher amount of water ($2.7\text{x}10^{-4}$ mmol), and the sample was analysed over 7 h by NMR (Figure 2.1 e and f). No significant changes were observed in ^{11}B or ^{19}F spectra. While borates typically undergo hydrolysis in the presence of water, indicating good stability of Ca-FPB in the presence of moisture.

2.2.4 Electrochemical characterization

A survey of the electrochemical activity of Ca-FPB-based electrolytes was performed evaluating the ability to deposit and dissolve calcium from an inert stainless-steel electrode by cyclic voltammetry (CV) in asymmetrical Ca | electrolyte | SS cell configuration shown Figure 2.2a.

The CV shows the first three cycles with large anodic peak and low reversibility probably due to the conditioning of the SS electrode with the formation of the so-called SEI. The further cycles reveal

reversible deposition/stripping behavior with almost negligible overpotential for deposition (0.15 V) and stripping (0.2 V) for more than 45 cycles.

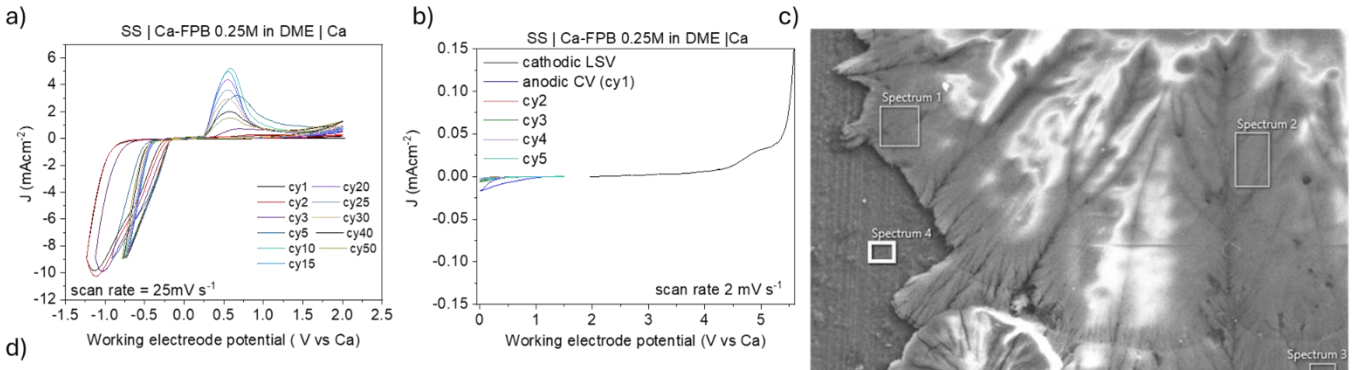

d)

Spectr.1	At. %	Spectr. 2	At. %	Spectr.3	At. %
O	41	O	39.6	C	46.4
Ca	22.4	Ca	21.6	O	22.9
C	19.8	C	20.6	Al	18.7
F	10.8	F	9.8	Ca	8.1
Al	6	Al	8.3	F	3.9

Spectr.4	At. %
C	73
O	23.9
Al	3.1

Figure 2.2 (a) CV and (b) electrochemical stability window of 0.25M Ca-FPB/ DME; (c) SEM and (d)EDX analysis of Ca deposit on carbon coated aluminium respectively.

Since it is of great interest to utilize Ca electrolytes in high voltage energy storage applications, the ESW of the 0.25 M Ca-FPB/DME electrolyte was evaluated by cathodic CV and anodic LSV in asymmetric cells Ca | Ca-FPB 0.25M in DME | SS. As seen in figure 2.2b, this electrolyte discloses promising ESW.

In particular, the cathodic LSV reveals an anodic stability up to 4.5 V vs. Ca^{2+}/Ca with current below 15 µA and exhibits almost negligible cathodic degradation down to 0.01 V vs. Ca^{2+}/Ca after the first cycles, symptoms of the formation of a stable SEI on the first cycle that hinder the degradation for the further cycles.

To prove the effective formation of calcium metal during plating with the 0.25 M Ca-FPB/DME electrolyte, a long chronopotentiometric deposition of calcium (4 hours) was performed on a aluminium carbon coated substrate at a current density of 0.1 mA cm^{-2}. *Post mortem* SEM and EDX analyses (Figure 2.2 c and d) of the electrode recovered from this cell confirm the successful deposition of Ca metal particles on the Al carbon coated surface. In particular, from the EDX analysis the presence of the degradation of the electrolyte can be observed on the Ca metal deposit, while the presence of fluorine coming from the absorbed salt on the electrode can be excluded since is not observed in spectrum 4 representing the carbon coating far from the calcium deposit. However, the

presence of Al, C and O is observed in all the spectra. The observation of aluminium and carbon suggest the formation of a thin Ca deposit that allow the detection of the substrate of nucleation under the calcium, while the presence of oxygen may come from both the nucleation substrate or from atmospheric contamination as a consequence of the rapid exposure of the sample during the charging in the SEM analysis chamber.

2.2.5 Conclusion

Overall, we introduced and successfully evaluated Ca-FPB as a novel salt for calcium-based aprotic electrolytes, leveraging the properties of its weakly coordinating anion. The 0.25 M Ca-FPB solution in DME demonstrated the ability to reversibly plate and strip calcium metal from an inert substrate with low overpotentials. Furthermore, the electrolyte showed wide electrochemical stability, with anodic decomposition potentials reaching up to 4.5 V vs. Ca^{2+}/Ca, confirming its suitability for high-voltage applications. These results identify Ca-FPB as a promising candidate for further development in both synthetic optimization and electrolyte engineering for calcium-ion battery systems. Nonetheless, its synthesis remains challenging due to the need for strictly inert conditions, the release of hydrogen gas, and high sensitivity to contamination. These limitations prompted the investigation of an alternative salt system with a more accessible and scalable synthetic route, which is introduced in the following section.

2.3 Extending the boron-based salt variety: the case of $CaB_{12}H_{12}$

2.3.1 Introduction

As previously discussed, in recent years novel electrolyte systems based on calcium tetrakis(hexafluoroisopropyloxy)borate, $Ca[B(hfip)_4]_2$, and its analogues, including Ca-FPB, have demonstrated the ability to enable reversible calcium metal deposition at room temperature, along with high oxidative stability. These features make them particularly attractive candidates for the development of next-generation calcium-based electrochemical energy storage systems.[38,39] However, their synthesis produces large amounts of hydrogen gas[41] and requires dedicated equipment for synthesis since everything must be done under inert atmosphere. Kisu et al. propose calcium monocarborane as efficient and stable electrolyte for CBs,[49] however, its production is prohibitively expensive.[50]

As already mentioned, given the lack of a commercially available, low cost or easily synthesized electrolyte, exploring new potential cathodes and anodes for calcium ion batteries has become even more challenging. In the light of these factors, the development of easily accessible electrolytes is one of the most critical prerequisites for the advancement of calcium-based energy storage systems.

In this study we propose a novel concept of electrolyte with a simple synthesis pathway inspired by the work of Wang et al. , who reported a high yield synthesis of alkaline dodecaborate (M $B_{12}H_{12}$; with M= Na, K). In the following, it will be demonstrated that this synthesis pathway can be optimized for calcium dodecaborate as well. Dodecaborates are already well known, mainly as hydrogen storage [51–53] but have also been studied as possible solid electrolytes for solid state batteries.[52,54,55]

In particular, Koettgent et al. explored the potential of $CaB_{12}H_{12}$ as a solid-state electrolyte in a Ca-based system, revealing, however, a high migration barrier for Ca^{2+} ion. Consequently, in the present study, it was decided to study the electrochemical behaviour of Ca dodecaborate simply as an electrolyte salt in conventional and non-conventional electrolyte systems. In particular, despite some solubility issues, it was demonstrated that a Ca dodecaborate-based electrolyte produced with a non-conventional solvent such as N-methyl-2-pyrrolidone (NMP) enables reversible plating/stripping of calcium metal.

In the following sections, after the description of the synthesis and the characterization of Ca dodecaborate, its electrochemical performance as calcium electrolyte salt are presented.

2.3.2 Experimental section

2.3.2.1 Synthesis of calcium dodecahydro-closo-dodecaborate

The synthesis of $CaB_{12}H_{12}$ was carried out under an inert atmosphere, either inside an argon-filled glovebox (MBraun, $O_2 \leq 0.1$ ppm; $H_2O \leq 0.1$ ppm), or in a stainless-steel autoclave, by adaptingthe synthesis route from a solvothermal method reported elsewhere [52] and schematised in Figure 2.3.

In a typical experiment, 0.04 g of $Ca(BH_4)_2$ was dissolved in 12 mL of diglyme under stirring for 15 min. The solution was transferred to a Teflon chamber and then, 1.2 mL of $DMS{\cdot}BH_3$ was added to the system. The Teflon chamber was put into the autoclave and closed, transferred outside the glovebox and put inside an oven at room temperature. The temperature was increased by 20°C every 10 minutes up to the required temperature. The autoclave was left 24 h at this temperature and then cooled down to room temperature. In this study, three temperatures were investigated (200°, 215° and 230°C). The corresponding samples are named $CaB_{12}H_{12}$@T (Where T=200, 215 or 230°C). The autoclave was transferred back to the glovebox and the obtained solid was filtered and washed with fresh diglyme (3x10 mL), followed by a drying process under vacuum overnight.

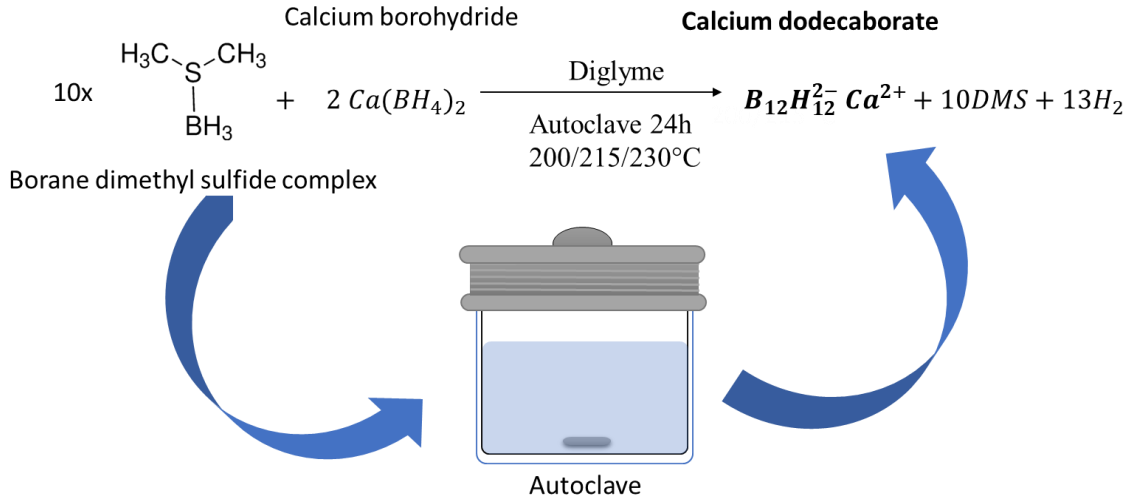

Figure 2.3 Schematic representation of autoclave synthesis of $CaB_{12}H_{12}$

2.3.2.2 Physico-chemical characterization

The samples were characterized by different techniques. IR spectra were collected using a Nexus instrument (ThermoFisher, equipped with an attenuated total reflection accessory from 600 to 4000 cm^{-1}). The samples were transferred to the IR apparatus in a vial under Ar atmosphere, and they were analyzed under air (avoiding the contact with air until the last minute). NMR analyses were carried out in a BRUKER Ultrashield Avance 400 (^{11}B nucleus, 128 MHz, deuterated solvent: dimethyl sulfoxide DMSO).

2.3.2.3 Electrolyte formulation and electrochemical characterization

In order to understand the electrochemical behavior of the newsalts, the activity of $CaB_{12}H_{12}$@200/215/230 in a series of electrolytes (summarized in Table 1) was tested. The solvents used for their formulation were all purchased anhydrous from Sigma Aldrich and further dried for 5 days under activated molecular sieves (3A, Sigma Aldrich). LP30 commercial electrolyte was obtained from Solvionic to facilitate a comparative analysis and conductivity calculation of our electrolyte. After the drying step, the appropriate amount of $CaB_{12}H_{12}$ was added to the solvent and let stir for 1 week. $CaB_{12}H_{12}$@215 0.5 M in NMP was also tested with Boron trifluoride diethyl etherate (BF_3OEt_2, Sigma Aldrich) in 0.02 M concentration as additive. Ca electrode disks (9 mm diameter) were made by scratching and punching a Ca foil from ACI alloy Inc. Whatman glass fibre disks (thickness 1.55mm) soaked with known volume (80 µL) of electrolyte were employed as separators. The assembly of the cell and all the manipulations were carried out inside an Ar-filled glovebox. The testing cells used for the electrochemical experiment were ECC-STD EL-Cell, assembled in symmetric Ca | electrolyte | Ca configuration. This configuration was employed for

preliminary electrochemical experiments, includingLSV and CV, aimed at elucidating the optimal electrolyte formulation in relation to charge transfer current and the reversibility of the plating/stripping process. Furthermore, it was utilized for advanced tests, such as galvanostatic cycling (GC), with electrochemical impedance spectroscopy (EIS) measurements carried out after each discharge cycle. Stainless steel (SS) electrodes were employed as blocking electrodes in a symmetrical configuration: SS | electrolyte | SS, for conductivity tests performed by EIS. Additionally, an asymmetrical SS | electrolyte | Ca configuration was employed to determine the ESW.

Finally, to demonstrate the successful deposition of Ca metal onto an inert substrate, an asymmetrical configuration (Ca | electrolyte | Au) was utilized. Subsequently, an extended plating under galvanostatic conditions was conducted, and the deposited material was characterized via *ex situ* dispersive EDX analysis (Oxford Instruments X-Max 50 mm2) and optical microscopy (Keyence). All the electrochemical tests were performed using Biologic MPG and VSP potentiostats.

2.3.3 Results and discussion

2.3.3.1 ^{11}B Nuclear Magnetic Resonance

The ^{11}B NMR spectra of the analysed samples are shown in Figure 2.4a. The solids obtained at 200°, 215° and 230°C show a doublet centred at -15 ppm, characteristic of the 12 boron atoms of the $[B_{12}H_{12}]^{2-}$ anion[56–58]. This is the main signal, and it is an indication of the successful synthesis of $CaB_{12}H_{12}$. However, other signals are also present in the spectra. All solids present two doublets centred at -29 ppm and -1 ppm, indicating the formation of the $[B_{10}H_{10}]^{2-}$ anion[59]. $CaB_{12}H_{12}$@200°C and $CaB_{12}H_{12}$@230°C also show a multiplet between -16 and -22 ppm, which is attributed to the presence of the $[B_{11}H_{11}]^{2-}$ anion[60]. None of the syntheses conducted at three different temperatures produced a single pure compound. However, among the three attempts, the temperature of 215°C resulted in the purest form of calcium dodecaborate.

The absence of intense signals between 5 and 20 ppm discards the presence of B─O environments (as in borates), confirming that the O─H bonds present in the IR spectra shown below are due to adsorbed water.

2.3.3.2 Infrared Spectroscopy

The spectra of the synthesized calcium dodecahydro-closo-dodecaborate at different temperatures and those of commercial $Ca(BH_4)_2$ and diglyme (as references) are shown in Figure 2.4b. The spectrum of commercial diglyme shows the C─H stretching and bending bands between 2700-3000 cm^{-1} and 1200-1400 cm^{-1}, respectively. The intense band at 1050 cm^{-1} corresponds to the C─O

stretching vibration of the molecule. $Ca(BH_4)_2$ exhibits bands between 2200 and 2400 cm^{-1}, which correspond to the stretching of the B─H bonds, and another group of signals between 1000 and 1300 cm^{-1}, attributed to the deformation modes of the $(BH_4)^-$ anion[61,62].

The spectra of the $CaB_{12}H_{12}$ samples synthesized at different temperatures are very similar. The B─H stretching mode has shifted in comparison with $Ca(BH_4)_2$: it appears in the 2350-2600 cm^{-1} region, similarly to other dodecahydro-*closo*-dodecaborates.[63,64] The B─H stretching bands of $Ca(BH_4)_2$ are not visible anymore in the $CaB_{12}H_{12}$ spectra, indicating a complete transformation of the borohydride. The band centred at 1050 cm^{-1} is the typical stretching mode of the B─B bond of the boron cage, while the bands between 650 and 800 cm^{-1} correspond to the rocking and bending modes of the B─H bond.[59,65] The broad band between 3300 and 3600 cm^{-1} is assigned to the stretching band of O─H bonds, probably representing adsorbed water. All synthesized samples show the stretching C─H bands between 2700-3000 cm^{-1}, indicating that some solvent is still present in the structure.

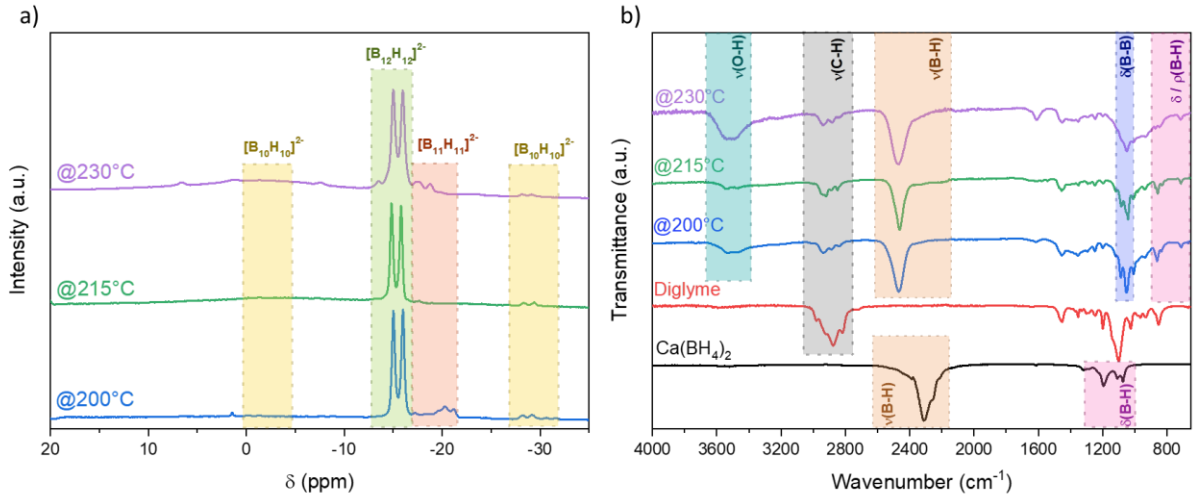

Figure 2.4 a) ^1H CP-MAS ^{11}B NMR spectra of the solids obtained after synthesis at 200°, 215° and 230°C (the solids were dissolved in DMSO); b) IR spectra of $Ca(BH_4)_2$, diglyme and the $CaB_{12}H_{12}$ synthesized salts at the three different temperatures

2.3.3.3 Electrochemical characterization

From the outset, the critical solubility of all the salts was evident. When dropped onto the Whatman separator, they can induce asymmetric behavior due to the insoluble particles being confined to one side of the glass fibre separator. The electrochemical behavior of $CaB_{12}H_{12}$ was evaluated testing all the electrolyte formulations, summarized in Table 1, even with partial solubility by LSV and CV in symmetric cell configuration Ca / electrolyte / Ca (Figure 2.5 a and b respectively).

Table 1 Schematic representation of electrolyte formulations

Salt	Conc.(M)	Solvent	Solubility
$CaB_{12-x}H_{12-x}$ (200°C)	0.25	DMSO	Partial (opalescent)
$CaB_{12-x}H_{12-x}$ (215°C)	0.1-0.25-0.5	NMP	Partial (opalescent)
	0.25	ACN	No (colloidal precipitate)
	0.25	DMSO	Partial (opalescent)
$CaB_{12-x}H_{12-x}$ (230°C)	0.5-0.25	DMSO	Partial (opalescent)
	0.1	NMP	Yes
	0.5- 0.25	NMP	Partial (opalescent)
	0.25	DME/THF 1:1 (v/v)	No (colloidal precipitate)

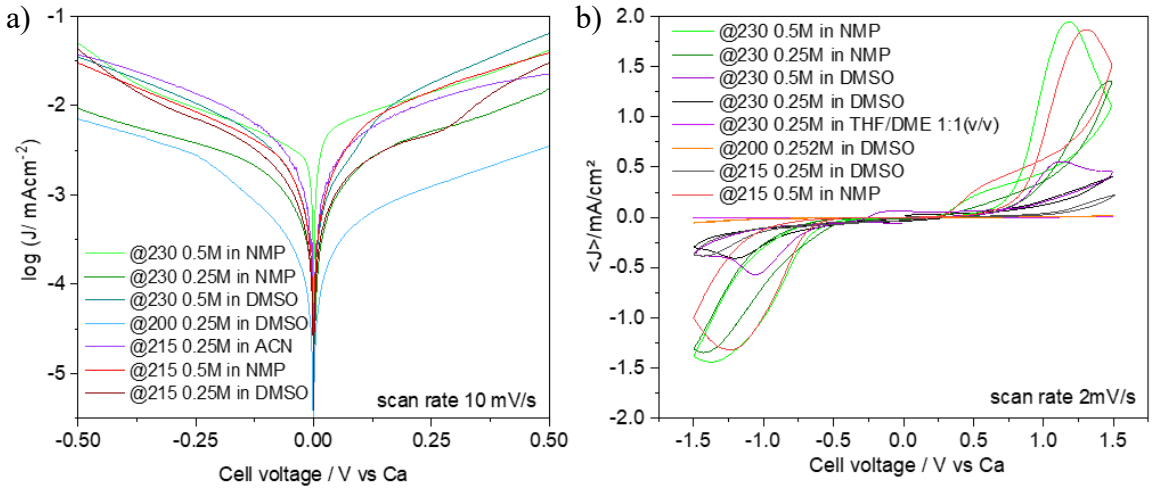

Figure 2.5 a) LSV and b) CV of all the electrolytes formulations.

From this preliminary evaluation, $CaB_{12}H_{12}$@215 and $CaB_{12}H_{12}$@230 in NMP overcome all the other formulations in terms of plating/stripping reversibility and current. For this reason, the electrochemical characterisation was specifically carried out only on electrolytes produced with these two salts dissolved in NMP, aiming to achieve the optimal formulation that minimizes plating/stripping overpotential and maximizes reversibility. Both salts, $CaB_{12}H_{12}$@215 and $CaB_{12}H_{12}$@230, were compared in LSV and CV tests in symmetric cell Ca | electrolyte | Ca, at three different concentrations: 0.1, 0.25 and 0.5 M. Based on a preliminary analysis of the CV shown in Figure 2.6, it is evident that the more concentrated formulations at 0.5 M of both salts exhibit the highest currents in CV. However, for all the three concentrations, $CaB_{12}H_{12}$@230 shows also higher deactivation and worse reversibility during cycling than $CaB_{12}H_{12}$@215. For this reason, further characterisations were carried out only with $CaB_{12}H_{12}$@215.

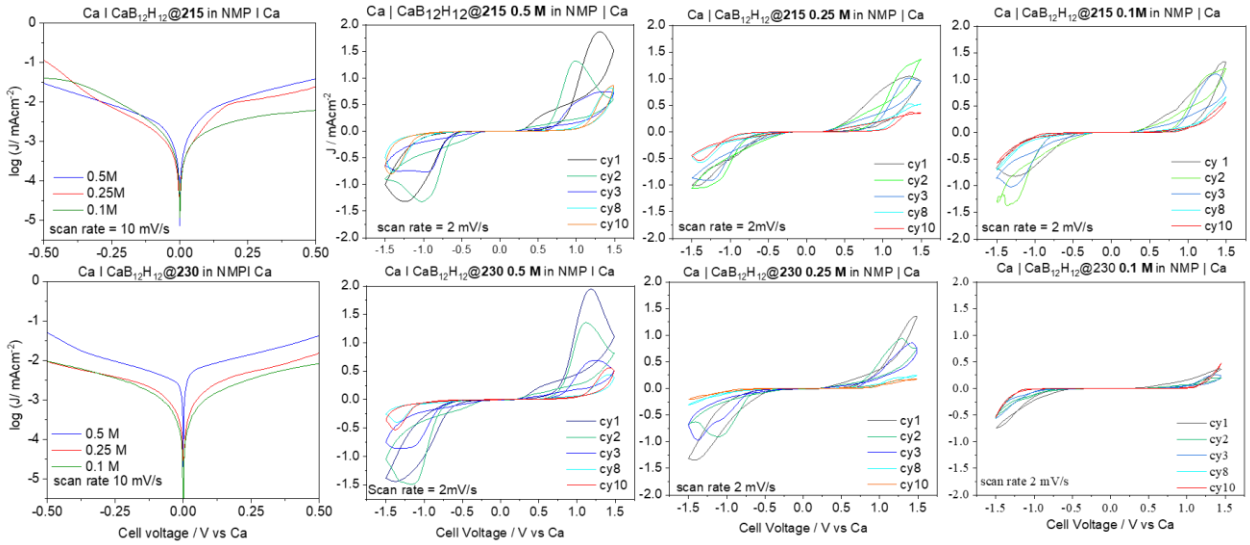

Figure 2.6 LSV and CV of $CaB_{12}H_{12}$@215 in line a) and $CaB_{12}H_{12}$@230 in line b) at the three different concentrations.

In Figures 2.7 a and b, are shown the LSV and the firsts cycles of CV of $CaB_{12}H_{12}$@215 in NMP at the three concentrations. These voltammograms are important to understand the stripping/deposition behavior of calcium. To highlight anodic and cathodic overpotential and to compare the current of charge transfer, the LSV were plotted as log(J) vs the Cell Voltage (V vs. Ca^{2+}/Ca). The LSV of $CaB_{12}H_{12}$@215 in Figure 2.7a, shows a non-ideal increase of the current with increasing concentration. In fact, the results of the Tafel fitting summarized in Table 2 shows similar charge transfer current for 0.5 and 0.1 M formulations, whereas that at 0.25 M, while showing lower charge transfer current, it exhibits a higher symmetry in the anodic and cathodic processes. On the contrary, the curves for 0.5 and 0.1 M solutions disclose inverted limitations for the cathodic and anodic reactions.

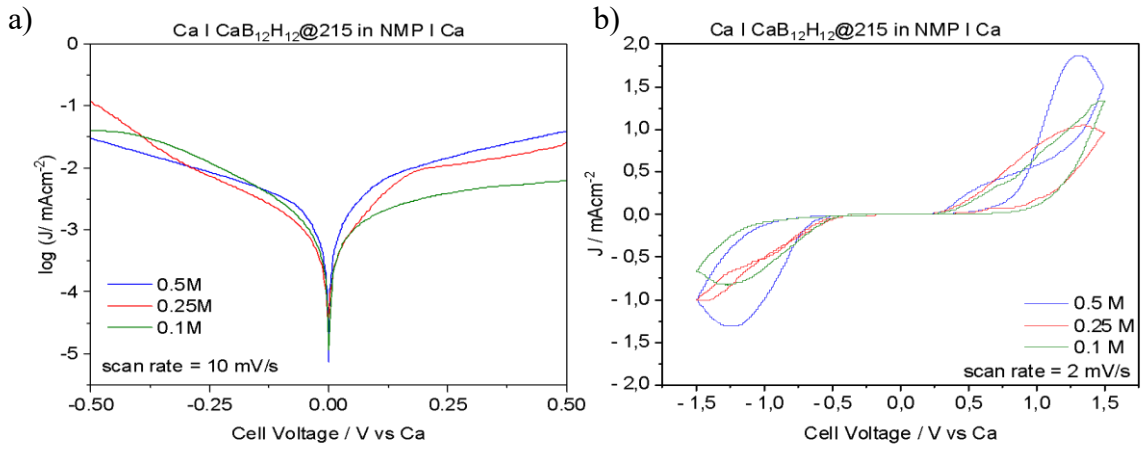

Figure 2.7 a) LSV and b) CV of $CaB_{12}H_{12}$@215 in NMP at 0.1, 0.25 and 0.5M

Table 2. Result of the Tafel fitting for $CaB_{12}H_{12}$@215 for the three concentrations

$CaB_{12}H_{12}$@215	0.1M	0.25M	0.5M
I° ($uAcm^{-2}$)	2.32	0.85	2.45
Bc (mV)	0.27	0.56	0.65
Ba (mV)	0.73	0.44	0.35

To go deeper in understanding the behavior of this electrolyte, conductivity tests were carried out for the tree concentration in symmetric SS | electrolyte | SS cells. The molar conductivity (Λ) of the electrolyte at each concentration was evaluated using equations 1 and 2 which, combined in eq. 3, lead to eq. 4 below:

Eq.1 $$R = \rho \cdot \frac{L}{S}$$ Eq. 2 $$\chi = \frac{1}{\rho} = \Lambda \cdot C_{electrolyte}$$

Eq.3 $$\frac{R_x}{R_{LP30}} = \frac{\rho_x}{\rho_{LP30}} \frac{L}{S} \frac{S}{L} = \frac{\chi_{LP30}}{\chi_x} = \frac{\Lambda_{LP30} C_{LP30}}{\Lambda_x C_x}$$

Eq.4 $$\Lambda_x = \Lambda_{LP30} \frac{C_{LP30}}{C_x} \cdot \frac{R_{LP30}}{R_x}$$

In this equation, R is the resistance of the electrolyte measured by EIS (Ω), ρ is the resistivity of the electrolyte (Ω*cm), L is the distance between the electrodes or the cell thickness (cm), S is the cross-sectional area of the electrode (cm^2), χ is the ionic conductivity (S/cm) and, Λ is the molar

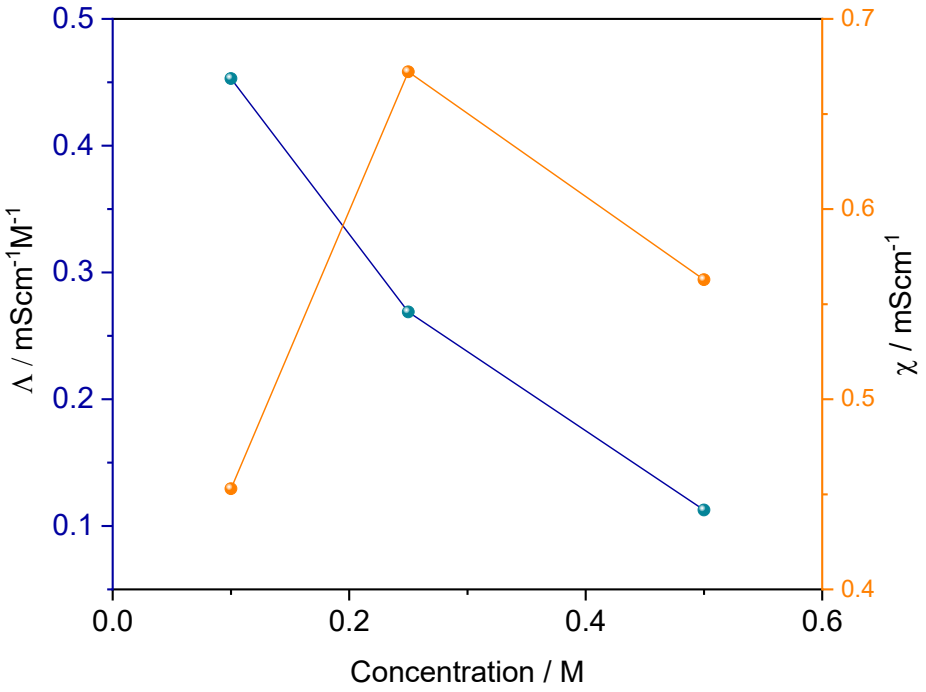

Figure 2.8 conductivity plot of $CaB_{12}H_{12}$@215 at 0.1, 0.25 and 0.5M

conductivity ($S \cdot cm^2 \cdot mol^{-1}$), C is the concentration in the electrolyte (M=mol/L), and χ is the conductivity(S/cm, the known value for LP30 is $\chi_{25°C}^{LP30} = 1.\ 119 * 10^{-2}\ \frac{S}{cm}$ at $C_{LP30} = 1\ M$)[66]

Table 3. Value of conductivity plot compared to LP30 values.

		Ca Dodecaborate@215		
	LP30	0.1M	0.25M	0.5M
$\chi\ (mS/cm)$	11.19	0.45	0.67	0.56
Λ (mS/cm*M)	1.119	0.453	0.269	0.113

The results of these tests, shown in Figure 2.8 and Table 3, are consistent with the CV response reported in Figure 2.7. In particular, the decrease of the molar conductivity Λ with increasing concentration reflects the growing degree of ionic association in solution, which leads to a marked non-ideal behaviour of the electrolyte. This trend is typical of weakly dissociated salts, where ion–ion interactions become progressively more significant at higher concentrations.

It is also worth noting that $CaB_{12}H_{12}$@215 at 0.25 M exhibits the lowest charge-transfer current in the Tafel analysis, yet it shows the highest ionic mobility and thus the highest molar conductivity. This apparent discrepancy highlights the fact that ionic mobility in the bulk electrolyte does not directly translate into interfacial charge-transfer kinetics, which are strongly influenced by local phenomena at the electrode–electrolyte interface.

Taken together, these results underline the need to identify an electrolyte formulation that balances bulk ion transport with interfacial charge-transfer efficiency. For this reason, further investigations focused on the 0.25 M and 0.5 M solutions of $CaB_{12}H_{12}$@215, which exhibited the highest ionic mobility and the highest current response, respectively, allowing us to evaluate the trade-off between these two key properties.

To determine the electrochemical stability window of these electrolytes, anodic and cathodic CV analyses were carried out in asymmetric Ca | $CaB_{12}H_{12}$@215 0.25 and 0.5M in NMP | SS cells, both starting from OCV. For the anodic CV, the voltage is increased up to 5 V vs. Ca^{2+}/Ca in order to complete the first degradation pick, while the potential limit was decreased for the consecutive cycles to 4 V vs Ca^{2+}/Ca to evaluate the continuation of the oxidative degradation processes. To evaluate the degradation in reduction before plating, the cathodic CV was stopped at 0.01 V vs Ca^{2+}/Ca. Figures 2.9 a and b show the ESW of the electrolyte at 0.5 and 0.25 M respectively. As expected, the electrolyte at 0.25 M exhibits nearly half the degradation currents compared to the 0.5 M

concentration, indicating that the degradation is primarily due to the decomposition of the salt rather than the solvent. These ESW demonstrate, for both salts, low cathodic degradation and anodic stability up to 3 V with currents below 0.02 mA/cm^2 after the first irreversible degradation process for $CaB_{12}H_{12}$@215 0.5 M concentration and up to 4 V with current below 0.02 mA/cm^2 for the 0.25 M one.

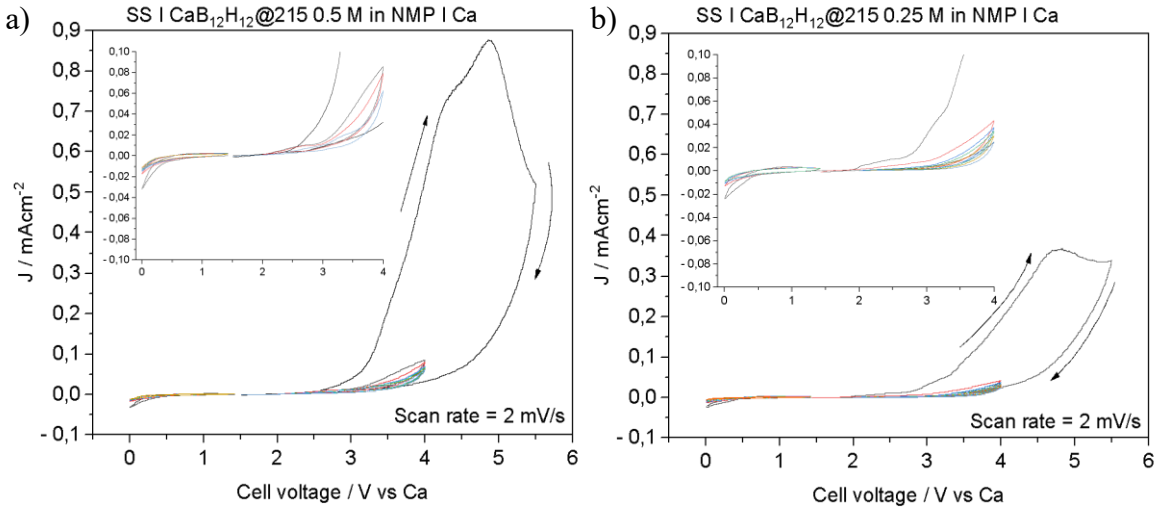

Figure 2.9 Electrochemical stability window of $CaB_{12}H_{12}$ a) 0.5M and b) 0.25M in NMP

To understand the plating/stripping behavior of Ca with 0.5 and 0.25 M $CaB_{12}H_{12}$@215 in NMP electrolytes, and its evolution in galvanostatic cycling conditions, polarisation tests with constant current were carried out in symmetric Ca | electrolyte | Ca cells. The resutls of these tests agre shown in Figures 2.10 and 2.11 for the electrolyte with 0.5 and 0.25 M concentrations, respectively. The galvanostatic cycling is preceded by 1 hour of OCV with EIS every 10 minutes and proceeds at low current for the first two cycles to facilitate the formation of the SEI and at higher current for the subsequent cycles. All the cycles of the GC are followed by EIS after every discharge.

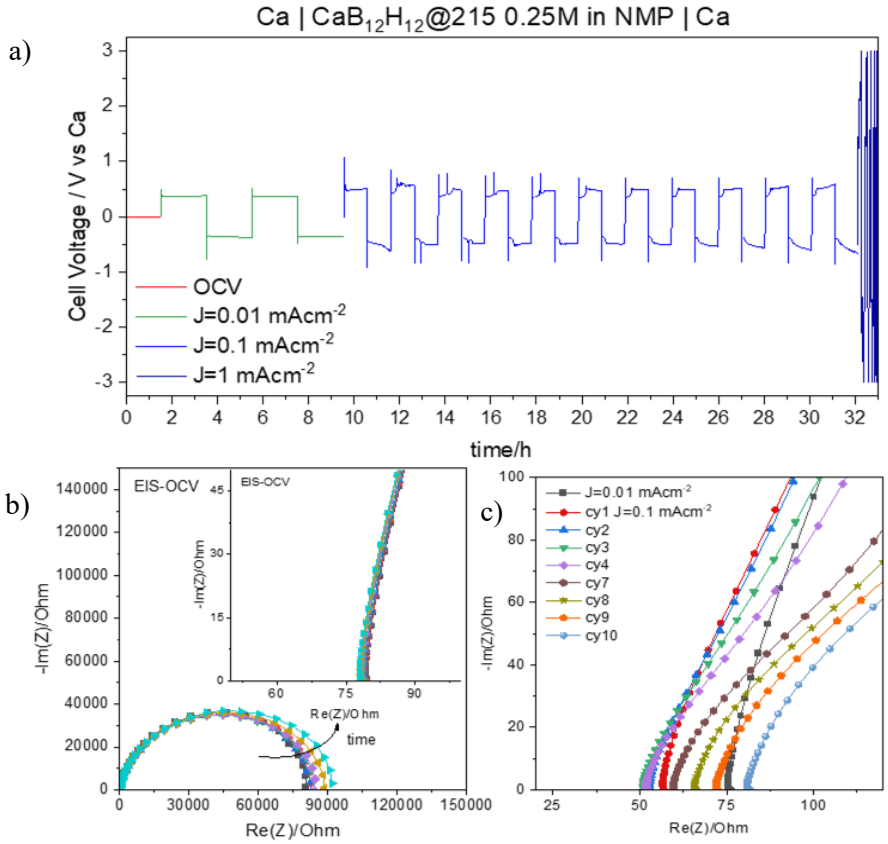

Figure 2.10. Ca | $CaB_{12}H_{12}$@215 0.25M in NMP | Ca cell tested by a) OCV and GC at different current with b) EIS after every 10 minutes during OCV and c) after every discharge of the GC

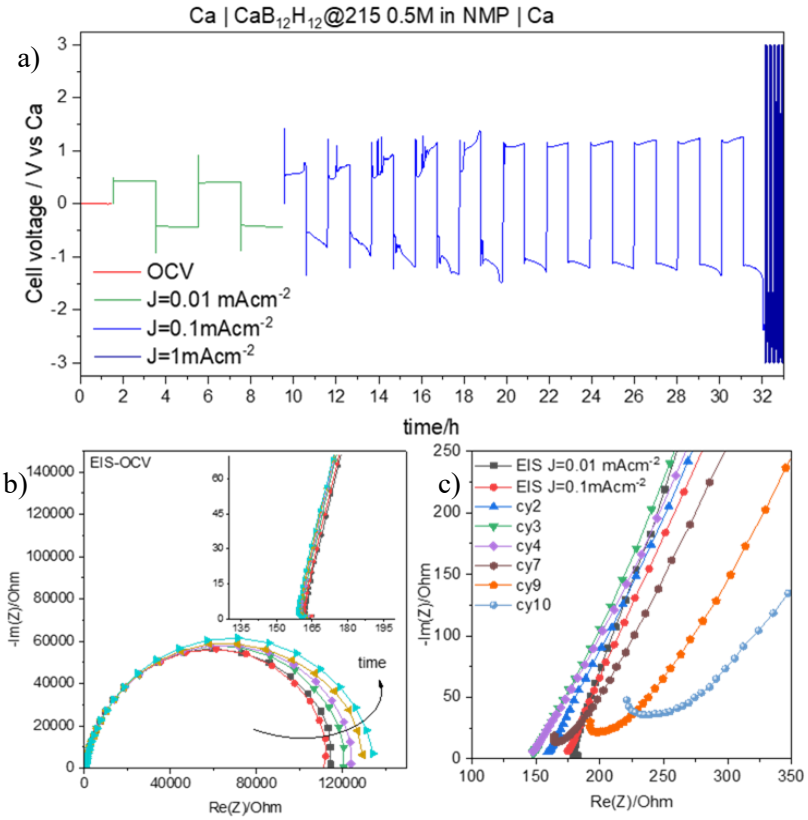

Figure 2.11. Ca | $CaB_{12}H_{12}$@215 0.25M in NMP | Ca cell tested by a) OCV and GC at different current with b) EIS after every 10 minutes during OCV and c) after every discharge of the GC.

The EIS spectrum measured at OCV, shown in Figure 2.10b, indicates a gradual increase in capacitance and resistance, probably due to the thickening of the SEI. $CaB_{12}H_{12}$@215 0.25M in Figure 2.10b shows a similar trend but, with almost half of the resistance of the electrolyte, in accordance with the conductivity tests. After the beginning of the galvanostatic cycling (Figure 2.10a and 2.11a), both electrolytes show overpotentials below 0.5 V for the first cycles at lower current and exhibit an initial voltage peak probably due to the breaking of the passivation film at the surface of the electrode before the start of the plating/stripping processes. As the cycles progress, this behaviour is maintained showing the instability of the SEI and the growth of the overpotential upon cycling for $CaB_{12}H_{12}$@215 0.5M while, despite the potential peak still visible in the galvanostatic profile, a similar growth of the overpotential with time was not observed for the 0.25 M concentration.

The growth of overpotentials in Figure 2.10a can be explained by the evolution of the EIS spectra during galvanostatic cycling shown in Figure 2.10c. These EIS highlight a gradual increase of the resistance of the electrolyte from around 100 to 200 Ohm after cycles. This behavior can be due to the degradation of the salt and so the loss of active species in solutions, leading to the increase of the plating/stripping potentials. As already mentioned, the $CaB_{12}H_{12}$@215 0.25M formulation shows a similar trend for the first cycles, even though with a lower potential peaks, and with overpotentials below 1 V for all the cycles at 0.1mAcm^{-2}, sign of higher stability and reversibility. In particular, it is interesting to notice that the EIS during galvanostatic cycling (Figure 2.11c) shows an activation process leading to an increase of the electrolyte resistance during the first cycles, which however increases again upon cycling, ending at a value very similar to that measured at OCV. These tests revealed that both electrolytes allow reversible plating/stripping at 0.01 and 0.1 mAcm^{-2}, even though with limiting overpotential at high current densities In particular, $CaB_{12}H_{12}$@215 0.25M discloses the best electrochemical performance in terms of plating/stripping overpotentials and reversibility. Furthermore, to improve the performances of this electrolyte, $CaBF_3OEt_2$ was tested as additive at a 0.02 M concentration in $CaB_{12}H_{12}$@215 0.5M. The same conditions for CV and galvanostatic test were used to evaluate its performance. The two electrodes with and without additive are compared in Figure 2.12.

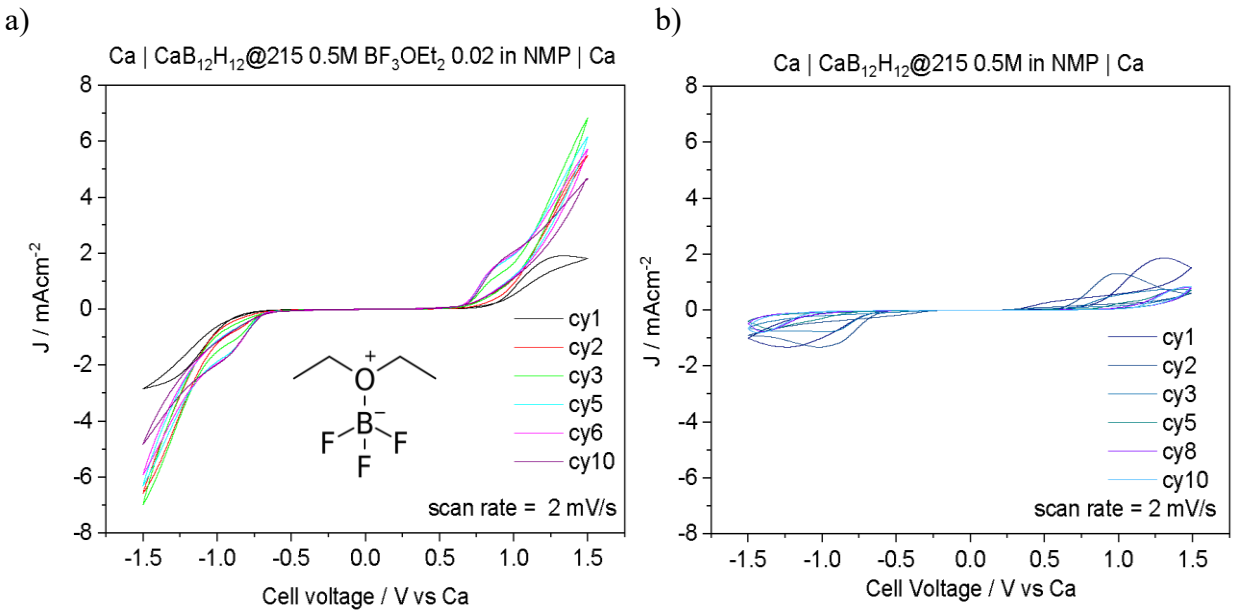

Figure 2.12 CV of a) $CaB_{12}H_{12}$@215 0.5M and b) with BF_3OEt_2 as additive.

.

The results shown in Figure 2.12b clearly indicate that the electrolyte with the additive exhibits similar overpotential to the other one, with however a significant increase in plating/stripping currents.

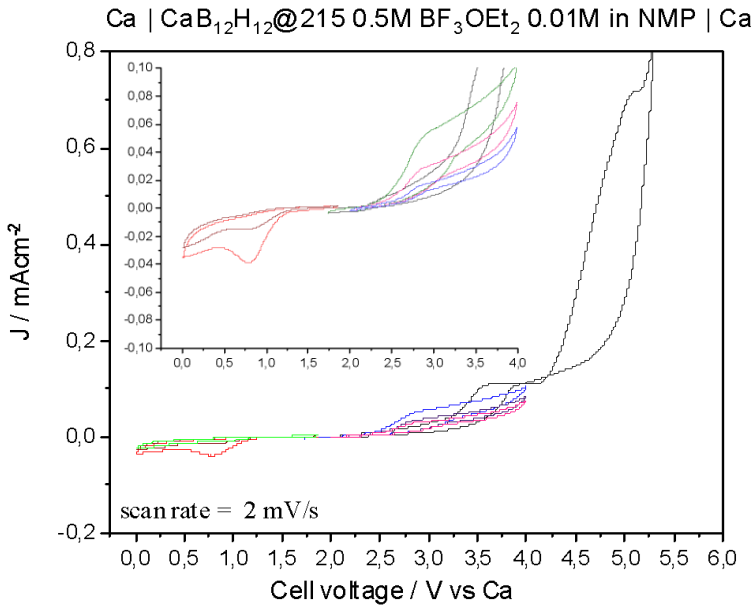

Figure 2.13 ESW of $CaB_{12}H_{12}$@215 0.5M with BF_3OEt_2 as additive

However, as shown in Figure 2.13, the use of this additive reduces the ESWto 2.75 V vs. Ca^{2+}/Ca. In spite of this reduction in ESW, the galvanostatic profile and the EIS spectra shown in Figure 2.11 clearly indicate that this additive promotes the growth of a more stable and conductive interface on

Ca metal. Moreover, the galvanostatic profile shown in Figure 2.12a exhibits a smoother profile than that measured in the absence of the additive (Figure 2.14a). Indeed, the absence of voltage peaks and the lower overpotential observed during the plating and stripping of Ca clearly evidence the creation of more stable and less passivating interfaces on Ca metal. The EIS spectra shown in Figure 2.14b, on the other hand, confirm the positive effect of this additive, which promotes the electrolyte conductivity which decreases from around 165 Ohm at OCV without the additive to 18 Ohm.

As shown in Figure 2.14c, the distance of high frequency intercept of the AC response with the real axis, with respect to the axes origin, slightly increases during galvanostatic cycling, indicating the consumption of the mobile Ca^{2+} ions in the electrolyte. However, the electrolyte resistance after the test is still lower (around 50 Ohm) than the initial resistance of the electrolyte without additive.

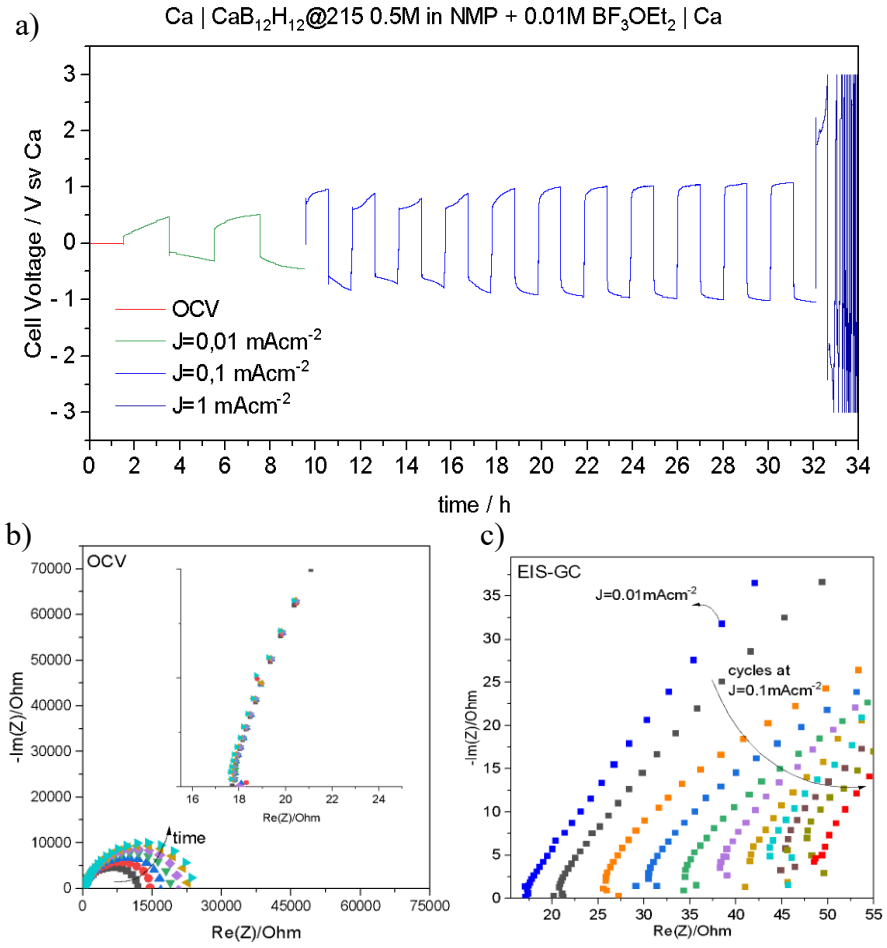

Figure 2.14 Ca | $CaB_{12}H_{12}$@215 0.5M in NMP +0.01M BF_3OEt_2 | Ca cell tested by a) OCV and GC at different current with b) EIS after every 10 minutes during OCV and c) after every discharge of GC.

To validate the effective ability of our electrolyte to electrodeposit calcium onto an inert substrate, a long plating test on an Au electrode was carried out. *Post mortem* characterization by optical microscopy clearly revealed the formation of deposits of Ca metal, further confirmed by EDX analysis (Figure 2.15).

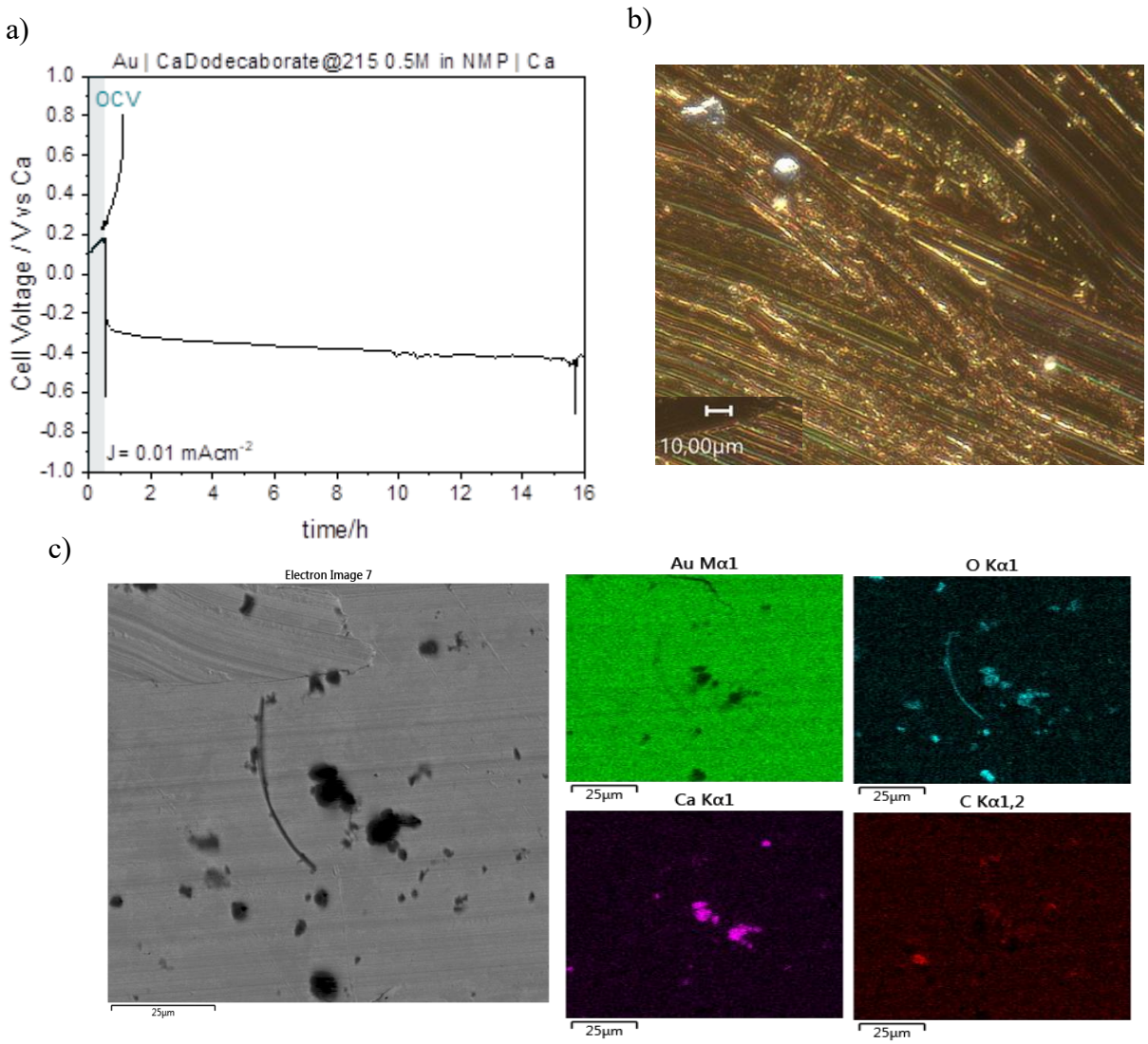

Figure 2.15 a) potential profile of the galvanostatic plating of Ca on Au; b) light optic microscope image of Ca deposit; c) backscattered electrode image of Ca deposit with, on the right, the EDX elemental mapping.

2.3.4 Conclusion

In this section, a new electrolyte for calcium batteries based on $CaB_{12}H_{12}$ is introduced and validated. Different synthesis temperatures and solvents were tested in order to achieve the best electrolyte formulations. $CaB_{12}H_{12}$ synthetized at 215°C shows the highest purity and dissolved in NMP, enables reversible plating/ stripping of Ca metal. The effect of the concentration on the electrochemical performance was analysed in detail, revealing $CaB_{12}H_{12}$ 0.5M in NMP as the formulation with the highest current in CV, and $CaB_{12}H_{12}$ 0.25M in NMP as the best electrolyte formulation in terms of

conductivity, ESW and reversible Ca plating/stripping performance in galvanostatic conditions. This electrolyte can be further improved by adding BF_3OEt_2, which enhances ionic conductivity and helps stabilize the calcium metal surface under galvanostatic cycling Finally, Ca metal plating on Au was proved by *post mortem* characterization using optical microscopy and EDX.

To contextualise the performance of $CaB_{12}H_{12}$@215 within the broader landscape of calcium electrolytes, the 0.25 M formulation exhibits an ionic conductivity of 0.67 mS cm^{-1} and an oxidative stability of approximately 3 V vs Ca^{2+}/Ca at room temperature. hese values can be compared with those of $Ca(TFSI)_2$-based electrolytes. Several studies report room-temperature conductivities below 0.1 mS cm^{-1} in carbonate-based solvents,[84] and only modest improvements up to 0.2–0.3 mS cm^{-1} in ether-based formulations,[95] in agreement with broader literature surveys.[96]

Calcium monocarborane electrolytes[97] achieve higher room-temperature conductivities (≈3–4 mS cm^{-1}) and anodic stabilities of about 4 V, placing them among the most competitive non-fluorinated systems currently available. The present state-of-the-art is represented by $Ca[B(hfip)_4]_2$ in DME, which delivers conductivities close to 8 mS cm^{-1} and oxidative stability up to 4.8 V.[77] These comparisons indicate that $CaB_{12}H_{12}$@215 performs consistently with weakly dissociated calcium salts and highlight both its promise and its current limitations relative to the highest-performing electrolytes reported to date.

Despite these promising advances, further efforts are required to enhance the solubility of $CaB_{12}H_{12}$ in more conventional solvents. Additionally, detailed studies aimed at characterising the nature and evolution of the SEI, together with long-term degradation mechanisms, remain essential to fully assess the applicability of this electrolyte in practical calcium-based battery systems.

2.4 General conclusion

This study explored the development of Ca-FPB and $CaB_{12}H_{12}$ as innovative calcium salts as aprotic electrolytes for calcium batteries, with the aim of addressing the limitations of currently available commercial salts. Ca-FPB exhibited excellent electrochemical stability and enabled reversible calcium plating/stripping at room temperature with low overpotentials, though its complex synthesis, requiring strictly inert conditions and high sensitivity to contamination, presents challenges for scalability. To overcome these limitations, $CaB_{12}H_{12}$ was investigated as an alternative. When synthesized at 215 °C and dissolved in NMP, it demonstrated favourable electrochemical performance, with the 0.25 M formulation offering optimal conductivity, stability, and reversibility. The addition of BF_3OEt_2 further improved calcium metal interface stability. Despite these promising results, both systems require further investigation, particularly regarding the formation and evolution of the solid electrolyte interphase (SEI).

Taken together, these findings highlight that the development of calcium-compatible electrolytes must balance performance with synthetic accessibility. Future efforts should prioritize understanding the interfacial processes at the calcium metal surface, especially the SEI formation and composition, which are critical to enabling long-term reversibility. While many challenges remain, this work represents an initial step toward the rational design of next-generation electrolytes for calcium-based energy storage systems.

2.5 Bibliography

(1) Cheng, H.; Sun, Q.; Li, L.; Zou, Y.; Wang, Y.; Cai, T.; Zhao, F.; Liu, G.; Ma, Z.; Wahyudi, W.; Li, Q.; Ming, J. Emerging Era of Electrolyte Solvation Structure and Interfacial Model in Batteries. *ACS Energy Lett* 2022, *7* (1), 490–513. https://doi.org/10.1021/ACSENERGYLETT.1C02425/ASSET/IMAGES/LARGE/NZ1C02425_0013.JPEG.

(2) Qian, K.; Winans, R. E.; Li, T. Insights into the Nanostructure, Solvation, and Dynamics of Liquid Electrolytes through Small-Angle X-Ray Scattering. *Adv Energy Mater* 2021, *11* (4), 2002821. https://doi.org/10.1002/AENM.202002821.

(3) Philip, M. A.; Haasch, R. T.; Kim, J.; Yang, J.; Yang, R.; Kochetkov, I. R.; Nazar, L. F.; Gewirth, A. A. Enabling High Capacity and Coulombic Efficiency for Li-NCM811 Cells Using a Highly Concentrated Electrolyte. *Batter Supercaps* 2021, *4* (2), 294–303. https://doi.org/10.1002/BATT.202000192.

(4) Arroyo-De Dompablo, M. E.; Ponrouch, A.; Johansson, P.; Palacín, M. R. Achievements, Challenges, and Prospects of Calcium Batteries. *Chem Rev* 2020, *120* (14), 6331–6357. https://doi.org/10.1021/ACS.CHEMREV.9B00339/ASSET/IMAGES/LARGE/CR9B00339_0016.JPEG.

(5) de Araujo Lima e Souza, G.; Di Pietro, M. E.; Castiglione, F.; Fazzio Martins Martinez, P.; Middendorf, M.; Schönhoff, M.; Fraenza, C. C.; Stallworth, P.; Greenbaum, S.; Triolo, A.; Appetecchi, G. B.; Mele, A. Unveiling the Transport Properties of Protic Ionic Liquids: Lithium Ion Dynamics Modulated by the Anion Fluorine Reservoir. *Electrochim Acta* 2024, *475*. https://doi.org/10.1016/J.ELECTACTA.2023.143598.

(6) Ponrouch, A.; Tchitchekova, D.; Frontera, C.; Bardé, F.; Dompablo, M. E. A. De; Palacín, M. R. Assessing Si-Based Anodes for Ca-Ion Batteries: Electrochemical Decalciation of CaSi2. *Electrochem commun* 2016, *66*, 75–78. https://doi.org/10.1016/J.ELECOM.2016.03.004.

(7) Markevich, E.; Salitra, G.; Aurbach, D. Fluoroethylene Carbonate as an Important Component for the Formation of an Effective Solid Electrolyte Interphase on Anodes and Cathodes for Advanced Li-Ion Batteries. *ACS Energy Lett* 2017, *2* (6), 1337–1345. https://doi.org/10.1021/ACSENERGYLETT.7B00163/ASSET/IMAGES/LARGE/NZ-2017-00163N_0004.JPEG.

(8) Brutti, S.; Gentili, V.; Reale, P.; Carbone, L.; Panero, S. Mitigation of the Irreversible Capacity and Electrolyte Decomposition in a LiNi0.5Mn1.5O4/Nano-TiO2 Li-Ion Battery. *J Power Sources* 2011, *196* (22), 9792–9799. https://doi.org/10.1016/J.JPOWSOUR.2011.08.022.

(9) Röser, S.; Lerchen, A.; Ibing, L.; Cao, X.; Kasnatscheew, J.; Glorius, F.; Winter, M.; Wagner, R. Highly Effective Solid Electrolyte Interphase-Forming Electrolyte Additive Enabling High Voltage Lithium-Ion Batteries. *Chemistry of Materials* 2017, *29* (18), 7733–7739. https://doi.org/10.1021/ACS.CHEMMATER.7B01977/SUPPL_FILE/CM7B01977_SI_001.PDF.

(10) Maresca, G.; Ottaviani, M.; Ryan, K. M.; Brutti, S.; Appetecchi, G. B. Improved Compatibility of α-NaMnO2 Cathodes at the Interface with Ionic Liquid Electrolytes. *ChemSusChem* 2024. https://doi.org/10.1002/CSSC.202400514.

(11) Appetecchi, G. B.; Ottaviani, M.; Ryan, K. M.; Brutti, S. Physicochemical Investigation on the Hard Carbon Interface in Ionic Liquid Interface. 2024. https://doi.org/10.2139/SSRN.4760930.

(12) Giffin, G. A. The Role of Concentration in Electrolyte Solutions for Non-Aqueous Lithium-Based Batteries. *Nature Communications 2022 13:1* 2022, *13* (1), 1–6. https://doi.org/10.1038/s41467-022-32794-z.

(13) de Araujo Lima e Souza, G.; di Pietro, M. E.; Castiglione, F.; Fazzio Martins Martinez, P.; Fraenza, C. C.; Stallworth, P.; Greenbaum, S.; Triolo, A.; Battista Appetecchi, G.; Mele, A. Polymer Electrolytes Based on Protic Ionic Liquids with Perfluorinated Anions for Safe Lithium-Ion Batteries. *Electrochim Acta* 2024, *474*. https://doi.org/10.1016/J.ELECTACTA.2023.143466.

(14) Staniewicz, R. J. A Study of the Calcium-Thionyl Chloride Electrochemical System. *J Electrochem Soc* 1980, *127* (4), 782–789. https://doi.org/10.1149/1.2129758/XML.

(15) Peled, E.; Meitav, A.; Brand, M. Calcium Thionyl Chloride High-Rate Reserve Cell. *J Electrochem Soc* 1981, *128* (9), 1936–1938. https://doi.org/10.1149/1.2127768/XML.

(16) Meitav, A.; Peled, E. Calcium - Ca (AlCl4) 2 - Thionyl Chloride Cell: Performance and Safety. *J Electrochem Soc* 1982, *129* (3), 451–457. https://doi.org/10.1149/1.2123879/XML.

(17) Elster, E.; Cohen, R.; Peled, E. Solid Electrolyte Interphase (SEI) Electrodes Part VII. The Electrochemical Behaviour of Calcium in Ba(AlCl4)2 and Sr(AlCl4)2□thionyl Chloride Solutions (Extended Abstract). *J Power Sources* 1989, *26* (3–4), 423–425. https://doi.org/10.1016/0378-7753(89)80157-0.

(18) Aurbach, D.; Skaletsky, R.; Gofer, Y. The Electrochemical Behavior of Calcium Electrodes in a Few Organic Electrolytes. *J Electrochem Soc* 1991, *138* (12), 3536–3545. https://doi.org/10.1149/1.2085455/XML.

(19) Wei, Q.; Zhang, L.; Sun, X.; Liu, T. L. Progress and Prospects of Electrolyte Chemistry of Calcium Batteries. *Chem Sci* 2022, *13* (20), 5797–5812. https://doi.org/10.1039/D2SC00267A.

(20) Ponrouch, A.; Frontera, C.; Bardé, F.; Palacín, M. R. Towards a Calcium-Based Rechargeable Battery. *Nature Materials 2015 15:2* 2015, *15* (2), 169–172. https://doi.org/10.1038/nmat4462.

(21) Biria, S.; Pathreeker, S.; Li, H.; Hosein, I. D. Plating and Stripping of Calcium in an Alkyl Carbonate Electrolyte at Room Temperature. *ACS Appl Energy Mater* 2019, *2* (11), 7738–7743. https://doi.org/10.1021/ACSAEM.9B01670/SUPPL_FILE/AE9B01670_SI_001.PDF.

(22) Forero-Saboya, J.; Davoisne, C.; Dedryvère, R.; Yousef, I.; Canepa, P.; Ponrouch, A. Understanding the Nature of the Passivation Layer Enabling Reversible Calcium Plating. *Energy Environ Sci* 2020, *13* (10), 3423–3431. https://doi.org/10.1039/D0EE02347G.

(23) Wang, D.; Gao, X.; Chen, Y.; Jin, L.; Kuss, C.; Bruce, P. G. Plating and Stripping Calcium in an Organic Electrolyte. *Nature Materials 2017 17:1* 2017, *17* (1), 16–20. https://doi.org/10.1038/nmat5036.

(24) Ta, K.; Zhang, R.; Shin, M.; Rooney, R. T.; Neumann, E. K.; Gewirth, A. A. Understanding Ca Electrodeposition and Speciation Processes in Nonaqueous Electrolytes for Next-Generation Ca-Ion Batteries. *ACS Appl Mater Interfaces* 2019, *11* (24), 21536–21542. https://doi.org/10.1021/ACSAMI.9B04926.

(25) Jie, Y.; Tan, Y.; Li, L.; Han, Y.; Xu, S.; Zhao, Z.; Cao, R.; Ren, X.; Huang, F.; Lei, Z.; Tao, G.; Zhang, G.; Jiao, S. Electrolyte Solvation Manipulation Enables Unprecedented Room-Temperature Calcium-Metal Batteries. *Angewandte Chemie International Edition* 2020, *59* (31), 12689–12693. https://doi.org/10.1002/ANIE.202002274.

(26) Kisu, K.; Kim, S.; Shinohara, T.; Zhao, K.; Züttel, A.; Orimo, S. ichi. Monocarborane Cluster as a Stable Fluorine-Free Calcium Battery Electrolyte. *Scientific Reports 2021 11:1* 2021, *11* (1), 1–8. https://doi.org/10.1038/s41598-021-86938-0.

(27) Leon, N. J.; Xie, X.; Yang, M.; Driscoll, D. M.; Connell, J. G.; Kim, S.; Seguin, T.; Vaughey, J. T.; Balasubramanian, M.; Persson, K. A.; Liao, C. Room-Temperature Calcium Plating and Stripping Using a Perfluoroalkoxyaluminate Anion Electrolyte. *Journal of Physical Chemistry C* 2022, *126*

(32), 13579–13584. https://doi.org/10.1021/ACS.JPCC.2C03272/SUPPL_FILE/JP2C03272_SI_001.PDF.

(28) Geiger, W. E.; Barrière, F. Organometallic Electrochemistry Based on Electrolytes Containing Weakly-Coordinating Fluoroarylborate Anions. *Acc Chem Res* 2010, *43* (7), 1030–1039. https://doi.org/10.1021/AR1000023/ASSET/IMAGES/MEDIUM/AR-2010-000023_0017.GIF.

(29) Huang, M.; Feng, S.; Zhang, W.; Lopez, J.; Qiao, B.; Tatara, R.; Giordano, L.; Shao-Horn, Y.; Johnson, J. A. Design of S-Substituted Fluorinated Aryl Sulfonamide-Tagged (S-FAST) Anions to Enable New Solvate Ionic Liquids for Battery Applications. *Chemistry of Materials* 2019, *31* (18), 7558–7564. https://doi.org/10.1021/ACS.CHEMMATER.9B02353/ASSET/IMAGES/MEDIUM/CM9B02353_M004.GIF.

(30) Mandai, T.; Naya, H.; Masu, H. Comparative Studies on [B(HFIP)4]-Based Electrolytes with Mono- and Divalent Cations. *Journal of Physical Chemistry C* 2023, *127* (17), 7987–7997. https://doi.org/10.1021/ACS.JPCC.3C01160.

(31) Tutusaus, O.; Mohtadi, R.; Arthur, T. S.; Mizuno, F.; Nelson, E. G.; Sevryugina, Y. V. An Efficient Halogen-Free Electrolyte for Use in Rechargeable Magnesium Batteries. *Angewandte Chemie International Edition* 2015, *54* (27), 7900–7904. https://doi.org/10.1002/ANIE.201412202.

(32) Herb, J. T.; Nist-Lund, C. A.; Arnold, C. B. A Fluorinated Alkoxyaluminate Electrolyte for Magnesium-Ion Batteries. *ACS Energy Lett* 2016, *1* (6), 1227–1232. https://doi.org/10.1021/ACSENERGYLETT.6B00356/SUPPL_FILE/NZ6B00356_SI_001.PDF.

(33) Zhao-Karger, Z.; Gil Bardaji, M. E.; Fuhr, O.; Fichtner, M. A New Class of Non-Corrosive, Highly Efficient Electrolytes for Rechargeable Magnesium Batteries. *J Mater Chem A Mater* 2017, *5* (22), 10815–10820. https://doi.org/10.1039/C7TA02237A.

(34) Lau, K.-C.; Seguin, T. J.; Carino, E. V.; Hahn, N. T.; Connell, J. G.; Ingram, B. J.; Persson, K. A.; Zavadil, K. R.; Liao, C. Widening Electrochemical Window of Mg Salt by Weakly Coordinating Perfluoroalkoxyaluminate Anion for Mg Battery Electrolyte. *J Electrochem Soc* 2019, *166* (8), A1510–A1519. https://doi.org/10.1149/2.0751908JES/XML.

(35) Dominko, R.; Pavčnik, T.; Lužanin, O.; Moskon, J.; Gaberscek, M.; Bitenc, J. Advanced Electrolytes for Mg and Ca Batteries Based on Alkoxyborates and Alkoxyaluminates. *ECS Meeting Abstracts* 2024, *MA2024-02* (9), 1419–1419. https://doi.org/10.1149/MA2024-0291419MTGABS.

(36) Forero-Saboya, J. D.; Tchitchekova, D. S.; Johansson, P.; Palacín, M. R.; Ponrouch, A.; Forero-Saboya, J. D.; Tchitchekova, D. S.; Palacín, M. R.; Ponrouch, A.; Johansson, P. Interfaces and Interphases in Ca and Mg Batteries. *Adv Mater Interfaces* 2022, *9* (8), 2101578. https://doi.org/10.1002/ADMI.202101578.

(37) Forero-Saboya, J.; Ponrouch, A. Electrolyte, Solvation Shell and Interphase for Ca and Mg Metal Anode Based Batteries. *ECS Meeting Abstracts* 2020, *MA2020-01* (2), 178. https://doi.org/10.1149/MA2020-012178MTGABS.

(38) Li, Z.; Fuhr, O.; Fichtner, M.; Zhao-Karger, Z. Towards Stable and Efficient Electrolytes for Room-Temperature Rechargeable Calcium Batteries. *Energy Environ Sci* 2019, *12* (12), 3496–3501. https://doi.org/10.1039/C9EE01699F.

(39) Pavčnik, T.; Forero-Saboya, J. D.; Ponrouch, A.; Robba, A.; Dominko, R.; Bitenc, J. A Novel Calcium Fluorinated Alkoxyaluminate Salt as a next Step towards Ca Metal Anode Rechargeable Batteries. *J. Mater. Chem. A* 2023, *11* (27), 14738–14747. https://doi.org/10.1039/d3ta02084c.

(40) Nelson, Y. A.; Irshad, A.; Kim, S.; Waddington, M. A.; Salamat, C. Z.; Gembicky, M.; Rheingold, A. L.; Carta, V.; Tolbert, S. H.; Narayan, S. R.; Spokoyny, A. M. Vertex Differentiation Strategy for Tuning the Physical Properties of Closo-Dodecaborate Weakly Coordinating Anions. *Inorg Chem* 2023, *62* (37), 15084–15093. https://doi.org/10.1021/ACS.INORGCHEM.3C01992/SUPPL_FILE/IC3C01992_SI_001.PDF.

(41) Luo, J.; Bi, Y.; Zhang, L.; Zhang, X.; Liu, T. L. A Stable, Non-Corrosive Perfluorinated Pinacolatoborate Mg Electrolyte for Rechargeable Mg Batteries. *Angewandte Chemie International Edition* 2019, *58* (21), 6967–6971. https://doi.org/10.1002/anie.201902009.

(42) D'Anna, V.; Spyratou, A.; Sharma, M.; Hagemann, H. FT-IR Spectra of Inorganic Borohydrides. *Spectrochim Acta A Mol Biomol Spectrosc* 2014, *128*, 902–906. https://doi.org/10.1016/J.SAA.2014.02.130.

(43) Goel, N.; Sinha, N.; Kumar, B. Growth and Properties of Sodium Tetraborate Decahydrate Single Crystals. *Mater Res Bull* 2013, *48* (4), 1632–1636. https://doi.org/10.1016/J.MATERRESBULL.2013.01.007.

(44) Koilraj, P.; Thakur, R. S.; Srinivasan, K. Solid State Structural Transformation of Tetraborate into Monoborate in the Interlayer Galleries of Reconstructed ZnAl Layered Double Hydroxide. *Journal of Physical Chemistry C* 2013, *117* (13), 6578–6586. https://doi.org/10.1021/JP311285G.

(45) Tsen, W. C.; Lee, C. F.; Su, Y. R.; Gu, J. H.; Suen, M. C. Effect of Novel Aliphatic Fluoro-Diol Content on Synthesis and Properties of Waterborne Polyurethanes. *J Appl Polym Sci* 2019, *136* (21), 47356. https://doi.org/10.1002/APP.47356.

(46) Wang, X.; Wang, W.; Liu, Y.; Ren, M.; Xiao, H.; Liu, X. Characterization of Conformation and Locations of C-F Bonds in Graphene Derivative by Polarized ATR-FTIR. *Anal Chem* 2016, *88* (7), 3926–3934. https://doi.org/10.1021/ACS.ANALCHEM.6B00115/ASSET/IMAGES/LARGE/AC-2016-00115D_0010.JPEG.

(47) Chen, G.; Qiao, L.; Xu, G.; Li, L.; Li, J.; Li, L.; Liu, X.; Cui, Z.; Zhang, S.; Cheng, S.; Han, C.; Wang, S.; Zhou, X.; Cui, G. A Highly-Fluorinated Lithium Borate Main Salt Empowering Stable Lithium Metal Batteries. *Angewandte Chemie International Edition* 2024, *63* (19), e202400797. https://doi.org/10.1002/ANIE.202400797.

(48) Murugan, S.; Klostermann, S. V.; Frey, W.; Kästner, J.; Buchmeiser, M. R. A Sodium Bis(Perfluoropinacol) Borate-Based Electrolyte for Stable, High-Performance Room Temperature Sodium-Sulfur Batteries Based on Sulfurized Poly(Acrylonitrile). *Electrochem commun* 2021, *132*, 107137. https://doi.org/10.1016/J.ELECOM.2021.107137.

(49) Kisu, K.; Kim, S.; Shinohara, T.; Zhao, K.; Züttel, A.; Orimo, S. ichi. Monocarborane Cluster as a Stable Fluorine-Free Calcium Battery Electrolyte. *Scientific Reports 2021 11:1* 2021, *11* (1), 1–8. https://doi.org/10.1038/s41598-021-86938-0.

(50) *Cesium (CAS Number 12539-26-3) : Strem Product Catalog*. https://www.strem.com/catalog/v/55-5525/cesium_12539-26-3 (accessed 2023-11-09).

(51) Grahame, A.; Aguey-Zinsou, K.-F. Inorganics Properties and Applications of Metal (M) Dodecahydro-Closo-Dodecaborates (M N=1,2 B 12 H 12) and Their Implications for Reversible Hydrogen Storage in the Borohydrides. https://doi.org/10.3390/inorganics6040106.

(52) Wang, J.; Steenhaut, T.; Li, H.-W.; Filinchuk, Y. High Yield Autoclave Synthesis of Pure M 2 B 12 H 12 (M = Na, K). *Cite This: Inorg. Chem* 2023, *62*. https://doi.org/10.1021/acs.inorgchem.2c03810.

(53) Grahame, A.; Aguey-Zinsou, K. F. Properties and Applications of Metal (M) Dodecahydro-Closo-Dodecaborates (Mn=1,2B12H12) and Their Implications for Reversible Hydrogen Storage in the Borohydrides. *Inorganics 2018, Vol. 6, Page 106* 2018, *6* (4), 106. https://doi.org/10.3390/INORGANICS6040106.

(54) First-Principles Study of CaB 12 H 12 as a Potential Solid-State Conductor for Ca. 2020. https://doi.org/10.1039/x0xx00000x.

(55) Gigante, A.; Duchêne, L.; Moury, R.; Pupier, M.; Remhof, A.; Hagemann, H. Direct Solution-Based Synthesis of Na4(B12H12)(B10H10) Solid Electrolyte. *ChemSusChem* 2019, *12* (21), 4832–4837. https://doi.org/10.1002/CSSC.201902152.

(56) Wang, J.; Steenhaut, T.; Li, H.-W.; Filinchuk, Y. High Yield Autoclave Synthesis of Pure M2B12H12 (M = Na, K). *Inorg Chem* 2023. https://doi.org/10.1021/ACS.INORGCHEM.2C03810.

(57) Moury, R.; Gigante, A.; Hagemann, H. An Alternative Approach to the Synthesis of NaB3H8 and Na2B12H12 for Solid Electrolyte Applications. *Int J Hydrogen Energy* 2017, *42* (35), 22417–22421. https://doi.org/10.1016/J.IJHYDENE.2017.02.044.

(58) Pylypko, S.; Ould-Amara, S.; Zadick, A.; Petit, E.; Chatenet, M.; Cretin, M.; Demirci, U. B. The Highly Stable Aqueous Solution of Sodium Dodecahydro-Closo-Dodecaborate Na2B12H12 as a Potential Liquid Anodic Fuel. *Appl Catal B* 2018, *222*, 1–8. https://doi.org/10.1016/J.APCATB.2017.09.068.

(59) Ould-Amara, S.; Petit, E.; Granier, D.; Yot, P. G.; Demirci, U. B. Alkaline Aqueous Solution of Sodium Decahydro-Closo-Decaborate Na2B10H10 as Liquid Anodic Fuel. *Renew Energy* 2019, *143*, 551–557. https://doi.org/10.1016/J.RENENE.2019.05.019.

(60) Gigante, A.; Duchêne, L.; Moury, R.; Pupier, M.; Remhof, A.; Hagemann, H. Direct Solution-Based Synthesis of Na4(B12H12)(B10H10) Solid Electrolyte. *ChemSusChem* 2019, *12* (21), 4832–4837. https://doi.org/10.1002/CSSC.201902152.

(61) Liu, A.; Xie, S.; Dabiran-Zohoory, S.; Song, Y. High-Pressure Structures and Transformations of Calcium Borohydride Probed by Combined Raman and Infrared Spectroscopies. 2010. https://doi.org/10.1021/jp1009115.

(62) Dematteis, E. M.; Baricco, M. Hydrogen Desorption in Mg(BH4)2-Ca(BH4)2 System. *Energies 2019, Vol. 12, Page 3230* 2019, *12* (17), 3230. https://doi.org/10.3390/EN12173230.

(63) Sadikin, Y.; Didelot, E.; Łodziana, Z.; Černý, R. Synthesis and Crystal Structure of Solvent-Free Dodecahydro Closo-Dodecaborate of Nickel, NiB12H12. *Dalton Transactions* 2018, *47* (16), 5843–5849. https://doi.org/10.1039/C8DT00381E.

(64) Kochneva, I. K.; Avdeeva, V. V.; Polyakova, I. N.; Malinina, E. A. Mixed-Ligand Polymeric and Binuclear Silver(I) Complexes with the Dodecahydro-Closo-Dodecaborate Anion and Bipyridylamine. *Polyhedron* 2016, *109*, 19–25. https://doi.org/10.1016/J.POLY.2016.01.045.

(65) Didelot, E.; Sadikin, Y.; Łodziana, Z.; Černý, R. Hydrated and Anhydrous Dodecahydro Closo-Dodecaborates of 3d Transition Metals and of Magnesium. *Solid State Sci* 2019, *90*, 86–94. https://doi.org/10.1016/J.SOLIDSTATESCIENCES.2019.02.005.

(66) *Product E001 / 1M LiPF6 in EC:DMC (1:1 vol.%) 99.9%*. https://en.solvionic.com/products/1m-lipf6-in-ec-dmc-1-1-vol.-99.9 (accessed 2023-10-04).

Chapter III:

Pseudocapacitive carbon electrodes as counter electrodes in calcium-ion batteries

3.1 Introduction

The aim of this chapter is to develop a reliable, metal-free electrochemical setup for calcium-ion systems by exploring a pseudo-capacitive configuration. Here we demonstrate the use of a capacitive carbonaceous electrode suitable for application in Ca-ion batteries, together with its experimental validation in Ca-ion cells. A key focus is the establishment of a stable reference framework, which is essential for the accurate characterization of novel electrode materials and for overcoming the limitations typically associated with calcium metal electrodes.

As discussed in Chapters 1 and 2, the use of calcium metal as a reference or counter-electrode presents significant challenges due to interfacial passivation and poor reversibility, which undermine both stability and reproducibility of electrochemical testing.[1–3] To address these issues, we adopt a pseudo-capacitive configuration based on activated carbon (AC) which avoids the complications of calcium metal and provides a stable, inert environment for electrochemical measurements.[4]

AC operates within the electrochemical stability window of calcium-based electrolytes and stores charge via the formation of an electrostatic double-layer, enabling a cleaner and more reliable setup for studying calcium-ion intercalation materials.[4,5] On the other hand, being AC a capacitive electrode, its its successful implementation requires a careful calibration of its working potential and the validation of the applicability in different cell configurations to ensure accurate and consistent results.[4]

Although well established in lithium-based systems,[6] this strategy has only recently begun to be explored in calcium-ion cells.[4] In this chapter, we evaluate its feasibility through the electrochemical characterization of two insertion-type materials: a Prussian Blue Analogue (PBA) as a positive electrode and titanium oxide nanotubes (TNTs) as a negative electrode, enabling comparative investigation of their calcium-ion storage behavior.

The following sections will first describe the manufacturing of the activated carbon (AC) as a capacitive electrode, followed by the electrochemical evaluation of the AC as a capacitive electrode. The subsequent chapters will address the characterization of the selected positive and negative electrode materials.

3.2 Manufacture of AC electrode

Active carbon electrodes were prepared starting from a high-surface-area activated carbon (NC-series carbon, PC NC2-3 Ultracapacitor electrode material), dispersed with PTFE (aqueous solution, 60% w/w) in a weight ratio of 95:5. The mixture was placed in a beaker containing ethanol to facilitate dispersion and mixing of the two components. The suspension was stirred with a magnetic stirrer at 60 °C until complete evaporation of ethanol. The resulting AC–PTFE powder was then further processed by adding a few drops of ethanol to improve particle cohesion, and pressed on a glass plate until a homogeneous, rubber-like mass was obtained. This mass was subsequently flattened on the glass plate using a glass stick, producing a uniform and flexible film with a thickness below 100 µm. Circular electrodes with a diameter of 12 mm were then punched from the film and subsequently dried under vacuum at 150 °C for 24 h.

3.3 Pseudo-capacitive approach

To validate the pseudo-capacitive electrochemical setup for calcium-ion battery testing, preliminary experiments were conducted to evaluate the electrochemical behavior of AC as a counter-electrode and Au as quasi-reference electrode (QRE). The AC electrode was first calibrated with ferrocene (Fc) and in three electrode cell configurations (illustrated in figure 3.1a) using a common calcium-based electrolyte based on $Ca(TFSI)_2$ dissolved in DME.

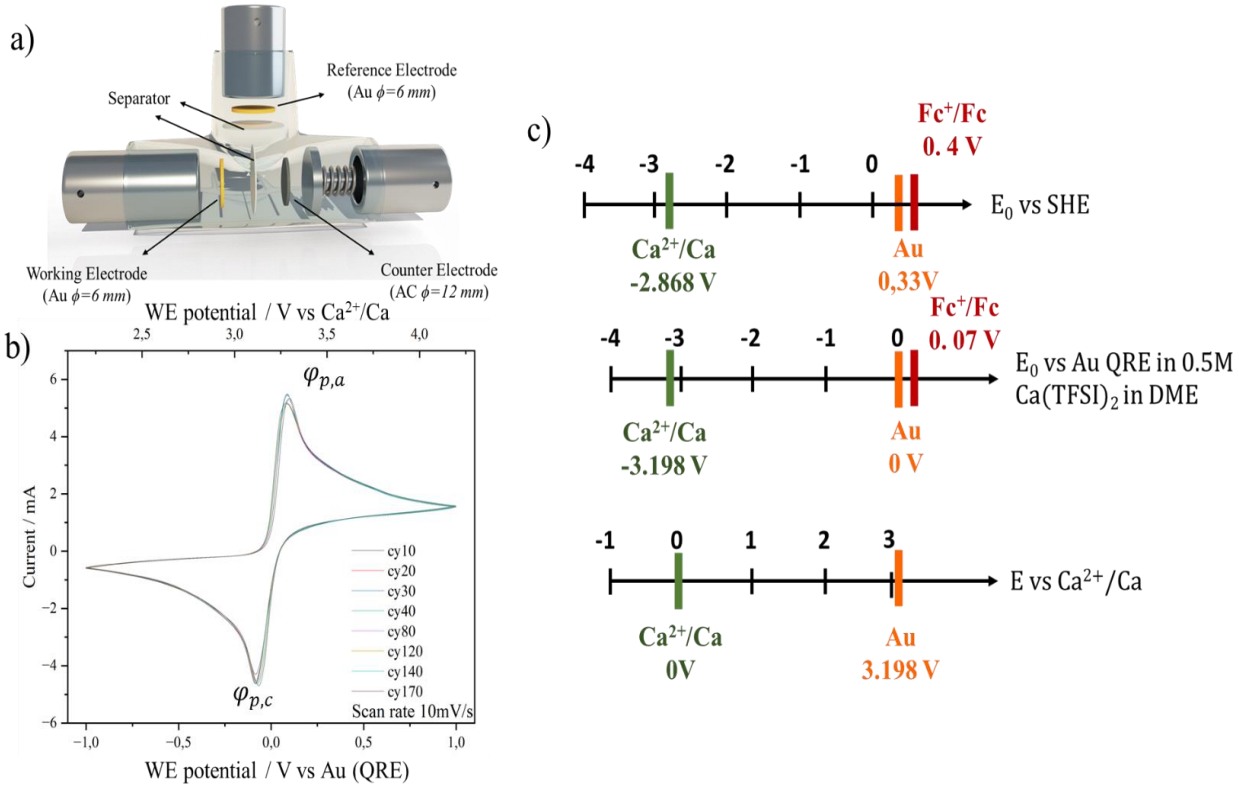

Figure 3.1 a) Scheme of the three-electrode Swagelok cell. b) Cyclic voltammogram (CV) of 0.05 M Fc in 0.5 M $Ca(TFSI)_2$ in DME solution at 10 mV s−1 (WE and QRE: Au, CE: AC). c) Position of the Fc+/Fc vs. SHE (upper), vs Au QRE and the Ca^{2+}/Ca (below).

Figure 3.1a shows the schematic of the three-electrode Swagelok cell employed in this study. The key advantage of using AC as the counter-electrode lies in its purely capacitive charge storage mechanism, which does not involve faradaic processes. This ensures minimal contamination of the electrolyte by decomposition products. However, it should be considered that its functioning alters the activity of Ca^{2+} in the electrolyte, and therefore the corresponding thermodynamic and kinetic landscapes.[5]Nevertheless, this issue is mitigated by using an excess amount of electrolyte, which keeps concentration variations almost negligible.[6–8]

In this study, 0.5 M $Ca(TFSI)_2$ in DME was chosen due to its well-documented electrochemical stability in this type of system.[4] To validate the use of Au as a QRE, careful calibration and stability test were carried out.[6] The calibration procedure employed the ferrocenium/ferrocene (Fc^+/Fc) redox couple, a well-established reference system whose redox potential versus the standard hydrogen electrode (SHE) is relatively insensitive to the electrolyte composition.[9] Therefore, it serves as an effective reference for calibrating the Au QRE. It is important to know that any drift in the Fc^+/Fc redox potential versus the Au QRE reflects changes in the potential of the Au QRE itself.[9]

Figure 3.1b presents the cyclic voltammogram (CV) obtained for a three-electrode cell using a solution of 0.05 M Fc in the 0.5 M $Ca(TFSI)_2$/DME electrolyte, AC used as the counter electrode, and two Au sheets as working and reference electrodes. The redox potential of Fc^+/Fc versus Au QRE was calculated using the equation:

$$\varphi_{(Fc^+/Fc)} = (\varphi_{p,c} + \varphi_{p,a}) / 2$$

where $\varphi_{p,c}$ and $\varphi_{p,a}$ are the cathodic and anodic peak potentials, respectively. Figure 3.1c compares the redox potential of Fc^+/Fc versus SHE and Au QRE. The Fc^+/Fc redox potential versus Au QRE that is 0.07 V lower than versus SHE, resulting in a 0.33 V versus SHE and shift in all potential values measured against Au. Consequently, the redox potential of the Ca^{2+}/Ca couple is estimated at 3.198 V vs. Au QRE. It is worth noting that the potential of the Au QRE vs. SHE may vary with changes in electrolyte composition or the physical and chemical properties of the AC material due to alterations in ionic speciation that influence the double-layer formation at the AC/electrolyte interface.[9] Furthermore, the surface chemistry of the AC, particularly the presence of different chemical groups at its surface, can significantly affect interface charging phenomena.[10–12] Thus, recalibration is necessary whenever the electrolyte or AC material is changed.

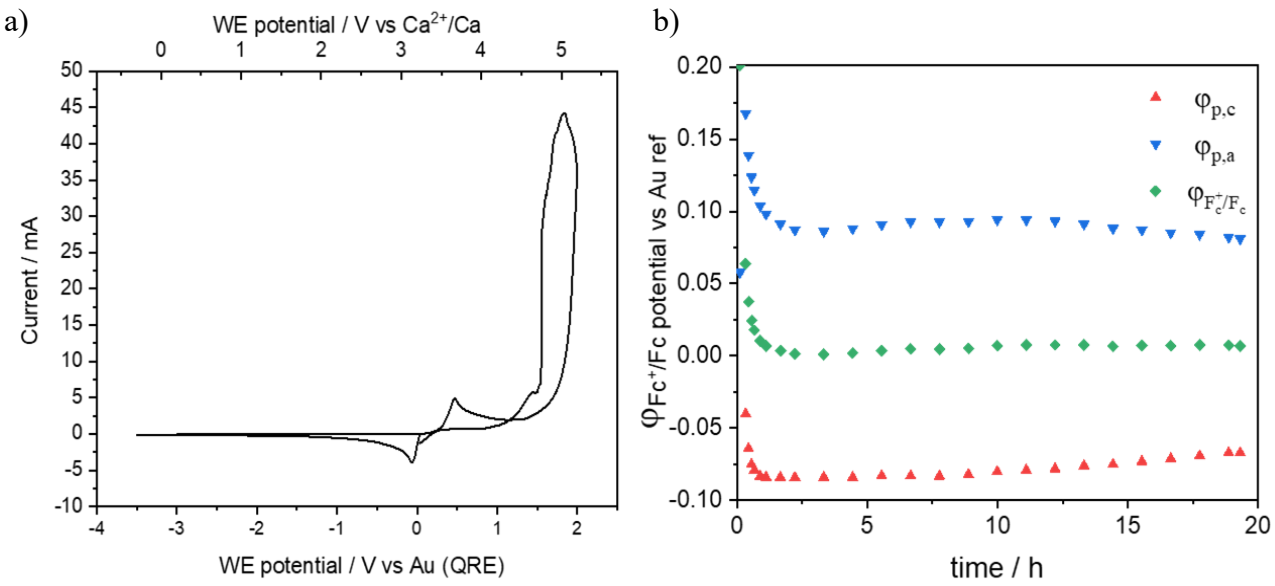

Figure 3.2 a) stability CV with same cell configuration and scan rate of Figure 3.1; b) calculated redox potential of the CV in figure 3.1. plotted versus time.

To assess the stability of the Au as QRE, continuous CV measurements were performed, monitoring any drift in the Fc^+/Fc redox couple versus AC QRE. Figure 3.1b shows overlapping CV curves recorded in a three-electrode configuration using AC as the counter electrode, and Au as both QRE and working electrode in a 0.05 M Fc + 0.5 M $Ca(TFSI)_2$ in DME electrolyte. The close overlap of the CV curves confirms the stability of the AC QRE. The time-dependent potential of the Fc^+/Fc redox couple versus Au QRE is reported in Figure 3.2b. In figure 3.2a we confirm that AC operates within the electrochemical stability window of these calcium-based electrolytes, i.e., between 0 and 4.5 V vs. Ca^{2+}/Ca. In pseudo-reference systems, the redox couple that corresponds to the thermodynamic equilibrium is not well-defined. Hence, measurement stability depends on maintaining a constant electrode potential and bulk solution composition. The effectiveness of carbon-based CE relies on their high surface area to minimize potential drift.

Generally, potential drift is associated with the specific adsorption or desorption of ions on the AC surface, which charges the electrode and alters the interface potential.[9] In the systems studied here, the ionic composition and concentration remained constant throughout the measurements thanks to the high surface area of the AC and quite large amount of electrolyte in the cell, as confirmed in figure 3.2b.

These results demonstrate that AC counter-electrodes and Au QREs can be reliably employed in DME-based electrolytes. This validation step is essential for establishing a consistent alternative for the further evaluation of novel cathode and anode materials in calcium-ion systems.

3.4 Conclusions

In this chapter, we have validated the use of a pseudo-capacitive electrochemical setup employing AC as a counter-electrode and gold (Au) as QRE for calcium-ion systems. This configuration has the potential to overcome key limitations associated with the use of calcium metal electrodes, such as interfacial passivation and poor reversibility, enabling more stable and reproducible electrochemical measurements.

Through systematic calibration using the Fc^{+}/Fc redox couple, we confirmed the stability of the Au QRE in $Ca(TFSI)_2$/DME-based electrolytes and demonstrated that AC electrodes operate well within the electrochemical stability window of this system. Continuous CV tests confirmed minimal potential drift and reliable performance of the AC/Au combination, provided that ionic concentration and electrode surface conditions remain stable.

These findings establish a robust and inert platform suitable for fundamental studies on calcium-ion intercalation materials. With this validated setup, we are now equipped to investigate the electrochemical behavior of candidate electrode materials, such as the Prussian Blue Analogue and titanium oxide nanotubes, under controlled and reproducible conditions, as discussed in the following sections.

3.5 Bibliography

(1) Schmidt, T. S.; Beuse, M.; Zhang, X.; Steffen, B.; Schneider, S. F.; Pena-Bello, A.; Bauer, C.; Parra, D. Additional Emissions and Cost from Storing Electricity in Stationary Battery Systems. *Environ Sci Technol* **2019**, *53* (7), 3379–3390. https://doi.org/10.1021/ACS.EST.8B05313/ASSET/IMAGES/LARGE/ES-2018-05313C_0007.JPEG.

(2) *Executive summary – Electricity 2025 – Analysis - IEA*. https://www.iea.org/reports/electricity-2025/executive-summary (accessed 2025-04-07).

(3) Wang, S.; Yu, J.; Okubo, K. Life Cycle Assessment on the Reuse and Recycling of the Nickel-Metal Hydride Battery: Fleet-Based Study on Hybrid Vehicle Batteries from Japan. *J Ind Ecol* **2021**, *25* (5), 1236–1249. https://doi.org/10.1111/JIEC.13126.

(4) Forster, P. M.; Smith, C. J.; Walsh, T.; Lamb, W. F.; Palmer, M. D.; von Schuckmann, K.; Trewin, B.; Allen, M.; Andrew, R.; Birt, A.; Borger, A.; Boyer, T.; Broersma, J. A.; Cheng, L.; Dentener, F.; Friedlingstein, P.; Gillett, N.; Gutiérrez, J. M.; Gütschow, J.; Hauser, M.; Hall, B.; Ishii, M.; Jenkins, S.; Lamboll, R.; Lan, X.; Lee, J.-Y.; Morice, C.; Kadow, C.; Kennedy, J.; Killick, R.; Minx, J.; Naik, V.; Peters, G.; Pirani, A.; Pongratz, J.; Ribes, A.; Rogelj, J.; Rosen, D.; Schleussner, C.-F.; Seneviratne, S.; Szopa, S.; Thorne, P.; Rohde, R.; Rojas Corradi, M.; Schumacher, D.; Vose, R.; Zickfeld, K.; Zhang, X.; Masson-Delmotte, V.; Zhai, P. Indicators of Global Climate Change 2022: Annual Update of Large-Scale Indicators of the State of the Climate System and the Human Influence . **2023**. https://doi.org/10.5194/ESSD-2023-166.

(5) *Climate Change - NASA Science*. https://science.nasa.gov/climate-change/ (accessed 2025-04-22).

(6) Akinyele, D. O.; Rayudu, R. K. Review of Energy Storage Technologies for Sustainable Power Networks. *Sustainable Energy Technologies and Assessments* **2014**, *8*, 74–91. https://doi.org/10.1016/J.SETA.2014.07.004.

(7) Akinyele, D.; Belikov, J.; Levron, Y. Battery Storage Technologies for Electrical Applications: Impact in Stand-Alone Photovoltaic Systems. *Energies 2017, Vol. 10, Page 1760* **2017**, *10* (11), 1760. https://doi.org/10.3390/EN10111760.

(8) Malik, F. H.; Hussain, G. A.; Alsmadi, Y. M. S.; Haider, Z. M.; Mansoor, W.; Lehtonen, M. Integrating Energy Storage Technologies with Renewable Energy Sources: A Pathway Toward Sustainable Power Grids. *Sustainability 2025, Vol. 17, Page 4097* **2025**, *17* (9), 4097. https://doi.org/10.3390/SU17094097.

(9) Olabi, A. G. Renewable Energy and Energy Storage Systems. *Energy* **2017**, *136*, 1–6. https://doi.org/10.1016/J.ENERGY.2017.07.054.

(10) Ould Amrouche, S.; Rekioua, D.; Rekioua, T.; Bacha, S. Overview of Energy Storage in Renewable Energy Systems. *Int J Hydrogen Energy* **2016**, *41* (45), 20914–20927. https://doi.org/10.1016/J.IJHYDENE.2016.06.243.

(11) Scrosati, B. History of Lithium Batteries. https://doi.org/10.1007/s10008-011-1386-8.

(12) Zhao, B.; Hu, J.; Hui, D.; Qu, Z.; Liu, L.; Gao, C. Broadband Equivalent Modeling and Common-Mode Voltage Conduction Analysis of Electrochemical Energy Storage System. *IEEE Access* **2023**, *11*, 44167–44175. https://doi.org/10.1109/ACCESS.2023.3270327.

(13) *Scopus - Analyze search results | Signed in*. https://www.scopus.com/term/analyzer.uri?sort=plf-f&src=s&sid=1413303347ea7079aa03e5bcd4d60251&sot=a&sdt=a&sl=22&s=TITLE-ABS-KEY%28battery%29&origin=resultslist&count=10&analyzeResults=Analyze+results (accessed 2025-05-21).

(14) Beaudet, A.; Larouche, F.; Amouzegar, K.; Bouchard, P.; Zaghib, K. Key Challenges and Opportunities for Recycling Electric Vehicle Battery Materials. *Sustainability 2020, Vol. 12, Page 5837* **2020**, *12* (14), 5837. https://doi.org/10.3390/SU12145837.

(15) Prime, J.; Abdulkadir Ahmed, I.; Akande, D.; Elhassan, N.; Escamilla, G.; Jamdade, A.; Melnikov, Y.; Whiteman, A. Renewable Energy Statistics 2024, International Renewable Energy Agency. **2024**, 2–10.

(16) Hassan, Q.; Algburi, S.; Sameen, A. Z.; Al-Musawi, T. J.; Al-Jiboory, A. K.; Salman, H. M.; Ali, B. M.; Jaszczur, M. A Comprehensive Review of International Renewable Energy Growth. *Energy and Built Environment* **2024**. https://doi.org/10.1016/J.ENBENV.2023.12.002.

(17) Hassan, Q.; Algburi, S.; Sameen, A. Z.; Al-Musawi, T. J.; Al-Jiboory, A. K.; Salman, M.; Ali, M.; Jaszczur, M. ARTICLE IN PRESS Energy and Built Environment Xxx (Xxxx) Xxx A Comprehensive Review of International Renewable Energy Growth. **2024**. https://doi.org/10.1016/j.enbenv.2023.12.002.

(18) Nykvist, B.; Nilsson, M. Rapidly Falling Costs of Battery Packs for Electric Vehicles. *Nature Climate Change 2014 5:4* **2015**, *5* (4), 329–332. https://doi.org/10.1038/nclimate2564.

(19) Fotouhi, A.; Auger, D. J.; Propp, K.; Longo, S.; Wild, M. A Review on Electric Vehicle Battery Modelling: From Lithium-Ion toward Lithium–Sulphur. *Renewable and Sustainable Energy Reviews* **2016**, *56*, 1008–1021. https://doi.org/10.1016/J.RSER.2015.12.009.

(20) Kwon, B.; Ha, S.; Kim, D. M.; Koo, D.; Lee, J.; Lee, K. T. Electrochemically Active Red P/BaTiO3-Based Protective Layers Suppressing Li Dendrite Growth for Li Metal Batteries. *Adv Mater Interfaces* **2020**, *7* (20), 2001037. https://doi.org/10.1002/ADMI.202001037.

(21) Accardo, A.; Dotelli, G.; Musa, M. L.; Spessa, E. Life Cycle Assessment of an NMC Battery for Application to Electric Light-Duty Commercial Vehicles and Comparison with a Sodium-Nickel-Chloride Battery. *Applied Sciences 2021, Vol. 11, Page 1160* **2021**, *11* (3), 1160. https://doi.org/10.3390/APP11031160.

(22) Junlong, L.; Leung, &; Wah, A. O. A Critical Review on Electric Vehicle Batteries — Based on Life Cycle Assessment Method. *Studies in Social Science & Humanities* **2023**, *2* (8), 33–50. https://doi.org/10.56397/SSSH.2023.08.05.

(23) Stoppato, A.; Benato, A.; De Vanna, F. Environmental Impact of Energy Systems Integrated with Electrochemical Accumulators and Powered by Renewable Energy Sources in a Life-Cycle Perspective. *Applied Sciences 2021, Vol. 11, Page 2770* **2021**, *11* (6), 2770. https://doi.org/10.3390/APP11062770.

(24) Hiremath, M.; Derendorf, K.; Vogt, T. Comparative Life Cycle Assessment of Battery Storage Systems for Stationary Applications. *Environ Sci Technol* **2015**, *49* (8), 4825–4833. https://doi.org/10.1021/ES504572Q/SUPPL_FILE/ES504572Q_SI_001.PDF.

(25) Kern, A.; Johnson, J. X.; Mathieu, J. L. Environmental Impacts of Using Energy Storage Aggregations to Provide Multiple Services.

(26) Barke, A.; Cistjakov, W.; Steckermeier, D.; Thies, C.; Popien, J. L.; Michalowski, P.; Pinheiro Melo, S.; Cerdas, F.; Herrmann, C.; Krewer, U.; Kwade, A.; Spengler, T. S. Green Batteries for Clean Skies:

Sustainability Assessment of Lithium-Sulfur All-Solid-State Batteries for Electric Aircraft. *J Ind Ecol* **2023**, *27* (3), 795–810. https://doi.org/10.1111/JIEC.13345.

(27) He, H.; Tian, S.; Tarroja, B.; Ogunseitan, O. A.; Samuelsen, S.; Schoenung, J. M. Flow Battery Production: Materials Selection and Environmental Impact. *J Clean Prod* **2020**, *269*, 121740. https://doi.org/10.1016/J.JCLEPRO.2020.121740.

(28) Stievano, L.; de Meatza, I.; Bitenc, J.; Cavallo, C.; Brutti, S.; Navarra, M. A. Emerging Calcium Batteries. *J. Power Sources* **2021**, *482* (August 2020), 228875. https://doi.org/10.1016/j.jpowsour.2020.228875.

(29) Liu, Y. ; Zhang, C. ; Hao, Z. ; Cai, X. ; Liu, C. ; Zhang, J. ; Wang, S. ; Chen, Y.; Liu, Y.; Zhang, C.; Hao, Z.; Cai, X.; Liu, C.; Zhang, J.; Wang, S.; Chen, Y. Study on the Life Cycle Assessment of Automotive Power Batteries Considering Multi-Cycle Utilization. *Energies 2023, Vol. 16, Page 6859* **2023**, *16* (19), 6859. https://doi.org/10.3390/EN16196859.

(30) Wang, M.; Jiang, C.; Zhang, S.; Song, X.; Tang, Y.; Cheng, H.-M. Reversible Calcium Alloying Enables a Practical Room-Temperature Rechargeable Calcium-Ion Battery with a High Discharge Voltage. **2018**. https://doi.org/10.1038/s41557-018-0045-4.

(31) Smith, L.; Ibn-Mohammed, T.; Astudillo, D.; Brown, S.; Reaney, I. M.; Koh, S. C. L. The Role of Cycle Life on the Environmental Impact of Li6.4La3Zr1.4Ta0.6O12 Based Solid-State Batteries. *Adv Sustain Syst* **2021**, *5* (2), 2000241. https://doi.org/10.1002/ADSU.202000241.

(32) Rajapakse, M.; Karki, B.; Abu, U. O.; Pishgar, S.; Musa, M. R. K.; Riyadh, S. M. S.; Yu, M.; Sumanasekera, G.; Jasinski, J. B. Intercalation as a Versatile Tool for Fabrication, Property Tuning, and Phase Transitions in 2D Materials. *npj 2D Materials and Applications 2021 5:1* **2021**, *5* (1), 1–21. https://doi.org/10.1038/s41699-021-00211-6.

(33) Zhou, J.; Lin, Z.; Ren, H.; Duan, X.; Shakir, I.; Huang, Y.; Duan, X. Layered Intercalation Materials. *Advanced Materials* **2021**, *33* (25), 2004557. https://doi.org/10.1002/ADMA.202004557.

(34) Arroyo-De Dompablo, M. E.; Ponrouch, A.; Johansson, P.; Palacín, M. R. Achievements, Challenges, and Prospects of Calcium Batteries. *Chem Rev* **2020**, *120* (14), 6331–6357. https://doi.org/10.1021/ACS.CHEMREV.9B00339/ASSET/IMAGES/LARGE/CR9B00339_0016.JPEG.

(35) Shanmukaraj, D.; Ranque, P.; Ben Youcef, H.; Rojo, T.; Poizot, P.; Grugeon, S.; Laruelle, S.; Guyomard, D. Review—Towards Efficient Energy Storage Materials: Lithium Intercalation/Organic Electrodes to Polymer Electrolytes—A Road Map (Tribute to Michel Armand). *J Electrochem Soc* **2020**, *167* (7), 070530. https://doi.org/10.1149/1945-7111/AB787A.

(36) Li, X.; Zhang, Y.; Liao, Y.; Yu, G. Environmental Impact Assessment of Battery Boxes Based on Lightweight Material Substitution. *Scientific Reports 2024 14:1* **2024**, *14* (1), 1–13. https://doi.org/10.1038/s41598-024-53238-2.

(37) Arroyo-De Dompablo, M. E.; Ponrouch, A.; Johansson, P.; Palacín, M. R. Achievements, Challenges, and Prospects of Calcium Batteries. *Chem Rev* **2020**, *120* (14), 6331–6357. https://doi.org/10.1021/ACS.CHEMREV.9B00339/ASSET/IMAGES/LARGE/CR9B00339_0016.JPEG.

(38) Ding, Y.; Zhang, C.; Zhang, L.; Zhou, Y.; Yu, G. Pathways to Widespread Applications: Development of Redox Flow Batteries Based on New Chemistries. *Chem* **2019**, *5* (8), 1964–1987. https://doi.org/10.1016/J.CHEMPR.2019.05.010/ASSET/531530B8-6843-4B59-BC9A-F12581CD67C8/MAIN.ASSETS/GR8.JPG.

(39) Nissen, D. A. A Study of the Anode-Electrolyte Interface in a Thermal Battery. *J Electrochem Soc* **1979**, *126* (2), 176–180. https://doi.org/10.1149/1.2129001/XML.

(40) Miles, M. H.; Fine, D. A.; Fletcher, A. N. The Calcium Anode in Molten Nitrate Electrolytes. *J Electrochem Soc* **1978**, *125* (8), 1209–1214. https://doi.org/10.1149/1.2131651/XML.

(41) Sammells, A. F.; Schumacher, B. Secondary Calcium Solid Electrolyte High Temperature Battery. *J Electrochem Soc* **1986**, *133* (1), 235–236. https://doi.org/10.1149/1.2108533/XML.

(42) Pujare, N. U.; Semkow, K. W.; Sammells, A. F. A Calcium Oxygen Secondary Battery. *J Electrochem Soc* **1988**, *135* (1), 260–261. https://doi.org/10.1149/1.2095574/XML.

(43) Staniewicz, R. J. A Study of the Calcium-Thionyl Chloride Electrochemical System. *J Electrochem Soc* **1980**, *127* (4), 782–789. https://doi.org/10.1149/1.2129758/XML.

(44) Bradley, J.; Mitchell, P. J.; Hagan, W. P.; Tuck, C. D. S. Reduction of Calcium Corrosion in Thionyl Chloride-Based Electrolytes. *J Power Sources* **1989**, *28* (4), 361–365. https://doi.org/10.1016/0378-7753(89)80065-5.

(45) Peled, E.; Meitav, A.; Brand, M. Calcium Thionyl Chloride High-Rate Reserve Cell. *J Electrochem Soc* **1981**, *128* (9), 1936–1938. https://doi.org/10.1149/1.2127768/XML.

(46) Peled, E.; Tulman, R.; Golan, A.; Meitav, A. Calcium / Ca (AlCl4) 2 — Thionyl Chloride High Rate Cell. *J Electrochem Soc* **1984**, *131* (10), 2314–2316. https://doi.org/10.1149/1.2115248/XML.

(47) Peled, E.; Elster, E.; Tulman, R.; Kimel, J. Calcium/Ca(AlCl4)2-Thionyl Chloride (TC) Cell. Effect of Temperature and Cell Parameters on Performance. *J Power Sources* **1985**, *14* (1–3), 93–98. https://doi.org/10.1016/0378-7753(85)88017-4.

(48) Elster, E.; Cohen, R.; Peled, E. Solid Electrolyte Interphase (SEI) Electrodes Part VII. The Electrochemical Behaviour of Calcium in Ba(AlCl4)2 and Sr(AlCl4)2thionyl Chloride Solutions (Extended Abstract). *J Power Sources* **1989**, *26* (3–4), 423–425. https://doi.org/10.1016/0378-7753(89)80157-0.

(49) J, B.; P, M. Current Status of Calcium/Thionyl Chloride Batteries. *Chemistry & Industry (Chichester)* **1990**, No. 5, 135–137.

(50) Aurbach, D.; Skaletsky, R.; Gofer, Y. The Electrochemical Behavior of Calcium Electrodes in a Few Organic Electrolytes. *J Electrochem Soc* **1991**, *138* (12), 3536–3545. https://doi.org/10.1149/1.2085455/XML.

(51) Blomgren, G. E. The Development and Future of Lithium Ion Batteries. *J Electrochem Soc* **2017**, *164* (1), A5019–A5025. https://doi.org/10.1149/2.0251701JES/XML.

(52) Aurbach, D.; Lu, Z.; Schechter, A.; Gofer, Y.; Gizbar, H.; Turgeman, R.; Cohen, Y.; Moshkovich, M.; Levi, E. Prototype Systems for Rechargeable Magnesium Batteries. *Nature 2000 407:6805* **2000**, *407* (6805), 724–727. https://doi.org/10.1038/35037553.

(53) Amatucci, G. G.; Badway, F.; Singhal, A.; Beaudoin, B.; Skandan, G.; Bowmer, T.; Plitz, I.; Pereira, N.; Chapman, T.; Jaworski, R. Investigation of Yttrium and Polyvalent Ion Intercalation into Nanocrystalline Vanadium Oxide. *J Electrochem Soc* **2001**, *148* (8), A940. https://doi.org/10.1149/1.1383777/XML.

(54) Whittingham, M. S. Chemistry of Intercalation Compounds: Metal Guests in Chalcogenide Hosts. *Progress in Solid State Chemistry* **1978**, *12* (1), 41–99. https://doi.org/10.1016/0079-6786(78)90003-1.

(55) Guilmeau, E.; Maignan, A.; Wan, C.; Koumoto, K. On the Effects of Substitution, Intercalation, Non-Stoichiometry and Block Layer Concept in TiS2 Based Thermoelectrics. *Physical Chemistry Chemical Physics* **2015**, *17* (38), 24541–24555. https://doi.org/10.1039/C5CP01795E.

(56) Lerf, A.; Schöllhorn, R. Solvation Reactions of Layered Ternary Sulfides AxTiS2, AxNbS2, and AxTaS2. *Inorg Chem* **1977**, *16* (11), 2950–2956. https://doi.org/10.1021/IC50177A057/ASSET/IC50177A057.FP.PNG_V03.

(57) Schöllhorn, R.; Meyer, H. Cathodic Reduction of Layered Transition Metal Chalcogenides. *Mater Res Bull* **1974**, *9* (9), 1237–1245. https://doi.org/10.1016/0025-5408(74)90042-7.

(58) Chen, S. M. Preparation, Characterization, and Electrocatalytic Oxidation Properties of Iron, Cobalt, Nickel, and Indium Hexacyanoferrate. *Journal of Electroanalytical Chemistry* **2002**, *521* (1–2), 29–52. https://doi.org/10.1016/S0022-0728(02)00677-0.

(59) Wang, R. Y.; Wessells, C. D.; Huggins, R. A.; Cui, Y. Highly Reversible Open Framework Nanoscale Electrodes for Divalent Ion Batteries. *Nano Lett* **2013**, *13* (11), 5748–5752. https://doi.org/10.1021/NL403669A/SUPPL_FILE/NL403669A_SI_001.PDF.

(60) Hayashi, M.; Arai, H.; Ohtsuka, H.; Sakurai, Y. Electrochemical Characteristics of Calcium in Organic Electrolyte Solutions and Vanadium Oxides as Calcium Hosts. *J Power Sources* **2003**, *119–121*, 617–620. https://doi.org/10.1016/S0378-7753(03)00307-0.

(61) Hayashi, M.; Arai, H.; Ohtsuka, H.; Sakurai, Y. Electrochemical Insertion/Extraction of Calcium Ions Using Crystalline Vanadium Oxide. *Electrochemical and Solid-State Letters* **2004**, *7* (5), A119. https://doi.org/10.1149/1.1675951/XML.

(62) Bervas, M.; Klein, L. C.; Amatucci, G. G. Vanadium Oxide–Propylene Carbonate Composite as a Host for the Intercalation of Polyvalent Cations. *Solid State Ion* **2005**, *176* (37–38), 2735–2747. https://doi.org/10.1016/J.SSI.2005.09.009.

(63) See, K. A.; Gerbec, J. A.; Jun, Y. S.; Wudl, F.; Stucky, G. D.; Seshadri, R. A High Capacity Calcium Primary Cell Based on the Ca–S System. *Adv Energy Mater* **2013**, *3* (8), 1056–1061. https://doi.org/10.1002/AENM.201300160.

(64) Kim, H.; Boysen, D. A.; Newhouse, J. M.; Spatocco, B. L.; Chung, B.; Burke, P. J.; Bradwell, D. J.; Jiang, K.; Tomaszowska, A. A.; Wang, K.; Wei, W.; Ortiz, L. A.; Barriga, S. A.; Poizeau, S. M.; Sadoway, D. R. Liquid Metal Batteries: Past, Present, and Future. *Chem Rev* **2013**, *113* (3), 2075–2099. https://doi.org/10.1021/CR300205K/ASSET/CR300205K.FP.PNG_V03.

(65) Kim, H.; Boysen, D. A.; Ouchi, T.; Sadoway, D. R. Calcium–Bismuth Electrodes for Large-Scale Energy Storage (Liquid Metal Batteries). *J Power Sources* **2013**, *241*, 239–248. https://doi.org/10.1016/J.JPOWSOUR.2013.04.052.

(66) Ouchi, T.; Kim, H.; Ning, X.; Sadoway, D. R. Calcium-Antimony Alloys as Electrodes for Liquid Metal Batteries. *J Electrochem Soc* **2014**, *161* (12), A1898–A1904. https://doi.org/10.1149/2.0801412JES/XML.

(67) Poizeau, S.; Sadoway, D. R. Application of the Molecular Interaction Volume Model (MIVM) to Calcium-Based Liquid Alloys of Systems Forming High-Melting Intermetallics. *J Am Chem Soc* **2013**, *135* (22), 8260–8265. https://doi.org/10.1021/JA4013886/ASSET/IMAGES/MEDIUM/JA-2013-013886_0009.GIF.

(68) Ouchi, T.; Kim, H.; Spatocco, B. L.; Sadoway, D. R. Calcium-Based Multi-Element Chemistry for Grid-Scale Electrochemical Energy Storage. *Nature Communications 2016 7:1* **2016**, *7* (1), 1–5. https://doi.org/10.1038/ncomms10999.

(69) Wang, R. Y.; Wessells, C. D.; Huggins, R. A.; Cui, Y. Highly Reversible Open Framework Nanoscale Electrodes for Divalent Ion Batteries. *Nano Lett* **2013**, *13* (11), 5748–5752. https://doi.org/10.1021/NL403669A/SUPPL_FILE/NL403669A_SI_001.PDF.

(70) Shiga, T.; Kondo, H.; Kato, Y.; Inoue, M. Insertion of Calcium Ion into Prussian Blue Analogue in Nonaqueous Solutions and Its Application to a Rechargeable Battery with Dual Carriers. *Journal of Physical Chemistry C* **2015**, *119* (50), 27946–27953. https://doi.org/10.1021/ACS.JPCC.5B10245/SUPPL_FILE/JP5B10245_SI_002.PDF.

(71) Tojo, T.; Sugiura, Y.; Inada, R.; Sakurai, Y. Reversible Calcium Ion Batteries Using a Dehydrated Prussian Blue Analogue Cathode. *Electrochim Acta* **2016**, *207*, 22–27. https://doi.org/10.1016/J.ELECTACTA.2016.04.159.

(72) Lipson, A. L.; Han, S. D.; Kim, S.; Pan, B.; Sa, N.; Liao, C.; Fister, T. T.; Burrell, A. K.; Vaughey, J. T.; Ingram, B. J. Nickel Hexacyanoferrate, a Versatile Intercalation Host for Divalent Ions from Nonaqueous Electrolytes. *J Power Sources* **2016**, *325*, 646–652. https://doi.org/10.1016/J.JPOWSOUR.2016.06.019.

(73) Liu, M.; Rong, Z.; Malik, R.; Canepa, P.; Jain, A.; Ceder, G.; Persson, K. A. Spinel Compounds as Multivalent Battery Cathodes: A Systematic Evaluation Based on Ab Initio Calculations. *Energy Environ Sci* **2015**, *8* (3), 964–974. https://doi.org/10.1039/C4EE03389B.

(74) Rong, Z.; Malik, R.; Canepa, P.; Sai Gautam, G.; Liu, M.; Jain, A.; Persson, K.; Ceder, G. Materials Design Rules for Multivalent Ion Mobility in Intercalation Structures. *Chemistry of Materials* **2015**, *27* (17), 6016–6021. https://doi.org/10.1021/ACS.CHEMMATER.5B02342/SUPPL_FILE/CM5B02342_SI_001.PDF.

(75) Ponrouch, A.; Tchitchekova, D.; Frontera, C.; Bardé, F.; Dompablo, M. E. A. De; Palacín, M. R. Assessing Si-Based Anodes for Ca-Ion Batteries: Electrochemical Decalciation of CaSi2. *Electrochem commun* **2016**, *66*, 75–78. https://doi.org/10.1016/J.ELECOM.2016.03.004.

(76) Wang, D.; Gao, X.; Chen, Y.; Jin, L.; Kuss, C.; Bruce, P. G. Plating and Stripping Calcium in an Organic Electrolyte. *Nature Materials 2017 17:1* **2017**, *17* (1), 16–20. https://doi.org/10.1038/nmat5036.

(77) Li, Z.; Fuhr, O.; Fichtner, M.; Zhao-Karger, Z. Towards Stable and Efficient Electrolytes for Room-Temperature Rechargeable Calcium Batteries. *Energy Environ Sci* **2019**, *12* (12), 3496–3501. https://doi.org/10.1039/C9EE01699F.

(78) Shyamsunder, A.; Blanc, L. E.; Assoud, A.; Nazar, L. F. Reversible Calcium Plating and Stripping at Room Temperature Using a Borate Salt. *ACS Energy Lett* **2019**, *4* (9), 2271–2276. https://doi.org/10.1021/ACSENERGYLETT.9B01550/SUPPL_FILE/NZ9B01550_SI_001.PDF.

(79) Lin, H.; Meng, J.; Guo, W.; Li, R.; Yi, Y.; Ma, Y.; Cheung, C. F.; Aurbach, D.; Xu, Z. L. Deciphering the Dynamic Interfacial Chemistry of Calcium Metal Anodes. *Energy Environ Sci* **2024**, *17* (18), 6548–6558. https://doi.org/10.1039/D4EE01257G.

(80) Dugas, R.; Forero-Saboya, J. D.; Ponrouch, A. Methods and Protocols for Reliable Electrochemical Testing in Post-Li Batteries (Na, K, Mg, and Ca). *Chemistry of Materials* **2019**, *31* (21), 8613–8628. https://doi.org/10.1021/ACS.CHEMMATER.9B02776/ASSET/IMAGES/LARGE/CM9B02776_0011.JPEG.

(81) Liu, X.; Elia, G. A.; Passerini, S. Evaluation of Counter and Reference Electrodes for the Investigation of Ca Battery Materials. *Journal of Power Sources Advances* **2020**, *2*, 100008. https://doi.org/10.1016/J.POWERA.2020.100008.

(82) Jao, W. Y.; Tseng, L. C.; Lin, Y.; Chen, Y. C.; Hu, C. C. Stability Promotion of Carbon-Based Quasi-Reference Electrodes in Nonaqueous Calcium Ion Electrolytes. *Journal of Physical Chemistry C* **2024**, *128*, 2025. https://doi.org/10.1021/ACS.JPCC.4C05509/ASSET/IMAGES/LARGE/JP4C05509_0005.JPEG.

(83) Liang, J.; Wang, M.; Zhu, S.; Zhu, D.; Wang, R.; Wang, J.; Cui, L.; Huang, M.; Zhang, W.; An, Q.; Zhang, L.; Zhao, K. Corrosion of Calcium Metal in Ca(TFSI)2/DMAc Electrolyte and Its Solution via Alloy Interface and Competitive Solvation. *Angewandte Chemie International Edition* **2025**, e202502729. https://doi.org/10.1002/ANIE.202502729.

(84) Ponrouch, A.; Frontera, C.; Bardé, F.; Palacín, M. R. Towards a Calcium-Based Rechargeable Battery. *Nature Materials 2015 15:2* **2015**, *15* (2), 169–172. https://doi.org/10.1038/nmat4462.

(85) Transactions and Communications. *Journal of the Society of Chemical Industry* **1944**, *63* (5), 125–160. https://doi.org/10.1002/JCTB.5000630501.

(86) Leon, N. J.; Xie, X.; Yang, M.; Driscoll, D. M.; Connell, J. G.; Kim, S.; Seguin, T.; Vaughey, J. T.; Balasubramanian, M.; Persson, K. A.; Liao, C. Room-Temperature Calcium Plating and Stripping Using a Perfluoroalkoxyaluminate Anion Electrolyte. *Journal of Physical Chemistry C* **2022**, *126* (32), 13579–13584. https://doi.org/10.1021/ACS.JPCC.2C03272/SUPPL_FILE/JP2C03272_SI_001.PDF.

(87) Wang, Y.-S.; Yeh, H.-W.; Tang, Y.-H.; -, al; Asselin, G. M.; Paden, O.; Qiu, W. Steps Towards the Use of TiS2 Electrodes in Ca Batteries. *J Electrochem Soc* **2020**, *167* (7), 070532. https://doi.org/10.1149/1945-7111/AB7A82.

(88) Biria, S.; Pathreeker, S.; Genier, F. S.; Hosein, I. D. A Highly Conductive and Thermally Stable Ionic Liquid Gel Electrolyte for Calcium-Ion Batteries. *ACS Appl Polym Mater* **2020**, *2* (6), 2111–2118. https://doi.org/10.1021/ACSAPM.9B01223/SUPPL_FILE/AP9B01223_SI_001.PDF.

(89) Stievano, L.; de Meatza, I.; Bitenc, J.; Cavallo, C.; Brutti, S.; Navarra, M. A. Emerging Calcium Batteries. *J Power Sources* **2021**, *482*, 228875. https://doi.org/10.1016/J.JPOWSOUR.2020.228875.

(90) Aurbach, D.; Lu, Z.; Schechter, A.; Gofer, Y.; Gizbar, H.; Turgeman, R.; Cohen, Y.; Moshkovich, M.; Levi, E. Prototype Systems for Rechargeable Magnesium Batteries. *Nature 2000 407:6805* **2000**, *407* (6805), 724–727. https://doi.org/10.1038/35037553.

(91) Liu, X.; Elia, G.; Passerini, S. Evaluation of Counter and Reference Electrodes for the Investigation of Ca Battery Materials. *ECS Meeting Abstracts* **2022**, *MA2022-01* (1), 63. https://doi.org/10.1149/MA2022-01163MTGABS.

(92) Xu, Z. L.; Park, J.; Wang, J.; Moon, H.; Yoon, G.; Lim, J.; Ko, Y. J.; Cho, S. P.; Lee, S. Y.; Kang, K. A New High-Voltage Calcium Intercalation Host for Ultra-Stable and High-Power Calcium Rechargeable Batteries. *Nat Commun* **2021**, *12* (1). https://doi.org/10.1038/S41467-021-23703-X.

(93) Chae, M. S.; Heo, J. W.; Hyoung, J.; Hong, S. T. Double-Sheet Vanadium Oxide as a Cathode Material for Calcium-Ion Batteries. *ChemNanoMat* **2020**, *6* (7), 1049–1053. https://doi.org/10.1002/CNMA.202000011.

(94) Chae, M. S.; Kwak, H. H.; Hong, S. T. Calcium Molybdenum Bronze as a Stable High-Capacity Cathode Material for Calcium-Ion Batteries. *ACS Appl Energy Mater* **2020**, *3* (6), 5107–5112. https://doi.org/10.1021/ACSAEM.0C00567/SUPPL_FILE/AE0C00567_SI_001.PDF.

(95) Shyamsunder, A.; Blanc, L. E.; Assoud, A.; Nazar, L. F. Reversible Calcium Plating and Stripping at Room Temperature Using a Borate Salt. *ACS Energy Lett* **2019**, *4* (9), 2271–2276. https://doi.org/10.1021/ACSENERGYLETT.9B01550.

(96) Gummow, R. J.; Vamvounis, G.; Kannan, M. B.; He, Y. Calcium-Ion Batteries: Current State-of-the-Art and Future Perspectives. *Advanced Materials* **2018**, *30* (39), 1801702. https://doi.org/10.1002/ADMA.201801702.

(97) Kisu, K.; Kim, S.; Shinohara, T.; Zhao, K.; Züttel, A.; Orimo, S. ichi. Monocarborane Cluster as a Stable Fluorine-Free Calcium Battery Electrolyte. *Scientific Reports 2021 11:1* **2021**, *11* (1), 1–8. https://doi.org/10.1038/s41598-021-86938-0.

(98) Celeste, A.; Agostini, M.; De Bonis, A.; Brutti, S. Insight the Lithiation Process of Micro and Nanoparticles TiO2-Anatase Based Electrodes. *Electrochim Acta* **2025**, *535*, 146618. https://doi.org/10.1016/J.ELECTACTA.2025.146618.

(99) Liu, Z.; Andreev, Y. G.; Robert Armstrong, A.; Brutti, S.; Ren, Y.; Bruce, P. G. Nanostructured TiO2(B): The Effect of Size and Shape on Anode Properties for Li-Ion Batteries. *Progress in Natural Science: Materials International* **2013**, *23* (3), 235–244. https://doi.org/10.1016/J.PNSC.2013.05.001.

Chapter IV

Positive electrode for CIBs

4.1 Introduction to Cathode Materials for CIBs: Focus on Prussian Blue Analogues

The development of efficient and stable cathode materials remains a central challenge in the advancement of calcium-ion battery technology.[1] Since the initial investigations into Ca^{2+} intercalation in metal oxides and sulphides in the 1960s, progress in this area has been limited for decades, primarily due to the lack of suitable electrolytes that could support reversible calcium cycling.[2,3] A major breakthrough occurred in 2016, when Ponrouch et al. reported reversible calcium plating and stripping in conventional organic solvents, [4] renewing interest in the design of viable cathode materials.[5–7] Despite this progress, the number of experimental studies on positive electrodes for CIBs remains relatively small, and the field is still in an early phase of development.[8,9]

Various families of materials have been proposed and tested as potential cathodes, including layered oxides,[10,11] spinels,[12] perovskites,[13] chalcogenides,[14] phosphates,[15,16] nitrides,[17] and carbon-based compounds.[18,19] Conversion-type materials have also drawn attention due to their potential to bypass the kinetic limitations associated with calcium intercalation.[20] However, many of these materials exhibit slow ion diffusion, poor structural stability, or irreversible electrochemical behavior.[1,21] For instance, early studies on V_2O_5-based materials showed only partial or limited calcium intercalation.[21] Nanostructured vanadium oxide aerogels demonstrated higher specific capacities, but maintaining performance over extended cycling remained challenging.[22]

Other promising efforts include the use of hydrated vanadium oxides, such as $V_2O_5 \cdot 0.63H_2O$, and one-dimensional $CaV_6O_{16} \cdot 7H_2O$ nanostructures, both of which benefit from large diffusion channels and hydrated frameworks that facilitate Ca^{2+} mobility. [23,24] In these systems, good capacity retention and rate capabilities have been observed, suggesting that nanostructuring and water-mediated ion transport can partially overcome the intrinsic limitations of Ca^{2+} intercalation.

Layered molybdenum oxides such as α-MoO_3 have also been explored in organic calcium electrolytes, delivering moderate reversible capacities.[10,11] Even though structural stability during intercalation and deintercalation was confirmed, the calcium content has to be restricted to preserve reversibility ($0<x<0.3$ in Ca_xMoO_3).[10] Similarly, spinel-type Mn_2O_4 and related polymorphs of $CaMn_2O_4$ have been analysed both theoretically and experimentally.[12,25] Among them, spinel-like structures exhibited more favourable Ca^{2+} mobility due to larger polyhedral diffusion paths, although practical implementation remains limited.[25]

Research into calcium cobaltite, such as $Ca_3Co_2O_6$ and $Ca_2Co_2O_5$, has revealed that the dimensionality of the Co-O framework significantly influences ion mobility and structural stability.[26–28] Experimental and DFT studies confirmed that one-dimensional and two-dimensional arrangements enable more accessible diffusion pathways than fully three-dimensional frameworks.[25,27] However, issues of limited reversibility and electrolyte compatibility persist.[27,29]

As previously discussed in Chapter I, molybdenum chalcogenides with the general formula Mo_6X_8 (X = S, Se, Te), known as Chevrel phases, are of particular interest for their unique structural and electrochemical characteristics. [1] Computational investigations by Smeu et al.[30] have suggested their suitability for calcium-based energy storage, though no experimental validation has yet been reported.[31] Alongside these, the layered dichalcogenide TiS_2 has been examined by Tchitchekova et al. for its ability to intercalate Ca^{2+} and Mg^{2+} using carbonate-based electrolytes.[32] Their study provided the first clear demonstration of reversible calcium intercalation in TiS_2, supported by X-ray diffraction (XRD) and Ca L_2-edge absorption tomography. Verrelli et al. expanded on this by showing that reversible Ca^{2+} insertion is achievable at room temperature in propylene carbonate-based electrolytes through solvent co-intercalation. [33]

Among the various materials investigated, Prussian Blue Analogues (PBAs) have emerged as particularly promising candidates for calcium-ion cathodes due to their no toxicity, unique structural properties and electrochemical behavior. [1,34] PBAs exhibit a highly ordered, open-framework structure, typically described by the general formula $AxMM'(CN)_6 \cdot nH_2O$, where *A* denotes interstitial alkali and alkaline earth cation (including Ca^{2+}), M is connected to the nitrogen ends of the cyanide groups and is usually high-spin (HS), while M', bonded to the carbon end of the cyanides, is low-spin (LS), since these two ends behave respectively as weak and strong field ligands.[35] The framework of PBAs, characterized by the three-dimensional network of transition metals and cyanide ligands, provides substantial lattice stability and allows for efficient ion diffusion.[36–38] Their cubic lattice and large interstitial voids offer sufficient space for relatively large cations, while the framework's chemical tunability allows optimization of ionic diffusion and structural stability.[37,38]

Materials like $K_2BaFe(CN)_6$ demonstrated modest yet reversible capacities, though with limited cycle life.[39] More recently, PBAs such as KNiFe-PBA have shown enhanced structural stability and electrochemical reversibility in Ca-based organic electrolytes using a pseudocapacitive approach with Ag as QRE and an activated carbon based counter electrode.[40] These materials preserve their framework integrity over repeated cycling, despite delivering only moderate absolute capacities (around 40mAh/g).[40]

Early studies on PBA such us $K_{1.67}Mn_{0.65}Fe_{0.35}Fe(CN)_{60.92}\cdot 0.45H_2O$, exhibit good cycling stability and remarkable electrochemical performance, making them candidates for large ion intercalation such us K^+.[36] The ability of PBAs to accommodate larger calcium ions in their crystal lattice is facilitated by their large channels and open cubic framework, which contrasts favourably with traditional intercalation materials that often struggle with ion size constraints[34,36,40]. Consequently, the structural characteristics of PBAs, alongside their performance in potassium-ion systems, suggest potential for the development of high-performance CIBs.[37]

However, the specific performance of $K_{1.67}Mn_{0.65}Fe_{0.35}Fe(CN)_{60.92}\cdot 0.45H_2O$ in calcium intercalation has never been reported so far in the literature[36] and for this reason and considering its structural features and potential suitability for multivalent ion storage, the following section presents a detailed investigation and electrochemical characterization of this material as a cathode for CIBs.

4.2 PBA as cathode for CIBs

4.2.1 Introduction

The PBA $K_{1.67}Mn_{0.65}Fe_{0.35}[Fe(CN)_6]_{0.92}\cdot 0.45H_2O$ (MF21) represents an interesting candidate positive electrode active material for calcium metal and CIBs. In this chapter we investigate the reversible intercalation reactions of calcium ions into MF21 in a nonaqueous electrolyte. This material was synthesised by a simple precipitation method and its functional properties were investigated by combining several complementary *ex situ* and *operando* physico-chemical characterization techniques. This MF21 demonstrates reversible redox activity of Ca intercalation/deintercalation demonstrated by galvanostatic cycling and confirmed by XRD, X-ray fluorescence (XRF) and the redox active species were identified by Mossbauer spectroscopy. Overall M21 shows Mn redox activity despite suffering a quick fade in capacity likely due to the passivation products on Ca counter-electrode surface that hinder any redox activity after a few cycles. To circumvent this setback further electrochemical characterisation was performed by adopting the pseudo-capacitive approach outlined in chapter III.

4.2.2 Experimental Section

4.2.2.1 Synthesis of the PBA

$K_{1.67}$ Mn $_{0.65}Fe_{0.35}[Fe(CN)_6]_{0.92}\cdot 0.45H_2O$ (MF21) was synthesised by precipitation method. Two solutions A and B were prepared at 60 °C. Solution A was obtained by dissolving 8 mmol of $K_4Fe(CN)_{6.3}H_2O$ in 100 mL of saturated KCl solution; solution B was a mixture of 8 mmol of $MnSO_4.H_2O$ and $FeSO_4.7H_2O$ at the required 2:1 stoichiometric ratio in 80 mL of KCl. Solution B was poured rapidly into solution A under intense stirring. The temperature was kept at 60 °C for 24 hours of agitation. The obtained suspension was washed five times with deionized water and then two

times with ethanol and finally centrifuged at 20000 rpm before being dried under vacuum. An additional drying step at 100 °C overnight was applied before the characterizations and electrode formulation to ensure that the interstitial water was removed completely.

4.2.2.2 Materials characterization and data analysis

Powder XRD patterns of the synthesised materials were collected on a Bruker Advance D8 diffractometer with a Cu Kα radiation source (λ = 1.5418 Å) and a step size of 0.02° in the range of 10-100 °. Lattice parameters were obtained by profile matching using Fullprof package40.

Transmission ^{57}Fe Mossbauer spectra were collected at room temperature with a triangular velocity waveform. A gas-filled proportional counter was used for the detection of γ-rays. A 0.5 GBq ^{57}Co:Rh source, kept at room temperature. Velocity calibration was performed with an α-Fe foil at room temperature. Absorbers containing 5 to 25 mg cm^{-2} were protected from air using thermally sealed coffee-bags. The Mössbauer spectra were fitted by using the PC-Mos II computer program with appropriate superpositions of Lorentzian lines. In this way, hyperfine parameters such as the isomer shift (δ), the electric quadrupole splitting (Δ), the full line width at half maximum (Γ) and the relative resonance areas (Area) of the different components of the absorption patterns were determined.

Thermogravimetric analysis (TGA) was performed to determine the amount of interstitial water of MF21. The measurement was carried out on a thermic simultaneous analyzer model STA 449 F1 Jupiter® (NETZSCH) from room temperature to 450 °C under Argon atmosphere with a thermal step of 5 °C/min. The amount of interstitial water was calculated based on the mass loss at 100 °C.

For the electrochemical tests, electrode films were prepared by tape-casting on aluminum foil (18 μm, GoodFellow), a slurry obtained by mixing MF21-PBA with Super P carbon (Alfa Aesar) and polyvinylidene fluoride (PVdF, Solef® 5130) as conductive additive and binder, respectively, with a mass ratio of 60/30/10 in N-methyl-2-pyrrolidone (NMP, Sigma Alrich) in a planetary ball mill. The casted film was dried in air before punching out round-shape electrodes with the diameter of 1.27 cm, which were then further dried under vacuum at 80 °C overnight. Coin cells (CR2032) of MF21, K, Li and Ca metal were assembled in an Ar-filled glovebox (O2 < 0.5 ppm, H2O < 0.5 ppm) using 0.5M $Ca(TFSI)_2$ and 0.3M $Ca[b(HFIP)_4]_2$ in DME as electrolytes, a Whatman glass fibre disks as separators. For the evaluation by the pseudo-capacitive approach, three electrode cells were assembled with MF21 as working electrode, AC as counter electrode and Au as QRE using 0.5 M $Ca(TFSI)_2$ in DME.

For the *ex situ* and operando analyses, electrodes were prepared by thoroughly mixing MF21 with Super P carbon and PTFE (polytetrafluoroethylene) with a weight ratio of 60/30/10 to form a homogeneous film. The film was cut into electrode disks with the diameter of 11 mm (operando XRD

and XAS) or 14 mm (*ex situ* Mössbauer spectroscopy). Operando XRD and XAS experiments were carried out using a special electrochemical cell equipped with a Be window. A thin aluminum foil (thickness = 2 μm) put between the working electrode and the Be window was used as the positive current collector. The mass loading of the electrodes used for the ex-situ Mössbauer spectroscopy was around 25 mg cm–2, whereas it was ≤ 10 mg cm^{-2} for the operando XRD and operando XAS measurements.

4.2.3 Result and discussion

In this study, we investigated Ca^{2+} intercalation in MF21-PBA structures by comparing two conditions. First, the as-prepared (potassiated) MF21 was cycled against calcium metal in 0.3 M $Ca[b(HFIP)_4]_2$ electrolyte (Figure 4.1a). Then, the same material was de-potassiated via galvanostatic cycling against lithium (using LiTFSi 0.5M in DME as electrolyte), washed with fresh DME and subsequently tested against calcium in the same electrolyte and cell configuration (Figure 4.1b). For reference, Figure 4.1c shows the cycling behavior of MF21 versus potassium.

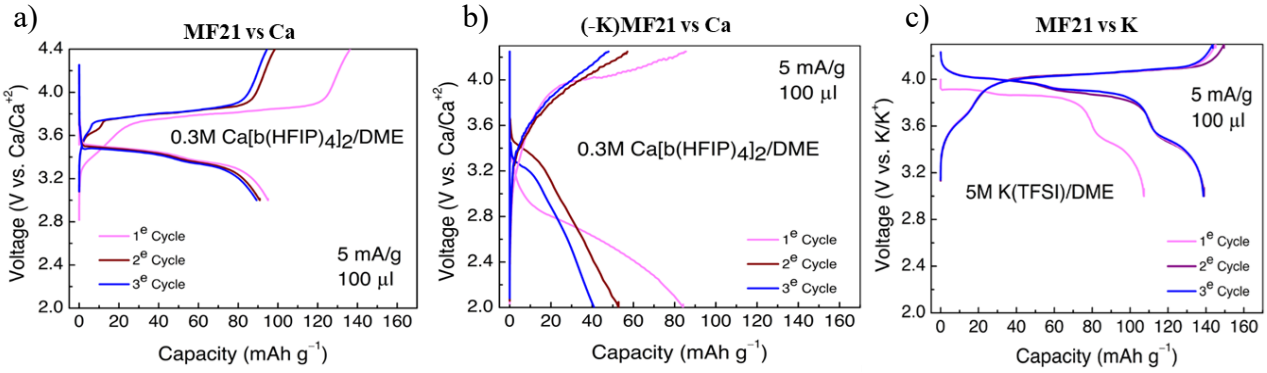

Figure 4.1 Galvanostatic cycling of a) pristine MF21 and b) depotassiated (-K)MF21 against Ca metal; c) galvanostatic cycling of MF21 vs K.

Comparing Figures 4.1a and 1b, several key differences emerge. Most notably, the de-potassiated MF21 exhibits about half the capacity of the potassiated material. Moreover, in the de-potassiated sample, the charge/discharge curves show only a single, broad plateau. This suggests that only one transition metal is participating to the redox activity during calcium insertion.[41] Alternatively, it is possible that, unlike the potassiated MF21 (Figure 4.1a) where two distinct voltage plateaus indicate sequential redox processes of Fe and Mn, the de-potassiated material exhibits a mixed redox behavior. In this case, Fe and Mn may gradually change oxidation state in parallel with the state of charge, resulting in a single, sloped plateau during cycling.[42] These findings confirm, as already reported, a stronger a higher affinity of MF21 for potassium.[36,43–45] This suggests that in the pristine sample

(Figure 4.1a), the electrochemical activity is predominantly due to K^+ insertion rather than Ca^{2+}. The rapid capacity fading observed in the de-potassiated MF21 (Figure 4.1b) could be attributed to surface passivation of the calcium metal anode.[46] After cycling the de-potassiated MF21, the cell was opened, and a black layer was observed on the separator and on Ca metal (Figure 4.2a). This passivation film may hinder Ca-ion diffusion at the electrode–electrolyte interface. When the cell was reassembled using the same MF21 electrode with a fresh electrolyte, separator and a new calcium metal counter electrode, the system nearly recovered its initial capacity (Figure 4.2c). These tests evidence the electrochemical activity of the MF21 as positive intercalation electrode, showing a reversible capacity of calcium intercalation/deintercalation in MF21 as a cathode for CIBs.

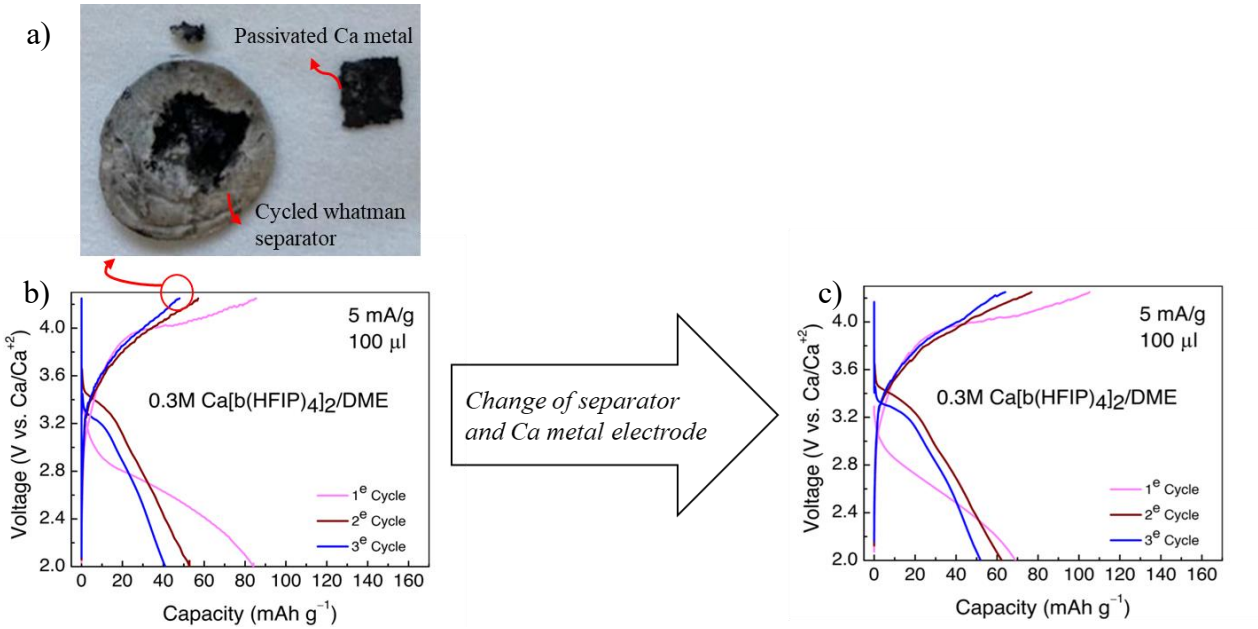

Figure 4.2 a) Whatman and Ca metal electrode after 3 cycles; b) and c) represent the galvanostatic cycling of the depotassiated (-K)MF21 against Ca metal, respectively before and after the renewing of the passivated Ca electrode and Whatman separator.

XRF was used to confirm the presence of calcium in the MF21 electrode after cycling, at different states of charge. Specifically, one measurement was taken at the end of the first charge (EOC), corresponding to the initial de-potassiation vs. Li, and another at the end of the first discharge (EOD), i.e., after Ca insertion. The results, summarized in the table shown in Figure 4.3a, confirm the presence of calcium in the calciated electrode.

a)

XRF data table

	K / (Mn + Fe)	Ca / (Mn + Fe)	Mn / Fe
Pristine	0.9	0	0.5
EOC	0.37	0	0.5
EOD	0.33	0.74	0.5

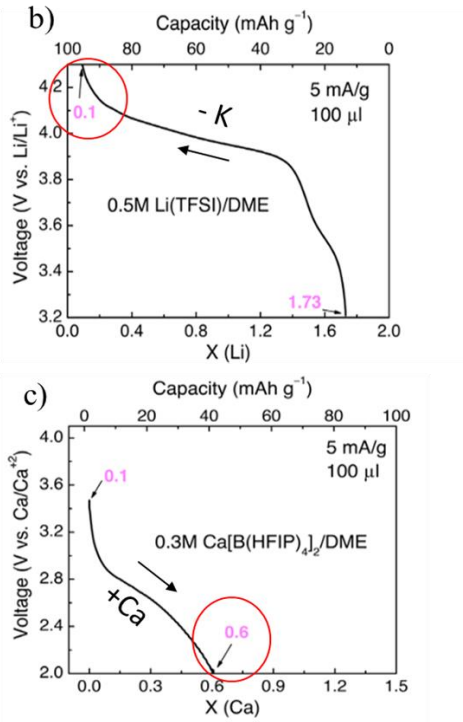

Figure 4.3 a)XRF table, b) and c) galvanostatic curve of the samples with circled the corresponding state of charge, representing the depotassiation and calciation of MF21 respectively

To further confirm the intercalation of Ca within the structure and not just adsorbed on the surface, the same samples, i.e., pristine electrode, EOC and EOD were analysed by XRD. The XRD pattern of dried pristine MF21 (Figure 4.4a) was previously discussed in detail by our group.[36] The MF21 lattice results results slightly contracted and exhibits a greater lattice distortion compared to other reported isostructural containing high-spin Mn or Fe.[34,38,47,48] This distortion arise from partial oxidation of Mn^{2+} or Fe^{2+} to Mn^{3+} or Fe^{3+} at the M1 site during synthesis or drying. [36]

The XRD profiles collected at different states of charge (Figure 4.4 b and c) reveal a noticeable shift of diffraction peaks toward smaller angles upon Ca insertion, indicating an expansion of the lattice parameters.[49] This shift coupled with the XRF results provides direct evidence of bulk calcium intercalation into the PBA framework.

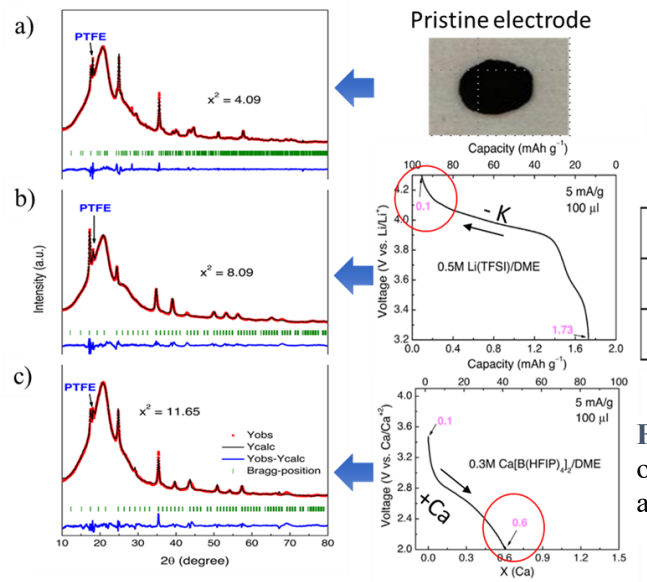

d)

XRD Data Table

	a (Å)	b (Å)	c (Å)	β (°)	System	Space group
Pristine	10.1	10.1	10.1	92.9	monoclinic	P 21/c
EOC	10.3	10.3	10.3	90	cubic	Fm-3m
EOD	10.1	10.1	10.1	92.9	monoclinic	P 21/c

Figure 4.4 a) b) c) are the XRD pattern of the samples on the right i.e. pristine, at EOC and EOD respectively; and d) the corresponding table.

To understand the redox activity of the transition metal species during calcium intercalation in the MF21 structure as well as the potential partial oxidation of the pristine sample, the material was analysed by Mössbauer spectroscopy under the same conditions as the XRF measurements (Figure 4.5). Mössbauer spectroscopy enables the quantification of both high-spin (HS) and low-spin (LS) Fe oxidation states, allowing us to estimate from the fitted area the number of electrons exchanged per formula unit at the EOC and EOD. From this, we deduced the contribution of Fe to the overall capacity, while the remaining portion was attributed to Mn. Moreover, these results indicate a partial oxidation in the pristine MF21 material due to the presence of Fe^{3+} in the pristine electrode.

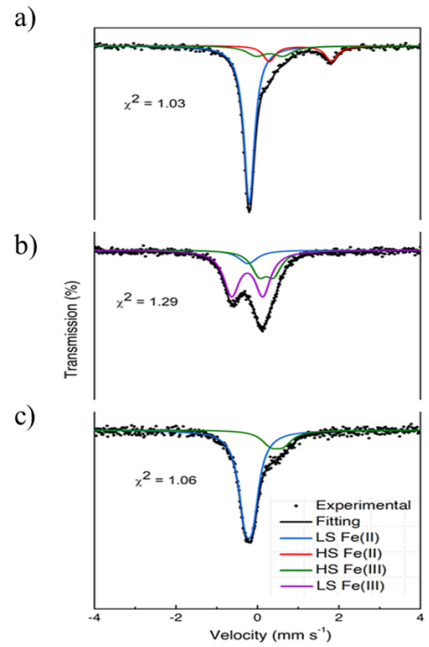

d)

Mössbauer data table

	QS (mm s^{-1})	IS (mm s^{-1})	LW	Area (%)	Site
Pristine	0.00	-0.21	0.29 (1)	70 (1)	LS Fe $^{2+}$
	1.5 (2)	1.01 (1)	0.29 (2)	15 (2)	HS Fe $^{2+}$
	0.64 (5)	0.25 (5)	-0.52 (5)	15 (6)	HS Fe $^{3+}$
EOC	0.79 (2)	-0.27	0.49 (2)	60 (4)	LS Fe $^{3+}$
	0.47 (3)	0.23 (1)	0.58 (5)	30 (2)	HS Fe $^{3+}$
	0.00	-0.20 (1)	0.43 (12)	11	LS Fe $^{2+}$
EOD	0.00 (1)	-0.21	0.35 (1)	72	LS Fe $^{2+}$
	0.3 (3)	0.38 (2)	0.50 (6)	28 (2)	HS Fe $^{3+}$

Figure 4.5 a), b) and c) are the Mossbauer spectroscopy of the samples of the electrode pristine, at EOC and EOD respectively; d) report the corresponding table results.

Based on these calculations and comparing them with the galvanostatic profile of the charge and the discharge shown in figure 4.3 b and c, respectively, we estimate that Fe accounts for approximately 62 mAh/g at EOC and 54.3 mAh/g at EOD. Comparing the capacity achieved in the galvanostatic profiles, with the redox activity calculated from Mössbauer analysis, we conclude that potassium deintercalation is mainly supported by Fe redox activity, with a minor contribution from Mn, and that the calcium intercalation is mainly supported by the Fe activity.

To further understand the calcium intercalation mechanism within the MF21 lattice, we conducted operando XRD analysis during galvanostatic cycling measurements shown in Figure 4.6. The in situ XRD patterns reveal a structural "breathing" behaviour, i.e., reversible variation in lattice parameters during charge and discharge. This observation indicates a monophasic intercalation mechanism, wherein the structural framework of MF21 remains intact while undergoing the galvanostatic cycle, disclosing reversible expansion and contraction during Ca^{2+} insertion and extraction.

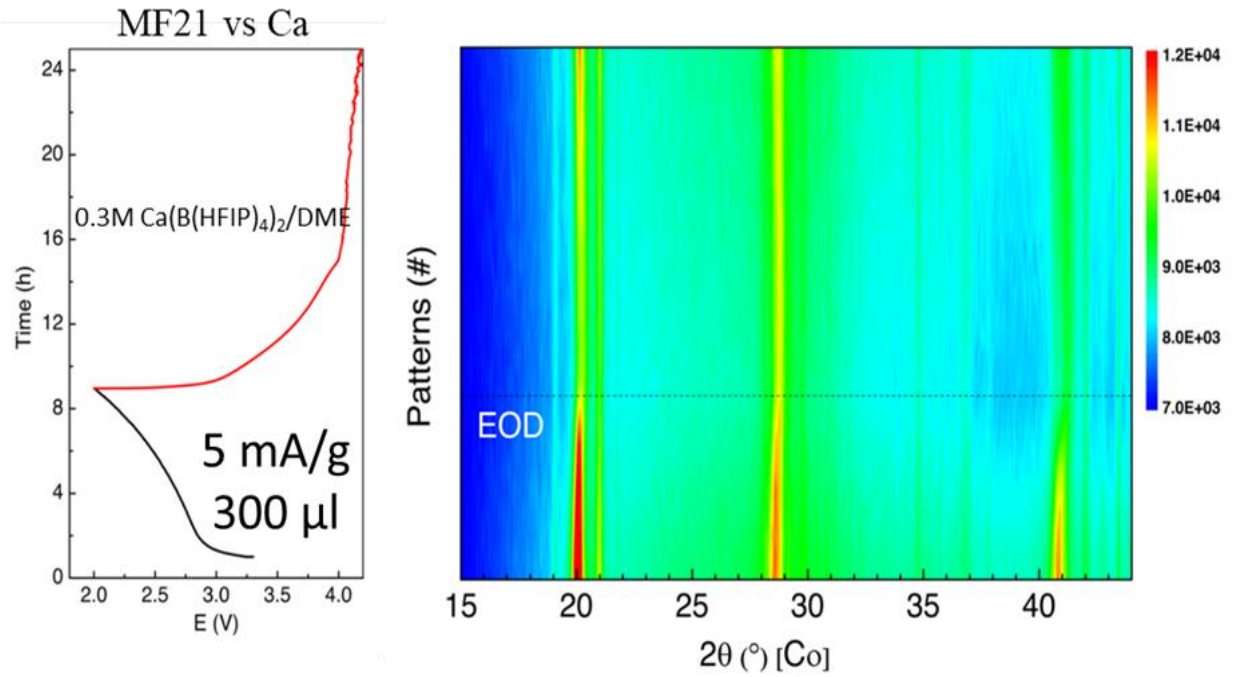

Figure 4.6 galvanostatic curves of charge and discharge on the left and on the right the corresponding in situ XRD on the right of MF21 vs Ca; the patterns of the PBA show obvious peaks at about 19.5; 28.8; 35.4; 40.7 and 43.8 that gradually shift to smaller angles by monophasic mechanism.

We subsequently tested the MF21 electrode using a three-electrode configuration, employing activated carbon as the counter electrode, as described in Chapter III. This setup was designed to isolate the behaviour of the cathode material from the complications associated with calcium metal as previously shown in Figure 3.1a.

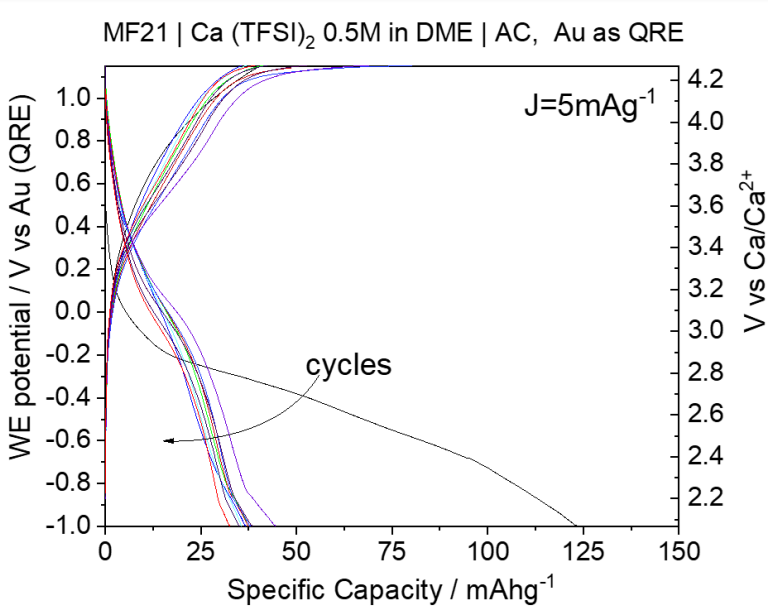

Figure 4.7 Galvanostatic cycling of MF21 against AC counter electrode and Au as QRE with $Ca(TFSI)_2$ 0.5M in DME as electrolyte.

Figure 4.7 presents the galvanostatic cycling obtained with this configuration. An initial, non-reversible charge is observed, which is likely attributed to parasitic reactions or initial irreversible intercalation processes. Despite a rapid initial capacity fade, the system quickly stabilizes into a highly reversible cycling pattern, even if with limited capacity. This behavior, characterized by limited capacity but good reversibility, is similar to what has already been reported for other PBAs cycled with calcium.[40]

The reduced capacity may also be influenced by the different electrolyte used in this configuration, highlighting the strong dependence of intercalation behavior on electrolyte chemistry.

These results suggest that, when using this cell setup, MF21 exhibits a limited but stable intercalation capability and raises new questions about the possible parasitic reactions occurring when calcium metal is used, which should be further investigated to better understand and control their effect on cell performance.

4.2.4 Conclusion

In summary, our findings confirm that calcium reversibly intercalates into the MF21 structure in aprotic electrolyte, without compromising the integrity of the open-framework PBA lattice. However, in full cells using calcium metal as the counter electrode, a rapid capacity fade is observed. This is likely caused by the formation of passivation products at the Ca/electrolyte interface, which progressively hinder Ca^{2+} transport and block intercalation.[50]

Ex-situ XRD confirmed that the MF21 framework remains crystalline during cycling, Mössbauer analysis reveals an initial partial oxidation of the material and that the electrochemical activity is mainly supported by Fe redox activity, with only a minor contribution from Mn. Operando XRD revealed a monophasic intercalation/deintercalation mechanism, characterized by reversible lattice expansion and contraction. Altogether, these results highlight the need for improved electrolyte formulations and optimized cell designs to fully exploit MF21 as a cathode for CIBs.

To discriminate the activity of MF21 cathode to the issues related to calcium metal, the material was tested in a three-electrode configuration using activated carbon as a capacitive counter electrode and Au as quasi-reference electrode in a pseudo capacitive cell setup described in Chapter III. In this setup, the system showed a clear stabilization of the electrochemical response over cycling; however, with limited capacity. This suggests that possible electrolyte-dependent reactions may occur during cycling and further investigations of MF21 in this configuration are needed in order to assess possible solvent co-intercalation and initial dissolution of the active material.

Although no literature reports are available on the electrochemical behaviour of this specific Prussian Blue Analogue composition with Mg^{2+} or Zn^{2+} ions, meaningful contextualisation can be achieved by considering structurally related PBAs studied in other multivalent systems. PBAs explored for Mg^{2+} intercalation typically exhibit limited capacities, generally ranging between 20 and 60 mAh g^{-1}, reflecting the slow diffusion kinetics imposed by the high charge density and strong solvation of Mg^{2+}.[51] In contrast, several PBAs investigated for Zn^{2+} storage, mostly in aqueous electrolytes, display higher capacities between 100 and 150 mAh g^{-1}, although their behaviour is strongly influenced by framework composition and water-mediated co-intercalation processes.[52–53]

These comparisons highlight that the electrochemical performance of PBAs is governed not only by the nature of the migrating ion and electrolyte environment but also by structural parameters such as vacancy content, hydration degree and transition-metal distribution within the framework. In this context, the studied PBA (MF21) cathode delivers reversible Ca^{2+} intercalation with capacities ranging from 80 to 40 mAh g^{-1} at 5 mA g^{-1} in Ca-metal half-cells, and approximately 30 mAh g^{-1} in the pseudo-capacitive configuration, values that are fully consistent with the expectations for divalent-ion storage in PBAs under aprotic conditions. Altogether, these observations emphasise both the intrinsic challenges associated with Ca^{2+} intercalation and the crucial role of framework chemistry in determining the electrochemical response of multivalent-ion insertion materials.

4.3 Bibliography

(1) Stievano, L.; de Meatza, I.; Bitenc, J.; Cavallo, C.; Brutti, S.; Navarra, M. A. Emerging Calcium Batteries. *J Power Sources* 2021, *482*, 228875. https://doi.org/10.1016/J.JPOWSOUR.2020.228875.

(2) Ponrouch, A.; Palacin, M. R. On the Road toward Calcium-Based Batteries. *Curr Opin Electrochem* 2018, *9*, 1–7. https://doi.org/10.1016/J.COELEC.2018.02.001.

(3) Levi, E.; YGofer; Aurbach, D. On the Way to Rechargeable Mg Batteries: The Challenge of New Cathode Materials. *Chemistry of Materials* 2010, *22* (3), 860–868. https://doi.org/10.1021/CM9016497/ASSET/IMAGES/MEDIUM/CM-2009-016497_0001.GIF.

(4) Ponrouch, A.; Frontera, C.; Bardé, F.; Palacín, M. R. Towards a Calcium-Based Rechargeable Battery. *Nature Materials 2015 15:2* 2015, *15* (2), 169–172. https://doi.org/10.1038/nmat4462.

(5) Wang, D.; Gao, X.; Chen, Y.; Jin, L.; Kuss, C.; Bruce, P. G. Plating and Stripping Calcium in an Organic Electrolyte. *Nature Materials 2017 17:1* 2017, *17* (1), 16–20. https://doi.org/10.1038/nmat5036.

(6) Shyamsunder, A.; Blanc, L. E.; Assoud, A.; Nazar, L. F. Reversible Calcium Plating and Stripping at Room Temperature Using a Borate Salt. *ACS Energy Lett* 2019, *4* (9), 2271–2276. https://doi.org/10.1021/ACSENERGYLETT.9B01550/SUPPL_FILE/NZ9B01550_SI_001.PDF.

(7) Nielson, K. V.; Luo, J.; Liu, T. L. Optimizing Calcium Electrolytes by Solvent Manipulation for Calcium Batteries. *Batter Supercaps* 2020, *3* (8), 766–772. https://doi.org/10.1002/BATT.202000005.

(8) Dugas, R.; Forero-Saboya, J. D.; Ponrouch, A. Methods and Protocols for Reliable Electrochemical Testing in Post-Li Batteries (Na, K, Mg, and Ca). *Chemistry of Materials* 2019, *31* (21), 8613–8628. https://doi.org/10.1021/ACS.CHEMMATER.9B02776/ASSET/IMAGES/LARGE/CM9B02776_0011.JPEG.

(9) Tchitchekova, D. S.; Monti, D.; Johansson, P.; Bardé, F.; Randon-Vitanova, A.; Palacín, M. R.; Ponrouch, A. On the Reliability of Half-Cell Tests for Monovalent (Li + , Na +) and Divalent (Mg 2+ , Ca 2+) Cation Based Batteries . *J Electrochem Soc* 2017, *164* (7), A1384–A1392. https://doi.org/10.1149/2.0411707JES/XML.

(10) Cabello, M.; Nacimiento, F.; Alcántara, R.; Lavela, P.; Pérez Vicente, C.; Tirado, J. L. Applicability of Molybdite as an Electrode Material in Calcium Batteries: A Structural Study of Layer-Type CaxMoO3. *Chemistry of Materials* 2018, *30* (17), 5853–5861. https://doi.org/10.1021/ACS.CHEMMATER.8B01116/SUPPL_FILE/CM8B01116_SI_001.PDF.

(11) Tojo, T.; Tawa, H.; Oshida, N.; Inada, R.; Sakurai, Y. Electrochemical Characterization of a Layered α-MoO3 as a New Cathode Material for Calcium Ion Batteries. *Journal of Electroanalytical Chemistry* 2018, *825*, 51–56. https://doi.org/10.1016/J.JELECHEM.2018.08.008.

(12) Liu, M.; Rong, Z.; Malik, R.; Canepa, P.; Jain, A.; Ceder, G.; Persson, K. A. Spinel Compounds as Multivalent Battery Cathodes: A Systematic Evaluation Based on Ab Initio Calculations. *Energy Environ Sci* 2015, *8* (3), 964–974. https://doi.org/10.1039/C4EE03389B.

(13) Arroyo-De Dompablo, M. E.; Krich, C.; Nava-Avendaño, J.; Palacín, M. R.; Bardé, F. In Quest of Cathode Materials for Ca Ion Batteries: The CaMO3 Perovskites (M = Mo, Cr, Mn, Fe, Co, and Ni). *Physical Chemistry Chemical Physics* 2016, *18* (29), 19966–19972. https://doi.org/10.1039/C6CP03381D.

(14) Tchitchekova, D. S.; Ponrouch, A.; Verrelli, R.; Broux, T.; Frontera, C.; Sorrentino, A.; Bardé, F.; Biskup, N.; Arroyo-De Dompablo, M. E.; Palacín, M. R. Electrochemical Intercalation of Calcium and Magnesium in TiS2: Fundamental Studies Related to Multivalent Battery Applications. *Chemistry of Materials* 2018, *30* (3), 847–856. https://doi.org/10.1021/ACS.CHEMMATER.7B04406/SUPPL_FILE/CM7B04406_SI_002.AVI.

(15) Wang, J.; Tan, S.; Xiong, F.; Yu, R.; Wu, P.; Cui, L.; An, Q. VOPO4·2H2O as a New Cathode Material for Rechargeable Ca-Ion Batteries. *Chemical Communications* 2020, *56* (26), 3805–3808. https://doi.org/10.1039/D0CC00772B.

(16) Lipson, A. L.; Kim, S.; Pan, B.; Liao, C.; Fister, T. T.; Ingram, B. J. Calcium Intercalation into Layered Fluorinated Sodium Iron Phosphate. *J Power Sources* 2017, *369*, 133–137. https://doi.org/10.1016/J.JPOWSOUR.2017.09.081.

(17) Verrelli, R.; Black, A. P.; Frontera, C.; Oro-Sole, J.; Arroyo-De Dompablo, M. E.; Fuertes, A.; Rosa Palacín, M. On the Study of Ca and Mg Deintercalation from Ternary Tantalum Nitrides. *ACS Omega* 2019, *4* (5), 8943–8952. https://doi.org/10.1021/ACSOMEGA.9B00770/ASSET/IMAGES/MEDIUM/AO-2019-00770S_M002.GIF.

(18) Canepa, P.; Sai Gautam, G.; Hannah, D. C.; Malik, R.; Liu, M.; Gallagher, K. G.; Persson, K. A.; Ceder, G. Odyssey of Multivalent Cathode Materials: Open Questions and Future Challenges. *Chem Rev* 2017, *117* (5), 4287–4341. https://doi.org/10.1021/ACS.CHEMREV.6B00614/ASSET/IMAGES/LARGE/CR-2016-00614E_0045.JPEG.

(19) Wu, S.; Zhang, F.; Tang, Y. A Novel Calcium-Ion Battery Based on Dual-Carbon Configuration with High Working Voltage and Long Cycling Life. *Advanced Science* 2018, *5* (8). https://doi.org/10.1002/ADVS.201701082.

(20) Yu, X.; Boyer, M. J.; Hwang, G. S.; Manthiram, A. Toward a Reversible Calcium-Sulfur Battery with a Lithium-Ion Mediation Approach. *Adv Energy Mater* 2019, *9* (14), 1803794. https://doi.org/10.1002/AENM.201803794.

(21) Verrelli, R.; Black, A. P.; Pattanathummasid, C.; Tchitchekova, D. S.; Ponrouch, A.; Oró-Solé, J.; Frontera, C.; Bardé, F.; Rozier, P.; Palacín, M. R. On the Strange Case of Divalent Ions Intercalation in V2O5. *J Power Sources* 2018, *407*, 162–172. https://doi.org/10.1016/J.JPOWSOUR.2018.08.024.

(22) Bervas, M.; Klein, L. C.; Amatucci, G. G. Vanadium Oxide-Propylene Carbonate Composite as a Host for the Intercalation of Polyvalent Cations. *Solid State Ion* 2005, *176* (37–38), 2735–2747. https://doi.org/10.1016/J.SSI.2005.09.009.

(23) Chae, M. S.; Heo, J. W.; Hyoung, J.; Hong, S. T. Double-Sheet Vanadium Oxide as a Cathode Material for Calcium-Ion Batteries. *ChemNanoMat* 2020, *6* (7), 1049–1053. https://doi.org/10.1002/CNMA.202000011.

(24) Liu, L.; Wu, Y.-C.; Rozier, P.; Taberna, P.-L.; Simon, P. Ultrafast Synthesis of Calcium Vanadate for Superior Aqueous Calcium-Ion Battery. *Research* 2019, *2019*. https://doi.org/10.34133/2019/6585686.

(25) Dompablo, M. E. A. De; Krich, C.; Nava-Avendaño, J.; Biškup, N.; Palacín, M. R.; Bardé, F. A Joint Computational and Experimental Evaluation of CaMn2O4 Polymorphs as Cathode Materials

for Ca Ion Batteries. *Chemistry of Materials* 2016, *28* (19), 6886–6893. https://doi.org/10.1021/ACS.CHEMMATER.6B02146/SUPPL_FILE/CM6B02146_SI_001.PDF.

(26) Boulahya, K.; Parras, M.; González-Calbet, J. M. New Commensurate Phases in the Family (A3Co2O6)(α)(A3Co3O9)(β) (A = Ca, Sr, Ba). *Chemistry of Materials* 2000, *12* (1), 25–32. https://doi.org/10.1021/CM991028G.

(27) Torres, A.; Bardé, F.; Arroyo-de Dompablo, M. E. Evaluation of Cobalt Oxides for Calcium Battery Cathode Applications. *Solid State Ion* 2019, *340*. https://doi.org/10.1016/J.SSI.2019.115004.

(28) Cabello, M.; Nacimiento, F.; González, J. R.; Ortiz, G.; Alcántara, R.; Lavela, P.; Pérez-Vicente, C.; Tirado, J. L. Advancing towards a Veritable Calcium-Ion Battery: CaCo2O4 Positive Electrode Material. *Electrochem commun* 2016, *67*, 59–64. https://doi.org/10.1016/J.ELECOM.2016.03.016.

(29) Tchitchekova, D. S.; Frontera, C.; Ponrouch, A.; Krich, C.; Bardé, F.; Palacín, M. R. Electrochemical Calcium Extraction from 1D-Ca3Co2O6. *Dalton Transactions* 2018, *47* (33), 11298–11302. https://doi.org/10.1039/C8DT01754A.

(30) Smeu, M.; Hossain, M. S.; Wang, Z.; Timoshevskii, V.; Bevan, K. H.; Zaghib, K. Theoretical Investigation of Chevrel Phase Materials for Cathodes Accommodating Ca2+ Ions. *J Power Sources* 2016, *306*, 431–436. https://doi.org/10.1016/J.JPOWSOUR.2015.12.009.

(31) Mei, L.; Xu, J.; Wei, Z.; Liu, H.; Li, Y.; Ma, J.; Dou, S. Chevrel Phase Mo6T8 (T = S, Se) as Electrodes for Advanced Energy Storage. *Small* 2017, *13* (34). https://doi.org/10.1002/SMLL.201701441.

(32) Tchitchekova, D. S.; Ponrouch, A.; Verrelli, R.; Broux, T.; Frontera, C.; Sorrentino, A.; Bardé, F.; Biskup, N.; Arroyo-De Dompablo, M. E.; Palacín, M. R. Electrochemical Intercalation of Calcium and Magnesium in TiS2: Fundamental Studies Related to Multivalent Battery Applications. *Chemistry of Materials* 2018, *30* (3), 847–856. https://doi.org/10.1021/ACS.CHEMMATER.7B04406.

(33) Wang, Y.-S.; Yeh, H.-W.; Tang, Y.-H.; -, al; Asselin, G. M.; Paden, O.; Qiu, W. Steps Towards the Use of TiS2 Electrodes in Ca Batteries. *J Electrochem Soc* 2020, *167* (7), 070532. https://doi.org/10.1149/1945-7111/AB7A82.

(34) Yang, Y.; Zhou, J.; Wang, L.; Jiao, Z.; Xiao, M.; Huang, Q. an; Liu, M.; Shao, Q.; Sun, X.; Zhang, J. Prussian Blue and Its Analogues as Cathode Materials for Na-, K-, Mg-, Ca-, Zn- and Al-Ion Batteries. *Nano Energy* 2022, *99*, 107424. https://doi.org/10.1016/J.NANOEN.2022.107424.

(35) Robin, M. B. The Color and Electronic Configurations of Prussian Blue. *Inorg Chem* 1962, *1* (2), 337–342. https://doi.org/10.1021/IC50002A028/ASSET/IC50002A028.FP.PNG_V03.

(36) Le Pham, P. N.; Wernert, R.; Cahu, M.; Sougrati, M. T.; Aquilanti, G.; Johansson, P.; Monconduit, L.; Stievano, L. Prussian Blue Analogues for Potassium-Ion Batteries: Insights into the Electrochemical Mechanisms. *J Mater Chem A Mater* 2023, *11* (6), 3091–3104. https://doi.org/10.1039/D2TA08439B.

(37) Ma, L.; Cui, H.; Chen, S.; Li, X.; Dong, B.; Zhi, C. Accommodating Diverse Ions in Prussian Blue Analogs Frameworks for Rechargeable Batteries: The Electrochemical Redox Reactions. *Nano Energy* 2021, *81*, 105632. https://doi.org/10.1016/J.NANOEN.2020.105632.

(38) Le Pham, P. N.; Wernert, R.; Cahu, M.; Sougrati, M. T.; Aquilanti, G.; Johansson, P.; Monconduit, L.; Stievano, L. Prussian Blue Analogues for Potassium-Ion Batteries: Insights into the

Electrochemical Mechanisms. *J Mater Chem A Mater* 2023, *11* (6), 3091–3104. https://doi.org/10.1039/D2TA08439B.

(39) Padigi, P.; Goncher, G.; Evans, D.; Solanki, R. Potassium Barium Hexacyanoferrate – A Potential Cathode Material for Rechargeable Calcium Ion Batteries. *J Power Sources* 2015, *273*, 460–464. https://doi.org/10.1016/J.JPOWSOUR.2014.09.101.

(40) Tojo, T.; Sugiura, Y.; Inada, R.; Sakurai, Y. Reversible Calcium Ion Batteries Using a Dehydrated Prussian Blue Analogue Cathode. *Electrochim Acta* 2016, *207*, 22–27. https://doi.org/10.1016/J.ELECTACTA.2016.04.159.

(41) Lipson, A. L.; Pan, B.; Lapidus, S. H.; Liao, C.; Vaughey, J. T.; Ingram, B. J. Rechargeable Ca-Ion Batteries: A New Energy Storage System. *Chem. Mater.* 2015, *27* (24), 8442–8447. https://doi.org/10.1021/acs.chemmater.5b04027.

(42) Wu, J.; Song, J.; Dai, K.; Zhuo, Z.; Wray, L. A.; Liu, G.; Shen, Z. X.; Zeng, R.; Lu, Y.; Yang, W. Modification of Transition-Metal Redox by Interstitial Water in Hexacyanometalate Electrodes for Sodium-Ion Batteries. *J Am Chem Soc* 2017, *139* (50), 18358–18364. https://doi.org/10.1021/jacs.7b10460.

(43) Shi, W.; Nie, P.; Shang, X.; Yang, J.; Xie, Z.; Xu, R.; Liu, J. Berlin Green-Based Battery Deionization-Highly Selective Potassium Recovery in Seawater. *Electrochim Acta* 2019, *310*, 104–112. https://doi.org/10.1016/J.ELECTACTA.2019.04.122.

(44) Crumblis, A. L.; Lug, P. S.; Morosoff, N. Alkali Metal Cation Effects in a Prussian Blue Surface-Modified Electrode. *Inorg Chem* 1984, *23* (26), 4701–4708. https://doi.org/10.1021/IC00194A057/ASSET/IC00194A057.FP.PNG_V03.

(45) Itaya, K.; Uchida, I.; Neff, V. D. Electrochemistry of Polynuclear Transition Metal Cyanides: Prussian Blue and Its Analogues. *Acc Chem Res* 1986, *19* (6), 162–168. https://doi.org/10.1021/AR00126A001/ASSET/AR00126A001.FP.PNG_V03.

(46) Liu, X.; Elia, G. A.; Passerini, S. Evaluation of Counter and Reference Electrodes for the Investigation of Ca Battery Materials. *Journal of Power Sources Advances* 2020, *2*, 100008. https://doi.org/10.1016/j.powera.2020.100008.

(47) Ma, L.; Cui, H.; Chen, S.; Li, X.; Dong, B.; Zhi, C. Accommodating Diverse Ions in Prussian Blue Analogs Frameworks for Rechargeable Batteries: The Electrochemical Redox Reactions. *Nano Energy* 2021, *81*, 105632. https://doi.org/10.1016/J.NANOEN.2020.105632.

(48) Du, G.; Pang, H. Recent Advancements in Prussian Blue Analogues: Preparation and Application in Batteries. *Energy Storage Mater* 2021, *36*, 387–408. https://doi.org/10.1016/J.ENSM.2021.01.006.

(49) Tay, I. R.; Xue, J.; Lee, W. S. V. Methods for Characterizing Intercalation in Aqueous Zinc Ion Battery Cathodes: A Review. *Advanced Science* 2023, *10* (26), 2303211. https://doi.org/10.1002/ADVS.202303211.

(50) Liu, X.; Elia, G.; Passerini, S. Evaluation of Counter and Reference Electrodes for the Investigation of Ca Battery Materials. *ECS Meeting Abstracts* 2022, *MA2022-01* (1), 63. https://doi.org/10.1149/MA2022-01163MTGABS.

(51) Marzak, P.; Mizuno, F.; et al. Intercalation of Mg^{2+} into Electrodeposited Prussian Blue Analogues. *Electrochimica Acta* **2019**, *319*, 390–398.

(52) Xing, Z.; et al. Active Cation-Integration High-Entropy Prussian Blue Analogues as Efficient Cathodes for Zn Storage. *Nano Research* **2023**, *16*, 12345–12358.

(53) Meng, Y.; et al. Prussian Blue Analogues for Zinc Hybrid-Ion Batteries. *J. Mater. Chem. A* **2025**, *13*, 1–15.

Chapter V

Novel negative electrodes for electrochemical calcium redox reactions

5.1 Introduction

Although the use of calcium metal as a negative electrode remains a promising avenue, particularly in the light of the recent progress discussed in chapter II, it does not yet meet the requirements for practical applications, largely due to its low coulombic efficiency. An alternative strategy involves the use of materials capable of reacting electrochemically with calcium, thereby forming the basis of CIB systems that do not rely on metallic calcium. While this approach may involve a trade-off in terms of specific capacity, it offers several practical benefits. First, calcium-based compounds are generally less prone to surface passivation than metallic calcium,[1]

Subsequently, Lerner et al.[2] synthesized a graphite intercalation compound (GIC) with the composition $[Ca(EN)_2]C_{26}$ through a chemical reaction between calcium metal and graphite powder in liquid ethylenediamine (EN), carried out under inert conditions at moderate temperatures (25–100 °C). These studies confirmed that chemical calcium intercalation into graphite can occur under specific thermal conditions.

In 2008, Ogumi et al.[3] reported for the first time the electrochemical insertion of Ca^{2+} into graphite using an organic electrolyte. Graphite (either natural or synthetic i.e. Highly Oriented Pyrolytic Graphite, HOPG) served as the working electrode, while a 0.2 M $Ca(CF_3SO_3)_2$ solution in dimethyl sulfoxide (DMSO) was used as the electrolyte. Although the authors suggested simultaneous Ca^{2+} insertion and solvent co-intercalation, the details of this process were not fully elucidated. Later, Takao et al.[4] explored the electrochemical behavior of Ca^{2+} intercalation into graphite using 0.5 M $Ca(ClO_4)_2$ in an EC:EMC (1:2, v/v) electrolyte. The degree of calcium intercalation ranged from 14.5 to 42.3 µmol, corresponding to chemical formulas between $Ca_{0.0318}C_6$ and $Ca_{0.0444}C_6$. However, evidence for Ca^{2+} de-intercalation from graphite remains limited.

More recently, substantial progress has been made. It has been shown that graphite functions as a viable Ca^{2+} host anode in the presence of $Ca(TFSI)_2$ dissolved in tetraglyme (G4).[5] Under these conditions, the graphite anode delivered reversible capacities of 62 mAh g^{-1} at 0.05 A g^{-1} and 47 mAh g^{-1} at 1.0 A g^{-1}. Both experimental and theoretical analyses confirmed the co-intercalation of Ca^{2+} solvated by a single G4 molecule, forming the ternary compound, Ca-G4·C_{72}. Despite the associated dimensional changes, this system demonstrated unprecedented electrochemical performance for Ca-ion storage.

Further advances were achieved by Kang et al.[6] , who demonstrated reversible Ca^{2+} intercalation into graphite using a dimethylacetamide (DMAc)-based electrolyte. The system employed natural graphite as the working electrode and Ca metal as the counter electrode. Galvanostatic cycling, between 0.2 and 1.5 V showed a stable capacity at 50 mA g^{-1}, with multiple voltage plateaus possibly representing different staging intermediates. The graphite anode delivered a capacity of 85 mAh g^{-1} over 200 cycles and retained 75% of its specific capacity (67 mAh g^{-1}) even at high rates (2000 mA g^{-1}). Cyclic Voltammetry (CV) at scan rates from 0.025 to 1 mV s^{-1} revealed four distinct de-intercalation processes, consistent with the GC results. DFT calculations and experimental data evidence jointly indicate that the intercalated phase corresponds to a ternary graphite intercalation structure of nominal composition $[Ca\text{-}(DMAc)_4]C_{50}$, rather than an isolated molecular compound. These findings provide critical insights into the design of CIBs using commercially available graphite. Nevertheless, the large size of solvated Ca^{2+} could restrict capacity and requires further optimizations.[7]

Other intercalation anode such us spinel-structured lithium titanate ($Li_4Ti_5O_{12}$, LTO) is recognized as one of the most promising anode materials for lithium-ion batteries due to its favourable electrochemical characteristics.[8] Building on its performance in Li-based systems, Jeong et al.[9] explored its applicability in CIBs. Their investigations revealed that LTO-based CIBs delivered discharge capacities around 85 mAh g^{-1} when employing a 0.1 M $Ca(SO_3CF_3)_2$ electrolyte in a PC:DMC (1:10 v/v) mixture, and approximately 145 mAh g^{-1} when using 0.1 M $Ca(TFSI)_2$ in THF. These results underscore the critical influence of electrolyte composition on the electrochemical response of LTO in CIBs. Nevertheless, there is still a lack of direct evidence confirming whether the recorded capacities result from reversible Ca^{2+} intercalation into the bulk LTO. Further investigations are necessary to clarify the mechanisms and the effect of electrolyte composition.[7]

Transition metal oxides (TMOs), such as two-dimensional (2D) VO_2 and MoO_2 have also been proposed as viable anode materials for CIBs. [10,11] Theoretical modeling has shown that VO_2 offers excellent Ca^{2+} mobility, with a low diffusion barrier of 0.306 eV and a specific capacity up to 260 mAh g^{-1} when Ca^{2+} ions occupy the centre of hexagonal V–O coordination environments. Importantly, the metallic properties of the VO_2 layers are preserved upon ion adsorption. Similarly, DFT simulations for MoO_2 have revealed ultrafast Ca^{2+} diffusivity (barrier: 0.22 eV) and a theoretical capacity of 1256 mAh g^{-1} with an average voltage of 0.35 V, associated with the formation of Ca_3MoO_2; however, the reported stoichiometry appears rather unconventional. In particular, the oxygen deficiency implied by Ca_3MoO_2 would require atypical oxidation states of Mo that are not

commonly observed in stable molybdenum oxides. This raises questions regarding the chemical plausibility and thermodynamic stability of such a phase.

Notably, while the reversible incorporation/de-incorporation of Li^+, Na^+, or K^+ into crystalline inorganic hosts such as TiO_2, MoO_2, or graphite has been well established, similar evidence for bare Ca^{2+} intercalation into structurally preserved ordered anode materials remains absent from the current literature.[12–16]

In this context, in the next paragraph, we present our investigation on nanostructured titanium oxide nanotubes as a promising negative electrode capable of reversibly accommodating Ca^{2+} ions.

5.2 Nanostructured titanium oxide nanotubes as negative electrode for CIBs

The reversible electrochemical activity of anatase nanotubes in galvanostatic tests at room temperature is carried out either in a calcium metal half-cell or in a pseudocapacitive hybrid cell using a liquid Ca^{2+} aprotic electrolyte. The experimental evidence of an electrochemical intercalation of Ca^{2+} in the anatase lattice is obtained by *ex situ* Ti and Ca K-edge X-ray absorption spectroscopy (XAS). The structural modifications induced by the incorporation of calcium into the TiO_2 structure was analysed by modelling the extended X-ray absorption fine structure (EXAFS) region of the XAS spectra in close comparison to analogous lithiated and sodiated anatase samples.

5.2.1 Experimental methods

5.2.1.1 Synthesis of the anatase nanotubes

Anatase nanotubes (a-NTs) were synthesized by optimized alkaline hydrothermal route.[17] Bulk Titania (TiO_2 powder, Sigma Aldrich) was dispersed in 10 M NaOH (98%, Sigma Aldrich) solution (Ti:Na = 1:13 w/w) with a series of stirring and sonication steps followed by heating at 150 °C for 2 hours in a Teflon-lined autoclave. The hydrothermal treatment is known to produce sodium-titanate nanosheets that roll-up and form nanotubes in solution.[17] After this process, the product is filtered and washed to remove the excess of NaOH. The product obtained by this stage of the process consists of hydrated Na-titanate nanotubes, $Na_yH_{1-y}Ti_nO_{2n-1}$, which were ion exchanged, using a 0.01 M aqueous solution of hydrochloric acid added dropwise under continuous stirring until pH = 4 was reached to obtain the de-sodiated $H_2Ti_3O_7$. In order to confirm and describe the evolution of morphology and composition of the sodiated NTs upon acidification, four samples at different stages of the ion-exchange were collected and investigated with field-emission scanning electron microscopy (FESEM, see below for technical details) and EDX (energy-dispersive X-rays Bruker probe). The final product was filtered, washed with a minimal amount of water, and dried overnight at 80 °C under vacuum. The sample was annealed at 380 °C for 5 minutes with a heating rate of 0.4 °C/min.

5.2.1.2 Physico-chemical characterization

FESEM coupled with EDX experiments were carried out at the CNIS Center for Nanotechnology and Innovation of Sapienza by employing an Auriga Zeiss electron microscope. Wide-angle XRD patterns were collected by using either a Philips X'PERT or a Bruker Advance D8 diffractometer, both equipped with a Cu Kα source, λ = 1.5418 Å using in all cases an angular scan in the range of 10°-100°with a step size of 0.02°. Micro-Raman spectroscopy experiments were carried out using a Dilor Raman system equipped with an He-Ne (632.7 nm) laser source, a Semrock RazorEdge® ultrasteep long-pass edge filter and a Peltier cooled CCD detector. Transmission electron microscopy (TEM) analysis was carried out using a FEI Tecnai cryo-TEM instrument: samples were prepared by evaporating a drop of an ethanol suspension of anatase NTs onto a holey carbon Cu mesh grid.

5.2.1.3 Cells assembly and electrochemical tests

Electrode composite films were prepared by tape-casting on Cu foil (0.1mm, Sigma Aldrich). The composite slurry was obtained by mixing a-NTs with a conductive carbon additive (Super P, Alfa Aesar) and polyvinylidene fluoride (PVdF, Solef® 5130) as the binder with a mass ratio of 70/20/10, respectively, in ^{18}N-methyl-2-pyrrolidone (NMP, Sigma Alrich). The casted film was dried in air before punching out circular electrodes (diameter 9 mm), which were then further dried *in vacuo* at 90 °C overnight. a-NTs composite electrodes were also prepared on Al foil (18 μm, GoodFellow) following the same procedure to minimize the current collector corrosion in the aprotic electrolyte.[18] Pelletized a-NTs electrodes were manufactured starting from the same composite mixture by using a hydraulic press at room temperature and a Specac 13 mm die set at 5 tons cm^{-2}. Free standing capacitive electrodes were made using activated carbon (AC, YP-50F, Kuraray) and polytetrafluoroethylene dispersion (PTFE 60 wt% in water, Sigma Aldrich), used as received. The mass ratio of AC active material and PTFE binder was 95/5. Calcium metal (ACI Alloys, Inc) electrodes were obtained starting from calcium foils rolled using a calendaring machine (MTI corp.) to an approximate thickness of 100 mm. The surface of the Ca foils was scratched in the glove box to remove the passivating layer and punched into disks (diameter 9 mm). Lithium (Li, 99.9 %, Sigma Aldrich) and sodium (Na, 99.8 % Sigma Aldrich) electrodes were punched (diameter 9 mm) from thin foils and pressed onto a stainless-steel current collector.

Electrolytes for calcium-based cells were formulated and prepared starting from solvents dried under molecular sieves and calcium salts in an Iteco Eng SGS30 Ar-glove box with a moisture content below 1 ppm. Molecular sieves (3 Å, Alfa Aesar) were preliminarily dried at 300 °C for 24 h in a

Muffle Furnace (Nabertherm up to 1100 °C). Tetrahydrofuran (THF, Sigma Aldrich, 99.9 %), 1,2-dimethylglycol ether (DME, Sigma Aldrich, 99.5%) were dried over the pre-dried molecular sieves for one week. Calcium bis(trifluoromethanesulfonyl imide ($Ca(TFSI)_2$, Solvionic, 99.5 %) was dried at 100 °C under vacuum before use, whereas calcium borohydride ($Ca(BH_4)_2$, Sigma Aldrich) was used as received. Calcium-based electrolytes were prepared by dissolving the appropriate amount of $Ca(TFSI)_2$ in DME to obtain a molality of 0.5 mol/kg for the pseudo capacitive cell tests, and by dissolving $Ca(BH_4)_2$ in THF to obtain a molality of 1 mol/kg for the electrochemical tests in Ca metal half-cells. The aprotic electrolyte for lithium cells was a commercial formulation from Merck (*i.e.*, LP30, 1 mol/l solution of lithium hexafluorophosphate ($LiPF_6$) in an ethylene carbonate (EC) - dimethyl carbonate (DMC) 1:1 vol. solvent mixture). The aprotic electrolyte for the sodium cell was prepared by dissolving 1 mol of $NaClO_4$ (Alfa Aesar) per liter of EC-propylene carbonate (PC) 1:1 vol solvent mixture (Sigma Aldrich).

In all cases, Whatman glass fiber disks (thickness 1.55 mm) soaked with 0.1 ml of electrolyte were used as the separators. The assembly of cells (a-NTs / electrolyte / CE) and all the manipulations were carried out inside Ar-filled glove boxes (O_2 and $H_2O < 1$ ppm). The testing cells for the electrochemical experiments were made by assembling a-NTs / electrolyte / Ca, Li, or Na using ECC-STD cells, and a-NTs / electrolyte / AC, Ca as reference electrodes using ECC-Ref commercial cells from EL-Cell. Electrochemical tests were carried out using an MTI battery testing system or an IVIUM Vertex electrochemical testing station. Current rates were calculated with respect to the mass of the active material in the electrodes.

5.2.1.4 XAS measurements and data analysis

XAS experiments were carried out at the XAFS beamline of ELETTRA Synchrotron[19] on pristine materials and *post mortem* electrodes. After cycling, the electrochemical cells were disassembled in an Ar-filled glove box to recover the *post mortem* electrodes, which were carefully washed three times in THF and dried *in vacuo* at room temperature for 30 minutes. For the sake of comparison, similar experiments were carried out on cells *vs.* calcium, sodium and lithium to follow the electrochemical incorporation of the corresponding cations in the electrodes. Pristine samples were prepared by carefully grinding the powder in an agate mortar inside an Ar-filled glove box with boron nitride as dispersing agent to produce pellets with the optimal thickness and mass loading of the atomic species under study, *i.e.*, Ca and Ti. All samples were sealed between two Kapton windows to avoid direct contact with ambient air and loaded into a multi-sample holder operating in high vacuum conditions. Ti K-edge and, when relevant, Ca K-edge XAS measurements were carried out in transmission geometry with a Si(111) double crystal monochromator, while the storage ring was operating at 2

GeV with a beam current of 200 mA. All spectra were collected with the same experimental set-up, allowing for direct comparison among the peak intensities. Energy calibration was carried out using as reference standards $CaCO_3$ for the Ca K-edge and a titanium metal foil for the Ti K-edge. No relevant drifts or shifts of the photon energy were observed during the experiments. The Ca K-edge XAS spectrum of a 0.1 M $CaCl_2$ aqueous solution (slightly acidic) was measured as a reference. The experimental setup for this sample can be found in Ref. [20]. At least two spectra were recorded and averaged for each sample. For the comparison of the X-ray absorption near edge structure (XANES) data, a linear background was fit to the pre-edge region and then subtracted from the entire spectrum, while the jump was normalized with respect to unity with the post-edge asymptotic value chosen where the XAS oscillations are small enough to be negligible. The number of Ca^{2+} ions trapped into the a-NT anode per formula unit of TiO_2 was derived by the corresponding jump of the spectra collected at the Ca and Ti K-edge on *post mortem* samples.

The EXAFS portion of the Ca K-edge XAS spectrum collected on the Ca^{2+}-intercalated a-NTs was analysed with the GNXAS code.[21,22] Amplitudes and phase shifts were calculated from clusters with fixed geometry within the muffin-tin (MT) approximation with MT radii of 0.90 Å for oxygen and 1.35 Å for calcium and titanium, as previously reported.[20] Advanced models for the exchange–correlation self-energy in the framework of the Hedin–Lundqvist scheme were used to take into account the photoelectron inelastic losses in the final state.[23] In the GNXAS approach, theoretical signals associated with *n*-body distribution functions are calculated following the multiple-scattering (MS) theory and summed to reconstruct the total theoretical contribution. A theoretical Ca-O single scattering (SS) signal was calculated to account for the first shell oxygen atoms, while the Ca-Ti contribution accounting for the second shell Ti atoms did not substantially improve the fit quality (*vide infra*). The two-body distributions are modelled as Γ-like functions depending on four structural parameters, namely the coordination number N, the average distance R, the Debye-Waller factor σ^2, and the asymmetry index β, which was optimized during the fitting procedure to obtain the best agreement with the experimental data. Note that in disordered systems, where large asymmetries in the pair distributions are observed, the average distance is no longer the maximum one, while these values coincide for symmetric Gaussian distributions ($\beta = 0$).[20,24,25] Least-squares minimizations were carried out directly on the raw data, without preliminary background subtraction or Fourier filtering. Additional non-structural parameters such as the edge ionization energy E_0, the amplitude reduction factor S_0^2, and the energy position and amplitude of the KM_1 double-electron excitation channel, modeled with an arctangent function, were also optimized during the fitting procedure.

5.3 Results

5.3.1 Preliminary anatase nanotubes characterization

Anatase nanotubes were synthesized following a well-established hydrothermal route forming as intermediate product sodiated tri-titania nanotubes, *i.e.*, $Na_2Ti_3O_7$, which are converted into $H_2Ti_3O_7$ by Na^+/H^+ ion-exchange with HCl.[17] In order to monitor the evolution/preservation of the morphology of the NTs during ion-exchange, four samples at different stages were collected at various pH and investigated by FESEM-EDX as shown in Figure 1. As expected, the titration by 0.01 M aqueous HCl is able to ion-exchange the Na^+ ions from the $Na_2Ti_3O_7$ lattice with H^+. At the end of the acidic washing, the residual Na/Ti atomic ratio is approximately 0.03, in line with the almost complete removal of Na^+ ions from the structure. This compositional change occurs without major alterations in the nano-morphology of the sample that preserves the nanotubular shape in the primary particles and morphological homogeneity across the sample (cf. Figure 5.1).

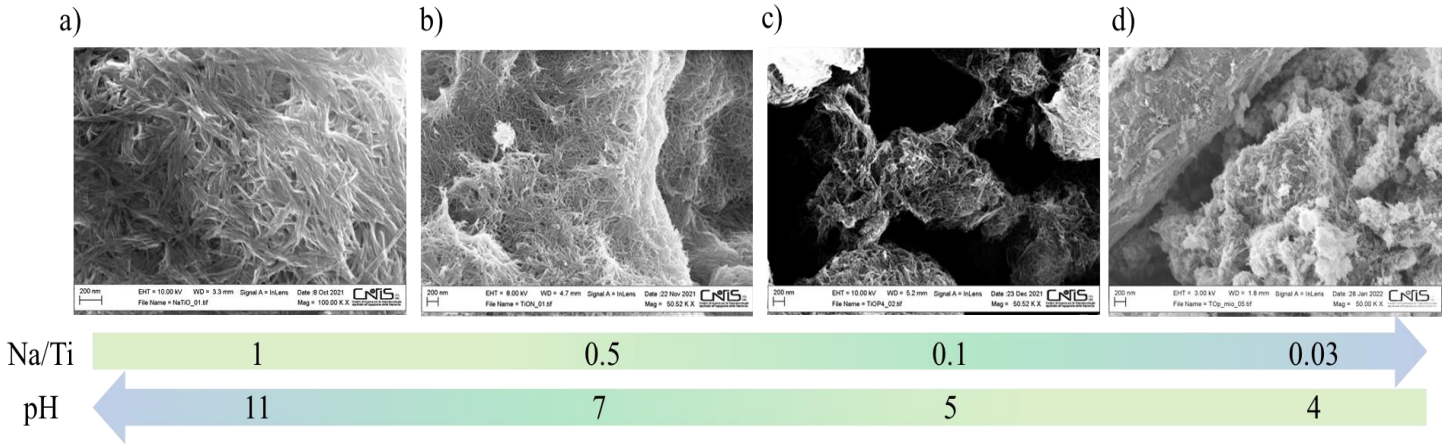

Figure 5.1 Morphological evolution of the hydrated NTs at various stages of the Na^+/H^+ ion-exchange process. The $Na_2Ti_3O_7$ phase obtained by hydrothermal reaction has been titrated with 0.01m aqueous HCl and the intermediate samples have been collected by filtration at different pH values and were dried at 80 °C overnight in air. The Na/Ti atomic ratio has been derived from EDX data.

After the ion-exchange procedure, the $H_2Ti_3O_7$ precursor was annealed in air at 380 °C to remove the structural water and promote the nano-crystallization of the Anatase NTs. [17] This high-temperature annealing preserves the nanotubular morphology of the samples as shown by the TEM micrograph in Figure 5.2. The de-hydrated nanotubes show a mean outer diameter of approximately 10 nm, an inner diameter of about 5-7 nm and a length ranging between 100 and 300 nm, in line with the literature.[17]

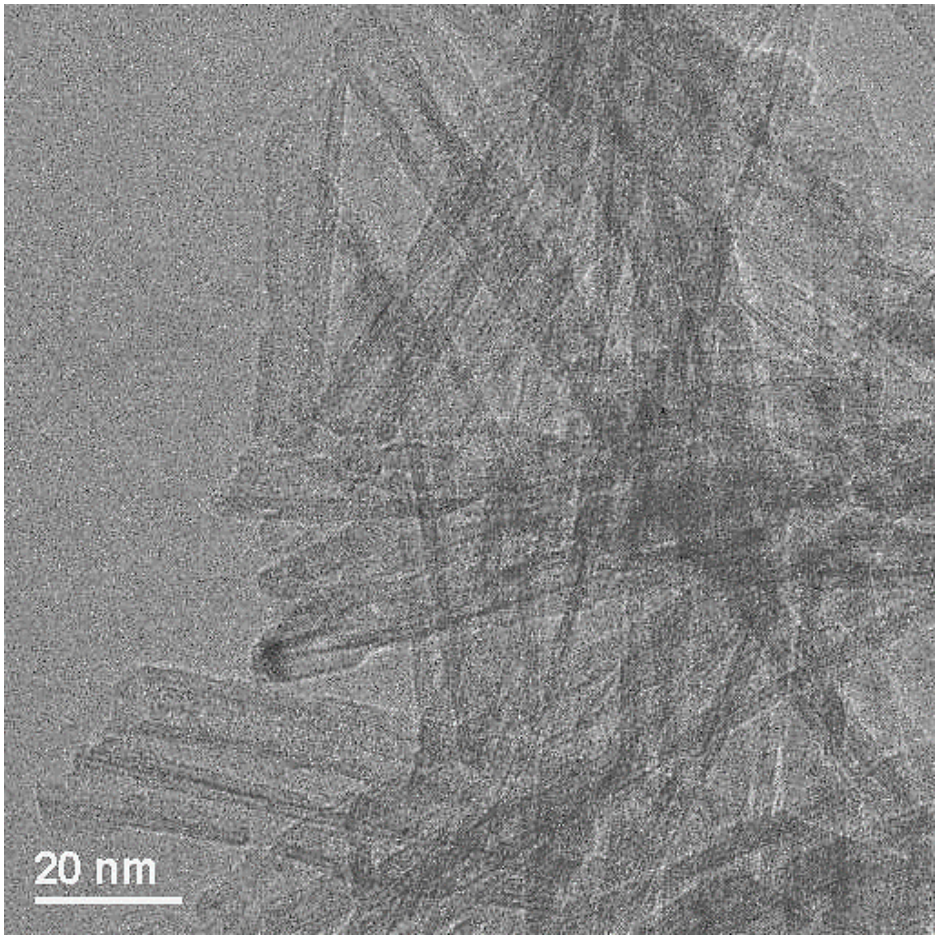

Figure 5.2 TEM micrograph of the a-NTs after annealing at 380 °C

The nature of the NTs after annealing at 380 °C was checked by Raman spectroscopy and XRD (Figures 5.3a-b), which confirm the structural rearrangement to well-crystallized anatase, indexed within the expected tetragonal systems (space group I41/amd).[17] All Raman bands of the annealed sample can be assigned to anatase phase:[26–32] the three Raman bands at 639, 197, and 149 cm^{-1} are assigned to the E_g modes,[26,33] while those at 280 and 698 cm^{-1} suggest the formation of a tubular structure[32] and the strong peak at 149 cm^{-1} is the fingerprint of the active mode of Ti-O-Ti bonds of anatase[26,32] as well as the 449 cm^{-1} band.[34] The band at 515 cm^{-1} corresponds respectively to the A_{1g} and B_{1g} modes of Ti-O bonds[26] whereas the 399 cm^{-1} band can be assigned to the B_{1g} modes[26].

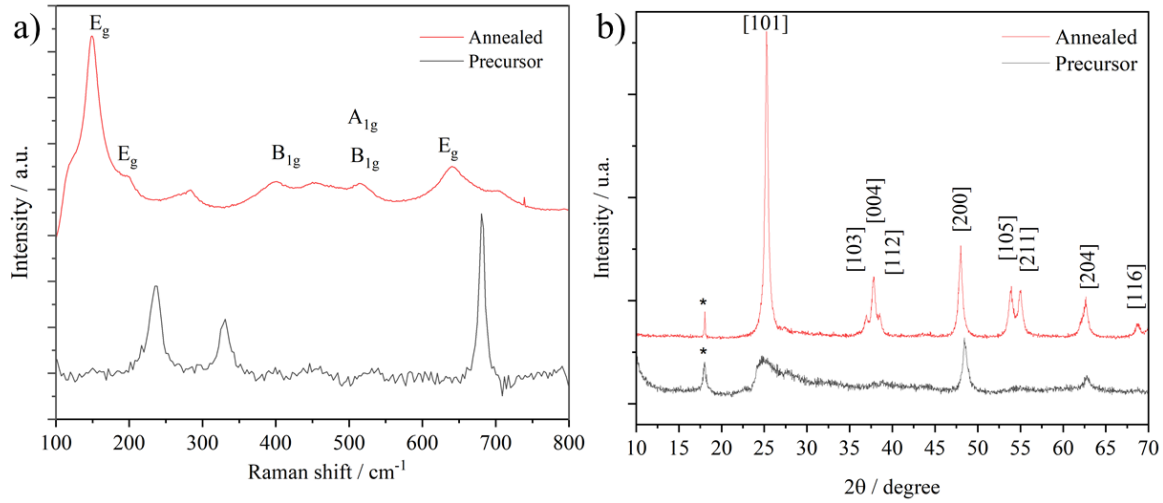

Figure 5.3(a) Raman spectra and (b) XRD patterns of the $H_2Ti_3O_7$ precursor and the TiO2 NTs after annealing. The vibrational modes and the Bragg lines are indexed by the TiO_2 anatase lattice (space group I41/amd). *These peaks are due to the sample holder.

The structural evolution into a nanosized anatase lattice in the post-annealing NTs is also confirmed by XRD (Figure 5.3b). The evolution of the XRD pattern from the precursor to the annealed sample follows the expected trend[35] and discloses an expected increase in crystallinity. While the precursor shows the typical feature of a poorly crystalline hydrated titania,[17] the XRD pattern of the annealed samples reveals the presence of characteristics peaks at 2θ = 25.6, 36.9, 37.8, 38.5, 48.0, 53.9, 55.0, 62.0 and 68.0° corresponding to the expected reflections of the (101), (103), (004) (112) (200) 105), (211) (204) and (116) lattice planes of anatase, respectively.[27,36–38]

5.3.2 Electrochemical Performance

The electrochemical activity of the anatase NTs in CIBs was tested using two remarkably different cell configurations:

C1. (+) Anatase NTs-based composite electrode / $Ca(BH_4)_2$ 1mol kg^{-1} THF / Calcium metal (-)

C2. (+) Anatase NTs-based composite electrode / $Ca(TFSI)_2$ 0.5mol kg^{-1} DME / Activated carbon capacitive composite electrode (-) with a Ca metal reference electrode

These configurations have advantages and disadvantages. (C1) is a typical half-cell configuration whereas (C2) is a hybrid faradic-capacitive cell configuration. In the C1 configuration, the electrolyte consisted of a 1 mol kg^{-1} solution of $Ca(BH_4)_2$ dissolved in THF. This electrolyte enables a partially reversible plating and stripping of Ca^{2+} ions onto/from a calcium metal foil at room temperature with low polarization.[39,40] However, it has a very narrow electrochemical stability window [40,41] restricting the electrochemical tests *vs.* Ca metal in the potential window between 0.01 and 1.8 V vs. Ca^{2+}/Ca. Unfortunately, up to now, a satisfactory aprotic electrolyte capable of delivering a fully reversible

Ca^{2+} ion deposition/stripping from the calcium metal surface is still an elusive task,[42] since strongly insulating passivation products easily precipitate at the Ca/electrolyte interphase thus easily preventing any electrochemical reaction[43] The performance recorded for Anatase NTs composite electrodes in a (C1) cell configuration is shown in Figure 5.4a.

In the C1 half-cell configuration, discharge capacities ranging between 110-220 $mAhg^{-1}$ are observed for the anatase NTs electrodes whereas much smaller values of 60-80 $mAhg^{-1}$ are recorded upon charge. These data suggest the possible electrochemical reversible intercalation/deintercalation of about 0.09-0.12 eq of Ca^{2+} in the TiO_2 lattice. On the other hand, our data highlight a rather poor coulombic efficiency that even in the best case never exceeds 54%, suggesting the occurrence of remarkable irreversible and/or parasitic phenomena.

The average cell voltage in the (C1) half cells is apparently 0.92-0.93 V vs. Ca^{2+}/Ca. This value is below the redox potential of the Ti^{4+}/Ti^{3+} redox couple of the corresponding Li^+ (de)intercalation in the anatase lattice.[17] By considering that (C1) is a two-electrode configuration, the observed average working potential can be strongly biased (*i.e.*, underestimated) by the possible occurrence of uncontrolled overpotentials at the negative counter-electrodes where the kinetically hindered electrochemical Ca-plating/stripping occurs.

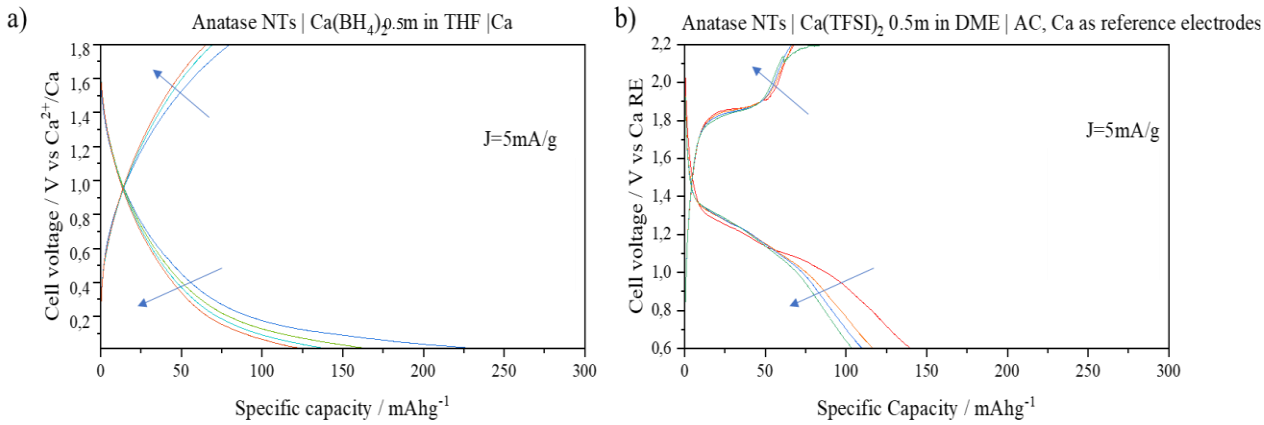

Figure 5.4 Performance of the a- NTs electrodes by using the (C1) or (C2) cell configurations. Current rate 5 mAg^{-1}; shown cycles are 2-5 of the whole galvanostatic test and are obtained after 1 activation cycle.

To adequately estimate the working electrode potential of anatase electrodes, electrochemical tests were also carried out in the C2 configuration (also implying the use of a calcium metal reference electrode). The results of these tests are shown in Figure 5.4b.

In contrast to C1 configuration, a pseudo-plateau below 1.4 V in the discharge curve and above 1.8 V upon charge is observed. The reversible specific capacities measured in the (C2) cells are, nevertheless, in remarkable agreement with those of the (C1) one, ranging from 60 to 75 $mAhg^{-1}$ (fairly below the theoretical capacity of 255 $mAhg^{-1}$ based on the Ti^{4+}/Ti^{3+} redox couple) with a coulombic efficiency below 59%.

The most remarkable difference between the experimental results obtained for the a-NTs electrodes in (C1) and (C2) cell configurations is the average working potential. In fact, in the case of the hybrid configuration with the reference electrode, estimate the mean working potential for the Ti^{4+}/Ti^{3+} redox couple in the anatase lattice while intercalating Ca^{2+} ions can be estimated at approximately 1.6 V *vs.* Ca^{2+}/Ca, a remarkably larger value than that obtained from the two-electrode (C1) configuration. As already mentioned, however, the working potential measured in the (C1) configuration likely underestimates the actual value due to the overpotentials of the redox reaction at the calcium metal counter-electrode. Furthermore, a E° value of 1.6 V *vs.* Ca^{2+}/Ca for calcium intercalation in anatase NTs nicely matches the working potential of the electrochemical intercalation of Li^+ ions in the same bulk phase.[17]

Overall, despite the technical complexity of the electrochemical tests on the a-NTs electrodes, our results suggest that the anatase lattice can reversibly accommodate approximately 0.1 eq. Ca^{2+} ions in its lattice at a working potential of approximately 1.6 V *vs.* Ca^{2+}/Ca.

5.3.3 Post mortem analysis by ex situ XANES

The possible intercalation of Ca^{2+} into the anatase lattice was studied by Ca and Ti K-edge XAS on *post mortem* electrodes collected from calcium-metal half-cells in the (C1) configuration submitted to a controlled discharge process. Among the numerous analytical methods employed to detect variations in local structure and oxidation state, in fact, XAS stands out as an ideal technique to study disordered or poorly crystalline systems.[24,25] The versatility of XAS in simultaneously recording information on different elements was therefore exploited to study the local structure of both Ca and Ti centres, thus disclosing data from both perspectives. To carry out such dual-edge XAS experiments, self-supported pelletized electrodes are mandatory, in consideration of the rather different concentrations of Ca and Ti. The performance of a-NT pelletized electrodes in metallic half-cells is shown in Figures 5.5a-b-c for Na, Li, and Ca-metal half-cells, respectively. Note that the cathodic voltage cutoff for a reversible incorporation of lithium ions in any TiO_2 polymorph is 1 V *vs.* Li^+/Li: at lower values, lithiated TiO_2 is irreversibly converted into other phases.[44] Owing to this, and

differently from the cases of Na^+ and Ca^{2+} intercalation, the electrochemical reduction of a-NTs *vs.* lithium was limited at potentials above 1 V *vs.* Li^+/Li.

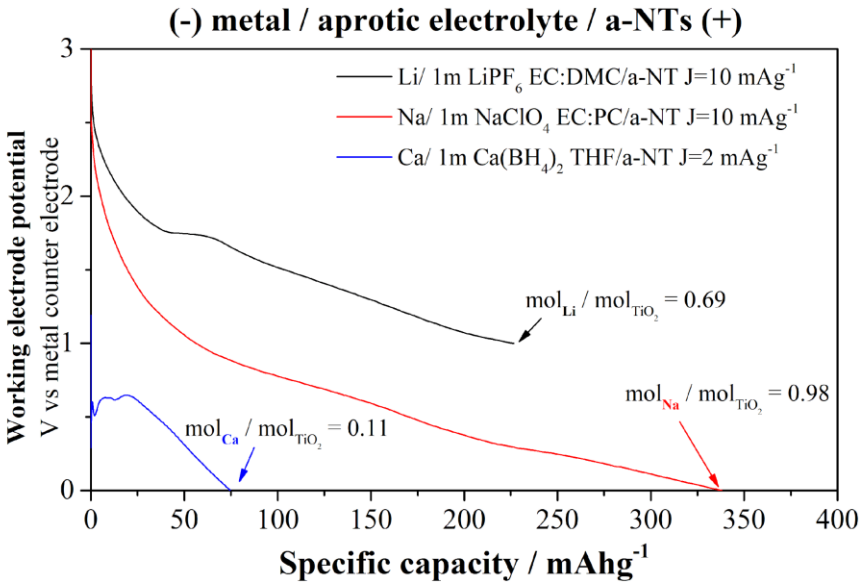

Figure 5.5 Performance of the a-NT pelletized electrodes in Li, Na, and Ca metal half-cell

As expected, the increase in mass loading of the electrodes while shifting from casted films (AM = 1 mg cm^{-2}) to pellets (AM = 20 mg cm^{-2}), slightly decreases the performance for both lithium[17] and sodium[45] intercalation with respect to the literature, as well as calcium in comparison to the data shown in Figure 5.4. Despite this, the reduction proceeded for all samples to a reasonable extent, confirming the reliability of the experimental approach. Overall, a nominal incorporation of 0.69, 0.98, and 0.11 eq. of Li^+, Na^+, and Ca^{2+} per TiO_2 formula unit was obtained, respectively.

Figure 6a shows the Ti K-edge normalized XANES spectra collected on pristine a-NTs and after full electrochemical intercalation of the Li^+, Na^+, and Ca^{2+} ions. All the XANES spectra show the typical profile of anatase with four distinct features in the pre-edge region, labeled A1, A2, A3, and B (inset of Figure 6a), an edge shoulder identified as C, plus two edge peaks labeled as D and E.[46–48] While the latter features derive from the allowed $1s \rightarrow 4p$ main dipole electronic transition, the less intense pre-edge features originate from the forbidden $1s \rightarrow 3d$ transitions made possible by the *p-d* orbital mixing induced by the lowering of the local symmetry of the TiO_6 octahedra.[49,50] In the case of TiO_2, these transitions are caused by the mixture of dipole and quadrupole excitations connecting the Ti *1s* orbital with *3d-4p-4s* hybridized states involving not only the absorbing centre but also the second shell Ti atoms, plus hybridization with the *2p* orbitals of the neighboring oxygen ligands. The assignment of the pre-edge transitions has been the center of a long-standing (and still ongoing) debate, in particular concerning the origin of the A2 peak, since this contribution is often more susceptible to modifications upon variation of the Ti local environment.[46–48,50–53] Nevertheless, a

consensus has somehow been reached about the relationship between the A2 contribution and the degree of crystallinity in the TiO_2 lattice.[46,48,50,54,55] This conclusion derives from the empirical observation that the height of the A2 peak is enhanced in the presence of distorted or defective Ti local environments (four- or five- instead of six-fold coordination) as well as for nanostructured materials. The latter finding can be correlated with a higher fraction of undercoordinated Ti centers at the surface of the nanoparticles compared to bulk anatase.[48,55] This is the case of the pristine a-NTs studied here, which show an intense A2 transition (inset of Figure 5.6a) accompanied by a shoulder at higher energies representing the A3 contribution. In contrast, as previously reported,[56] the A2 transition is much less intense in the XANES spectrum of bulk anatase, where it only appears as a shoulder on the low-energy side of the A3 pre-peak. On the other hand, the A2 contribution is even more intense in the XANES spectrum on a TiO_2(B)-based amorphous phase.[56] Furthermore, the amorphous phase shows a broadening of the D and E features in the so-called white-line region, which was previously connected to the increasing amorphization of the TiO_2 lattice.[48,51,54,57]

The XANES data collected on the a-NTs electrodes after the electrochemical intercalation of Li^+, Na^+, and Ca^{2+} ions (Figure 5.6a) show an intensity enhancement of all the four pre-edge transitions with respect to pristine a-NTs. This result was already observed for lithium[58–61] and sodium[54,55,62,63] uptake by anatase-based materials and connected with loss of crystallinity in the TiO_2 matrix caused by the electrochemical reaction. It is worth noting that, in the Ca^{2+}-intercalated a-NTs, the intensity of the four pre-edge peaks, and in particular of the A2 feature, is higher than in the lithiated sample, but lower than in the sodiated one. This evidence suggests that the Ca^{2+} intercalation introduces a degree of configurational disorder in the TiO_2 lattice that is between those of Li^+ and Na^+ intercalation, despite the much lower nominal loading of Ca^{2+} eq. per unit formula compared to Li^+ and Na^+ (*vide supra*). This trend is confirmed by the smoothing effect in the white-line region, following the same $Li^+ < Ca^{2+} < Na^+$ order. This result is perfectly reasonable if one considers the ionic radii of the three ions and in particular the smaller size of the Li^+ ion,[64] while the sodiation process in TiO_2-based anodes was previously observed to introduce severe structural modifications with a considerable degree of irreversibility.[54,55,62,63] In particular, Na^+ intercalation in anatase electrodes based on nanoparticles, where the ion uptake is expected to be more efficient, induces the loss of the typical anatase spectral profile In TiO_2, the octahedral site for the ions has a radius of 0.52 Å. All three ions have larger ionic radii (0.76, 1, and 1.02 Å for Li^+, Ca^{2+}, and Na^+ respectively) [62] Therefore, since the ionic radii are $Li^+ < Ca^{2+} < Na^+$ this is in line with a significant increasing local distortion for the intercalation of Li^+, Ca^{2+} and Na respectively. The characteristic four pre-edge peaks are indeed a fingerprint of the anatase polymorph due to the local D_{2d} symmetry of the Ti centers, corresponding to a slightly distorted octahedron with two oxide ions in the apical positions with

longer bond distances to Ti compared to the equatorial ones.[50] The splitting of the two A2 and A3 bands therefore mirrors a different degree of hybridization due to this distortion, while rutile generally shows only three pre-edge peaks due to its centro-symmetric D_{2h} Ti site.[46,47] Although the relative intensity of the pre-edge transitions in the Ca^{2+}-intercalated a-NTs is altered with respect to the pristine a-NTs (Figure 5.6a), the four peak fingerprint is preserved, thus suggesting that the anatase shape is substantially maintained in the electrode material even after the Ca^{2+} incorporation.

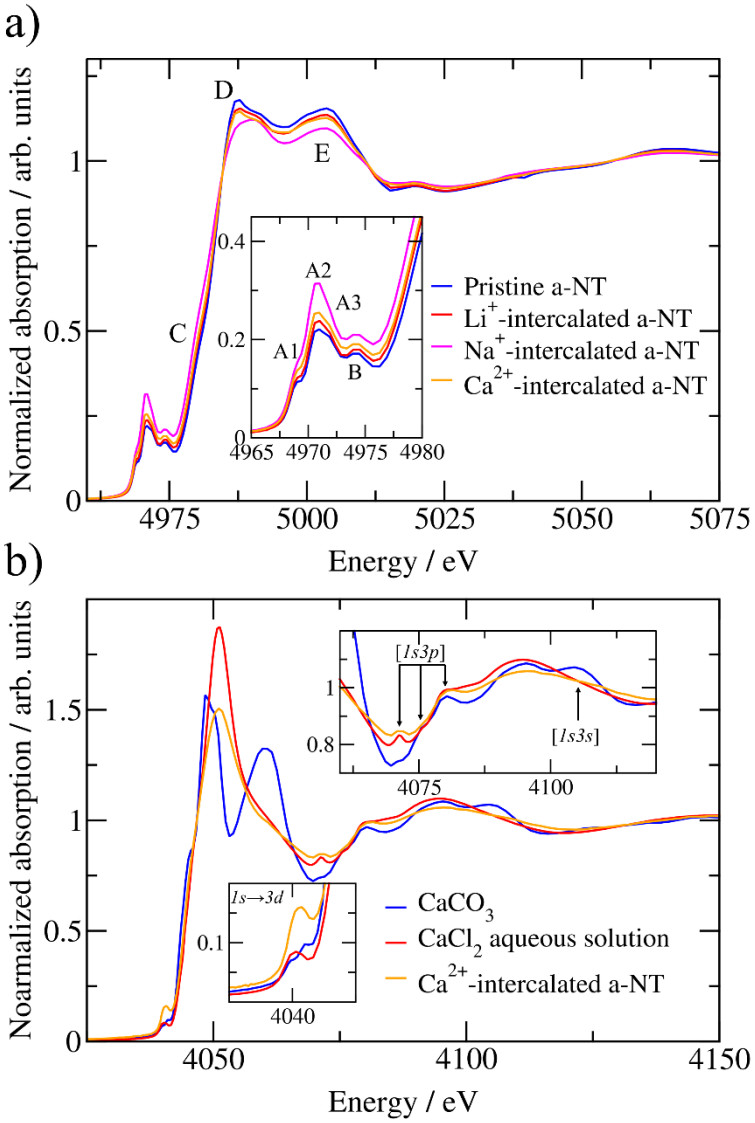

Figure 5.6 Normalized experimental XANES spectra (a) at the Ti K-edge, collected on pristine a-NTs and after full electrochemical intercalation of the Li^+, Na^+, and Ca^{2+} ions; (b) at the Ca K-edge, collected on the $CaCO_3$ standard, on a 0.1 M $CaCl_2$ aqueous solution,[20] and on a-NTs after full electrochemical Ca^{2+} intercalation. In the inset of Figure 6a the pre-edge peak region showing the A1, A2, A3, and B transitions is magnified. The upper inset of Figure 6b shows the energy region with the [1s3p] and [1s3s] double-electron excitation channels, while the lower inset shows the pre-edge peak region corresponding to the 1s→3d transition

In Figure 5.6b, the Ca K-edge XANES spectrum of Ca^{2+}-intercalated a-NTs, is compared with those of the $CaCO_3$ standard and of a 0.1 M $CaCl_2$ aqueous solution. The spectral profile of Ca^{2+}-intercalated a-NTs shows the presence of a small peak and two humps between 25 – 35 eV above the edge, plus an additional hump at higher energy (inset of Figure 5.6b). The origin of these features was previously identified with the [*1s3p*] and [*1s3s*] double-electron excitation channels, respectively, the former one appearing as a large multiplet spread in the experimental data due to mixed configurations.[22] At first glance, the XANES spectrum of the a-NTs is similar to that of the $CaCl_2$ aqueous solution, both being considerably different from that of $CaCO_3$. In aqueous solution the Ca^{2+} ion is coordinated by eight water molecules interacting *via* the oxygen atom to form a relatively disordered hydration complex.[20,65] The higher similarity with a disordered-like liquid system as compared to the $CaCO_3$ standard suggests the presence of a quite disordered environment around the Ca^{2+} ions intercalated in the TiO_2 lattice. This observation is also supported by the pre-edge peak corresponding to the $1s \rightarrow 3d$ transition (inset of Figure 5.6b). As already pointed out for the Ti K-edge spectra, this transition is forbidden but relaxation of the selection rule is made possible by the broken inversion symmetry introduced by the configurational disorder. The presence of a highly disordered coordination around the Ca^{2+} ions intercalated in the a-NTs is reinforced by the higher intensity of this transition compared to both the $CaCl_2$ aqueous solution and $CaCO_3$.

Finally, the amount of Ca^{2+} trapped in the a-NTs can be estimated from the ratio of the edge jumps of the Ca and Ti K-edge XANES spectra. This gives a Ca/Ti ratio of 0.13, in very good agreement with the value of 0.11 eq. per TiO_2 formula unit obtained from the electrochemical signature.

5.3.4 EXAFS data analysis

EXAFS data analysis was carried out to obtain a quantitative determination of the local structure around the Ca^{2+} ion after its incorporation in the a-NT material. To this purpose, the theoretical SS signal of the oxide nearest neighbours around the Ca^{2+} centers was calculated and the structural parameters of the Ca-O distribution were optimized to obtain the best agreement with the experimental data. The results of the least-squares minimization performed in the *k*-range 3.2 – 10.0 $Å^{-1}$, shown in the upper panel of Figure 5.7, highlight a very good agreement between theoretical and experimental signals in both EXAFS and Fourier transform (FT) spectra. Note that the [*1s3s*] double-electron excitation was included in the model background function, while the multiplet corresponding to the [*1s3s*] transition falls outside the analyzed energy range.[20]

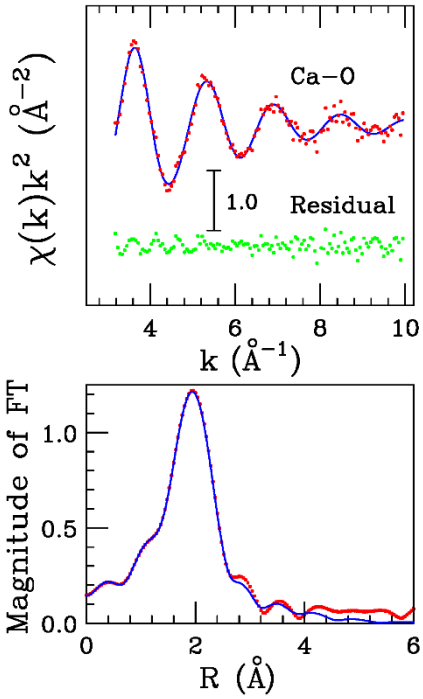

Figure 5.7. Analysis of the Ca K-edge EXAFS spectrum collected on a-NTs after full electrochemical Ca^{2+} intercalation. Upper panel: Ca-O theoretical signal (blue line) compared with the experimental data (red dots) and resulting residuals (green dots). Lower panel: non-phase shift corrected FTs of the best-fit EXAFS theoretical signal (blue line) and of the experimental data (red dots).

The optimized structural parameters for the Ca-O distribution are listed in Table 4, with E_0 = 5.6 eV above the first inflection point of the edge jump and S_0^2 = 0.90. These results show that the Ca^{2+} ions are surrounded by an average number of 5.8(5) oxygens at a mean distance of 2.42(2) Å, very similar to the case of the Ca^{2+} aqueous complex. This finding is not surprising given the similarity between the XANES spectrum of Ca^{2+}-intercalated a-NTs and that of the $CaCl_2$ aqueous solution (Figure 6b), and further corroborates the disordered environment around the incorporated Ca^{2+} ions.

Table 4 Structural parameters for the Ca-O two-body distribution obtained from the EXAFS data analysis of the Ca K-edge absorption spectrum collected on a-NTs after full electrochemical Ca^{2+} intercalation. N is the coordination number, R the average distance, σ^2 the Debye-Waller factor and β the asymmetry index.

	N	*R* (Å)	σ^2 (Å^2)	*β*
Sample A	5.8(5)	2.42(2)	0.009(2)	0.0(2)

It is worth noting that, even though the EXAFS signal is dominated by the first shell oxygen contribution, the residual curve in Figure 6a shows the presence of an additional weak oscillation, most likely corresponding to Ti atoms sitting beyond the first-shell oxygen atoms. To verify this

hypothesis, the EXAFS data analysis was carried out also by introducing the contribution of the second-shell Ti atoms with a SS Ca-Ti theoretical signal at an initial distance of 3.33 Å and a coordination number of 8.0, as taken in first approximation from the crystallographic structure of sodium titanate $NaTi_2O_4$.[66] The results of this fitting procedure are shown in Figure 5.8.

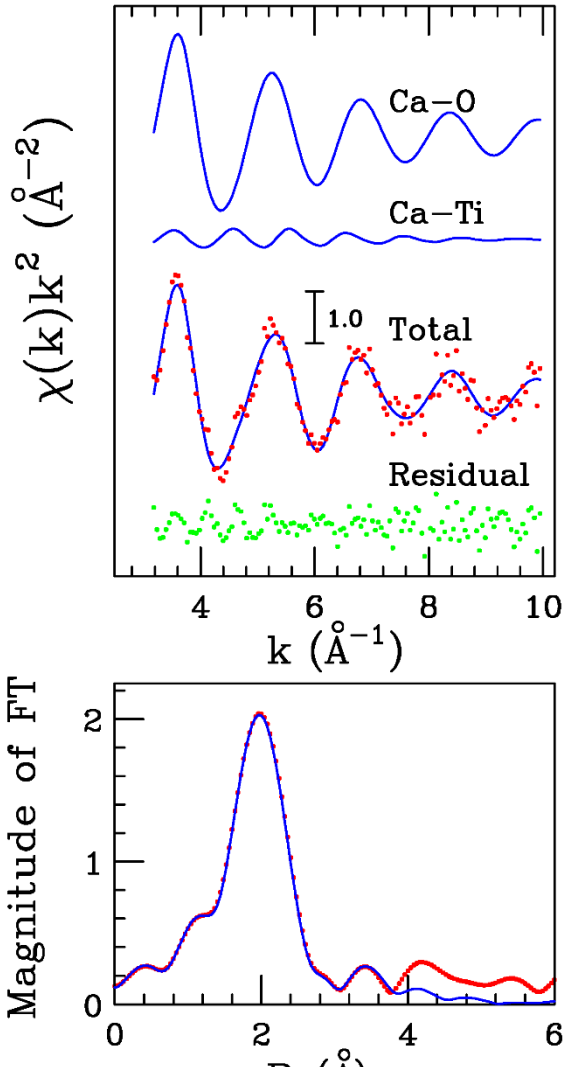

Figure 5.8 Analysis of the Ca K-edge EXAFS spectrum collected on a-NTs after full electrochemical Ca^{2+} intercalation carried out with the inclusion of the Ca-Ti contribution. Upper panel: Ca-O and Ca-Ti theoretical signals, total theoretical contribution (blue lines) compared with the experimental data (red dots) and resulting residuals (green dots). Lower panel: non-phase shift corrected Fourier transform (FT) of the best-fit EXAFS theoretical signal (blue line) and the experimental data (red dots).

As it can be observed, the inclusion of this additional contribution did not provide a significant improvement of the fit quality. Unfortunately, the Ca K-edge experimental XAS spectrum of this sample is quite noisy, and the available *k*-range is limited to 10.0 $Å^{-1}$. This hampers an adequate detection of the higher distance contributions and prevents the Ca-Ti structural parameters from being reliably extracted from the EXAFS data. For a similar reason, also the attempt to include a O-Ca-O

MS contribution involving the first shell oxygen atoms resulted in a negligible improvement of the fit quality.

To complement the XAS investigation, aNT electrodes were analysed by XRD before and after calcium insertion (Figure 5.9). The collected diffractograms reveal a shift towards smaller angles for the peak at 2θ = 48, corresponding to the (200) lattice plane reflections of anatase. This shift, observed between the pristine and *post mortem* samples, confirms lattice structural deformation before and after calcium ion insertion.

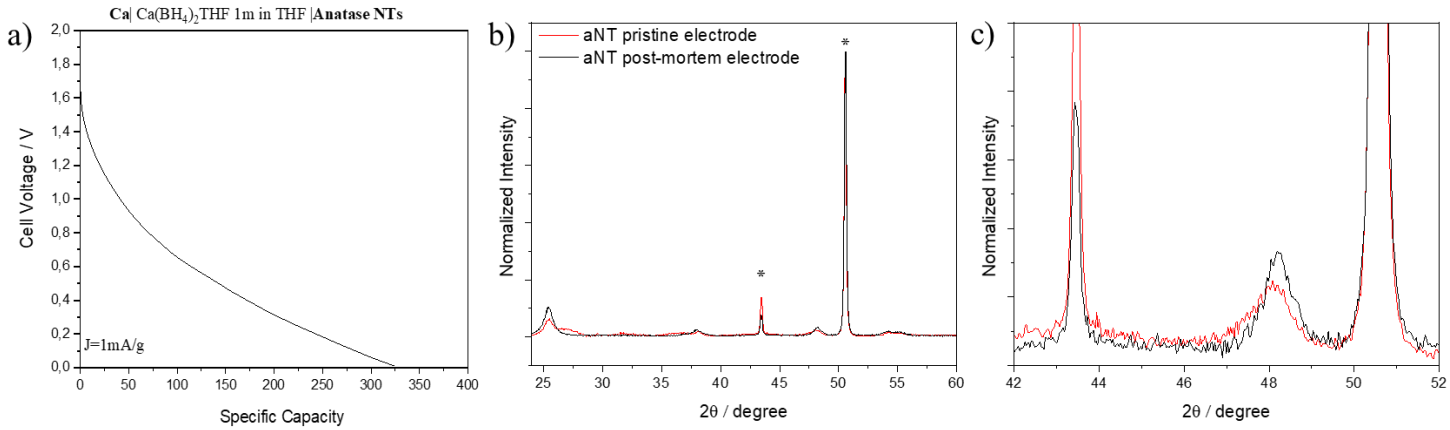

Figure 5.9 a) voltage profile of galvanostatic charge of aNT; b) XRD of pristine electrode of aNTS and b) after calciation of figure a). the two * peaks are attributed to the copper current collector; c) magnification of the shifted peak of figure b).

5.3.5 Conclusions

The electrochemical incorporation of Ca^{2+} ions in a-NTs synthesized via a hydrothermal route and characterized by FESEM EDX, XRD and Raman spectroscopy was demonstrated using both calcium metal and an activated carbon pseudo capacitive counter electrode in aprotic electrolytes. The material delivered a reversible incorporation of 0.10 to 0.12 equivalents of Ca^{2+} at an operating potential of approximately 1.6 V versus Ca^{2+}/Ca. Ex situ Ti and Ca K-edge XAS analyses confirmed that this electrochemical activity originates from a reversible intercalation process. The intercalation induces a noticeable increase in structural disorder around Ti sites, with a local environment intermediate between that observed upon lithiation and sodiation, despite the relatively small amount of incorporated Ca^{2+}. Nonetheless, the characteristic spectral fingerprint of anatase is preserved after intercalation. EXAFS fitting further indicates that Ca^{2+} ions occupy sites surrounded by an average of 5.8 (5) oxygen neighbours at 2.42 (2) Å, supporting the picture of a partially disordered yet structurally retained anatase framework.

The different electrochemical behaviours observed in the two testing configurations can be attributed, at least in part, to the nature of the electrolyte and to the accessible potential window. In pseudo capacitive cells, the enlarged voltage range enables the nanotubes to operate closer to their intrinsic redox activity, resulting in significantly higher specific capacities compared with Ca metal half cells. These results suggest that anatase nanotubes hold promise as anode materials for calcium ion systems, provided that suitable electrolyte environments are identified. However, the pseudo capacitive configuration also presents intrinsic complications, especially due to the well known initial irreversibility of TiO_2 based materials,[98,99] which makes the quantitative assessment in this setup more difficult. For these reasons, strategies aimed at mitigating the first cycle irreversible reactions, such as chemical pretreatments designed to reduce the density of reactive surface groups or to improve the initial Coulombic efficiency, could be beneficial and warrant further investigation.[98,99] In parallel, the development of new electrolyte formulations compatible with calcium metal half cells will be essential to enable a more conventional evaluation of TiO_2 nanotubes and to accurately assess their long term potential as anodes for calcium ion batteries

5.4 Ca-based alloy

5.4.1 Introduction

Alloy-type materials have emerged as promising alternatives to calcium metal anodes for CIBs, owing to their favourable characteristics such as high theoretical capacities and relatively low reaction potentials.[1,7,67] These systems, already investigated in the development of high-performance alkali metal batteries,[68] are now being considered for Ca-based energy storage.

In this context, Wolverton and co-workers[67] assessed the volumetric behavior and energy density of various Ca–metal (Ca_xM) alloy systems by DFT calculations. [67] This analysis showed that certain Ca-alloying phases could achieve energy densities comparable to or even exceeding those of graphite-based anodes used in current lithium-ion battery technologies, supporting their potential for application in CIBs. Additionally, a high-throughput computational screening method based on four selection criteria, i.e., calcination voltage, volume expansion, specific energy, and structural stability, to identify favourable Ca–metal systems. Their work highlighted a wide range of promising candidates, including metalloids such as Si, Sb and Ge; post-transition and transition metals like Zn, Al, Pb, Cu, Cd, $CdCu_2$, Ga, Bi, In, Tl, and Hg; and several noble metals such as Ag, Au, Pt, and Pd.

Ingram et al.[69] demonstrated a reversible CIB system utilizing a Sn anode, with thermodynamic calculations estimating the alloying potential with Ca to be approximately 0.8 V vs. Ca^{2+}/Ca. However, the cell suffered from pronounced capacity degradation, retaining only 50% of its capacity after 35 cycles. This loss was attributed to substantial volume changes in the Sn anode during cycling, insufficient passivation of the Sn surface, and increasing internal resistance.

Palacín and collaborators[70] conducted a detailed investigation of silicon-based anodes for CIBs through both theoretical calculations and experimental trials. DFT simulations predicted the formation of Ca_xSi intermetallic ($0.5 < x \leq 2$) at an average potential of ~0.4 V vs. Ca^{2+}/Ca, accompanied by a significant volume expansion of approximately 306%. Experimental work performed in a 0.45 M $Ca(BF_4)_2$ electrolyte (EC:PC) at 100 °C confirmed the feasibility of Ca–Si alloying reactions. Nevertheless, large volumetric changes were observed, leading to the amorphization of the dealloyed phase, structural collapse, and pronounced voltage hysteresis.

5.4.2 Ca-Zn alloy

5.4.2.1 Introduction

Alloys such as Ca–Sn have demonstrated enhanced cycling performance and greater electrochemical stability compared to pure calcium, primarily due to their ability to moderate the reactivity of calcium while enabling more reversible and predictable alloying–dealloying processes. [71–73]

Among the calcium-metal alloys, Ca-Zn alloys are particularly attractive due to the incorporation of zinc, a chemically stable and cost-effective element, which is expected to improve the electrolyte compatibility reducing the active calcium content.

The initial goal of this work was therefore to synthesize Ca–Zn alloys with a high calcium fraction, aiming to maximize the theoretical capacity and lower the operating potentials. Different synthetic strategies were explored in this regard. Electrochemical alloying, starting from zinc powder and metallic calcium, was first attempted but did not result in a reversible reaction. Ball milling mainly led to the formation of oxides rather than well-defined alloy phases, while annealing allowed the alloy formation and improved crystallinity, though with limited homogeneity and reversibility of the electrochemical activity. Ultimately, arc melting proved to be the most effective method, enabling rapid synthesis and better homogenization of the product. On the basis of this outcome, a comparative analysis was carried out between alloys with different calcium contents, namely a Ca-rich composition (Ca:Zn = 5:3) and a Zn-rich one (Ca:Zn = 1:2).

Based on the initial screening, $CaZn_2$ (1:2 atomic ratio) clearly emerged as the most promising formulation.

In this context, $CaZn_2$ was selected not only for its favourable electrochemical behavior but also because it represents the most thermodynamically stable intermetallic phase within the Ca-Zn binary system, a key advantage for mitigating phase transitions and degradation under operating conditions.[71] In this paragraph begins with a preliminary screening of Ca–Zn alloys with high calcium content, in which the electrochemical behavior of samples synthesized by arc melting (AM) and by annealing is compared. The analysis is then extended to highlight the differences between calcium-rich and calcium-deficient compositions, providing insight into the role of stoichiometry in determining the electrochemical response. Based on these results, particular attention is devoted to the $CaZn_2$ (1:2 atomic ratio) phase, which emerged as the most promising candidate for further investigation. This innovative alloy not only reveals good compatibility with $Ca(TFSI)_2$-based electrolytes, but its stability also paves the way for a standardized method to assess the performance of electrode candidates for CIBs. The integration of a calcium-zinc alloy provides a stable reference electrode that can reliably interface with 1,4,5,8-naphthalenetetracarboxylic dianhydride (NTCDA), one of the promising organic cathodes based in the state-of-the-art which have demonstrated reasonable capacities in previous studies but with rapid fade of capacity due to the use of Ca metal as counter electrode.[74,75] In conclusion, this work wants to introduce $CaZn_2$ alloy as possible robust and efficient counter electrode for CBs using conventional electrolyte based on $Ca(TFSI)_2$. This research

aims to not only advance the material science of CIBs, but also to propose a methodology for evaluating and optimizing novel electrode designs, thus fostering advancements in the field.

5.4.2.2 Experimental section

5.4.2.2.1 Synthesis and manipulation of Ca-Zn alloy

Different synthesis approaches were evaluated in order to obtain Ca–Zn alloys. Electrochemical alloying was first attempted, starting from zinc powder in direct contact with metallic calcium; however, no reversible alloying reaction was achieved under the tested conditions (details on electrode preparation and electrolyte formulation are provided in Section below).

For both annealing and arc melting routes, the initial target was the synthesis of Ca-rich alloys, motivated by the higher calcium content being expected to maximize capacity and reduce operating potentials, as discussed in the Introduction. In particular, stoichiometric ratios were selected in order to obtain the Ca_5Zn_3 intermetallic composition.

Mechanical milling of the elemental powders was investigated using a SPEX high-energy ball mill equipped with a stainless-steel jar and stainless-steel balls. The mass ratio of the Ca–Zn mixture to the milling balls was set to 1:10. Each milling cycle lasted 100 minutes, with repetitions tested from 3 up to 6 times, separated by 1-hour cooling intervals. This approach predominantly led to the formation of zinc and calcium oxides, with negligible evidence of alloy formation; therefore, the corresponding results are not reported here.

Thermal annealing experiments were performed by mixing zinc powder with small pieces of metallic calcium. The mixtures were heated from room temperature to 700 °C over 12 h with a heating rate of 10 °C min^{-1}. After holding at 700 °C, the temperature was decreased at a rate of 1 °C min^{-1} until reaching 450 °C, where the samples were held for an additional 8 h, and then cooled to room

temperature at the same rate. Although alloy-related reflections could be detected in the annealed samples, the resulting products exhibited multiphase compositions with limited homogeneity.

Arc melting was also employed as a synthesis route, performed under an inert atmosphere to melt the metallic precursors, producing a homogeneous molten alloy. Upon solidification, a dense ingot was obtained and subsequently ground manually to yield a uniform powder for further characterization, according to the scheme reported in Figure 5.10. Once the arc-melted Ca_5Zn_3 alloy was obtained, the resulting ingot was transferred into an argon-filled glovebox. Upon exposure to the atmosphere, the outer surface of the ingot became passivated, developing a dark appearance, as illustrated in Figure 10. Inside the glovebox (Ar atmosphere with O_2 and H_2O levels below 1 ppm), after gently scratching the surface and the ingot was manually ground to obtain a fine powder for subsequent characterization and the fabrication of self-standing electrodes.

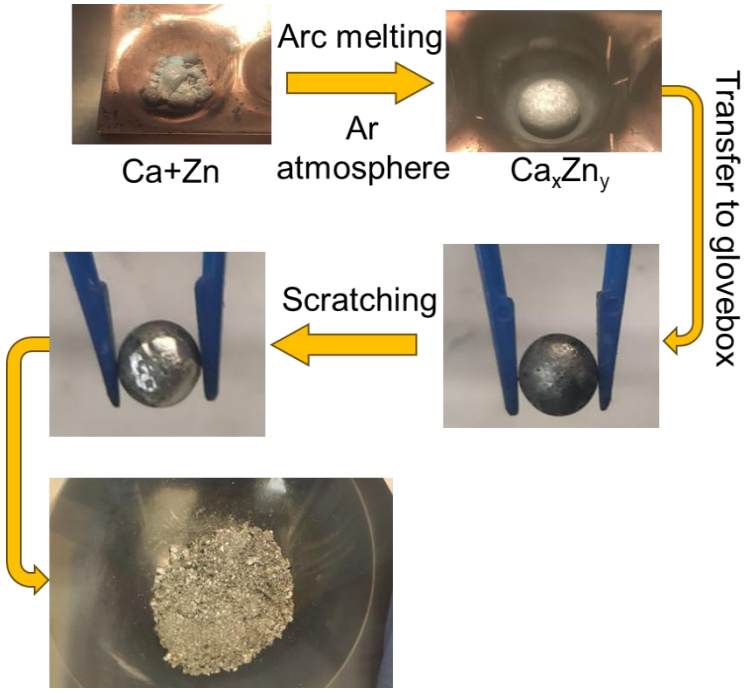

Figure 5.10 Schematic representation of arc melting synthesis procedure of Ca-Zn alloy

$CaZn_2$ was synthesized via direct electric arc melting of calcium and zinc in a stoichiometric 1:2 ratio, following the same methodology illustrated in the scheme of Figure 10. Four independent synthesis batches of the alloy were examined to evaluate the reproducibility and reversibility of the synthetic process by ICP-OES and XRD. Following initial assessment, the resulting materials were combined into a single composite batch for subsequent electrochemical characterizations.

5.4.2.3 . NTCDA-based Cathode Synthesis

Diimide polymer (PI/CNT) Polyimide (PI) was synthesized according to the reported procedure by Li et al.[75] 1,4,5,8-naphthalenetetracarboxylic dinahydride (NTCDA) (5.36 g, 20 mmol) and ethylenediamine (20 mmol) were mixed in 50 ml of NMP. The mixture was heated up to 150 °C.

After 12 h, the mixture was cooled down to room temperature and the suspension was filtered and washed with toluene and ethanol three times. The yellow powder was dried under vacuum at 120 °C overnight. Dried powder was then calcined in quartz tube at 300 °C in Ar atmosphere and additionally purified through Soxhlet extraction in ethanol (48h).

5.4.2.4 Electrolyte formulation

In the initial attempt of electrochemical alloying, starting from zinc powder and metallic calcium, a calcium borohydride-based electrolyte was employed. Specifically, 0.5 M $Ca(BH_4)_2$ dissolved in anhydrous tetrahydrofuran (THF) was used, with both the salt and solvent supplied by Sigma-Aldrich in anhydrous grade.

For the subsequent electrochemical studies, alternative electrolyte formulations were explored. Calcium bis(trifluoromethanesulfonyl)imide ($Ca(TFSI)_2$, 99.5% purity) was purchased from Solvionic and dried under vacuum at 150 °C overnight prior to use. All solvents, including 1,2-dimethoxyethane (G1), diethylene glycol dimethyl ether (G2), and triethyl phosphate, were purchased from Sigma-Aldrich in anhydrous grade and further dried over activated 3 Å molecular sieves (Sigma-Aldrich) for two weeks, with replacement of the sieves after the first week.

Two electrolyte formulations were prepared: 1) 0.4 M $Ca(TFSI)_2$ dissolved in DME, employed to initially evaluate the electrochemical activity of the Ca-based alloys against metallic calcium and 2) 0.4 M $Ca(TFSI)_2$ in a solvent mixture of G1, G2, and TEP 45:45:10 v/v respectively. This electrolyte was used for all subsequent electrochemical characterizations, as it provided improved current response during cycling.

5.4.2.5 Electrode preparation

For the initial attempt of electrochemical alloying, a calcium metal electrode (9 mm diameter) was prepared by punching disks from a calcium foil (ACI Alloys Inc.). The zinc electrode, obtained from zinc powder (Sigma-Aldrich), was tested in two different configurations: (i) as a pellet of zinc powder compacted to a 9 mm diameter, and (ii) as a self-standing electrode prepared with a composition of 70:20:10 wt% Zn powder, carbon black, and PTFE, using the same preparation procedure as that adopted for the Ca–Zn alloy electrodes, described in the following section.

Self-standing Ca-Zn alloy-based electrodes were prepared by manually mixing the alloy powder, granular PTFE (Sigma-Aldrich, ~1 μm particle size) as the binder, and conductive carbon (Super P, Alfa Aesar) in an agate mortar inside an argon-filled glovebox. The components were combined in a mass ratio of 70:10:20, respectively. The resulting black, gum-like composite was first rolled between a glass tube and a glass plate to form a preliminary sheet, and subsequently processed using a roller press to obtain a uniform electrode foil with a final thickness below 1 mm. From the final self-

standing electrode sheet, circular electrodes with a diameter of 8 mm were punched for cell assembly of the ordinary electrochemical characterization and 10 mm for the final test with the organic cathode.

NTCDA-based electrodes were prepared by mixing active material, Printex XE2 carbon black (Degussa, 950 m^2 g^{-1}), and polytetrafluoroethylene (PTFE, Sigma-Aldrich, 60% water dispersion) in weight ratio of 60:30:10. Components were mixed with isopropanol and ball milled using a Retch PM100 mill (300 rpm, 30 minutes). After milling, the black gum-like composite was additionally mixed in agate mortar with the addition of isopropanol, after which it was rolled between the parchment paper and the glass plate. Finally, the self-standing electrodes were punched out in a disk of 10 mm diameter and dried in vacuum at 50 °C overnight.

5.4.2.6 Physico-chemical characterization.

FESEM coupled with EDX experiments were carried out by employing an Auriga Zeiss electron microscope. Wide-angle XRD patterns were collected by using either a PANalytical X'Pert or a Bruker Advance D8 diffractometer, both equipped with a Cu Kα source (λ = 1.5418 Å) within the angular range 30°-70°with a step size of 0.02°.

To determine Ca/Zn ratio, the synthesised samples were analysed by ICP-OES (Agilent 5800 EV, Santa Clara, CA, USA). The samples for ICP-OES analysis were prepared by acid digestion in aqua regia and an aliquot was filtered using PTFE syringe filters with a pore size of 0.22 μm and diluted. Calibration curves were previously prepared for each metal, starting from a multi-element standard solution assessing adsorption based on specific wavelengths (λ). The Multielement standard solution for ICP was provided by Merck (Merk Life Science S.r.l., Milan, Italy).

5.4.2.7 Cell Assembly and electrochemical characterization.

ECC-STD laboratory cells (El-Cell GmbH) were employed for all electrochemical tests, except for the galvanostatic cycling with the organic cathode, for which a three-electrode ECC-Ref laboratory cell was used. All the electrochemical tests were conducted with Whatman glass fibre separators (GF/A Cytiva, thickness 0.26 mm), soaked with 80 μL of electrolyte prior to cell assembly.

Symmetric cell configurations were employed for both preliminary and advanced electrochemical testing. Electrochemical performance of the $CaZn_2$ alloys was evaluated by CV conducted between -2 and 2 V vs the open circuit voltage (OCV) with a scan rate of 2 mV s^{-1}. The preliminary measurements were carried out in symmetric cell configuration using either metallic calcium or $CaZn_2$ electrodes, with $Ca(TFSI)_2$ 0.4 M in DME as the electrolyte.

Calcium metal disk electrodes (9 mm diameter) were punched from Ca metal foil (ACI Alloys Inc.) and their surfaces were gently scratched with a scalpel immediately prior to use to remove the passivation layer.

The electrochemical stability window (ESW) of the electrolyte was evaluated using linear sweep voltammetry (LSV) and CV at a scan rate of 1 mV s^{-1} in asymmetric cells. For the LSV measurements, performed between the OCV and 6 V versus the alloy, $CaZn_2$ was paired with an aluminum electrode coated with Super P to assess anodic stability. For the CV tests, conducted between the OCV and 0 V versus the alloy, $CaZn_2$ was paired with a copper electrode coated with graphite to evaluate cathodic stability. The counter electrodes were prepared by casting a slurry of Super P or graphite onto aluminum or copper foil, respectively, followed by drying under vacuum at 90 °C overnight.

Galvanostatic cycling was conducted in symmetric cell configuration with current density of 1 mA g^{-1} and fixed capacity of 10 and 20 mAh g^{-1} for the preliminary and for the further characterization with $CaZn_2$-based alloy respectively. Electrochemical Impedance Spectroscopy (EIS) measurements were performed over a frequency range of 1 MHz to 100 mHz with an amplitude of 5 mV performed at the end of each cycle.

All electrochemical measurements were performed using Biologic MPG and VSP potentiostat at room temperature.

For the final electrochemical tests against organic cathodes, they were assembled facing $CaZn_2$ electrodes with the organic cathode material. Metallic lithium was selected as a quasi-reference electrode owing to its well-defined electrochemical potential. In addition, Li metal offers practical advantages in this cell configuration: its mechanical softness facilitates shaping and integration into the EL-cell architecture, ensuring stable interfacial contact throughout cycling. The use of calcium metal as reference was deliberately avoided, since its high reactivity and the continuous evolution of the Ca/electrolyte interface would induce potential drifts and compromise the reliability of the reference signal.

All operations were carried out in an argon-filled glovebox (with H_2O and O_2 <1pmm).

5.4.3 Results and discussion

5.4.3.1 Ca-Zn alloy preliminary examination

As a preliminary step, Ca–Zn alloys were investigated in order to identify the most suitable target composition for further study. The screening was focused on two aspects: (i) the effect of the synthesis route, by comparing annealing and arc melting, and (ii) the impact of calcium and zinc content on the

electrochemical behavior. To this end, Ca-rich compositions (Ca_5Zn_3) were initially synthesized and characterized. Structural analyses were carried out by XRD, morphology and composition were evaluated by SEM/EDX, and the electrochemical performance was assessed by galvanostatic cycling.

The XRD patterns of the alloys obtained by annealing and arc melting are reported in Figure 5.11. In both cases, the diffraction peaks can be assigned to Ca_5Zn_3 and Ca_3Zn phases. The simultaneous presence of these two phases suggests a deviation from the nominal stoichiometry, which can be ascribed to zinc loss during both synthesis processes, most likely due to Zn volatilization at high temperature. For the annealed samples, the reflections appear broader and less defined, consistent with a limited crystallinity. In contrast, the arc-melted alloy exhibits sharper and more intense peaks, indicating a higher degree of crystallinity and improved phase homogeneity, although minor contributions from Ca_3Zn are still detectable.

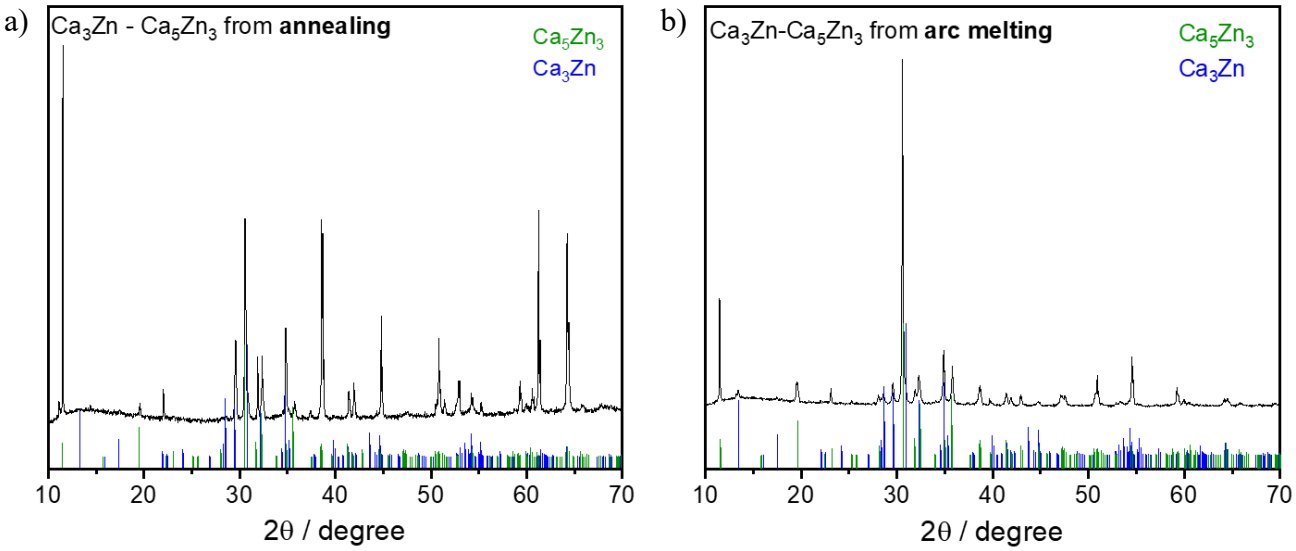

Figure 5.11. XRD patterns of Ca–Zn alloys with nominal Ca_5Zn_3 composition synthesized by annealing (a) and arc melting (b), compared with reference patterns of Ca_5Zn_3 (ICSD 55584) and Ca_3Zn (ICSD 58948).

SEM/EDX analyses provided further insights into the morphology and compositional distribution. In both cases, the average Ca/Zn ratios determined by EDX were in agreement with the nominal composition. However, the annealed alloys exhibited local inhomogeneities: some regions were covered by calcium oxide (Figure 5.12, panel b), while other areas appeared Ca-rich and Zn-deficient (Figure 5.12, panel a). Conversely, the arc-melted alloys (Figure 5.12, panels c and d) displayed a more homogeneous microstructure, with no detectable compositional deviations by EDX mapping.

In both synthesis routes, carbon and oxygen signals were detected, reasonably attributed to surface contamination due to brief exposure to air during SEM preparation.

a)

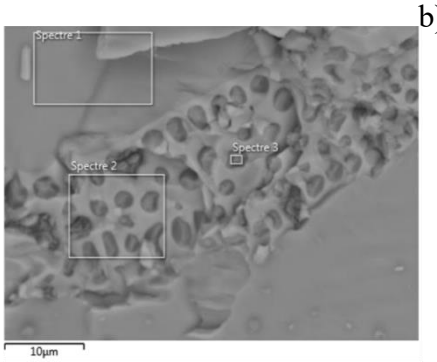

	% atomic		
Element	Spectre 1	Spectre 2	Spectre 3
C	9.48	10.62	11.76
O	10.64	18.52	25.12
Al	-	-	0.48
Si	-	0.10	0.57
K	-	-	0.18
Ca	61.16	52.72	55.43
Ni	-	0.56	0.53
Zn	18.73	17.48	5.93

b)

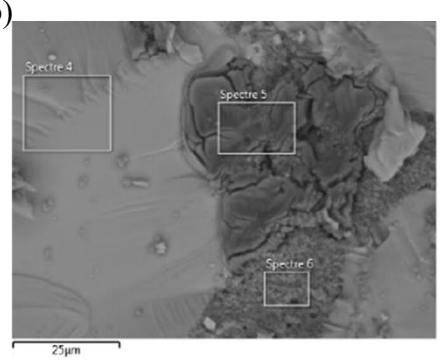

	% atomic		
Element	Spectre 4	Spectre 5	Spectre 6
C	10.53	3.02	1.95
O	9.96	47.65	18.29
Al	-	0.13	-
Si	-	0.10	0.14
Cl	-	0.14	0.9
Ca	50.78	48.45	78.16
Zn	28.73	0.51	1.37

c)

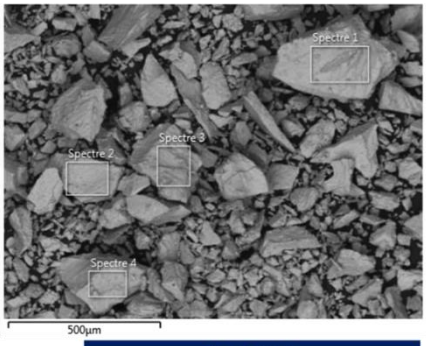

	% atomic			
Element	Spectre 1	Spectre 2	Spectre 3	Spectre 4
C	15.4	11.57	16.00	17.74
O	21.11	15.93	19.90	17.15
Ca	40.93	47.51	40.77	41.74
Zn	22.57	25.00	23.33	23.37

d)

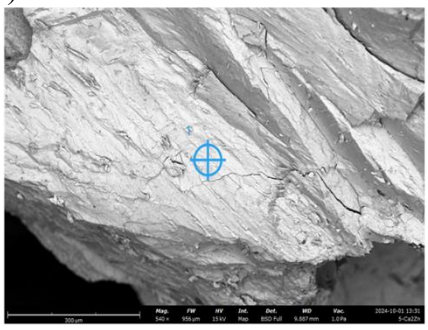

	% atomic
Element	Spectre
O	11.51
Ca	58.31
Zn	30.18

Figure 5.12. SEM micrographs of Ca–Zn alloys with nominal Ca_5Zn_3 composition synthesized by annealing (a, b) and arc melting (c, d), with corresponding EDX quantitative analyses reported in the tables below each image. Annealed samples show surface oxides (a) and Ca-rich/Zn-deficient regions (b), indicating compositional inhomogeneities, while arc-melted alloys display a more homogeneous microstructure with no pronounced deviations in Ca/Zn ratios.

The galvanostatic cycling results are shown in Figure 5.13. In Figure 5.13(a), the comparison between Ca_5Zn_3-based alloys obtained by annealing and arc melting is presented. Both samples exhibit low

overpotentials during the first cycles, which progressively increase upon cycling. However, the annealed alloy shows a much extreme rise in overpotentials, probably due to SEI thickening and structural instabilities induced by repeated expansion and contraction of the lattice during the cycling. This different behavior could also be correlated with the structural heterogeneity and impurities revealed by SEM/EDX.

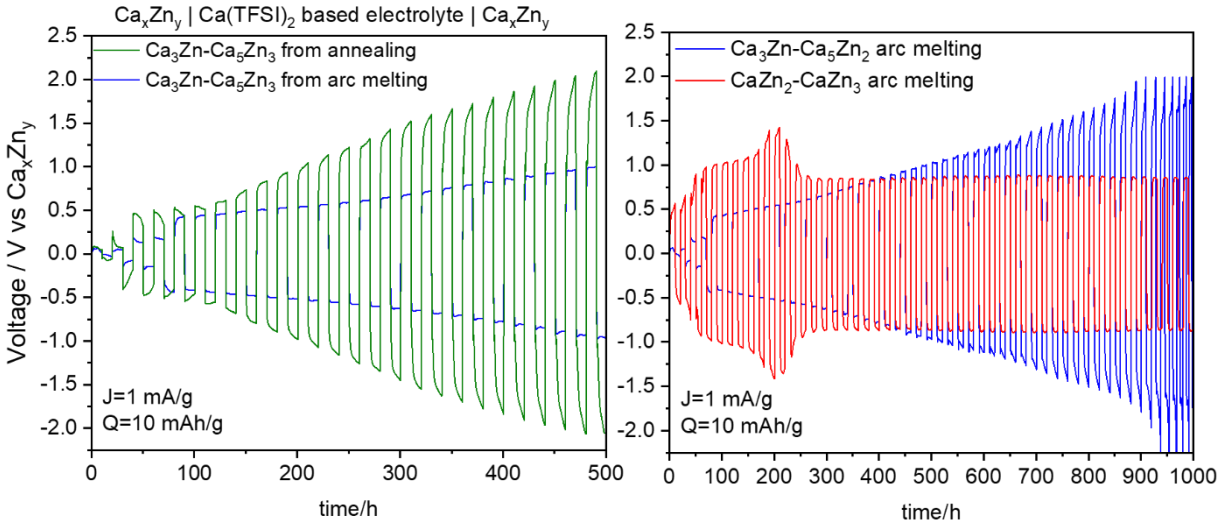

Figure 5.13 Galvanostatic cycling (GC) profiles of Ca–Zn alloys in symmetric cells with $Ca(TFSI)_2$ 0.4 M in G1, G2, and TEP as electrolyte: (a) comparison between Ca_5Zn_3 samples synthesized by annealing and arc melting; (b) comparison between arc-melted Ca-rich (Ca_5Zn_3) and Zn-rich ($CaZn_2$) alloys.

In Figure 5.13(b), arc-melted alloys with high calcium (Ca_3Zn-Ca_5Zn_3) and higher zinc content ($CaZn_2$-$CaZn_3$) are compared. The Ca-rich alloy initially exhibits lower overpotentials, which, however, increase continuously without stabilization throughout the test. On the contrary, the Zn-rich alloy shows higher initial overpotentials, which increase during the first ~200 hours but subsequently decrease and stabilize, remaining constant for the rest of the cycling. This highlights the superior long-term stability of the Zn-rich alloy, likely related to the reduced reactivity of its lower calcium content toward the electrolyte, leading to the formation of a more stable SEI.

Overall, these preliminary results indicate that arc melting is more effective than annealing in producing homogeneous alloys with improved electrochemical performance. In addition, Zn-rich compositions display enhanced cycling stability compared to Ca-rich ones, which suffer from progressive overpotential growth. On the basis of this screening, the subsequent investigation was focused on the $CaZn_2$ alloy, which emerged as the most promising formulation and will be discussed in detail in the following section.

5.4.3.2 $CaZn_2$ synthesis assessment and characterisation

The $CaZn_2$ alloy was synthesised by arc melting due to its ability to rapidly produce metallic compounds with high structural and chemical homogeneity. This technique, widely used in the synthesis of thermoelectric and intermetallic materials, offers advantages such as high energy input, fast reaction kinetics, and operation under vacuum conditions, which together facilitate the formation of well-defined and homogeneous phases.[76–78] Despite its widespread application in other materials science domains, AM remains underutilized in the synthesis of active materials for rechargeable battery systems.[76] The reproducibility of AM synthesis was verified by XRD and ICP analyses carried out on four independent batches (table 5 and figure 5.11). The XRD patterns of all samples show no discernible differences, indicating high structural consistency across the series. ICP-OES analysis confirms the bulk composition of the four synthesized batches, consistently showing Ca/Zn ratios close to the nominal stoichiometry of $CaZn_2$ (see table 5). This result highlights the effectiveness of arc melting in producing Ca–Zn alloy systems and the ability to produce multi-phase materials with controlled composition.

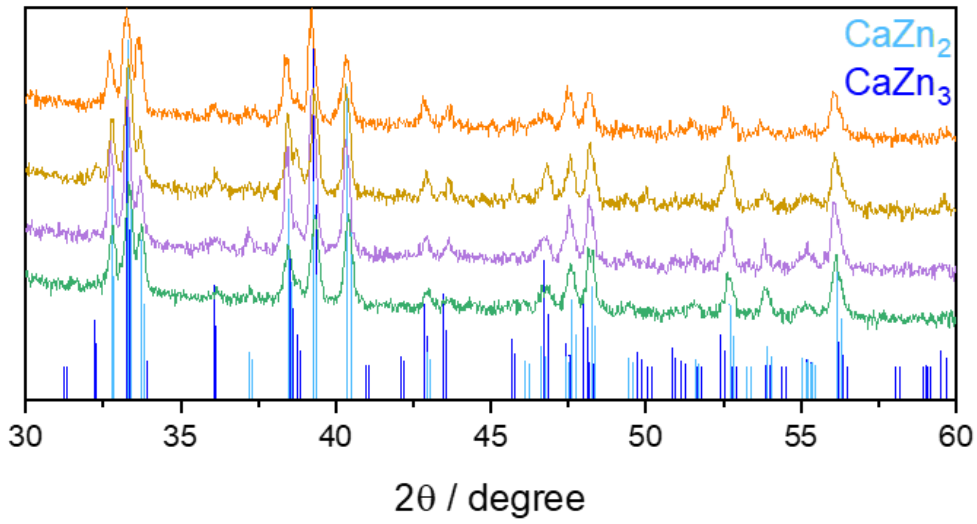

Figure 5.14 Diffraction pattern acquired for the 4 batch of $CaZn_2$

Table 5 ICP-OES table results

Batch	ppm Ca (RSD%)	ppm Zn (RSD%)	mol. ratio Zn/Ca
1	0.43 (0.36)	1.52 (0.11)	2.078 ± 0.008
2	1.35 (0.08)	3.99 (0.12)	1.812 ± 0.004
3	0.77 (0.14)	2.34 (0.49)	1.863 ± 0.012
4	1 (0.20)	3.29 (0.18)	2.017 ± 0.008

Once confirmed the reproducibility of the synthesis, the materials from the four synthesis batches were mixed and analysed by XRD (Figure 5.15a), which revealed the presence of two distinct intermetallic phases. Rietveld refinement (refined parameters reported in Table 6) of the diffraction pattern confirmed that the sample is composed predominantly of $CaZn_2$ (Imma), accounting for approximately 70.8 wt%, with a secondary phase of $CaZn_3$ ($P6_3/mmc$) making up the remaining 29.2 wt%. These results indicate that, under the AM synthesis conditions, $CaZn_2$ is the thermodynamically favoured product, although $CaZn_3$ also is formed in significant quantities. SEM imaging (Figure 5.15b) revealed a heterogeneous microstructure and the EDX elemental mapping (Figure 5.15c) confirmed a homogeneous distribution of calcium and zinc throughout the sample, in line with both the ICP quantification and the phase composition determined by XRD.

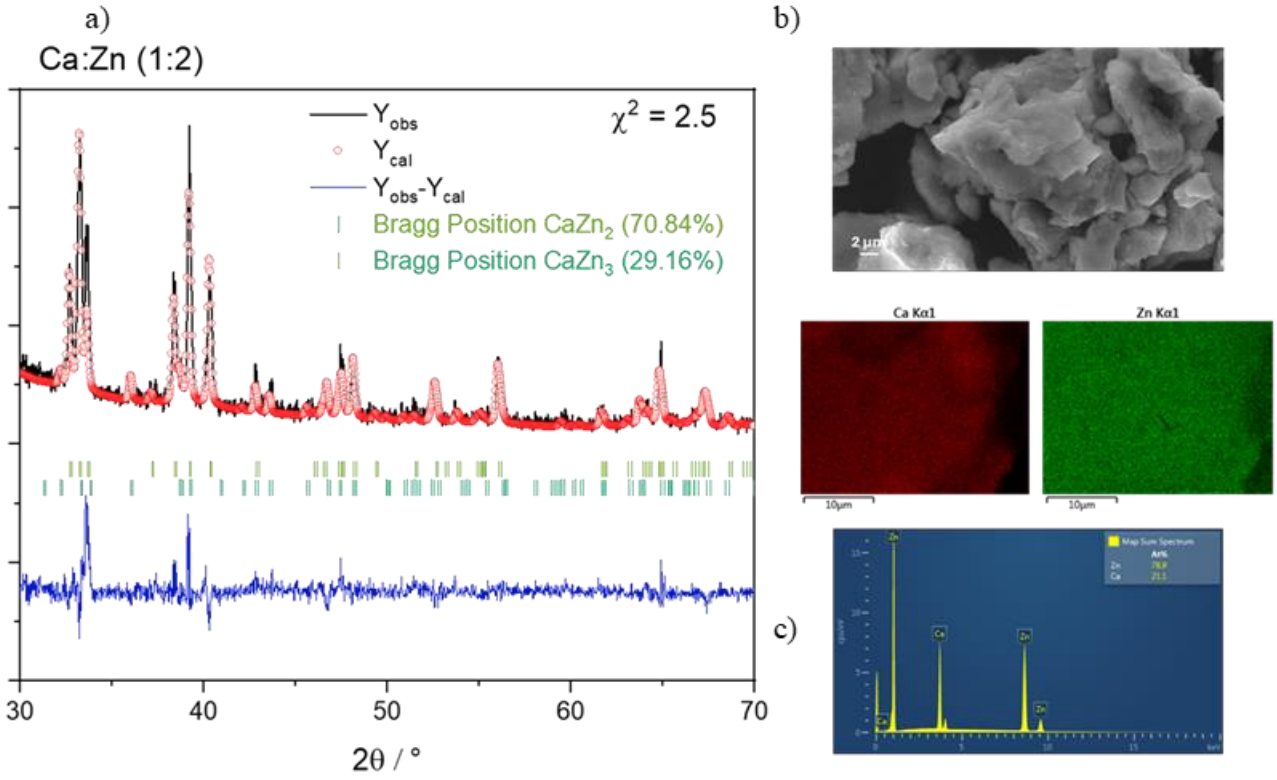

Figure 5.15 a) Rietveld Refinement, $CaZn_2$ phase was identified using the Inorganic Crystal Structure Database (ICSD, code: 418971), while $CaZn_3$ phase was modelled based on crystallographic data extracted from the literature[79] and implemented into a custom FullProf .pcr file for Rietveld refinement; b) SEM images and c) EDX maps and spectrum of $CaZn_2$

Table 6 Rietveld refinement table

Parameter	**$CaZn_2$ (Imma)**	**$CaZn_3$ ($P6_3/mmc$)**
Phase fraction	70.84 %	29.16 %
Unit cell parameters (Å, °)	a = 4.59048, b = 7.37729, c = 7.67133; α = β = γ = 90°	a = b = 9.17402, c = 7.29650; α = β = 90°, γ = 120°
Unit cell volume ($Å^3$)	259.792	531.821
Calculated density (g/cm^3)	4.425	4.963
Bragg R-factor (R_β)	25.9 %	32.0 %
Structural R-factor (Rf)	17.8 %	24.2 %
Atomic site occupancies (Zn, Ca)	Zn1 = 0.497, Ca1 = 0.262	Zn sites partially occupied (0.011–0.500), Ca sites with partial occupancy (Ca1 = 0.250, Ca2 = 0.028)
Overall fit indicators	Rp = 14.6 %, Rwp = 19.3 %, Rexp = 12.08 %, χ^2 = 2.54, Durbin-Watson = 0.815	

5.4.3.3 Electrochemical Compatibility of $CaZn_2$ with $Ca(TFSI)_2$-based electrolytes.

To assess the electrochemical performance of $CaZn_2$-based electrodes, preliminary tests were carried out using a symmetric cell configuration with a 0.4 M $Ca(TFSI)_2$ electrolyte dissolved in a ternary solvent mixture containing G1, G2, and TEP (Figure 16) CV test(Figure 5.16a) reveal well-defined, symmetric redox peaks centred around 0.5 V, with reduced polarization and improved reversibility compared to other formulations. These features indicate enhanced interfacial kinetics and a clear improvement in electrochemical activity during cycling. Galvanostatic cycling (Figure 5.16b) further confirms these trends, showing an initial overpotential increase in the first two cycles followed by a gradual decrease, leading to more stable charge/discharge voltage plateaus. EIS, performed after each cycle (Figures 5.16c and 5.16d), reveals stable charge transfer resistance and only a slight increase in electrolyte resistance, while the resistance associated with the SEI grows more noticeably. Overall,

these results suggest good cyclability and interfacial stability, though further investigations of SEI composition and evolution are required.

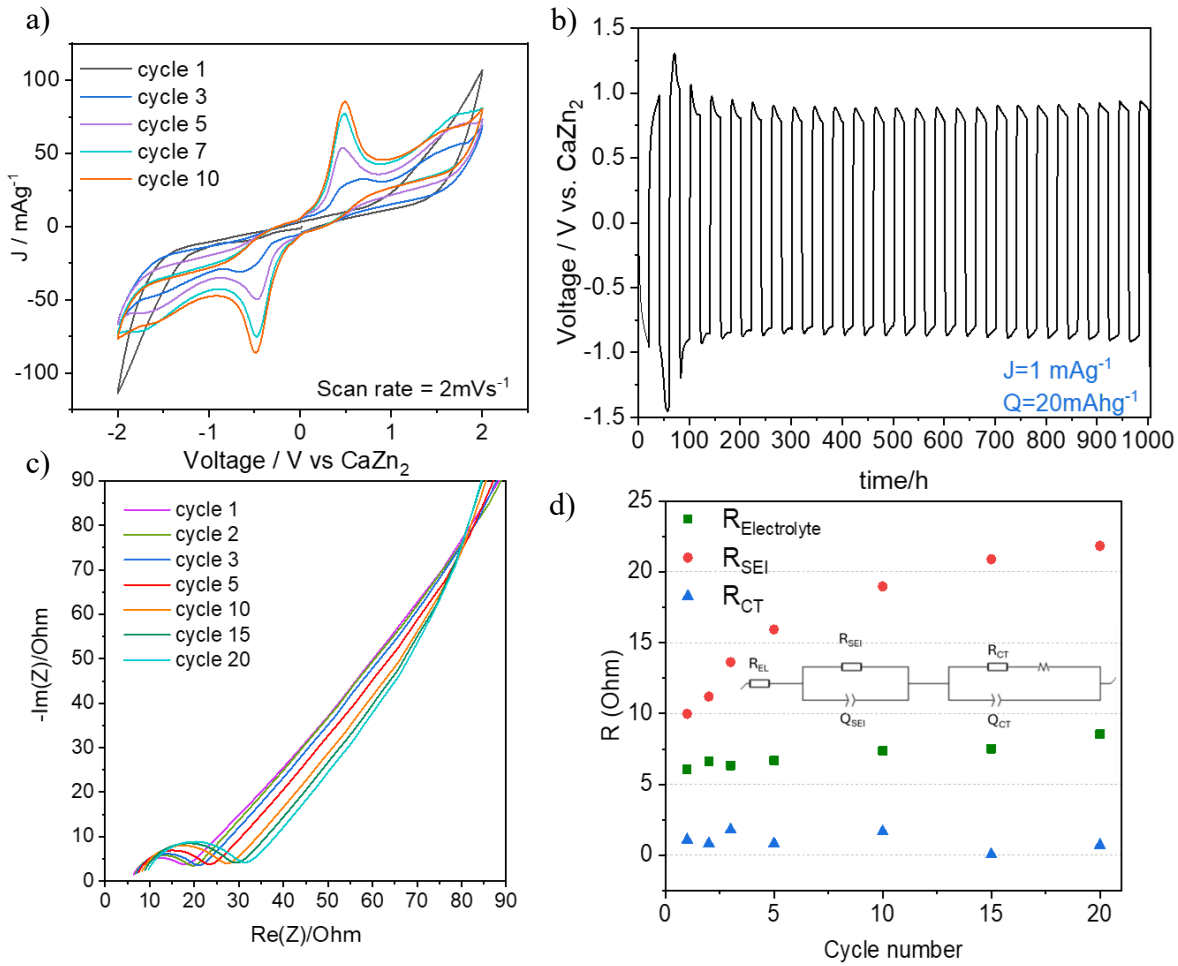

Figure 5.16 $CaZn_2$ | Ca(TFSI)2 0.4M in G1, G2, TEP | $CaZn_2$ – Symmetric cell configuration: a) cyclic voltammetry; b) galvanostatic cycling with c) EIS performed at the end of each cycle; d) Nyquist plot and the equivalent circuit of the EIS

In comparison, CV data for calcium metal electrodes in 0.4 M $Ca(TFSI)_2$ in DME (Figure 5.17a) show a measurable but rapidly declining faradaic response, accompanied by increasing overpotential that obscures the identification of clear anodic and cathodic peaks. This highlights the superior electrochemical behavior of the ternary solvent electrolyte used with $CaZn_2$ electrodes. The effectiveness of the ternary electrolyte formulation can be attributed to its inspiration from weakly coordinating anion (WCA) systems originally developed for magnesium batteries. As reported by Li et al., a solvent-engineered $Mg(TFSI)_2$ electrolyte minimized contact ion pairing, promoted facile ion-pair dissociation, and enabled dendrite-free Mg plating/stripping with excellent long-term stability and coulombic efficiency.[80] Inspired by this, our WCA-based electrolyte leads to improved redox behavior and cycling stability in the $CaZn_2$ system.

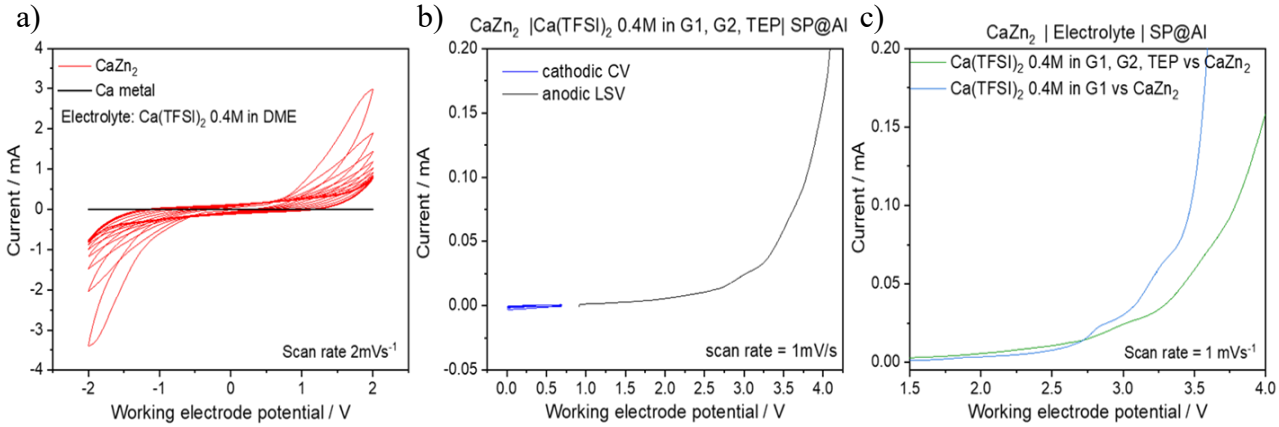

Figure 5.17 a) cyclic voltammetry in symmetric cell configuration of Ca metal and $CaZn_2$ based electrode; b) electrochemical stability window of the WCA-type electrolyte; c) comparison of the anodic stability of the two $Ca(TFSI)_2$-based electrolyte.

Finally, the ESW of the ternary electrolyte was evaluated (Figure 5.17b). The anodic stability of the ternary solvent mixture was comparable or slightly improved relative to $Ca(TFSI)_2$ in pure G1, with oxidative onset currents appearing around 2.9 V versus ~2.8 V for G1 alone (Figure 5.17c). This gradual increase in anodic current beyond the threshold supports the selection of the ternary mixture as the reference electrolyte for further full-cell studies.

5.4.3.4 Integration of Ca–Zn Alloy Counter Electrode in Practical Calcium-Ion Cells

To demonstrate the practical applicability of the Ca–Zn alloy as a counter electrode in CIBs, a full-cell configuration was assembled pairing the alloy with an NTCDA-based cathode, as shown in Figure 5.18. This setup serves to evaluate the performance of $CaZn_2$ with $Ca(TFSI)_2$-based electrolyte under conditions that more closely resemble real-device operation.

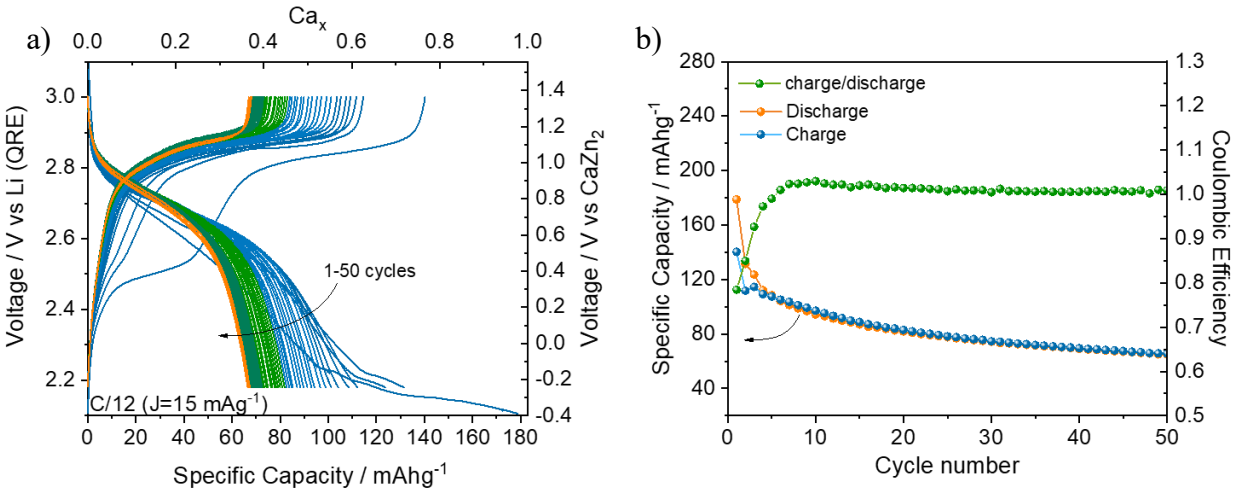

Figure 5.18 a) Voltage-capacity profile and b) cycling performance of the galvanostatic cycling of NTCDA | Ca(TFSI)2 0.4M in G1,G2, TEP | $CaZn_2$. In this configuration, lithium metal was employed as a quasi-reference electrode (QRE) due to its well-defined and relatively close electrochemical potential to that of calcium (with a difference of approximately 0.17 V),[81,82] as well as the ease of handling and cell assembly it offers due to his softness and ductility of lithium make it easier to process and integrate into the cell configurations, facilitating reproducible and robust cell assembly. This choice enabled simplified cell architecture and reliable potential control during the cathode cycling experiments.

Figure 5.18 presents the electrochemical behavior of the NTCDA-based organic cathode material during galvanostatic cycling. The mass of the counter electrode and the current density was selected so as to ensure that the workload of the counter electrode remains comparable to that used in previous galvanostatic cycling experiments performed on symmetric cells., with a current density on the counter electrode of approximately 1 mA/g. During the first cycle, the cell was discharged to lower potentials to promote the activation of the material. As a result, the material exhibited a capacity close to the theoretical value corresponding to the insertion of one calcium equivalent, with approximately 0.8 equivalents being reversibly exchanged in the following cycles. While a slight reduction in capacity is observed during the first 100 cycles, the coulombic efficiency rapidly approaches and stabilizes near 100%, indicating highly reversible electrochemical processes.

To investigate the effective electrochemical calcium incorporation of the organic cathode, a $CaZn_2$/NTCDA cell was discharged and analysed *ex situ* via *post mortem* EDX. The galvanostatic profile in Figure 5.19, displays two distinct potential slopes, consistent with the dual redox processes observed in Figure 18.

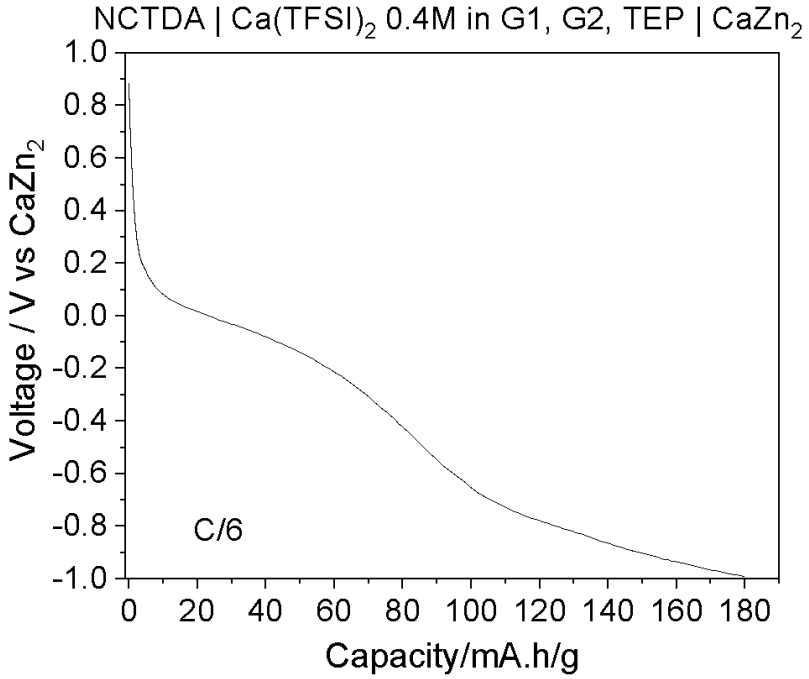

Figure 5.19. Galvanostatic profile of single discharge to further characterize the NCTDA-based cathode by EDX shown below

Cross-sectional EDX (Figure 5.20) reveals a calcium-rich core that decreases toward the surface, while zinc shows an opposite gradient, forming a distinct Zn-rich surface layer. This complementary distribution suggests a complex dual-ion mechanism, in which Ca^{2+} and Zn^{2+} are sequentially involved in the charge compensation.

a) b) c)

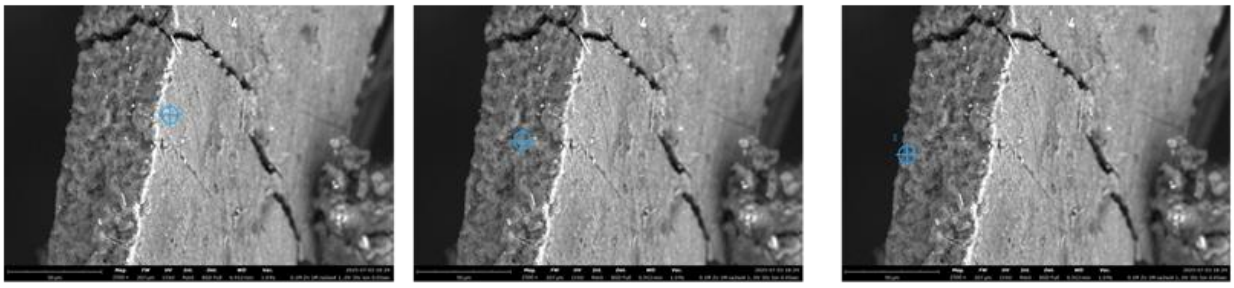

Element Symbol	Element Name	Atomic Conc.
C	Carbon	22.588
O	Oxygen	15.216
F	Fluorine	6.590
P	Phosphorus	3.705
S	Sulfur	13.882
Ca	Calcium	8.070
Zn	Zinc	29.950

Element Symbol	Element Name	Atomic Conc.
C	Carbon	68.746
O	Oxygen	15.063
F	Fluorine	7.774
P	Phosphorus	1.656
S	Sulfur	2.424
Ca	Calcium	2.910
Zn	Zinc	1.427

Element Symbol	Element Name	Atomic Conc.
C	Carbon	62.060
N	Nitrogen	5.530
O	Oxygen	17.723
F	Fluorine	6.606
P	Phosphorus	1.250
S	Sulfur	2.464
Ca	Calcium	3.441
Zn	Zinc	0.924

Figure 5.20 (a–c) Cross-sectional SEM images of the discharged NTCDA cathode, showing the locations of point EDX analyses performed progressively from the current collector side (a) to the separator interface (c). For each position, the corresponding elemental composition in atomic percentage is reported in the table below the image.

To support this hypothesis, a cross-sectional EDX analysis of an electrode partially discharged and stopped at the end of the first slope (Figure 5.21) was carried out.

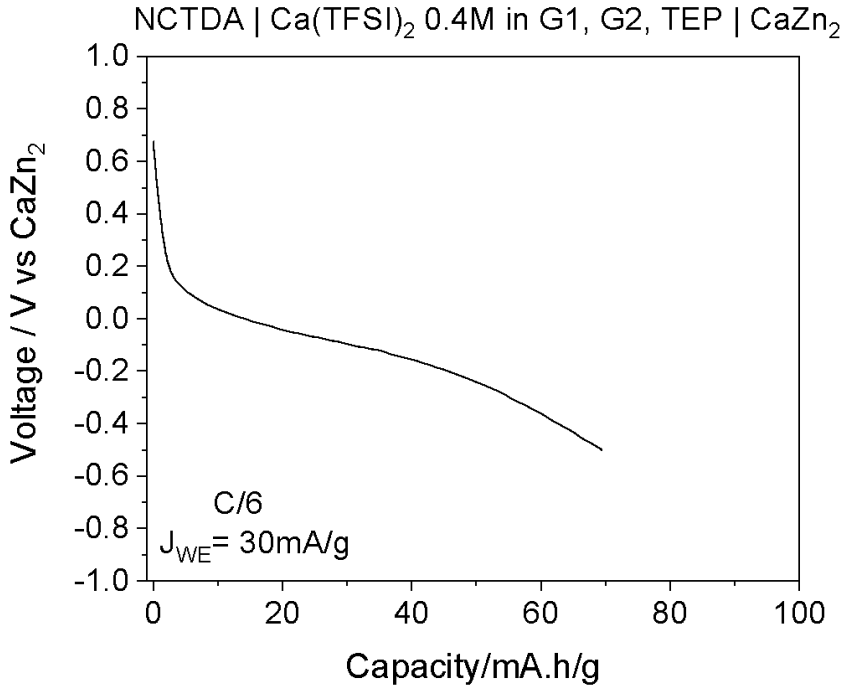

Figure 5.21 Galvanostatic profile of partially discharged NCTDA-based cathode to further characterize by EDX shown below.

As shown in Figure 5.22, calcium is homogeneously distributed across the entire electrode profile, whereas zinc is present only in trace amounts. These results reinforce the hypothesis of a mechanism in which calcium is the first ion to coordinate in the organic cathode material, followed subsequently by zinc.

a)

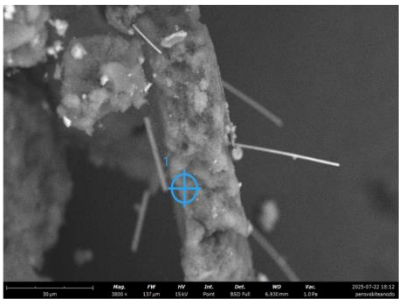

Element Symbol	Element Name	Atomic Conc.
C	Carbon	61.520
N	Nitrogen	5.927
O	Oxygen	23.397
F	Fluorine	6.963
Si	Silicon	1.202
S	Sulfur	0.395
Ca	Calcium	0.597

b)

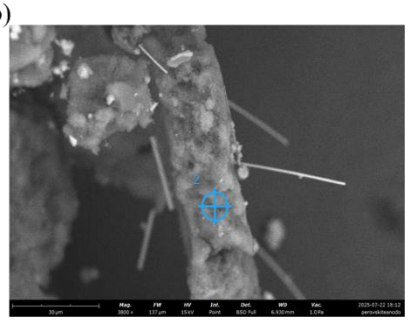

Element Symbol	Element Name	Atomic Conc.
C	Carbon	62.816
N	Nitrogen	5.435
O	Oxygen	22.474
F	Fluorine	6.086
Si	Silicon	1.657
P	Phosphorus	0.273
S	Sulfur	0.440
Ca	Calcium	0.668
Zn	Zinc	0.151

c)

Element Symbol	Element Name	Atomic Conc.
C	Carbon	61.224
N	Nitrogen	5.269
O	Oxygen	24.930
F	Fluorine	5.678
Si	Silicon	1.668
S	Sulfur	0.398
Ca	Calcium	0.638
Zn	Zinc	0.195

Figure 5.22 (a–c) Cross-sectional SEM images of the partially discharged NTCDA cathode, showing the locations of point EDX analyses performed progressively from the current collector side (a) to the separator interface (c). For each position, the corresponding elemental composition in atomic percentage is reported in the table below the image.

While further studies are needed to fully elucidate the reaction mechanism, the system already exhibits remarkable cycling stability and highly reversible redox behavior. When comparing our results with literature data where the analogue cathode material is cycled against calcium metal, [74] the use of $CaZn_2$ as the counter electrode resulted in a more stable and efficient system. This configuration not only allowed for extended cycling stability but also led to improved specific capacities and reduced overpotentials. In addition, it is possible to observe in figure 5.18a that the right y-axis reports the potential versus the alloy, clearly indicating that the cycling window remains within the ESW of the electrolyte. These enhancements highlight the advantages of $CaZn_2$ as a more practical and effective alternative to calcium metal as a counter electrode for calcium-based battery systems.

5.4.4 Conclusion

This work demonstrates the effectiveness of arc melting as a viable synthesis route for the preparation of Ca–Zn alloys and highlights their applicability as counter electrodes. In particular, the initial screening revealed that arc melting produces more homogeneous alloys compared to annealing and that Zn-rich compositions (Ca-Zn atomic ratio 1:2) provide superior cycling stability with respect to

Ca-rich ones, thus establishing the rationale for focusing on $CaZn_2$. This approach provides a simple and easily implementable system that improves both the stability and efficiency of electrochemical setups for studying calcium-based electrode materials. The primary objective of this study is to identify a counter electrode material that is stable, readily fabricated, and electrochemically reliable for the investigation of novel calcium-based electrodes. While further research aimed at optimizing electrode morphology, particularly through particle size reduction, gaining insight into the formation and evolution of the SEI, and employing alloys with higher calcium content to assess specific capacity and reduce the working potential is necessary, these aspects fall beyond the scope of the present work. Instead, this study aims to establish a practical and reproducible methodology, offering a promising alternative counter electrode material for the advancement of calcium-based battery technologies.

Nonetheless, the electrochemical mechanism underlying the alloy's behavior warrants further investigation, as preliminary findings suggest a complex interplay in which both calcium and zinc appear to participate actively. A more in-depth study will be essential to elucidate the precise reaction pathways and contribution of each metal to the overall electrochemical performance.

In conclusion, while significant obstacles remain in the route to commercialized calcium battery technologies, strategies such as employing calcium-zinc alloys present a pathway forward. The alignment of systematic testing methodologies and the exploration of alternative materials may accelerate the development of reliable calcium-based batteries, ultimately leading to innovative solutions tailored for next-generation energy storage applications. Continued collaborative research is needed to overcome the technical challenges and material limitations currently impeding progress in this field.

5.5 Preliminary examination of Ca-Sn alloy

The effectiveness of arc melting for the synthesis of Ca–Sn alloys was evaluated following the same approach adopted for Ca–Zn alloys. Specifically, the materials were characterized using SEM/EDX, ICP, and XRD analyses, followed by galvanostatic cycling and cyclic voltammetry tests in symmetric cells with the same electrolyte previously described.

5.5.1 Experimental section

5.5.1.1 Synthesis and manipulation

Ca–Sn alloy as well as Ca-Zn alloy were synthesized by direct arc melting of granular calcium and tin (Sigma-Aldrich, 99.9%) in different stoichiometric ratios (1:1, 1:2, 1:3, 1:4). The precursors were melted under argon atmosphere using a water-cooled copper hearth, with multiple remelting steps to

ensure homogeneity. The resulting ingots were immediately transferred into an argon-filled glovebox (O_2 and H_2O levels < 1 ppm), where the outer passivated layer was gently removed. The metallic core was then manually ground using an agate mortar to obtain fine powders, which were subsequently employed for structural, compositional, and electrochemical characterization.

5.5.1.2 Physico-chemical characterization.

ICP, XRD, and SEM/EDX analyses of the Ca–Sn alloys were performed under the same experimental conditions as those adopted for the Ca–Zn alloys, in order to allow direct comparison between the two systems

5.5.1.3 Cell assembly and electrode preparation

Cell assembly and electrode preparation for Ca–Sn alloys were carried out in an analogous way to that previously described for Ca–Zn alloys. Self-standing electrodes were fabricated using the same composition and procedure, ensuring consistency between the two systems

5.5.1.4 Electrochemical characterization

Electrochemical tests were conducted in symmetric cells using the electrolyte previously described. A preliminary investigation included cyclic voltammetry (CV) at a scan rate of 2 mV s^{-1}, followed by galvanostatic cycling (GC) at a current density of 1 mA g^{-1} and a specific capacity of 10 mAh g^{-1}. Four different Ca–Sn alloy batches with nominal compositions Ca:Sn = 1:1, 1:2, 1:3, and 1:4 were evaluated.

5.5.2 Result and discussion

SEM/EDX analyses presented in Figures 5.23 a and b refer to the Ca–Sn 1:2 alloy, shown here as representative of the entire series. The EDX maps reveal a higher oxygen content, indicating increased sensitivity of the alloy to atmospheric exposure, likely resulting from brief handling during the transfer from a sealed vial inside the glovebox to the SEM analysis chamber. Additionally, the sample exhibits both homogeneously distributed regions of calcium and tin, as well as more complex domains where metallic tin and Ca–Sn alloy phases are heterogeneously dispersed, as shown in Figure 5.23 a, b, and c.

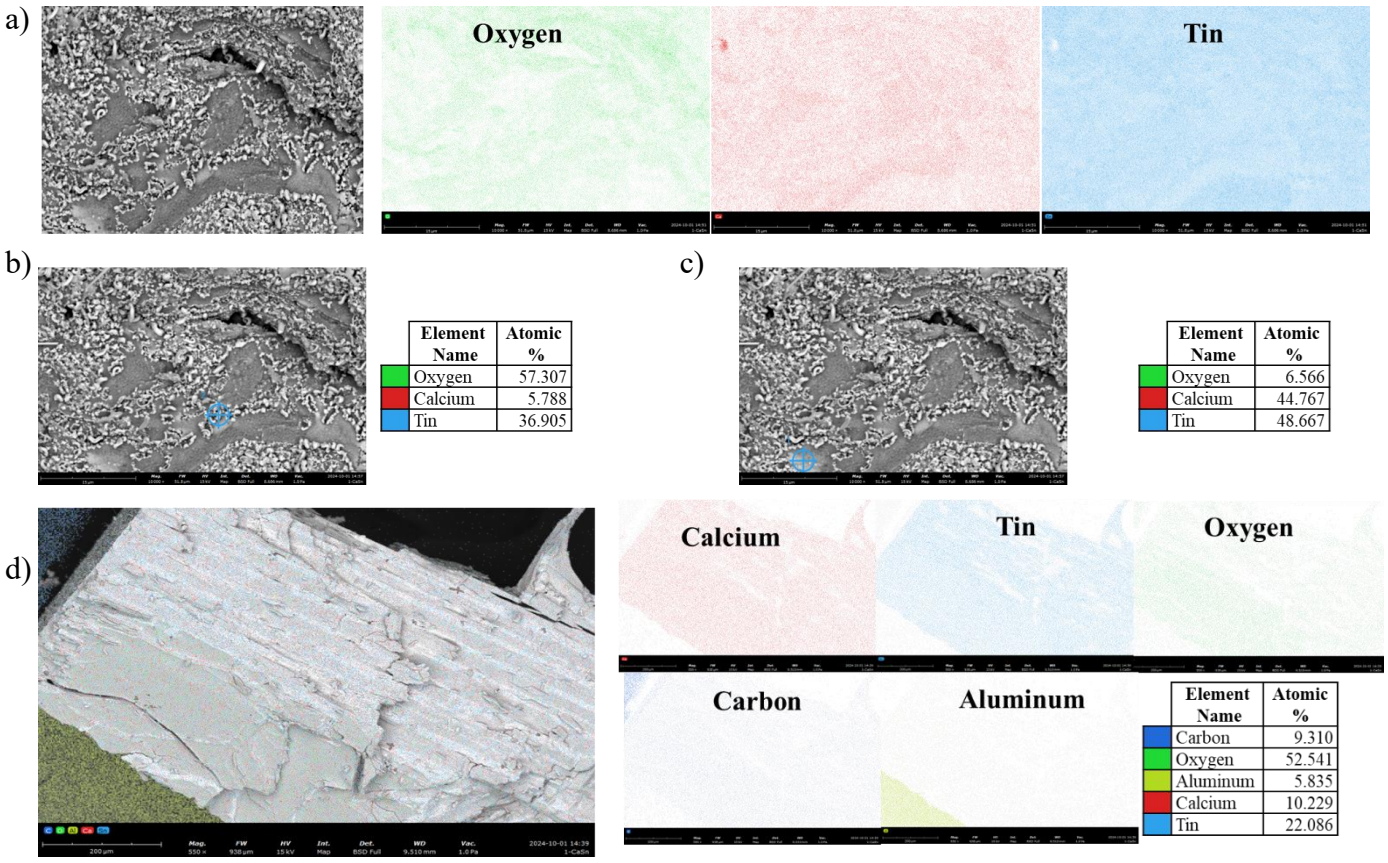

Figure 5.23 (a) and (d) SEM image and corresponding EDX elemental distribution on the right; (b) and (c) show point EDX analyses on different morphologies, with the corresponding elemental composition tables on the right.

The XRD patterns presented in Figure 5.24 illustrate the crystalline phases present in Ca–Sn alloys with varying Ca:Sn atomic ratios. As expected, all diffractograms present a multiphase composition. In particular, for the CaSn sample (1:1 atomic ratio, top panel), the dominant peaks correspond to the CaSn phase, with minor contributions from Ca_2Sn and trace amounts of $Ca_{0.15}Sn_{0.85}$. As the calcium content decreases (moving downward through the panels), the diffraction peaks progressively shift toward Sn-rich phases such as $CaSn_3$ and $Ca_{0.15}Sn_{0.85}$ indicating the successful formation of different intermetallic compounds depending on the initial stoichiometry. In samples with a higher Sn content, reflections associated with Sn-rich phases such as $CaSn_3$ become more prominent. Moreover, several samples display additional peaks attributable to CaO, suggesting partial surface oxidation of the

alloys, likely due to brief exposure to air during sample transfer in which calcium, being highly reactive, is particularly affected.

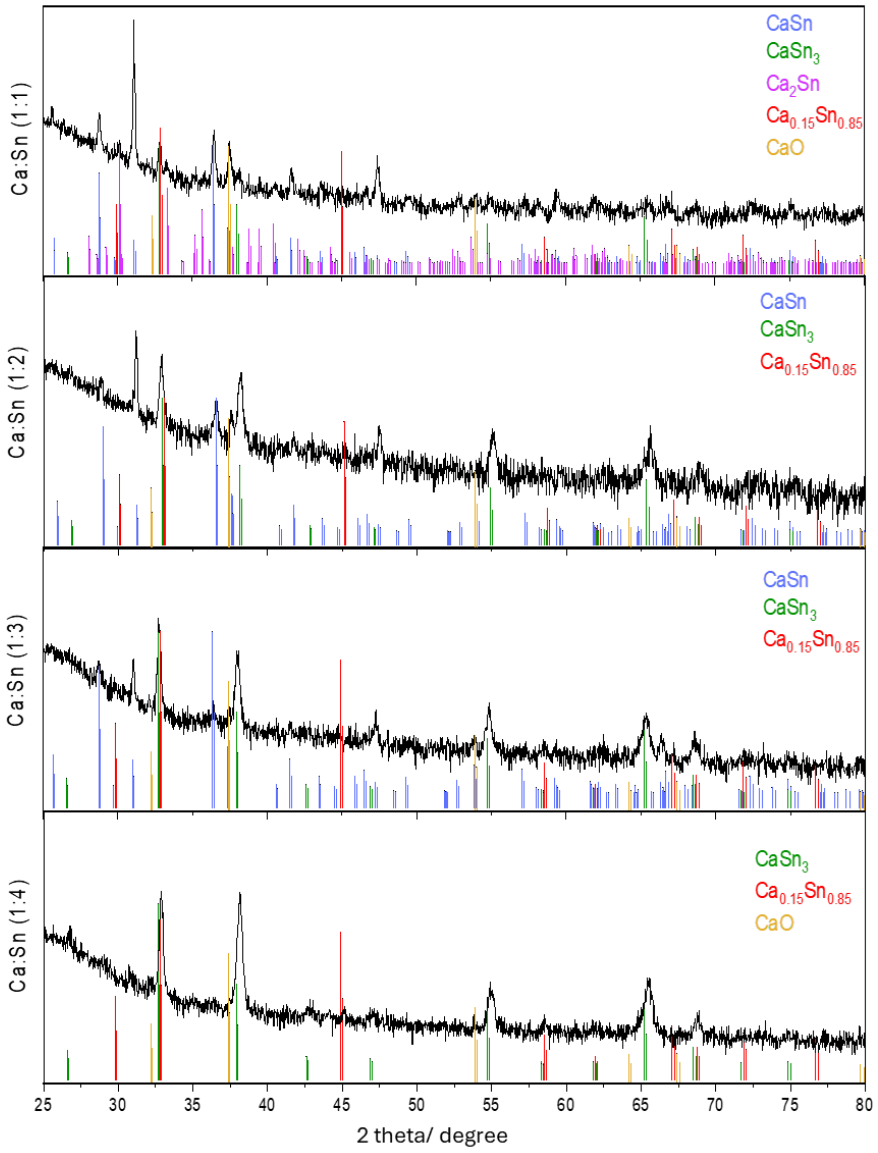

Figure 5.24. XRD patterns of Ca–Sn alloys with varying Ca:Sn atomic ratios synthesized via arc melting, compared with standard reference patterns from the ICSD database for the following phases: CaO (ICSD 26959), Ca_2Sn (ICSD 659611), $CaSn_3$ (ICSD 58934), CaSn (ICSD 165193), and $Ca_{0.15}Sn_{0.85}$ (ICSD 58963).

ICP-OES analysis reveals that increasing the Sn content in the precursor mixture leads to a weaker correlation between the nominal and the experimentally measured Sn/Ca atomic ratios (Table 7.). This discrepancy is likely attributed to the relatively high vapor pressure of tin, which is not only significantly higher than that of calcium but also exceeds that of zinc. For instance, at 1200 °C, tin exhibits a vapor pressure of approximately 10 kPa, compared to ~1 kPa for zinc and even lower values for calcium (~0.1 kPa).[83,84] This substantial volatility difference may explain why a partial loss of Sn is observed during arc melting, particularly at higher tin concentrations, while such effects are negligible in the Ca–Zn system.

Table 7 ICP-OES results.

Sample	ppm Ca (RDS%)	ppm Sn (RDS%)	Mol. Ratio Sn/Ca
Ca Sn (1:1)	0.87(0.26)	2.9(0.83)	1.126 ± 0.0012
Ca Sn (1:2)	0.59(0.11)	3.39(0.56)	1.940 ± 0.013
Ca Sn (1:3)	0.5(1.02)	3.38(0.44)	2.283 ± 0.034
Ca Sn (1:4)	0.4(1.03)	3.67(0.51)	3.098 ± 0.048

The CV profiles of Ca–Sn alloys with varying Ca/Sn ratios, shown in Figure 5.25, clearly indicate that all compositions exhibit pronounced current responses during the first cycle. However, these responses significantly fade in the subsequent cycles, indicating partial or full electrochemical deactivation, except for the CaSn 1:4 alloy, which shows a slight activation behavior. In this latter case, two symmetric redox peaks emerge, corresponding to reduction and oxidation processes, with an overpotential of approximately 0.8 V and current densities around 100 mA g^{-1}.

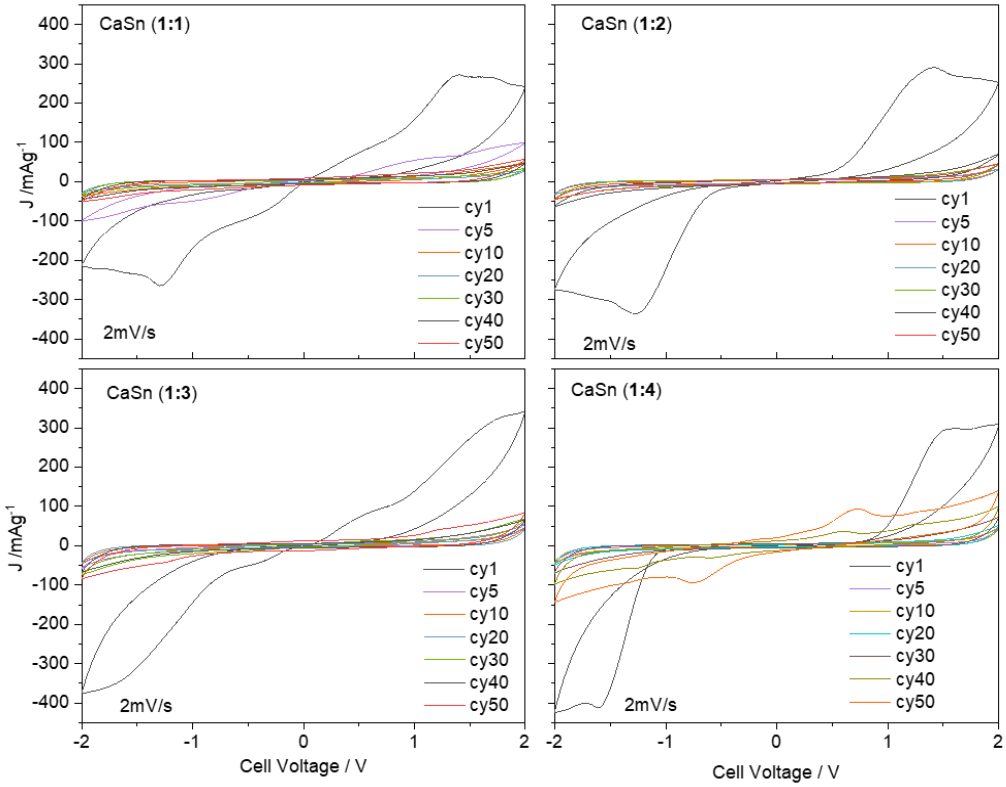

Figure 5.25 CV in symmetric cell configuration of the CaSn alloy with the different Sn/Ca ratio

Similarly, the galvanostatic curves (Figure 5.26) exhibit a comparable trend, although the extent of deactivation appears less pronounced and more gradual over cycling. All compositions exhibit low overpotentials during the initial cycles, with well-defined voltage plateaus suggestive of faradaic processes. Interestingly, while the CV data show decreasing activity with increasing Sn content, the

galvanostatic profiles indicate that overpotentials actually increase with higher Sn ratios. Nonetheless, in all cases, the overpotential remains below 0.5 V during the initial cycles, but exceeds 1 V in the subsequent ones, highlighting a general degradation in electrochemical reversibility over time. The observed deactivation during cycling and the progressive increase in overpotentials during further cycling can likely be attributed to a combination of mechanical instability caused by the volume expansion associated with alloying/dealloying processes, and the thickening of the SEI. Such performance degradation, reflected in increasing overpotentials and capacity fading during prolonged cycling, may be attributed to both mechanical instability caused by the significant volume expansion/contraction during alloying and dealloying processes, and to the progressive thickening of the sSEI. Notably, both phenomena have already been reported in literature as common failure mechanisms in alloying-type anodes for multivalent ion batteries.[7,69]

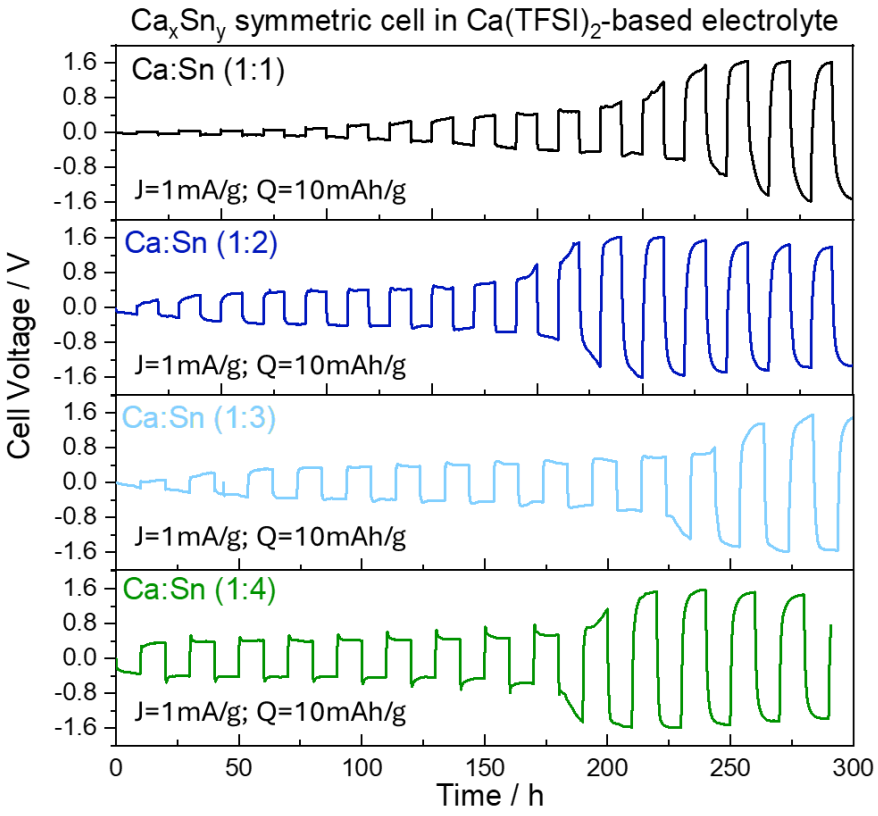

Figure 5.26 GC in symmetric cell configuration of the Ca-Sn alloy with the different Sn/Ca ratio

5.5.3 Conclusion

In this study, a preliminary investigation was carried out on the synthesis and electrochemical behavior of Ca–Sn alloys with different Ca/Sn atomic ratios. The arc melting technique confirmed its effectiveness as a rapid and reliable method for alloy preparation. However, issues related to the homogeneity of the final materials were observed, likely due to the high volatility of tin and its partial evaporation during synthesis.

All tested compositions exhibited promising electrochemical activity, particularly under galvanostatic cycling. Despite this, a progressive increase in overpotential during subsequent cycles was noted, indicating a gradual loss of electrochemical reversibility.

The causes of this performance degradation, potentially linked to structural instability caused by volume expansion or to the thickening of the solid electrolyte interphase, [67,85] require further dedicated investigation. Identifying the most stable and reversible composition will be essential for future studies, which should also focus on optimizing the working voltage range to improve the long-term stability and performance of these alloy-based electrodes.

5.6 Bibliography

(1) Stievano, L.; de Meatza, I.; Bitenc, J.; Cavallo, C.; Brutti, S.; Navarra, M. A. Emerging Calcium Batteries. *J Power Sources* 2021, *482*, 228875. https://doi.org/10.1016/J.JPOWSOUR.2020.228875.

(2) Xu, W.; Lerner, M. M. A New and Facile Route Using Electride Solutions to Intercalate Alkaline Earth Ions into Graphite. *Chemistry of Materials* 2018, *30* (19), 6930–6935. https://doi.org/10.1021/ACS.CHEMMATER.8B03421/SUPPL_FILE/CM8B03421_SI_001.PDF.

(3) Oltra, R.; Vuillemin Vuillemin, B.; Thebault, F.; -, al; Chintalapalle Ramana, O. V; Zaghib, K.; Mauger, A.; Takeuchi, S.; Iriyama, Y.; Abe, T.; Ogumi, Z. Electrochemical Intercalation of Calcium Ion into Graphite Electrode. *ECS Meeting Abstracts* 2008, *MA2008-02* (1), 206. https://doi.org/10.1149/MA2008-02/1/206.

(4) *Calcium Isotope Effects Accompanying Electrochemical Insertion of Calcium into Graphite from Electrolyte Solution*. https://www.jstage.jst.go.jp/article/radioisotopes/60/7/60_7_265/_article (accessed 2025-07-21).

(5) Richard Prabakar, S. J.; Bhairuba Ikhe, A.; Bae Park, W.; Chung, K.-C.; Park, H.; Kim, K.-J.; Ahn, D.; Seop Kwak, J.; Sohn, K.-S.; Pyo, M.; R Prabakar, S. J.; Ikhe, A. B.; Kwak, J. S.; Pyo, M.; Park, W. B.; Sohn, K.; Chung, K.; Park, H.; Kim, K.; Ahn, D. Graphite as a Long-Life Ca2+-Intercalation Anode and Its Implementation for Rocking-Chair Type Calcium-Ion Batteries. *Advanced Science* 2019, *6* (24), 1902129. https://doi.org/10.1002/ADVS.201902129.

(6) Park, J.; Xu, Z.-L.; Yoon, G.; Kwan Park, S.; Wang, J.; Hyun, H.; Park, H.; Lim, J.; Ko, Y.-J.; Soo Yun, Y.; Kang, K.; Park, J.; Xu, Z.; Yoon, G.; Park, S. K.; Park, H.; Kang, K.; Wang, J.; Hyun, H.; Lim, J.; Ko, Y.; Yun, Y. S. Stable and High-Power Calcium-Ion Batteries Enabled by Calcium Intercalation into Graphite. *Advanced Materials* 2020, *32* (4), 1904411. https://doi.org/10.1002/ADMA.201904411.

(7) Ji, B.; He, H.; Yao, W.; Tang, Y. Recent Advances and Perspectives on Calcium-Ion Storage: Key Materials and Devices. *Advanced Materials* 2021, *33* (2). https://doi.org/10.1002/ADMA.202005501.

(8) Zhao, B.; Ran, R.; Liu, M.; Shao, Z. A Comprehensive Review of Li4Ti5O12-Based Electrodes for Lithium-Ion Batteries: The Latest Advancements and Future Perspectives. *Materials Science and Engineering: R: Reports* 2015, *98*, 1–71. https://doi.org/10.1016/J.MSER.2015.10.001.

(9) Lee, C. H.; Kim, C. S.; Jeong, S. K. Electrochemical Properties of Li4Ti5O12 as a Negative Electrode for Calcium Secondary Batteries in Ca(TFSI)2/THF Electrolyte. *Key Eng Mater* 2017, *724*, 97–101. https://doi.org/10.4028/WWW.SCIENTIFIC.NET/KEM.724.97.

(10) Wang, Y.; Song, N.; Song, X.; Zhang, T.; Zhang, Q.; Li, M. Metallic VO2 Monolayer as an Anode Material for Li, Na, K, Mg or Ca Ion Storage: A First-Principle Study. *RSC Adv* 2018, *8* (20), 10848–10854. https://doi.org/10.1039/C8RA00861B.

(11) Rao, Y. C.; Yu, S.; Gu, X.; Duan, X. M. Prediction of MoO2 as High Capacity Electrode Material for (Na, K, Ca)-Ion Batteries. *Appl Surf Sci* 2019, *479*, 64–69. https://doi.org/10.1016/J.APSUSC.2019.01.206.

(12) Weng, S.; Yang, G.; Zhang, S.; Liu, X.; Zhang, X.; Liu, Z.; Cao, M.; Ateş, M. N.; Li, Y.; Chen, L.; Wang, Z.; Wang, X. Kinetic Limits of Graphite Anode for Fast-Charging Lithium-Ion Batteries. *Nanomicro Lett* 2023, *15* (1). https://doi.org/10.1007/s40820-023-01183-6.

(13) Tian, Y.; Yang, H.; Zeng, Y.; Qi, Y.; Wang, W.; Chen, H.; Yin, W.; Ke, Y.; Jian, Z.; Kan, W. H.; Kan, W. H.; Chen, W. Design of High-Performance Defective Graphite-Type Anodes for Sodium-Ion Batteries. *ACS Appl Energy Mater* 2023, *6* (7), 3854–3861. https://doi.org/10.1021/acsaem.2c04140.

(14) Zhao, X.; Wang, H.-E.; Chen, X.; Cao, J.; Zhao, Y.; Garbe Neale, Z.; Cai, W.; Sui, J.; Cao, G. Tubular MoO<inf>2</Inf> Organized by 2D Assemblies for Fast and Durable Alkali-Ion Storage. *Energy Storage Mater* 2018, *11*, 161–169. https://doi.org/10.1016/j.ensm.2017.10.010.

(15) Reeves, K. G.; Ma, J.; Fukunishi, M.; Salanne, M.; Komaba, S.; Dambournet, D. Insights into Li^+, Na^+, and K^+ Intercalation in Lepidocrocite-Type Layered TiO<inf>2</Inf> Structures. *ACS Appl Energy Mater* 2018, *1* (5), 2078–2086. https://doi.org/10.1021/acsaem.8b00170.

(16) Duan, L.; Li, X. Lithiated Mo<inf>4</Inf>O<inf>11</Inf> to Improve Excellent Cycle Stability of MoO<inf>2</Inf> Nanoparticles for Lithium-Ion Battery. *Synth Met* 2021, *272*. https://doi.org/10.1016/j.synthmet.2020.116672.

(17) Gentili, V.; Brutti, S.; Hardwick, L. J.; Armstrong, A. R.; Panero, S.; Bruce, P. G. Lithium Insertion into Anatase Nanotubes. *Chemistry of Materials* 2012, *24* (22), 4468–4476. https://doi.org/10.1021/cm302912f.

(18) Proffit, D. L.; Fister, T. T.; Kim, S.; Pan, B.; Liao, C.; Vaughey, J. T. Utilization of Ca K-Edge X-Ray Absorption Near Edge Structure to Identify Intercalation in Potential Multivalent Battery Materials. *J Electrochem Soc* 2016, *163* (13), A2508–A2514. https://doi.org/10.1149/2.0121613jes.

(19) Marini, U.; Marconi, B.; Petri, A.; Cicco, A. Di; Rosolen, M. J.; Marassi, R.; Aquilanti, G.; Minicucci, M.; Principi, E.; Novello, N.; Cognigni, A.; Olivi, L. Novel XAFS Capabilities at ELETTRA Synchrotron Light Source. *J Phys Conf Ser* 2009, *190* (1), 012043. https://doi.org/10.1088/1742-6596/190/1/012043.

(20) D'Angelo, P.; Petit, P. E.; Pavel, N. V. Double-Electron Excitation Channels at the Ca2+ K-Edge of Hydrated Calcium Ion. *Journal of Physical Chemistry B* 2004, *108* (31), 11857–11865. https://doi.org/10.1021/JP048511L/ASSET/IMAGES/LARGE/JP048511LF00006.JPEG.

(21) Filipponi, A. a; Di Cicco, A. b; Natoli, C. R. c. X-Ray-Absorption Spectroscopy and n-Body Distribution Functions in Condensed Matter. I. Theory. *Phys Rev B* 1995, *52* (21), 15122–15134. https://doi.org/10.1103/PhysRevB.52.15122.

(22) Filipponi, A. a; Di Cicco, A. b. X-Ray-Absorption Spectroscopy and n-Body Distribution Functions in Condensed Matter. II. Data Analysis and Applications. *Phys Rev B* 1995, *52* (21), 15135–15149. https://doi.org/10.1103/PhysRevB.52.15135.

(23) Hedin, L.; Lundqvist, S. Effects of Electron-Electron and Electron-Phonon Interactions on the One-Electron States of Solids. *Solid State Physics - Advances in Research and Applications* 1970, *23* (C), 1–181. https://doi.org/10.1016/S0081-1947(08)60615-3.

(24) Busato, M.; Melchior, A.; Migliorati, V.; Colella, A.; Persson, I.; Mancini, G.; Veclani, D.; D'Angelo, P. Elusive Coordination of the Ag+Ion in Aqueous Solution: Evidence for a Linear

Structure. *Inorg Chem* 2020, *59* (23), 17291–17302. https://doi.org/10.1021/ACS.INORGCHEM.0C02494/SUPPL_FILE/IC0C02494_SI_001.PDF.

(25) van Bokhoven, J. A.; Lamberti, C. X-Ray Absorption and X-Ray Emission Spectroscopy: Theory and Applications. *X-Ray Absorption and X-Ray Emission Spectroscopy: Theory and Applications* 2015, *1–2*, 1–845. https://doi.org/10.1002/9781118844243.

(26) Ohsaka, T.; Izumi, F.; Fujiki, Y. Raman Spectrum of Anatase, TiO2. *Journal of Raman Spectroscopy* 1978, *7* (6), 321–324. https://doi.org/10.1002/JRS.1250070606.

(27) Beuvier, T.; Richard-Plouet, M.; Brohan, L. Accurate Methods for Quantifying the Relative Ratio of Anatase and TiO 2(B) Nanoparticles. *Journal of Physical Chemistry C* 2009, *113* (31), 13703–13706. https://doi.org/10.1021/JP903755P.

(28) Salari, M.; Konstantinov, K.; Liu, H. K. Enhancement of the Capacitance in TiO 2 Nanotubes through Controlled Introduction of Oxygen Vacancies. https://doi.org/10.1039/c0jm04085a.

(29) Rendón-Rivera, A.; Toledo-Antonio, J. A.; Cortés-Jácome, M. A.; Angeles-Chávez, C. Generation of Highly Reactive OH Groups at the Surface of TiO 2 Nanotubes. *Catal Today* 2011, *166*, 18–24. https://doi.org/10.1016/j.cattod.2010.03.045.

(30) Tamilselvan, A.; Balakumar, S. Anatase TiO2 Nanotube by Electrochemical Anodization Method: Effect of Tubes Dimension on the Supercapacitor Application. *Ionics (Kiel)* 2016, *22* (1), 99–105. https://doi.org/10.1007/S11581-015-1526-8/METRICS.

(31) Hardwick, L. J.; Holzapfel, M.; Novák, P.; Dupont, L.; Baudrin, E. Electrochemical Lithium Insertion into Anatase-Type TiO2: An in Situ Raman Microscopy Investigation. *Electrochim Acta* 2007, *52* (17), 5357–5367. https://doi.org/10.1016/J.ELECTACTA.2007.02.050.

(32) Zakharova, G. S. TiO2 (Anatase) Films Nanotubes. *Russian Journal of Inorganic Chemistry* 2014, *59* (2), 24–28. https://doi.org/10.1134/S0036023614020235/METRICS.

(33) Single Crystal Laser Raman Spectroscopy. *Proc R Soc Lond A Math Phys Sci* 1968, *307* (1491), 407–429. https://doi.org/10.1098/RSPA.1968.0199.

(34) Hodos, M.; Haspel, H.; Horváth, E.; Kukovecz, Á.; Kónya, Z.; Kiricsi, I. Vibrational Spectroscopic Studies on the Formation of Ion-Exchangeable Titania Nanotubes. *AIP Conf Proc* 2005, *786*, 345–348. https://doi.org/10.1063/1.2103884.

(35) Gentili, V.; Brutti, S.; Hardwick, L. J.; Armstrong, A. R.; Panero, S.; Bruce, P. G. Lithium Insertion into Anatase Nanotubes. *Chemistry of Materials* 2012, *24* (22), 4468–4476. https://doi.org/10.1021/CM302912F/SUPPL_FILE/CM302912F_SI_001.PDF.

(36) Hamdan, S. A.; Ibrahim, I. M.; Ali, I. M. COMPARISON OF ANATASE AND RUTILE TiO 2 NANOSTRUCTURE FOR GAS SENSING APPLICATION. *Dig J Nanomater Biostruct 15* (4), 1001–1008.

(37) Salomatina, E. V.; Loginova, A. S.; Ignatov, S.; Knyazev, A. V.; Spirina, I. V.; Smirnova, L. A. Structure and Catalytic Activity of Poly(Titanium Oxide) Doped by Gold Nanoparticles in Organic Polymeric Matrix. *J Inorg Organomet Polym Mater* 2016, *26* (6), 1280–1291. https://doi.org/10.1007/S10904-016-0409-4.

(38) Oh, S. W.; Park, S. H.; Sun, Y. K. Hydrothermal Synthesis of Nano-Sized Anatase TiO2 Powders for Lithium Secondary Anode Materials. *J Power Sources* 2006, *161* (2), 1314–1318. https://doi.org/10.1016/J.JPOWSOUR.2006.05.050.

(39) Forero-Saboya, J.; Davoisne, C.; Dedryvère, R.; Yousef, I.; Canepa, P.; Ponrouch, A. Understanding the Nature of the Passivation Layer Enabling Reversible Calcium Plating. *Energy Environ. Sci.* 2020, *13* (10), 3423–3431. https://doi.org/10.1039/d0ee02347g.

(40) Wang, D.; Gao, X.; Chen, Y.; Jin, L.; Kuss, C.; Bruce, P. G. Plating and Stripping Calcium in an Organic Electrolyte. *Nature Mater.* 2018, *17*, 16–20. https://doi.org/10.1038/nmat5036.

(41) Shyamsunder, A.; Blanc, L. E.; Assoud, A.; Nazar, L. F. Reversible Calcium Plating and Stripping at Room Temperature Using a Borate Salt. *ACS Energy Lett* 2019, *4* (9), 2271–2276. https://doi.org/10.1021/ACSENERGYLETT.9B01550/ASSET/IMAGES/LARGE/NZ9B01550_0004.JPEG.

(42) Liu, X.; Elia, G. A.; Passerini, S. Evaluation of Counter and Reference Electrodes for the Investigation of Ca Battery Materials. *Journal of Power Sources Advances* 2020, *2*. https://doi.org/10.1016/J.POWERA.2020.100008.

(43) Li, Z.; Fuhr, O.; Fichtner, M.; Zhao-Karger, Z. Towards Stable and Efficient Electrolytes for Room-Temperature Rechargeable Calcium Batteries. *Energy Environ Sci* 2019, *12* (12), 3496–3501. https://doi.org/10.1039/C9EE01699F.

(44) Yang, Z.; Choi, D.; Kerisit, S.; Rosso, K. M.; Wang, D.; Zhang, J.; Graff, G.; Liu, J. Nanostructures and Lithium Electrochemical Reactivity of Lithium Titanites and Titanium Oxides: A Review. *J Power Sources* 2009, *192* (2), 588–598. https://doi.org/10.1016/J.JPOWSOUR.2009.02.038.

(45) Wei, Q.; Chang, X.; Butts, D.; DeBlock, R.; Lan, K.; Li, J.; Chao, D.; Peng, D. L.; Dunn, B. Surface-Redox Sodium-Ion Storage in Anatase Titanium Oxide. *Nature Communications 2023 14:1* 2023, *14* (1), 1–9. https://doi.org/10.1038/s41467-022-35617-3.

(46) Rossi, T. C.; Grolimund, D.; Nachtegaal, M.; Cannelli, O.; Mancini, G. F.; Bacellar, C.; Kinschel, D.; Rouxel, J. R.; Ohannessian, N.; Pergolesi, D.; Lippert, T.; Chergui, M. X-Ray Absorption Linear Dichroism at the Ti K Edge of Anatase TiO2 Single Crystals. *Phys Rev B* 2019, *10* (24), 245207. https://doi.org/10.1103/PHYSREVB.100.245207/FIGURES/7/MEDIUM.

(47) Luca, V. Comparison of Size-Dependent Structural and Electronic Properties of Anatase and Rutile Nanoparticles. *Journal of Physical Chemistry C* 2009, *113* (16), 6367–6380. https://doi.org/10.1021/JP808358V/SUPPL_FILE/JP808358V_SI_001.PDF.

(48) Angelomé, P. C.; Andrini, L.; Calvo, M. E.; Requejo, F. G.; Bilmes, S. A.; Soler-Illia, G. J. A. A. Mesoporous Anatase TiO2 Films: Use of Ti K XANES for the Quantification of the Nanocrystalline Character and Substrate Effects in the Photocatalysis Behavior. *Journal of Physical Chemistry C* 2007, *111* (29), 10886–10893. https://doi.org/10.1021/JP069020Z/SUPPL_FILE/JP069020ZSI20061229_102013.PDF.

(49) Yamamoto, T. Assignment of Pre-Edge Peaks in K-Edge x-Ray Absorption Spectra of 3d Transition Metal Compounds: Electric Dipole or Quadrupole? *X-Ray Spectrometry* 2008, *37* (6), 572–584. https://doi.org/10.1002/XRS.1103.

(50) Cabaret, D.; Bordage, A.; Juhin, A.; Arfaoui, M.; Gaudry, E. First-Principles Calculations of X-Ray Absorption Spectra at the K-Edge of 3d Transition Metals: An Electronic Structure Analysis of the

Pre-Edge. *Physical Chemistry Chemical Physics* 2010, *12* (21), 5619–5633. https://doi.org/10.1039/B926499J.

(51) Schneider, K.; Zajac, D.; Sikora, M.; Kapusta, C.; Michalow-Mauke, K.; Graule, T.; Rekas, M. XAS Study of TiO2-Based Nanomaterials. *Radiation Physics and Chemistry* 2015, *112*, 195–198. https://doi.org/10.1016/J.RADPHYSCHEM.2015.03.010.

(52) Joly, Y.; Cabaret, D.; Renevier, H.; Natoli, C. R. Electron Population Analysis by Full-Potential X-Ray Absorption Simulations. *Phys Rev Lett* 1999, *82* (11), 2398. https://doi.org/10.1103/PhysRevLett.82.2398.

(53) Farges, F.; Brown, G. E. Ti K-Edge XANES Studies of Ti Coordination and Disorder in Oxide Compounds: Comparison between Theory and Experiment. *Phys Rev B* 1997, *56* (4), 1809. https://doi.org/10.1103/PhysRevB.56.1809.

(54) Greco, G.; Mazzio, K. A.; Dou, X.; Gericke, E.; Wendt, R.; Krumrey, M.; Passerini, S. Structural Study of Carbon-Coated TiO2 Anatase Nanoparticles as High-Performance Anode Materials for Na-Ion Batteries. *ACS Appl Energy Mater* 2019, *2* (10), 7142–7151. https://doi.org/10.1021/ACSAEM.9B01101/ASSET/IMAGES/LARGE/AE9B01101_0008.JPEG.

(55) Siebert, A.; Dou, X.; Garcia-Diez, R.; Buchholz, D.; Félix, R.; Handick, E.; Greco, G.; Hasa, I.; Wilks, R. G.; Passerini, S.; Bär, M. Monitoring the Sodiation Mechanism of Anatase TiO2Nanoparticle-Based Electrodes for Sodium-Ion Batteries by Operando XANES Measurements. *ACS Appl Energy Mater* 2021, *4* (1), 164–175. https://doi.org/10.1021/ACSAEM.0C02025/SUPPL_FILE/AE0C02025_SI_001.PDF.

(56) Ceppetelli, A.; Busato, M.; Dilena, G.; Cavallo, C.; Navarra, M. A.; D'Angelo, P.; Silvestri, L.; Reale, P.; Santoni, A.; Stievano, L.; Brutti, S. Evidence of the Electrochemical Ca2+ Intercalation in Anatase Nanotubes. *Batter Supercaps* 2024, *7* (9). https://doi.org/10.1002/BATT.202400183.

(57) Wang, D.; Liu, L.; Sun, X.; Sham, T. K. Observation of Lithiation-Induced Structural Variations in TiO2 Nanotube Arrays by X-Ray Absorption Fine Structure. *J Mater Chem A Mater* 2014, *3* (1), 412–419. https://doi.org/10.1039/C4TA04873C.

(58) Fehse, M.; Monconduit, L.; Fischer, F.; Tessier, C.; Stievano, L. Study of the Insertion Mechanism of Lithium into Anatase by Operando X-Ray Diffraction and Absorption Spectroscopy. *Solid State Ion* 2014, *268* (PB), 252–255. https://doi.org/10.1016/J.SSI.2014.09.018.

(59) Lafont, U.; Carta, D.; Mountjoy, G.; Chadwick, A. V.; Kelder, E. M. In Situ Structural Changes upon Electrochemical Lithium Insertion in Nanosized Anatase TiO2. *Journal of Physical Chemistry C* 2010, *114* (2), 1372–1378. https://doi.org/10.1021/JP908786T/ASSET/IMAGES/MEDIUM/JP-2009-08786T_0010.GIF.

(60) Luca, V.; Hanley, T. L.; Roberts, N. K.; Howe, R. F. NMR and X-Ray Absorption Study of Lithium Intercalation in Micro- and Nanocrystalline Anatase. *ChemInform* 1999, *30* (43), no-no. https://doi.org/10.1002/CHIN.199943012.

(61) Ma, J.; Li, W.; Morgan, B. J.; Światowska, J.; Baddour-Hadjean, R.; Body, M.; Legein, C.; Borkiewicz, O. J.; Leclerc, S.; Groult, H.; Lantelme, F.; Laberty-Robert, C.; Dambournet, D. Lithium Intercalation in Anatase Titanium Vacancies and the Role of Local Anionic Environment. *Chem. Mater.* 2018, *30* (9), 3078–3089. https://doi.org/10.1021/acs.chemmater.8b00925.

(62) Li, J.; Liu, J.; Sun, Q.; Banis, M. N.; Sun, X.; Sham, T. K. Tracking the Effect of Sodium Insertion/Extraction in Amorphous and Anatase TiO2 Nanotubes. *Journal of Physical Chemistry C* 2017, *121* (21), 11773–11782. https://doi.org/10.1021/ACS.JPCC.7B01106/SUPPL_FILE/JP7B01106_SI_001.PDF.

(63) Li, W.; Fukunishi, M.; Morgan, B. J.; Borkiewicz, O. J.; Chapman, K. W.; Pralong, V.; Maignan, A.; Lebedev, O. I.; Ma, J.; Groult, H.; Komaba, S.; Dambournet, D. A Reversible Phase Transition for Sodium Insertion in Anatase TiO2. *Chem. Mater.* 2017, *29* (4), 1836–1844. https://doi.org/10.1021/acs.chemmater.7b00098.

(64) Shannon, B. Y. R. D.; H, M.; Baur, N. H.; Gibbs, O. H.; Eu, M.; Cu, V. Revised Effective Ionic Radii and Systematic Studies of Interatomic Distances in Halides and Chalcogenides. *Acta Crystallogr* 1976, *A32*, 751-767.

(65) Jalilehvand, F.; Spångberg, D.; Lindqvist-Reis, P.; Hermansson, K.; Persson, I.; Sandström, M. Hydration of the Calcium Ion. An EXAFS,Large-Angle X-Ray Scattering, and Molecular Dynamics Simulation Study. *J Am Chem Soc* 2001, *123* (3), 431–441. https://doi.org/10.1021/JA001533A/SUPPL_FILE/JA001533A_S.PDF.

(66) Akimoto, J.; Takei, H. Synthesis and Crystal Structure of NaTi2O4: A New Mixed-Valence Sodium Titanate. *J Solid State Chem* 1989, *79* (2), 212–217. https://doi.org/10.1016/0022-4596(89)90268-5.

(67) Yao, Z.; Hegde, V. I.; Aspuru-Guzik, A.; Wolverton, C.; Yao, Z.; Aspuru-Guzik, A.; Hegde, V. I.; Wolverton, C. Discovery of Calcium-Metal Alloy Anodes for Reversible Ca-Ion Batteries Ca-Ion Batteries. 2019. https://doi.org/10.1002/aenm.201802994.

(68) Liu, C.; Li, F.; Lai-Peng, M.; Cheng, H. M. Advanced Materials for Energy Storage. *Advanced Materials* 2010, *22* (8), E28–E62. https://doi.org/10.1002/ADMA.200903328.

(69) Lipson, A. L.; Pan, B.; Lapidus, S. H.; Liao, C.; Vaughey, J. T.; Ingram, B. J. Rechargeable Ca-Ion Batteries: A New Energy Storage System. *Chemistry of Materials* 2015, *27* (24), 8442–8447. https://doi.org/10.1021/ACS.CHEMMATER.5B04027/SUPPL_FILE/CM5B04027_SI_001.PDF.

(70) Ponrouch, A.; Tchitchekova, D.; Frontera, C.; Bardé, F.; Dompablo, M. E. A. De; Palacín, M. R. Assessing Si-Based Anodes for Ca-Ion Batteries: Electrochemical Decalciation of CaSi2. *Electrochem commun* 2016, *66*, 75–78. https://doi.org/10.1016/J.ELECOM.2016.03.004.

(71) Yao, Z.; Hegde, V. I.; Aspuru-Guzik, A.; Wolverton, C. Discovery of Calcium-Metal Alloy Anodes for Reversible Ca-Ion Batteries. *Adv Energy Mater* 2019, *9* (9). https://doi.org/10.1002/AENM.201802994.

(72) Biria, S.; Pathreeker, S.; Genier, F. S.; Hosein, I. D. A Highly Conductive and Thermally Stable Ionic Liquid Gel Electrolyte for Calcium-Ion Batteries. *ACS Appl Polym Mater* 2020, *2* (6), 2111–2118. https://doi.org/10.1021/ACSAPM.9B01223/SUPPL_FILE/AP9B01223_SI_001.PDF.

(73) Zhao-Karger, Z.; Xiu, Y.; Li, Z.; Reupert, A.; Smok, T.; Fichtner, M. Calcium-Tin Alloys as Anodes for Rechargeable Non-Aqueous Calcium-Ion Batteries at Room Temperature. *Nature Communications 2022 13:1* 2022, *13* (1), 1–9. https://doi.org/10.1038/s41467-022-31261-z.

(74) Lužanin, O.; Lautar, A. K.; Pavčnik, T.; Bitenc, J. Paving the Way for Future Ca Metal Batteries through Comprehensive Electrochemical Testing of Organic Polymer Cathodes. *Mater Adv* 2024, *5* (2), 642–651. https://doi.org/10.1039/D3MA00805C.

(75) Li, K.; Wang, Y.; Gao, B.; Lv, X.; Si, Z.; Wang, H. guo. Conjugated Microporous Polyarylimides Immobilization on Carbon Nanotubes with Improved Utilization of Carbonyls as Cathode Materials for Lithium/Sodium-Ion Batteries. *J Colloid Interface Sci* 2021, *601*, 446–453. https://doi.org/10.1016/J.JCIS.2021.05.081.

(76) Avila Cardenas, A.; Herlin-Boime, N.; Haon, C.; Monconduit, L. Si1-XGex Alloys as Negative Electrode for Li-Ion Batteries: Impact of Morphology in the Li+ Diffusion, Performance and Mechanism. *Electrochim Acta* 2024, *475*, 143691. https://doi.org/10.1016/J.ELECTACTA.2023.143691.

(77) Serrano-Sánchez, F.; Gharsallah, M.; Nemes, N. M.; Biskup, N.; Varela, M.; Martínez, J. L.; Fernández-Díaz, M. T.; Alonso, J. A. Enhanced Figure of Merit in Nanostructured (Bi,Sb) 2 Te 3 with Optimized Composition, Prepared by a Straightforward Arc-Melting Procedure OPEN. 2017. https://doi.org/10.1038/s41598-017-05428-4.

(78) Hinte, C.; Fantin, A.; Barienti, K.; Herbst, S.; Frenzel, J.; Eggeler, G.; Maier, H. J. A Comparative Study on Arc- and Vacuum Induction-Melting for Ti16.6Zr16.6Hf16.6Co10Ni20Cu20 High Entropy Shape Memory Alloy Production. *Discov Mater* 2024, *4* (1), 1–9. https://doi.org/10.1007/S43939-024-00134-1/TABLES/1.

(79) Fornasini, M. L.; Merlo, F. CaZn3: A Structure with Mixed BaLi4- and CeCu2-like Ordering. *urn:issn:0567-7408* 1980, *36* (8), 1739–1744. https://doi.org/10.1107/S0567740880007133.

(80) Li, C.; Guha, R. D.; Shyamsunder, A.; Persson, K. A.; Nazar, L. F. A Weakly Ion Pairing Electrolyte Designed for High Voltage Magnesium Batteries. *Energy Environ Sci* 2024, *17* (1), 190–201. https://doi.org/10.1039/D3EE02861E.

(81) Arroyo-De Dompablo, M. E.; Ponrouch, A.; Johansson, P.; Palacín, M. R. Achievements, Challenges, and Prospects of Calcium Batteries. *Chem Rev* 2020, *120* (14), 6331–6357. https://doi.org/10.1021/ACS.CHEMREV.9B00339/ASSET/IMAGES/LARGE/CR9B00339_0016.JPEG.

(82) Stievano, L.; de Meatza, I.; Bitenc, J.; Cavallo, C.; Brutti, S.; Navarra, M. A. Emerging Calcium Batteries. *J Power Sources* 2021, *482*. https://doi.org/10.1016/J.JPOWSOUR.2020.228875.

(83) *NIST Chemistry WebBook*. https://webbook.nist.gov/chemistry/ (accessed 2025-07-27).

(84) *Vapor Pressure Chart side 1.xls | Enhanced Reader*.

(85) Wang, M.; Jiang, C.; Zhang, S.; Song, X.; Tang, Y.; Cheng, H. M. Reversible Calcium Alloying Enables a Practical Room-Temperature Rechargeable Calcium-Ion Battery with a High Discharge Voltage. *Nature Chemistry 2018 10:6* 2018, *10* (6), 667–672. https://doi.org/10.1038/s41557-018-0045-4.

Chapter VI

Conclusion and perspectives

6.1 General Conclusions

In this PhD thesis I am reporting my investigations focused on all the three fundamental components of calcium-based batteries, i.e., the electrolyte, positive, and negative electrode, through a systematic and integrated approach. The objective of this PhD project was to provide a broad overview of these elements and to develop reliable materials and methodologies that could advance both the understanding and feasibility of calcium-ion energy storage systems.

The first part focused on the design and evaluation of two novel calcium salts, Ca-FPB and $CaB_{12}H_{12}$, as non-aqueous aprotic electrolytes. Ca-FPB demonstrated excellent electrochemical stability and the ability to reversibly plate and strip calcium metal at room temperature, but its complex and moisture-sensitive synthesis presents challenges for large-scale implementation. Owing to this synthetic complexity, further systematic electrochemical and physicochemical characterizations could not be carried out for the insufficient material availability. For this reason, the investigation was redirected toward an electrolyte featuring a significantly simpler and faster synthetic route, thereby ensuring adequate material supply and enabling a more comprehensive and reliable characterization workflow.

Within this framework, $CaB_{12}H_{12}$ emerged as a viable alternative, owing to its simple and fast one-step synthesis, which ensured consistent material availability throughout the study. It showed promising reversibility, especially when dissolved in NMP and combined with BF_3OEt_2 as an additive, though its electrochemical stability window was more limited. Issues with solubility and sensitivity to solvent interactions highlight the need for further optimization, particularly regarding the formation and evolution of the solid–electrolyte interphase (SEI). Building on these results, further progress could be achieved by refining the synthetic route in order to minimize solvent co-crystallization and obtain a purer material, with the aim of improving salt dissociation in a wider range of more conventional solvents, since the current formulation relies on NMP, a solvent that is incompatible with practical electrode architectures due to its ability to dissolve common polymeric binders and its associated toxicity and processing limitations. This consideration motivated a shift in focus toward calcium-ion systems based on intercalation electrodes, where the use of conventional and readily available electrolytes becomes feasible and the constraints associated with metallic calcium and non-standard solvent environments can be circumvented.

To enable more accurate evaluation of electrode materials, a pseudo-capacitive three-electrode setup was developed and validated, using activated carbon as the counter electrode and gold as a quasi-

reference electrode. This configuration provided a stable and inert electrochemical environment, avoiding the complications associated with calcium metal and proving to be a valuable tool for fundamental investigations of calcium-based systems.

As for cathode materials, the Prussian Blue Analogue MF21 was selected on the basis of previous studies conducted within our research group on potassium-ion cells, in which this open-framework material had demonstrated highly reversible K^+ intercalation and remarkable cycling stability.

In this work, we confirmed that calcium can reversibly intercalate into the MF21 structure in aprotic electrolyte without compromising the integrity of the open-framework lattice. Ex-situ XRD analyses showed that the crystal structure remains preserved upon cycling, while Mössbauer spectroscopy revealed that the electrochemical response is predominantly governed by Fe redox activity, with only a minor contribution from Mn. Operando XRD further demonstrated a monophasic intercalation and deintercalation mechanism, accompanied by reversible lattice expansion and contraction.

Despite this intrinsic structural reversibility, full cells assembled with calcium metal exhibited a rapid capacity fade. This degradation is likely associated with the progressive formation of passivation products at the Ca–electrolyte interface, which hinder Ca^{2+} transport and limit the accessibility of the intercalation sites.

To decouple the behavior of MF21 from the instability of calcium metal, the material was evaluated in a pseudo-capacitive three-electrode configuration using activated carbon as the counter electrode and gold as a quasi-reference electrode. In this setup and using a conventional electrolyte based on $Ca(TFSI)_2$, the electrochemical response showed a clear stabilization over cycling, although with significantly reduced capacity. Under these conditions, however, signs of active-material dissolution were detected, which limited the applicability of this configuration and prevented a more extended investigation.

Altogether, these findings demonstrate that MF21 retains structural integrity and supports Ca^{2+} insertion, yet its practical performance is strongly influenced by interfacial reactions and by the choice of electrolyte. The marked differences between its behavior in K^+ and Ca^{2+} systems further highlight the importance of ion-specific interactions, including solvation, desolvation and host–structure compatibility. A deeper investigation of solvent effects, ion-transport pathways and interfacial processes, particularly in pseudo-capacitive configurations, will therefore be essential to clarify the electrolyte-dependent mechanisms governing Ca^{2+} insertion and to guide the rational development of Prussian Blue Analogues optimized for calcium-ion batteries.

On the anode side, two classes of materials were explored. First, TiO_2 nanotubes in the anatase phase were shown to reversibly incorporate Ca^{2+} ions, as demonstrated by the clear spectroscopic evidence of calcium uptake without structural collapse. Although the amount of intercalated Ca^{2+} was modest, the preservation of the anatase framework indicates that titanium oxides can accommodate divalent ions in a structurally resilient manner. A comparison between Ca-metal half cells and the pseudo capacitive configuration revealed that the electrochemical response of TiO_2 is strongly influenced by the electrolyte environment and by the accessible potential window. The higher capacities observed in the pseudo capacitive setup suggest that the intrinsic redox capability of TiO_2 is greater than what can currently be accessed in Ca-metal cells, where electrolyte limitations and interfacial parasitic reactions restrict the effective reversibility of the insertion process. Taken together, these findings indicate that the principal challenges for TiO_2 as a calcium-ion anode arise not from intrinsic structural limitations but from interfacial instability, initial irreversibility and electrolyte compatibility, ultimately motivating the exploration of alternative anode materials capable of operating in simpler and more conventional electrolyte environments without the need for complex cell configurations.

In this context, the second part of the study focused on alloy-type anodes, with the initial goal of identifying a calcium-based negative electrode capable of operating in conventional electrolytes and providing stable and reversible electrochemical behavior. Several Ca–Zn and Ca–Sn compositions were synthesized by arc melting and systematically investigated to identify materials that could function as practical anodes in calcium-ion systems.

Among the Ca–Zn alloys, the 1:2 composition exhibited the most stable and reproducible electrochemical response, confirming its suitability for sustained cycling. However, its high zinc content places its operating potential in a range that is too elevated for use as an anode. For this reason, the role of CaZn 1:2 evolved from candidate anode to reliable counter electrode, providing a stable platform for studying other calcium-ion electroactive materials without introducing complications associated with calcium metal. In addition, preliminary observations indicate that both calcium and zinc may participate in the electrochemical reactions, suggesting a possible dual-ion mechanism that requires further investigation to clarify its nature and potential implications.

Ca–Sn alloys, on the other hand, showed encouraging initial electrochemical activity, particularly under galvanostatic cycling, yet suffered from progressive increases in overpotential. This deactivation appears to arise from mechanical instability associated with volume changes and from the thickening of interfacial layers. Future studies should aim to identify the most stable Ca–Sn stoichiometry and the optimal operating potential range, while exploring strategies to mitigate structural degradation and improve long-term reversibility.

In conclusion, while calcium-based batteries still face significant technical barriers, this work demonstrates that some progress is reachable through the development of advanced electrolytes, optimized electrode configurations, and alloy-based strategies. Taken together, the results presented in this work provide useful insights into the critical factors influencing the performance and stability of calcium-based batteries and offer a foundation for further development and targeted optimization of their core components.

6.2 Perspectives

The investigations presented in this thesis demonstrate that calcium-based batteries are both highly promising and exceptionally demanding. On the one hand, the development of advanced electrolytes, optimized electrode configurations, intercalation type cathodes and alloy type anodes provides encouraging progress; on the other hand, intrinsic challenges such as sluggish calcium ion mobility, the formation of unstable interphases and interfacial passivation remain formidable obstacles.

For context, it is instructive to recall that research on lithium-ion batteries began in the early nineteen seventies and reached commercial maturity only in the early nineteen nineties, after almost two decades of continuous development. By contrast, calcium ion systems are still in an exploratory phase, and their technical barriers are amplified by the divalent nature of Ca^{2+} and by the difficulty of working with calcium metal, whose interfacial instability and reactivity complicate both electrolyte design and electrode evaluation.

Another fundamental difficulty is the absence of widely accepted standards for the study of calcium-based systems. In contrast to lithium-ion research, where established testing protocols and reference conditions enable meaningful comparison across studies, calcium ion research lacks common criteria for electrolyte formulation, cell configuration, testing procedures and reporting practices. Therefore, multiple interdependent factors such as electrolyte formulation, interfacial chemistry and electrode architecture must be evaluated simultaneously, without the possibility of isolating individual contributions.

Future work should therefore focus on addressing both the material related and the methodological challenges. On the materials side, efforts should aim at developing electrolytes with wider stability windows and simple, scalable synthetic routes, and at designing electrode materials capable of fast and reversible Ca^{2+} insertion while maintaining structural integrity over cycling. On the methodological side, the research community will benefit from the establishment of reproducible testing procedures, clearly defined cell architectures and transparent benchmarking criteria for calcium ion systems.

Although large scale commercialization may not be immediate, calcium-based batteries represent a powerful platform for understanding fundamental multivalent ion electrochemistry. They offer a unique opportunity to explore the limits of divalent ion storage and to advance the broader field of alternative energy storage technologies.

Acknowledgements

This research was carried out with the support of the PNRR – CN4, National Centre for Sustainable Mobility, Spoke 13 – Electric Drivetrain and Batteries, within the project "Sustainable processes for electrochemical energy storage: analysis, raw materials transformation, recycling and reuse" (CUP B83C22002900007), funded by Next Generation EU.

This thesis marks the conclusion of a long journey that has shaped me both personally and professionally, and none of it would have been possible without the extraordinary people I met along the way.

First and foremost, I wish to express my deepest gratitude to my supervisors, Prof. Sergio Brutti and Prof. Lorenzo Stievano. I have known Sergio since my Bachelor thesis, and I consider myself truly fortunate to have crossed paths with him so early in my academic journey. Lorenzo welcomed me into the laboratories of Montpellier with generosity and trust. Both have been exceptional mentors: they supported me unfailingly, found time for me despite impossibly full schedules, guided me with constructive advice, and always listened to my ideas with openness and respect, something that should never be taken for granted.

They shared their expertise, encouraged scientific exchanges, and allowed me to travel, discover new laboratories, and understand the importance of interdisciplinary collaboration. I grew enormously thanks to them.

I am also particularly grateful because they stood by me not only scientifically, but also while confronting the legendary bureaucratic monsters of a double PhD programme between Sapienza and the University of Montpellier. More than once, it felt like facing the final boss of academia's administrative labyrinth, and I sincerely thank them for helping me survive it.

My warm thanks go to Cathy, whose patience and kindness helped me navigate French bureaucracy with a smile. I am equally indebted to Laure Monconduit, head of the group in Montpellier: despite her many responsibilities, she always found the time to offer insightful and encouraging feedback on my research.

A special and heartfelt thank you also goes to Frédéric Favier, head of the department. His support, both scientific and logistical, was invaluable. His readiness to help, always accompanied by a smile, made a profound difference during my time in Montpellier, and I am deeply grateful for this.

My gratitude extends to all the colleagues in Montpellier who supported me, taught me, and made the laboratory feel like home.

A special thanks to Julien for guiding me through countless experiments and repairing just as many of my misadventures. To Moulay, who always found the right words to lift the mood. To Bernard, the "lord of the diffractometers," who taught me so much about diffraction and data analysis. And to Romain, whose directness helped me identify weaknesses and improve my work.
I cannot list everyone, but I wish to thank the entire batteries, fuel-cell, and supercapacitor groups. Each of you contributed to making my time in Montpellier richer, happier, and unforgettable. I truly left a piece of my heart there.

My thanks also go to Ümit Demirci, who generously offered his time, expertise, laboratory spaces, and team, especially Carlos and Eymeric, with whom I navigated the unpredictable world of calcium electrolytes.

For the same topic, I warmly thank Jan Bitenc and the NIC group in Ljubljana. Tjaša, in particular, shared the countless calcium-related misadventures with immovable optimism and humour. I also thank Fran and all the colleagues who welcomed me with warmth during my stay.

Back in Rome, almost, I am deeply grateful to Laura Silvestri, my supervisor at ENEA, whose support, both scientific and human, made an enormous difference during difficult moments. A special thanks to Rocco, my office companion at ENEA, who became a sort of older brother throughout this journey. I also wish to express my sincere gratitude to Gianni, whose experience and technical insight taught me a great deal, and whose consistently positive and energetic attitude helped brighten even the most challenging days. And thanks to the whole ENEA group, who made even the long commute to Anguillara feel lighter.

My sincere thanks go also to Laura Simonelli, who welcomed me with enthusiasm at the ALBA synchrotron in Barcelona, and to the entire CLAESS team, whose competence and warmth made me feel instantly at home.

Returning to Sapienza, I must thank the amazing ENAM group. With you I found not only brilliant scientists but true friends, with whom I could discuss everything, from high-level science to the most unserious conversations. In particular, Andrea, Gabriele, and Nicholas deserve special mention: each of you supported me scientifically and personally, whether in Rome, ENEA, Montpellier, or all three. Thank you.

Finally, and most importantly, I want to express a special and heartfelt thank you to my family. Their unconditional support, trust, and love allowed me to reach this point. They were my foundation throughout every difficulty and my greatest source of strength. This achievement is as much theirs as it is mine.

To all the friends, colleagues, and companions who are not explicitly named here but who shaped these years: thank you.

This PhD has been intense and challenging, but also incredibly rich. It feels like a lifetime has passed since its beginning, and thanks to all of you, I have grown far beyond what I could have imagined. I feel profoundly lucky to have met every person who crossed my path during this journey.

Thank you all.